Quantum nonadiabatic dynamics study on molecules of interstellar interest

A Thesis submitted for the degree of
Doctor of Philosophy

By
Nagaprasad Reddy Samala

School of Chemistry
University of Hyderabad
Hyderabad 500046
India

December 2014

Dedicated to my beloved
family and friends...

Statement

I hereby declare that the matter embodied in this thesis is the result of investigations carried out by me in the School of Chemistry, University of Hyderabad, Hyderabad, under the supervision of Prof. Susanta Mahapatra.

In keeping with the general practice of reporting scientific observations, due acknowledgment has been made whenever the work described is based on the findings of other investigators.

(Nagaprasad Reddy Samala)

December 2014
Hyderabad-500046

Certificate

Certified that the work embodied in this thesis entitled "Quantum nonadiabatic dynamics study on molecules of interstellar interest" has been carried out by Mr. Nagaprasad Reddy Samala under my supervision and the same has not been submitted elsewhere for a degree.

December 2014
Hyderabad-500046

(Prof. Susanta Mahapatra)
Thesis supervisor

Dean
School of Chemistry
Prof. C. R. Rao Road
University of Hyderabad
Hyderabad-500046, India

Acknowledgments

I would like to memorize my initial Ph.D days, I used to irritate all the labmates with my questions, used to show their impatience, misunderstandings..., clarifications..., discussions..., fun hours..., celebrations at various occasions..., ... Wow what a wonderful and overwhelming experience with in this great HCU campus. I have learned so many things from my surroundings, it helps me a lot through out my life.

I owe my deepest gratitude to **Prof. Susanta Mahapatra** for giving this opportunity to work with him, his excellent guidance and constant encouragement throughout my research work. His determination and hard work are inspirational to my research career. The experience that I gained in the last five years through his suggestions, comments and even critiques will help me in all my future endeavors.

It has been a great and exciting experience to study at School of Chemistry because it was one of my dreams to study in this great campus. My sincere thanks to the former and present Deans and all the faculty members for their assistance during my Ph.D. years. A special thanks to Prof. K. D. Sen, Prof. M. Durga Prasad, Prof. M. V. Rajasekharan and Prof. T. P. Radhakrishnan for their wonderful lectures on Quantum chemistry, Molecular spectroscopy, Mathematics and coding with Fortran programming. I thank Prof. S. K. Das, Prof. Lepiné Franck, Prof. Victor Despré and Prof. Alexander Kuleff, for fruitful discussions on collaborative projects. I also thank all the non-teaching staff of the School of Chemistry for their assistance on various occasions.

I am very thankful to the Council of Scientific and Industrial Research (CSIR), New Delhi, for the financial support and the Centre for Modelling Simulation and Design (CMSD), University of Hyderabad, for computational facilities.

I am grateful to Sri Krishnadevaraya University, Anantapur, classmates and seniors for encouraging me to do Ph.D.

I consider it as an honor to work with my labmates Jayachander Rao, Sivaranjana Reddy, Tanmoy Mondal, Susanta Ghanta, Rajgopal(Sr), Rajgopal(Jr), Tanmoy Roy, Rudraditya Sarkar, Sugata Goswami, Krishna Reddy, Arpita Ghosh, Aleem, Subrahmanyam, Arun and Saritha, Sridhar and Dinesh of Prof. M. D. P. group for many fruitful discussions, help and their warm company on various occasions. Their association will remain forever in my memory.

I thank Mrs. Gitashree Mahapatra (madam), Anusha and Anish for providing me a

homely atmosphere in several occasions.

I would like to thank all my School of Chemistry friends Ramu, Anand, Siva, Sivarama Krishna, Sasi, Yasin, Ramakrishna(BR), Pavan, Tiru, Ramu Yadav, Gupta, Obayya, Hari, Ramesh anna, Durga Prasad, Kesav, Srujana, Ashok, Chandu, Praveen, Ravi anna, Kishore, Sudeer, Rama Krishna, Babu, Nagarjun, Srinu, Gangadhar, Anji anna, Sekhar anna, Santosh, Hareesh, Bhanu, Nagarjuna, Venu, Seshadri, Sudha Rani, Madhu, Chandu, Narayana, Ramu, Barath, Kishore, Rambabu, DK anna, Viji, Ramesh, Rama Raju, Kishore, Anand, Nagarjun, Ugandar, Ganesh, Vignesh, Sekhar Reddy, Srinu(D), Srinu, Chari, Karunakar, Nanda, Satish, Vikranth, Naveen, Srinu, Sasank, Siva, Durgesh etc. without them my life would have been boring.

I would like to take this opportunity in thanking Gopal Reddy, Madhusudhan Reddy, Subba Reddy, Subba Reddy. N, Chenna Kesava Reddy, Siva Prakash, Jaipal Reddy, Sivanaga raju for their unconditional love, affection, encouragement, understanding and support throughout my career. *"As I have lot of friends, it is indeed a difficult task to mention them all here. I acknowledge each and every one of them for their contribution from the bottom of my heart."*

I am indebted to all my teachers, especially my first teacher in my school days Siva Reddy sir and college teachers Obula Reddy sir, Venkatnatha Reddy sir and all the Chemistry faculty members of SKU, Anantapur for providing gifted education.

I am so lucky for having a big and combined family, I am truly thankful to god for giving the wonderful family. I take immense pleasure in thanking my parents (Jayanagi Reddy and Eswaramma (late)), brothers(Siva Nagi Reddy, Siva Nagarjuna Reddy, Naga Vardhan Reddy and Naga Maheswara Reddy), Sister-in-laws (Hari Krishnamma, Siva Lakshmi Devi, Sujana and Sunitha) and their kids (Jyothy, Sravanthi, Prakash, Vijay, Teja, Yesvanthi, Kavya and Praneeth), sisters (Naga Lakshmi, Naga Surya, Nagamma, Ammanni), brother-in-laws (Chenna Reddy (late), Krishna Reddy, Naga Bhusan Reddy (late) and Sreenivasa Reddy) and kids Gowtami, Laya and Tinku, and also the extended family members for their love, care and unconditional support.

I have so many memories, I will forever thankful to all my roommates Raj(Jr), Sridhar, Ramu, Anand, Siva and Sivarama Krishna, for being part of my life, collaborates with me on the experiments I have made on cooking and the fun hours they have spent with me and friends Sivaranjana Reddy, Gupta, Raj(Sr), Aleem, Krishna, Dinesh, Saritha, Sasi, Yasin, Ramakrishna(BR), Pavan, Ramu Yadav, Tiru, Obayya, sreenivas for creating un removable memories in my heart. I will carry all these memories through out my life.

-Nagaprasad

Glossary

aug-cc-pVDZ	augmented correlation-consistent polarized Valence Double-ζ
aug-cc-pVTZ	augmented correlation-consistent polarized Valence Triple-ζ
aug-cc-pVQZ	augmented correlation-consistent polarized Valence Quadrapule-ζ
ADT	adiabatic to diabatic transformation
B3LYP	Becke 3-Parameter (exchange), Lee, Yang and Parr
BO	Born-Oppenheimer
CASSCF	complete active space self consistent field
CC	coupled cluster
CCSD	coupled cluster singles and doubles
cc-pVDZ	correlation-consistent polarized Valence Double-ζ
CIs	conical intersections
CRD	cavity ringdown
DFT	density functional theory
DIBs	Diffuse interstellar bands
DOF	degrees of freedom
DVR	discrete variable representation
EOM-CCSD	equation of motion-coupled cluster singles and doubles
FC	Franck-Condon
FWHM	full width at the half maximum
HO	Harmonic oscillator
HOMO	highest occupied molecular orbital
ISM	interstellar medium
IREP	irreducible representation
JT	Jahn-Teller
LIF	laser-induced fluorescence
LVC	linear vibronic coupling
MATI	mass-analyzed threshold ionization
MCTDH	multi-configuration time-dependent Hartree
MO	molecular orbital
MP2	Møller-Plesset perturbation theory
MRCI	multi-reference configuration interaction
OVGF	outer valence Greens function
PAHs	polycyclic aromatic hydrocarbons
PESs	potential energy surfaces
PJT	pseudo-Jahn-Teller

Continued on next page

– *Continued from previous page*

PIRI	photo-induced Rydberg ionization
QVC	quadratic vibronic coupling
RT	Renner-Teller
REMPI	resonance enhanced multiphoton ionization
R2C2PI	resonant two-color two-photon ionization
SPFs	single particle functions
VIEs	vertical ionization energies
VEEs	vertical excitation energies
WP	wave packet
ZEKE	zero electron kinetic energy

Contents

1 Introduction

1.1 Vibronic coupling effects in the molecular photophysics

The Born-Oppenheimer (BO) approximation treats the electronic and nuclear motions separately, and simplifies the complex Schrödinger equation of atomic and molecular systems [1]. This approximation allows to generate the so called adiabatic potential energy surfaces (PESs) by calculating electronic energies at various fixed nuclear positions [2–4]. Our understanding of the fundamental chemical processes occurring on a single adiabatic PES is exceptionally good [5–8]. However, the BO approximation breaks down when two or more electronic states exist energetically close, and thus lead to nonadiabtic regimes of motion i.e. nuclei can move on multiple electronic states simultaneously [9–13]. Such scenarios necessitate explicit treatment of combined nuclear and electronic interactions, which are more commonly termed as vibronic interactions. When the PESs are degenerate or near degenerate, the vibronic coupling (VC) elements diverge at the degeneracy points and supersedes the nuclear mass effect. Therefore they can not be ignored any more, leading failure of well known BO approximation [2–4,9–13].

The signatures of vibronic coupling effects are omnipresent in molecular photophysics, particularly in the electronic spectroscopy of polyatomic molecules, and have been observed in the experiments: (i) breakdown of mirror image symmetry in the optical spectra (ii) appearance of symmetry forbidden transitions in the spectrum (iii) dominant vibrational progression due to non-totally symmetric vibrational modes (iv) complex optical spectrum with broad and diffuse vibronic bands and (v) lack of fluorescence emission due to ultrafast nonradiative decay.

Remarkable advances in laboratory experimental spectroscopy, theoretical and computational methodologies enabled tremendous insights in the understanding of the vibronic effects. Novel spectroscopic techniques with high sensitivity and high resolution such as matrix isolation spectroscopy (MIS), cavity ring down spectroscopy (CRDS), resonance-enhanced multiphoton ionization (REMPI), photodissociation of Vander Waals complexes and femtosecond pump-probe techniques have been provided rich and accurate information on the molecular energy levels and time scales of nuclear motions. Detailed knowledge on the structure and dynamics of the electronically excited species is thus obtained by monitoring the intensities and broadening of the spectral lines of the low-temperature gas phase spectra. One such example is the naphthalene cation where the vibronic structure of excited electronic states was extensively studied by using multiple

techniques [14–16].

Analysis and interpretation of the extensive experimental spectroscopic data is cumbersome, and is often become difficult without an appropriate theoretical model. Several theoretical concepts to understand the vibronic coupling mechanism have been presented in the literature [4,17], and among them most celebrated is the linear vibronic coupling (LVC) approach developed by Köppel, Domcke, and Cederbaum [3]. In the LVC model, an appropriate model Hamiltonian in a diabatic basis is a prerequisite to study of nuclear dynamics of a molecular system. Extensive quantum chemistry calculations are employed to estimate the parameters of the Hamiltonian, and the spectrum simulations are followed by solving the eigenvalue equation of the Hamiltonian. The vibrational progressions, spectral intensity and broadening of vibronic bands of small to medium-sized molecules were studied in greater detail, and remarkable agreement has been achieved with the experimental observations [3]. In addition, most intuitive details of the time-evolved molecular system can be obtained by solving the time-dependent Schrödinger equation using standard wavepacket propagation methods. Estimated dynamical variables from the time-evolved wavepacket studies such as electronic populations and nuclear densities enabled additional insights in understanding of the molecular vibronic dynamics.

One of the challenging task in the theoretical treatment of vibronic coupling problems is the intersecting potential energy curves. The well-known von Neumann and Wigner's non-crossing rule [18] only applies to diatomic molecules, and breaks down for polyatomic molecules due to the availability of three or more degrees of freedom for the internal atomic motion. In such situations, the electronic states cross and exhibit a double cone type of topography in the vicinity of the crossing termed as *conical intersection* (CI) [19–21].

Based on the molecular symmetry, the CIs are generally classified as: (i) symmetry required or enforced and (ii) accidental symmetry allowed intersections. In fact Jahn-Teller (JT) effect, yields conical intersection, otherwise it would be a degeneracy point as can be seen in linear molecules where there will be no CIs [20]. The degeneracy point in linear molecules cannot develop as conical intersection due to Renner-Teller (RT) effect [22]. They are merely glancing interactions. While the accidental CI corresponds to two states of distinct spatial symmetry, the CIs between two electronic states of same symmetry is called as same-symmetry accidental CIs. Symmetry-allowed (and accidental) CIs are ubiquitous in molecular systems where as same-symmetry CIs are very rare [23,24]. CIs are further classified, based on the topography of the intersecting PESs in the vicinity of a crossing, as peaked and sloped [25–27].

It is now fairly accepted that CIs serve as the "bottleneck" in photophysical and photo chemical transitions [28–31] and also referred to as photochemical funnels in the literature [32]. The book edited by Domcke, Yarkony and Köppel represent an excellent collection of articles in this emerging area of chemical dynamics [23]. Strictly speaking,

with respect to the main stream computational chemistry which considers electronic structure calculations of polyatomic molecules with fixed nuclei and the nuclear dynamics along the PESs, the CIs and the associated VC effects are important extensions which take into account the coupling between the electronic and nuclear motions.

CIs strongly influence the excited-state dynamics of molecules, and most importantly, their role in area of astrophysical spectroscopy, photochemistry, photobiology and reactive chemical dynamics have been extensively studied [3, 17, 23, 28–37]. Formation of multiple photoproducts is a typical example of the role of CIs in the photochemistry of organic hydrocarbon [26, 27]. Also, CIs provide an efficient pathway for radiationless decay, which occur in subpicosecond time scale, between electronic states. In such cases, the photoexcited state of the system is instantaneously transferred back to the ground state without undergoing any photochemical reaction thereby making the system highly photostable.

1.2 Photochemistry and photophysics of interstellar molecules

The diffuse interstellar bands (DIBs) are absorption features observed in the electromagnetic spectra of astronomical objects. These are caused by the absorption of light by the dust grains in the near infrared and UV-Visible wavelengths. Heger [38] was the first person to observe two of the strongest of these bands in 1921, and it was proved in 1934 by Merrill *et al.* [39] that these bands were originated from interstellar medium. The origin of DIBs was unknown and hotly disputed for many years, and tentatively attributed to the carbon bearing molecules such as carbon clusters and polycyclic aromatic hydrocarbons. According to recent spectral atlases, the number of reported DIBs exceeds over 500 [40, 41] and not a single feature has been positively identified with the laboratory spectra. Assignment of the DIBs remains one of the long standing mystery in astrophysical research.

The PAH-DIB proposal has been put forward more than two decades ago, and consistent efforts are being made (to date) by the laboratory and stellar spectroscopists to identify them by comparing the results from these two different types of measurements. From recent studies, in addition with PAH-DIB proposal, carbon clusters and carbon chains combination with hydrogens also (poly acetylenes and cumulene carbenes) shown to be a possible carriers of DIBs [42–45].

Identification and assignment of molecular carriers of DIBs has been one of the most challenging and notoriously difficult problem in stellar spectroscopy. Among many, PAHs particularly their radical cations (PAH^+s) were postulated to be promising molecular candidates since [46, 47]: (1) spectral range of DIBs in the UV region coincides with their electronic absorption range [48], (2) the PAH^+s are proposed to be more abundant

(falls in the third position after H_2 and CO [49]) in the interstellar medium and [50, 51] (3) they are photostable-survive despite being exposed to the strong UV radiation emitted by young stars and therefore could be the possible source of unidentified infra-red bands [52, 53].

For a successful identification of a particular molecular species in the interstellar medium, most important are the precise location of the spectral frequency and its line strength. Although the experimental laboratory high-resolution photelectron and absorption spectral studies provided crucial details, challenges remain in astrophysical molecular identification. One of the major difficulty is testing the molecular candidates by replicating the cold harsh conditions of the interstellar medium. Many experimental groups devoted to simulate those conditions in laboratory. For example, molecular beams and jets coupled with discharge or laser vaporization sources, resonance-enhanced multiphoton ionization combined with time of flight mass spectrometry (REMPI-TOF), plasma-frequency double modulation, electron detachment, ion trap and degenerate four-wave mixing are among the techniques. CRDS has been frequently applied for measurements of DIBs carrier candidates. In recent years, a number of so called broadband cavity enhanced absorption spectroscopy (BBCEAS) techniques have been capable of swiftly recording gas phase absorption spectra of transients, with spectral resolution equivalent to astronomical observations, are utilized to explore the potential candidates of DIB carriers [54].

Present thesis explores the structure and dynamics of some of the important interstellar molecules, viz., radical cations of medium sized PAH molecules tetracene (Tn^+), pentacene (Pn^+), hexacene (Hn^+), phenanthrene (Pnt^+), pyrene (Py^+) and acenaphthene (Acn^+). The corresponding neutral molecules are abbreviated as Tn, Pn, Hn, Pnt, Py and Acn in the rest of the chapters. In addition to PAHs, a detailed quantum mechanical study on astronomically important propadienylidene and diacetylene radical cation are also performed. The motivation behind this work primarily stems from the vast amount of data available from the experimental measurements on these systems by various groups and also the importance of these molecular systems in the interstellar medium [15, 16, 45, 55–88]. The linear isomer of propadienylidene was reported to absorb in the region of the DIBs observed at 5450 Å and 4881 Å [45]. Similarly the comparisons between the laboratory spectral data and astronomical stars data reveals that, many PAH molecular cations show absorptions very near to the DIB positions. Tn^+ absorption may be related to the 8648/8649/8621 Å DIBs [61, 71], Pn^+ may be a likely carrier of 8283.45 Å DIB [71], Pnt^+ could be responsible for 8572 Å DIB [61]. In 1990's Py^+ was a likely carrier of the 4430 Å DIB, and finally concluded that, substituted Py^+ or Py^+-like species is responsible for this band [83]. Acn^+ absorption placing very near to the 6491.88 Å DIB [86], a likely carrier of this DIB. In carbon chains, propadienylidene molecular data suggested that this neutral molecule is a "likely candidate" of molecular carrier of broad 5450 and 4881 Å DIBs [45]. In case of diacetylene radical cation the $\widetilde{X} \leftarrow \widetilde{A}$ absorption occurs in the same wavelength region of the observed 5069 Å DIB [44].

In addition to the primary interest of spectral identification, it appears logical to understand how the interaction of UV radiation with the interstellar aromatic molecules which promotes it to excited electronic states, is the first step in their photophysics or photochemistry. The lack of fluorescence emission and ultrafast nonradiative decay are indicative of complex vibronic coupling in the electronic excited states of these systems. Knowledge on the time scales of relaxation of the low-lying excited electronic states of these species is the major goal in the process of understanding of the molecular universe. This issue is discussed at length in the Chapters 3-6.

1.3 Outline of the thesis

Detailed theoretical background of vibronic interactions in polyatomic molecules is presented in Chapter 2. The concept of adiabatic and diabatic electronic basis is introduced. Construction of model diabatic electronic Hamiltonian utilizing elementary symmetry selection rules is elaborated with few representative examples. The strategy to estimate the parameters of the electronic Hamiltonian, in particular, is described in each chapter. Technical details of the first principles quantum dynamics calculations are also discussed. Spectrum simulations using the time-independent and time-dependent approaches are also discussed.

In Chapter 3, a detailed theoretical account of the electronic absorption spectroscopy of propadienylidene ($H_2C{=}C{=}C{:}$) molecule is presented. The structure and dynamics of first three low-lying excited electronic states of l-C_3H_2 are studied with a model diabatic vibronic Hamiltonian. Electronic structure calculations are carried out at the CASSCF-MRCI and EOM-CCSD level of theory employing the aug-cc-pVTZ basis set. Using the calculated electronic structure data suitable vibronic Hamiltonians are constructed utilizing a diabatic electronic basis and displacement coordinates of the normal vibrational modes. The theoretical results are discussed in relation to those recorded in recent experiments, theory and discussed in connection with the recorded DIBs.

A benchmark *ab initio* quantum dynamical study on photoinduced dynamics of four low-lying electronic states of Tn^+, Pn^+ and Hn^+ radical cations are presented in Chapter 4. The photoelectron spectra and decay rates of electronic states are calculated by developing a model vibronic Hamiltonian consisting of four electronic states by including 18 modes out of a total of 84 for Tn^+, 20 out of 102 for Pn^+ and 23 out of 120 for Hn^+. The theoretical results are compared with the recent experimental results. The fundamental issues such as broadening of vibronic bands, lack of fluorescence emission and photostability are discussed in detail in connection to the astrophysical observations. Highly resolved vibronic structures of some of these electronic bands of Tn^+ and Pn^+ are examined, compared with the high resolution ZEKE and matrix isolation spectral results and discussed in connection with the recorded DIBs.

In Chapter 5, a detailed quantum dynamical study on photoinduced dynamics of ground and first three low-lying electronic states of Pnt^+, Py^+ and Acn^+ radical cations are presented. The photoelectron spectra and decay rates of electronic states are calculated by developing a model vibronic Hamiltonian consisting of four electronic states by including reliable vibrational modes. We included 20 modes out of the total of 66 for Pnt^+, 22 out of 72 for Py^+, and 24 out of 60 for Acn^+. This study is aimed to unravel photostability, spectroscopy, and time-dependent dynamics of their excited electronic states in connection to the astrophysical observations. The theoretical results are compared with the recent experimental results. Highly resolved vibronic structures of some of these electronic bands are examined, compared with the high resolution zero electron kinetic energy (ZEKE) and matrix isolation spectral data and discussed in connection with the recorded DIBs.

Theoretical study of the photoelectron spectroscopy of diacetylene is presented in Chapter 6. State-of-the-art quantum chemistry calculations are carried out to establish potential energy surfaces and coupling surfaces of two energetically low-lying degenerate doublet electronic states of the diacetylene radical cation. Coupling of these electronic states caused by the RT and pseudo-Jahn-Teller (PJT) type of interactions is examined. The impact of these couplings on the nuclear dynamics of the participating electronic states is thoroughly investigated by quantum mechanical methods by including all vibrational modes and the results are compared with those observed in the experiments. The structure of the $\widetilde{X}$ and $\widetilde{A}$ bands are well resolved, nonadiabatic coupling between these two electronic states is quenched by the energy separation. The theoretical results are discussed in relation to those recorded in recent experiments, theory and discussed in connection with the recorded DIBs.

Final conclusions and future directions are presented in Chapter 7.

References

[1] M. Born and R. Oppenheimer, Ann. Phys. **84**, 457 (1927).

[2] C. J. Ballhausen and A. E. Hansen, Ann. Rev. Phys. Chem. **23**, 15 (1972).

[3] H. Köppel, W. Domcke and L. S. Cederbaum, Adv. Chem. Phys. **57**, 59 (1984).

[4] G. Fisher, *Vibronic coupling*, Academic press, London (1984).

[5] R. G. Bray and M.J. Berry, J. Chem. Phys. **71**, 4909 (1979).

[6] J. Ford, Advan. Chem. Phys. **24**, 155 (1973).

[7] D. F. Heller and S. Mukamel, J. Chem. Phys. **70**, 463 (1979).

[8] W. H. Miller *Dynamics of molecular collisions*, Plenum. Press, New York , (1976).

[9] H. Köppel, L. S. Cederbaum, and S. Mahapatra, *Theory of the JahnTeller Effect*, in *Handbook of high-resolution spectroscopy*, John Wiley & Sons, (2011).

[10] S. Mahapatra, Acc. Chem. Res. **42**, 1004 (2009).

[11] M. Baer, *Beyond Born-Oppenheimer: electronic non-adiabatic coupling terms and conical intersections*, John Wiley and Sons, (2006).

[12] M. S. Child in *Atom-Molecular collision theory*, edited by R. B. Bernstein, Plenum press, New York, (1979).

[13] B. DiBartolo, *Radiationless processes*, PLenum press, New York, (1980).

[14] J. Oomens, A. G. G. M. Tielens, B. G. Sartakov, G. V. Helden and G. Meijer Astrophys. J. **591**, 968 (2003).

[15] L. Biennier, F. Salama and L. J. Allamandola, J. Chem. Phys. **118**, 7863 (2003).

[16] L. Biennier, F. Salama M. Gupta ans A. O'Keefe Chem. Phys. Lett. **387**, 287 (2004).

[17] I. B. Bersuker *The Jahn-Teller Effect and Vibronic Interactions in Modern Chemistry* (Plenum Press, New York, 1984).

[18] J. V. Neumann and E. P. Wigner, Physik. Z. **30**, 467 (1929).

[19] H. A. Jahn and E. Teller, Proc. R. Soc. London, Ser. A **161**, 220 (1937).

[20] E. Teller, J. Phys. Chem. **41**, 109 (1937).

[21] G. Herzberg and H. C. Longuet-Higgins, Discuss. Farad. Soc. **35**, 77 (1963).

[22] R. Renner, Z. Phys. **92**, 172 (1934).

[23] *Conical Intersections: Electronic Structure, Dynamics and Spectroscopy*, edited by W. Domcke, D. R. Yarkony, and H. Köppel (WorldScientific, Singapore, 2004).

[24] *Conical Intersections: Theory, Computation and Experiment*, W. Domcke, D. R. Yarkony, H. Köppel, Eds., (World Scientific: Singapore, 2011).

[25] G. J. Atchity, S. S. Xantheas, K. Ruendenberg, J. Chem. Phys. **95**, 1862 (1991).

[26] A. Migani and M. Olivucci, Chapter 6, In; *Conical Intersections: Electronic Structure, Dynamics and Spectroscopy*, edited by W. Domcke, D. R. Yarkony, and H. Köppel (WorldScientific, Singapore, 2004).

[27] M. J. Paterson, M. A. Robb, L. Blancafort and A. D. DeBellis, J. Phys. Chem. A **109**, 7527 (2006).

[28] M. A. Robb, F. Bernardi, and M. Olivucci, Pure and Appl. Chem. **67**, 783 (1995).

[29] F. Bernardi, M. Olivucci, and M. A. Robb, Chem. Soc. Rev. **25**, 321 (1996).

[30] W. Domcke and G. Stock, Adv. Chem. Phys. **100**, 1 (1997).

[31] *Conical intersections in photochemistry, spectroscopy and chemical dynamics*, Chem. Phys. **259**, 121-337 (2000).

[32] J. Michl and V. Bonacic-Koutecky, *Electronic Aspects of Organic Photochemistry* (Wiley, New York, 1990).

[33] T. Carrington, Discuss. Farad. Soc. **53**, 27 (1972).

[34] C. A. Mead and D. G. Truhlar, J. Chem. Phs. **70**, 2284 (1979).

[35] M. Desouter-Lecomte, C. Galloy, J. C. Lorquet, and M. Vaz Pires, J. Chem. Phys. **71**, 3661 (1979).

[36] G. Fischer, *Vibronic Coupling* (Academic Press, London, 1984).

[37] I. B. Bersuker and V. Z. Polinger, *Vibronic Interactions in Molecules and Crystals* (Springer-Verlag, Berlin, 1989).

[38] M. L. Heger, Lick. Obs. Bull. **10**, 146 (1921).

[39] P. W. Merrill, Publ. Astron. Soc. Pac. **46**, 206 (1934).

[40] L. M. Hobbs et al. Astrophys. J. **680**, 1256 (2008).

[41] L. M. Hobbs et al. Astrophys. J. **705**, 32 (2009).

[42] J. P. Maier, Chem. Soc. Rev. **17**, 45 (1988).

[43] J. P. Maier, Chem. Soc. Rev. **26**, 21 (1997).

[44] J. Krełowski, Y. Beletsky, G.A. Galazutdinov, R. Kołos, M. Gronowski and G. Locurto, Astrophys. J. **714**, L64 (2010).

[45] J. P. Maier, G. A. H. Walker, D. A. Bohlender, F. J. Mazzotti, R. Raghunandan, J. Fulara, I. Garkusha, A. Nagy, Astrophys. J. **726**, 41 (2011).

[46] a) *Polycyclic Aromatic Hydrocarbons and Astrophysics,* edited by A. Leger, L. D'Hendecourt, N. Boccara, (Reidel, Dordrecht, 1987); b) L. J. Allamandola, Top. Curr. Chem. **153**, 1 (1990); c) J. Szczepanski, M. Vala, Nature London, **363**, 699 (1993); d) F. Salama, L. J. Allamandola, J. Chem. Soc., Faraday Trans. **89**, 2277 (1993); e) J. De Frees, M. D. Miller, D. Talbi, F. Pauzat, Y. Ellinger, Astrophys. J. **408**, 530 (1993); f) D. M. Hudgins, S. A. Sandford, L. J. Allamandola, J. Phys. Chem. **98**, 4243 (1994); g) F. Salama, C. Joblin, L. J. Allamandola, J. Chem. Phys. **101**, 10252 (1994); h) D. M. Hudgins, L. J. Allamandola, J. Phys. Chem.**99**, 8978 (1995).

[47] T. Shida, S. Iwata, J. Am. Chem. Soc. **95**, 3473 (1973).

[48] A. Léger, L. D'Hendecourt, Astron. Astrophys. **146**, 81 (1985).

[49] A. Léger, J. L. Puget, Astron. Astrophys. **137**, L5 (1984).

[50] J. R. Platt, J. R. Astrophys. J. **123**, 486 (1956).

[51] B. Donn, B. Astrophys. J. **152**, L129 (1968).

[52] L. J. Allamandola, A. G. Tielens, J. R. Barker, Astrophys. J. Suppl. Ser. **71**, 733 (1989).

[53] J. L. Puget, A. Léger, ARA&A, **27**, 161 (1989).

[54] A. J. Walsh, D. Zhao, W. Ubachs and H. Linnartz The diffuse interstellar bands, Proceedings IAU Symposium, **297**, (2013).

[55] P. Thaddeus, M. C. McCarthy, M. J. Travers, C. A. Gottlieb, W. Chen, Faraday Discuss. **109**, 121 (1998).

[56] R. A. Seburg, E. V. Patterson, J. F. Stanton, R. J. McMahon, J. Am. Chem. Soc. **119**, 5847 (1997).

[57] J. F. Stanton, J. T. DePinto, R. A. Seburg, J. A. Hodges, R. J. McMahon, J. Am. Chem. Soc. **119**, 429 (1997).

[58] J. A. Hodges, R. J. McMahon, K. W. Sattelmeyer J. F. Stanton, Astrophys. J. **544**, 838 (2000).

[59] H. Linnartz, N. Wehres, H. VanWinckel, G. A. H. Walker, D. A. Bohlender, A. G. G. M. Tielens, T. Motylewski, J. P. Maier, Astron. Astrophys. **511**, L3 (2010).

[60] J. F. Stanton, Faraday Discuss. **150**, 331 (2011).

[61] F. Salama, Origins of Life and Evolution of the Biosphere, **28**, 349 (1998).

[62] R. Boschi, E. Clar, W. Schmidt, J. Chem. Phys. **60**, 4406 (1974).

[63] O. Parisel, G. Berthier, Y. Ellinger, Astron. Astrophys. **266**, L1 (1992).

[64] M. S. Deleuze, A. B. Trofimov, L. S. Cederbaum, J. Chem. Phys. **115**, 5859 (2001).

[65] M. S. Deleuze, J. Chem. Phys. **116**, 7012 (2002).

[66] W. Schmidt, J. Chem. Phys. **66**, 828 (1977).

[67] E. S. Kadantsev, M. J. Stott, A. Rubio, J. Chem. Phys. **124**, 134901 (2006).

[68] G. Malloci, G. Mulas, C. Joblin, Astron. Astrophys. **426**, 105 (2004).

[69] R. Mondal, C. Tönshoff, D. Khon, D. C. Neckers, H. F. Bettinger, J. Am. Chem. Soc. **131**, 14281 (2009).

[70] F. Salama, C. Joblin, L. J. Allamandola, Planet. Space Sci. **43**, 1165 (1995).

[71] F. Salama, G. A. Galazutdinov, J. Krełowski, L. J. Allamandola, F. A. Musaev, Astrophys. J. **526**, 265 (1999).

[72] V. Coropceanu, M. Malagolo, D. A. da Dilva Filho, N. E. Gruhn, T. G. Bill, J. L. Brédas, Phys. Rev. Lett. **89**, 275503 (2002).

[73] E. Clar, J. M. Robertson, R. Schlögl, W. Schmidt, J. Am. Chem. Soc. **103**, 1320 (1981).

[74] J. Zhang, L. Pei, W. Kong, J. Chem. Phys. **128**, 104301 (2008).

[75] J. Zhang, F. Han, L. Pei, W. Kong, A. Li, Astrophys. J. **715**, 485 (2010).

[76] A. Amirav, U. Even, J. Jortner, J. Chem. Phys. **71**, 2319 (1979).

[77] A. Amirav, U. Even, J. Jortner, J. Chem. Phys. **75**, 3770 (1981).

[78] J. Szczepanski, J. Drawdy, C. Wehlburg, M. Vala, Chem. Phys. Lett. **245**, 539 (1995).

[79] J. Szczepanski, C. Wehlburg, M. Vala, Chem. Phys. Lett. **232**, 221 (1995).

[80] P. Bréchignac, T. Pino and N. Boudin, Spectrochimica Acta. A, **57**, 745 (2001).

[81] P. Bréchignac and T. Pino, Astron. Astophys, **343**, L49 (1999).

[82] X. Tan and F. Salama, Chem. Phys. Lett. **422**, 518 (2006).

[83] F. Salama and L. J. Allamandola, Nature, **358**, 42 (1992).

[84] F. Salama, C. Joblin and L. J. Allamandola, J.Chem.Phys. **101**, 10252 (1994).

[85] F. Salama and L. J. Allamandola, J. Chem. Soc., Faraday Trans. 1993, **89**, 2277 (1993).

[86] T. M. Halasinski, F. Salama and L. J. Allamandola, Astrophys. J. **628**, 555 (2005).

[87] F. Salama and L. J. Allamandola, Adv. Space Res. **15**, 3(413) (1995).

[88] M. K. Crawford, A. G. G. M. Tielens and L. J. Allamandola, Astrophys. J. **293**, L45 (1985).

2 Theoretical methodology

2.1 Born-Oppenheimer approximation and adiabatic representation

The quantum chemistry and dynamics of a molecule can be studied by solving the time-independent Schrödinger equation, which is commonly expressed as

$$\mathcal{H}(r,R)\Psi(r,R) = \mathcal{E}\Psi(r,R), \tag{2.1}$$

where $\Psi(r,R)$ and $\mathcal{E}$ represent the wavefunction and energy, respectively. The molecular Hamiltonian $\mathcal{H}$, consists of kinetic and potential energy terms of electrons and nuclei. It can be expressed in terms of electronic (r) and nuclear coordinates (R) is given by

$$\mathcal{H}(r,R) = \underbrace{\mathcal{T}_e(r) + \mathcal{U}(r,R)}_{\mathcal{H}_e} + \mathcal{T}_N(R) \tag{2.2}$$

where $\mathcal{T}_e$ and $\mathcal{T}_N$ are the operators for the electronic and nuclear kinetic energy terms, respectively. $\mathcal{U}(r,R)$ is the total potential energy of the electrons and nuclei (electron-electron, electron-nuclear and nuclear-nuclear interactions).

The nonseparability of $\mathcal{U}(r,R)$ in terms of electronic and nuclear motions makes the solution of Eq. 2.2 cumbersome. To tackle this nonseparability problem, one of the most fundamental approximation known as adiabatic approximation is proposed. This approximation consists of two steps: first, compute the electronic wavefunctions for fixed positions of the nuclei. Secondly, solve the nuclear motion using the computed potential energies. The rationale for this approximation derives from the much heavier mass (slower motion) of the nuclei relative to the electrons. This is also called as clamped nuclei approximation [1, 2]. Fixed nuclei means $\mathcal{T}_N = 0$ in the Hamiltonian. Then, the orthonormal electronic eigenfunctions $\psi_n(r;R)$ and electronic energy $\mathcal{V}_n(r;R)$ at a fixed nuclear position are calculated by solving electronic Schrödinger equation

$$\mathcal{H}_e(r,R)\psi_n(r;R) = (\mathcal{T}_e(r) + \mathcal{U}(r,R))\psi_n(r;R) = \mathcal{V}_n(r;R)\psi_n(r;R) \tag{2.3}$$

Within the adiabatic theorem, the final molecular wavefunction can be expressed as a product of electronic eigenfunction ($\psi_n(r;R)$) and the nuclear eigenfunction ($\chi(R)$) as

$$\Psi_i(r,R) = \sum_n \psi_n(r;R)\chi_{ni}(R). \tag{2.4}$$

Upon substitution of $\Psi_i(r,R)$ in Eq. (2.1), one readily obtains the following coupled differential equations

$$[\mathcal{T}_N(R) + \mathcal{V}_n(r;R) - \mathcal{E}]\,\chi_n(R) = \sum_m \Lambda_{nm}(R)\chi_m(R) \tag{2.5}$$

If we rewrite the fundamental set of equations given in Eq. 2.5 as a matrix Schrödinger equation, we have

$$[\mathcal{T}_N(R) + \mathcal{V}(r;R) - \mathbf{\Lambda} - \mathcal{E}]\,\chi = 0 \tag{2.6}$$

where

$$\sum_m \Lambda_{nm}(R) = -\int dr \psi_n^*(r;R)\,[\mathcal{T}_N(R), \psi_m(r;R)] \tag{2.7}$$

defines the nonadiabatic operator between the electronic states of n and m through the nuclear kinetic energy operator. The nuclear kinetic energy operator takes non-diagonal form in this adiabatic electronic representation. After some mathematical transformation, the quantity $\Lambda_{nm}(R)$ can be represented as [1,3]

$$\Lambda_{nm}(R) = -\sum_i \frac{\hbar^2}{M_i} F_{nm}^{(i)}(R)\frac{\partial}{\partial R_i} - \sum_i \frac{\hbar^2}{2M_i} G_{nm}^{(i)}(R) \tag{2.8}$$

where $F_{nm}^{(i)}(R)$ and $G_{nm}^{(i)}(R)$ represents the derivative coupling vector and scalar coupling, respectively, and given by

$$F_{nm}^{(i)}(R) = \langle \psi_n(r;R)|\nabla_i|\psi_m(r;R)\rangle \tag{2.9}$$

and

$$G_{nm}^{(i)}(R) = \langle \psi_n(r;R)|\nabla_i^2|\psi_m(r;R)\rangle \tag{2.10}$$

If Λ_{nm} in Eq. (2.5) is approximated to zero, which is also known as the BO approximation [2,4,5], then the molecular wavefunction simply becomes

$$\Psi_i^{BO}(r,R) = \sum_n \psi_n(r;R)\chi_{ni}^{BO}(R)$$

The electronic and nuclear eigenvalue equations are given by

$$[\mathcal{T}_e(r) + \mathcal{U}(r,R) - \mathcal{V}_n(r;R)]\,\psi_n(r;R) = 0$$

and

$$[\mathcal{T}_N(R) + \mathcal{V}_n(r;R) - \mathcal{E}]\,\chi_{ni}^{BO}(R) = 0.$$

2.2 Breakdown of BO approximation and diabatic representation

As mentioned in the previous section, Eq. 2.3 represents the electronic Schrödinger equation which can be rewritten as

$$\begin{aligned}\langle\psi_m(r;R)|\mathcal{H}_e(r;R)|\psi_n(r;R)\rangle &= \langle\psi_m(r;R)|\mathcal{V}_n(r;R)|\psi_n(r;R)\rangle \\ \langle\psi_m(r;R)|\mathcal{H}_e(r;R)|\psi_n(r;R)\rangle &= \mathcal{V}_n(r;R)\delta_{mn}\end{aligned}$$

Upon Differentiation with respect to R, the above equation transform to

$$\mathcal{V}_n\langle\frac{\partial}{\partial R}\psi_m|\psi_n\rangle + \langle\psi_m|\frac{\partial\mathcal{H}_e(r;R)}{\partial R}|\psi_n\rangle + \mathcal{V}_m\langle\psi_m|\frac{\partial}{\partial R}\psi_n\rangle = 0 \tag{2.11}$$

$$\langle\psi_m|\frac{\partial}{\partial R}|\psi_n\rangle = \frac{1}{(\mathcal{V}_n-\mathcal{V}_m)}\langle\psi_m|\frac{\partial\mathcal{H}_e(r;R)}{\partial R}|\psi_n\rangle$$

Finally, using the above equation, $F^{(i)}_{nm}(R)$ can be expressed as [1,6,7]

$$F^{(i)}_{nm}(R) = \frac{\langle\psi_m(r;R)|\nabla_i\mathcal{H}_e(r;R)|\psi_n(r;R)\rangle}{\mathcal{V}_n(R)-\mathcal{V}_m(R)}, \tag{2.12}$$

where $\mathcal{H}_e$ represents the electronic Hamiltonian for fixed nuclear coordinates. When the two surfaces become degenerate i.e., $\mathcal{V}_n(R) = \mathcal{V}_m(R)$, then the derivative coupling elements of Eq. (2.12) exhibit a singularity which in principle leads to discontinuity in both the electronic wavefunction and the derivative of energy. The adiabatic representation unsuitable for the computational study of the nuclear dynamics at the point of degeneracy because of extremely large derivative coupling, $F^{(i)}_{nm}(R)$. Inelastic atom-atom collisions and ultrafast radiationless decay of excited electronic states are the typical examples associated with the violation of the BO approximation [7,8]. To overcome the problem of singular derivative couplings of the adiabatic representation, the basis functions are replaced with diabatic basis which are smooth and slowly varying functions of nuclear coordinates [1,9–12]. A suitable unitary transformation of the adiabatic basis results diabatic basis functions:

$$\phi(r;R) = \mathbf{S}(R)\ \psi(r;R), \tag{2.13}$$

where $\phi(r;R)$ and $\psi(r;R)$ are electronic eigenfunctions in diabatic and adiabatic representations, respectively. $\mathbf{S}(R)$ is the orthogonal transformation matrix for a 2×2 Hamiltonian which is given by

$$\mathbf{S}(R) = \begin{pmatrix}\cos\theta(R) & -\sin\theta(R)\\ \sin\theta(R) & \cos\theta(R)\end{pmatrix} \tag{2.14}$$

The matrix $\mathbf{S}(R)$ is called the adiabatic-to-diabatic transformation (ADT) matrix. $\theta(R)$ represents the transformation angle. The necessary condition for such transformation is that the first-order derivative couplings of Eq. (2.9) should vanish in the new representation for all nuclear coordinates [13, 14] i.e.,

$$\int dr \psi_n^*(r;R) \frac{\partial}{\partial R_i} \psi_m(r;R) = 0. \tag{2.15}$$

This condition leads to the following differential equations for the transformation matrix [13, 15, 16]

$$\frac{\partial \mathbf{S}}{\partial R_i} + \mathbf{F^{(i)}}\mathbf{S} = 0, \tag{2.16}$$

where the elements of the first-order derivative coupling matrix $\mathbf{F^{(i)}}$ are given by Eq. (2.9). A unique solution of the above equation can be obtained only when starting from a finite subspace of electronic states [14]. Therefore, for polyatomic molecular systems rigorous diabatic electronic states do not exist [14]. Several approximate schemes are therefore developed to construct diabatic electronic states [16–18].

2.2.1 The model diabatic vibronic Hamiltonian

One of such approximation is a quasi diabatic Hamiltonian method proposed by Köppel *et al.* [1]. In this scheme, it is assumed that a diabatic basis is already existed and a model diabatic Hamiltonian in such basis is constructed using symmetry arguments in terms of dimensionless normal coordinates. The dimensionless normal coordinates of the electronic ground state are thus used to construct the vibronic Hamiltonian for the final states of the excited/ionized species. The latter coordinates can be obtained by performing electronic structure calculations employing a suitable quantum chemistry software. The mass-weighted normal coordinates (q_i) obtained during the diagonalization of the force field are then converted into the dimensionless form by

$$Q_i = (\omega_i/\hbar)^{\frac{1}{2}} q_i, \tag{2.17}$$

where ω_i is the harmonic frequency of the i^{th} vibrational mode. These actually describes the normal displacement coordinates from the equilibrium configuration, $\mathbf{Q} = 0$, of the reference state. The basic vibronic Hamiltonian describing the photoinduced molecular process is then given by [1]

$$\mathcal{H} = (\mathcal{T}_\mathcal{N} + \mathcal{V}_0)\mathbf{1}_n + \Delta\mathcal{H}. \tag{2.18}$$

where $\mathbf{1_n}$ is a n×n unit matrix and $(\mathcal{T}_\mathcal{N} + \mathcal{V}_0)$ is the Hamiltonian for the unperturbed electronic reference ground state. This reference state is vertically well separated in energy from the excited states and is treated as harmonic. Accordingly, $\mathcal{T}_\mathcal{N}$ and $\mathcal{V}_0$ are

given by

$$\mathcal{T}_{\mathcal{N}} = -\frac{1}{2}\sum_{i}\omega_i\left[\frac{\partial^2}{\partial Q_i^2}\right], \tag{2.19}$$

and

$$\mathcal{V}_0 = \frac{1}{2}\sum_{i}\omega_i Q_i^2, \tag{2.20}$$

are the kinetic energy and potential energy operators, respectively. The quantity $\Delta\mathcal{H}$ in Eq. (2.18) describes any change in the electronic energy upon photoexcitation or photoionization process. This is a $(n \times n)$ non-diagonal matrix, where the diagonal elements are the diabatic potential energy surfaces of the electronic states. The coupling between these surfaces is described by off-diagonal elements. These elements can be expanded in Taylor series in terms of normal coordinates as [1]

$$W_{nn}(Q) = W_0(Q) + E_n + \sum_{i}\kappa_i^{(n)}Q_i + \sum_{ij}\gamma_{ij}^{(n)}Q_iQ_j + ... \tag{2.21}$$

and

$$W_{nn'}(Q) = W_{nn'}(0) + \sum_{i}\lambda_i^{(nn')}Q_i + ..., \tag{2.22}$$

respectively. The quantities, κ and γ, are termed as intrastate coupling parameters. λ is the interstate coupling parameter. These set of coupling parameters are derived by using the following equations:

$$\kappa_i^{(n)} = (\partial W_{nn}/\partial Q_i)_0 \tag{2.23}$$

$$\lambda_i^{(nn')} = (\partial W_{nn'}/\partial Q_i)_0 \tag{2.24}$$

$$\gamma_{ij}^{(n)} = \frac{1}{2}[(\partial^2 W_{nn}/\partial Q_iQ_j)_0] \tag{2.25}$$

Here E_n denotes the vertical ionization/excitation energy of the n^{th} excited electronic state from the reference state. It should be noted that symmetry selection rules are employed to determine the possible coupling between the states:

$$\Gamma_m \times \Gamma_{Q_i} \times \Gamma_n \supset \Gamma_A, \tag{2.26}$$

where Γ_m, Γ_n and Γ_{Q_i} denote the irreducible representations (IREPs) of the electronic states m, n and the i^{th} vibrational mode, respectively. Γ_A denotes the totally symmetric representation within the given point group.

2.2.2 Electronic structure calculations

In order to evaluate the coupling parameters of the vibronic Hamiltonian, a series of calculations are performed. First, harmonic vibrational frequencies (ω) and mass-weighted

normal coordinates are obtained by diagonalization of the force constant matrix of the reference (ground-state) optimized geometry. A mathematical transformation is employed to convert mass-weighted coordinates to dimensionless normal displacement coordinates (Q) [19].

In the second step, for molecules of closed-shell configuration in the ground electronic state, the outer valence Green's function (OVGF), equation-of-motion coupled-cluster singles and doubles (EOM-CCSD) and multi reference configuration interaction (MRCI) methods have been employed to compute the vertical excitation/ionization energies at the reference geometry $\mathbf{Q} = 0$ [20, 21]. Analogously, the vertical excitation/ionization energies of molecule along each relevant vibrational mode for various nuclear geometries, for example Q=+0.50 and Q=-0.50, are then computed. The obtained energies plus the harmonic potential of the reference state are equated with the adiabatic potential energies ($\mathbf{V}$) of the final electronic state. A least-squares curve fitting and numerical finite difference approaches are used to evaluate relevant coupling parameters.

2.3 Calculation of vibronic spectrum

The transition probability is calculated by the Fermi's golden rule

$$P(E) = \sum_v \left| \langle \Psi_v^f | \hat{T} | \Psi_0^i \rangle \right|^2 \delta(E - E_v^f + E_0^i), \tag{2.27}$$

$|\Psi_0^i\rangle$ is the initial vibronic ground state of of the reference state with energy E_0^i. $|\Psi_v^f\rangle$ corresponds to the final vibronic state of of the photoionized or excited molecule with energy E_v^f. The quantity $\hat{T}$ represents the transition dipole operator that describes the interaction of the electron with the external radiation of energy E during the photoionization/excitation process. The ground electronic state is vibronically decoupled from the other states, the reference state can be expressed as simple product of the electronic Φ^0 and nuclear (χ_0^0) components:

$$|\Psi_0^i\rangle = |\Phi^0\rangle|\chi_0^0\rangle, \tag{2.28}$$

The final vibronic state $|\Psi_v^f\rangle$ in the coupled electronic manifold of n interacting states is expressed as

$$|\Psi_v^f\rangle = \sum_n |\Phi^n\rangle|\chi_v^n\rangle, \tag{2.29}$$

Using Eqs. (2.28-2.29), the excitation function Eq. (2.27) is rewritten as

$$P(E) = \sum_{v} \left| \sum_{n} \tau^{n} \langle \chi_{v}^{n} | \chi_{0}^{0} \rangle \right|^{2} \delta(E - E_{v}^{f} + E_{0}^{i}), \tag{2.30}$$

where

$$\tau^{n} = \langle \Phi^{n} | \hat{T} | \Phi^{0} \rangle \tag{2.31}$$

represent the matrix elements of the transition dipole operator of the final electronic state n. In diabatic basis, these elements depends very weakly on nuclear coordinates Q. Hence, in the study of photoinduced processes presented in this thesis, the transition dipole matrix elements are treated as constants. This approximation is known as Condon approximation [22].

2.3.1 Time-independent matrix diagonalization approach

Within the time-independent approach, the vibronic Schrödinger equation

$$\mathcal{H} |\Psi_{n}^{f}\rangle = E_{n} |\Psi_{n}^{f}\rangle, \tag{2.32}$$

is solved by expanding the vibronic eigenstates $\{|\Psi_{n}^{f}\rangle\}$ in the direct product harmonic oscillator basis of the reference state [1] as

$$|\Psi_{n}^{f}\rangle = \sum_{\{|K_{i}\rangle\}} a_{K_{1},\ldots,K_{l}}^{n} |K_{1}\rangle |K_{2}\rangle \ldots |K_{l}\rangle |\phi_{n}\rangle \tag{2.33}$$

In above equation, $|K_{i}\rangle$ represents the K^{th} level of i^{th} vibrational mode and $|\phi_{m}\rangle$ is the electronic wavefunction. In the numerical calculations, the oscillator basis for a given vibrational mode is chosen based on the convergence behavior of the spectral envelope. The representation of Hamiltonian matrix in a direct product Harmonic oscillator basis leads to highly sparse matrix, which is eventually tri-diagonalized by using Lanczos algorithm [23]. It should be noted that the obtained diagonal elements of the resulting eigenvalue matrix give the position of the vibronic lines. The relative intensities can be obtained from the squared first components of the Lanczos eigenvectors [1, 12]. Subsequently, the stick vibronic lines are convoluted [1] with a Lorentzian line shape function of appropriate FWHM Γ to match the experimental resolution

$$L(E) = \frac{1}{\pi} \frac{\frac{\Gamma}{2}}{E^{2} + (\frac{\Gamma}{2})^{2}}. \tag{2.34}$$

2.3.2 Time-dependent wavepacket propagation approach

The intensity of the electronic spectrum ($P(E)$) is calculated by Fourier transformation of the delta function ($\delta(x) = \frac{1}{2\pi}\int_{-\infty}^{+\infty} e^{ixt/\hbar}$) of a WP evolving on the final vibronic state of the molecule as

$$P(E) \approx 2Re \int_0^\infty e^{iEt/\hbar} \langle \Psi_i(0)|\tau^\dagger e^{-i\mathcal{H}t/\hbar}\tau|\Psi_i(0)\rangle dt, \tag{2.35}$$

$$\approx 2Re \int_0^\infty e^{iEt/\hbar}\ C_f(t)\ dt. \tag{2.36}$$

Here, the quantity $C_f(t) = \langle \Psi_f(0)|\Psi_f(t)\rangle$ is the time autocorrelation function. $\Psi(0)$ represents the reference state (ground-state) WP. Vertical transition of the latter WP places the initial WP on the final vibronic state at $t = 0$, i. e., $\Psi_f(0)$. Under the influence of Hamiltonian, the time evolution of the WP is described by $|\Psi_f(t)\rangle = e^{-i\mathcal{H}t/\hbar}|\Psi_f(0)\rangle$.

Employing suitable time-dependent function, the obtained time autocorrelation function is damped and then Fourier transformation to generate the spectrum. In this thesis, a function of type

$$f(t) \quad = \quad exp[-t/\tau_r] \quad , \tag{2.37}$$

is used. τ_r in the above equation represents the relaxation time. This process is equivalent to convoluting the spectrum with a Lorentzian line shape function (cf., Eq. (2.34)) of FWHM, $\Gamma = 2/\tau_r$.

2.3.3 Wavepacket propagation by MCTDH algorithm

The matrix diagonalization approach often becomes computationally tedious with an increase in the electronic and nuclear degrees of freedom. A WP propagation approach within the multi-configuration time-dependent Hartree (MCTDH) framework has been quite successful in this situation [24–27]. This is a grid based method which utilizes a discrete variable representation (DVR) basis combined with the fast Fourier transformation and powerful integration schemes. In this scheme all multi-dimensional quantities are expressed in terms of one-dimensional ones employing the idea of mean-field or Hartree approach. In addition this scheme uses optimal time-dependent single-particle functions (SPFs). These provide efficiency to the method by keeping the size of the basis optimally small. Furthermore, multi-dimensional SPFs are designed by appropriately choosing the set of system coordinates so as to reduce the number of particles and hence the computational overheads. The basic MCTDH wavefunction ansatz is expressed as

$$\Psi(Q_1, ..., Q_f, t) = \Psi(R_1, ..., R_p, t) \tag{2.38}$$

$$= \sum_{\alpha=1}^{\sigma} \sum_{j_1=1}^{n_1^{(\alpha)}} ... \sum_{j_p=1}^{n_p^{(\alpha)}} A^{(\alpha)}_{j_1,...,j_p}(t) \prod_{k=1}^{p} \varphi^{(\alpha,k)}_{jk}(R_k, t)|\alpha\rangle \tag{2.39}$$

Here, f and p represents the number of vibrational degrees of freedom and MCTDH particles. $A^{(\alpha)}_{j_1,...,j_p}$ denote the MCTDH expansion coefficients. The basis functions $\varphi^{(\alpha,k)}_{jk}$ are the n_k SPFs for each degree of freedom k associated with the electronic state α.

We refer to the literature [25–27] for the operational principles, successes and shortcomings of MCTDH scheme. In this thesis, the Heidelberg MCTDH package [24] is employed to propagate WPs.

References

[1] H. Köppel, W. Domcke and L. S. Cederbaum, Adv. Chem. Phys. **57**, 59 (1984).

[2] G. Fisher, *Vibronic coupling*, Academic press, London (1984).

[3] B. H. Lengsfield and D. R. Yarkony, Adv. Chem. Phys. **82**, 1 (1992).

[4] C. J. Ballhausen and A. E. Hansen, Ann. Rev. Phys. Chem. **23**, 15 (1972).

[5] M. Born and R. Oppenheimer, Ann. Phys. **84**, 457 (1927).

[6] H. Köppel, L.S. Cederbaum and S. Mahapatra, *Theory of the JahnTeller Effect*, in *Handbook of high-resolution spectroscopy*, John Wiley & Sons, (2011).

[7] S. Mahapatra, Acc. Chem. Res. **42**, 1004 (2009).

[8] M. Baer, *Beyond Born-Oppenheimer: electronic non-adiabatic coupling terms and conical intersections*, John Wiley and Sons, (2006).

[9] W. Lichten, Phys. Rev. **131**, 229 (1963).

[10] F. T. Smith, Phys. Rev. **179**, 111 (1969).

[11] T. F. O'Malley, Adv. At. Mol. Phys. **7**, 223 (1971).

[12] H. Köppel and W. Domcke: in *Encyclopedia of computational chemistry* edited by P. v. R. Schleyer, Wiley, New York (1998), p 3166.

[13] M. Baer, Chem. Phys. Lett. **35**, 112 (1975).

[14] C. A. Mead, D. G. Truhlar, J. Chem. Phys. **77**, 6090 (1982).

[15] M. Baer, Chem. Phys. **15**, 49 (1976).

[16] V. Sidis, Adv. Chem. Phys. **82**, 73 (1992).

[17] T. Pacher, L. S. Cederbaum and H. Köppel, Adv. Chem. Phys. **84**, 293 (1993).

[18] A. Thiel and H. Köppel, J. Chem. Phys. **110**, 9371 (1999). Institut für festkörperforschung, Stuttgart, Germany (2007).

[19] E. B. Wilson Jr., J. C. Decius, and P. C. Cross, *Molecular vibrations*, McGraw-Hill, New York (1955).

[20] L. S. Cederbaum and W. Domcke, Adv. Chem. Phys. **36**, 205 (1977).

[21] L. S. Cederbaum, J. Phys. B, **8**, 290 (1975).

[22] W. Domcke, H. Köppel and L. S. Cederbaum, Mol. Phys. **43**, 851 (1981).

[23] J. Cullum and R. Willoughby, *Lanczos algorithms for large symmetric eigenvalue problems*, Birkhäuser, Boston (1985), Vols. I and II.

[24] G. A. Worth, M. H. Beck, A. Jäckle, and H. -D. Meyer, *The MCTDH Package*, Version 8.2, (2000), University of Heidelberg, Heidelberg, Germany. H. -D. Meyer, Version 8.3 (2002), Version 8.4 (2007). See http://mctdh.uni-hd.de.

[25] H. -D. Meyer, U. Manthe and L. S. Cederbaum, Chem. Phys. Lett. **165**, 73 (1990).

[26] U. Manthe, H. -D. Meyer and L. S. Cederbaum, J. Chem. Phys. **97**, 3199 (1992).

[27] M. H. Beck, A. Jäckle, G. A. Worth and H. -D. Meyer, Phys. Rep. **324**, 1 (2000).

3 Theoretical Study on Electronic Absorption Spectroscopy of Propadienylidene Molecule vis-â-vis the Observed Diffuse Interstellar Bands[1]

3.1 Introduction

Assignment of numerous diffuse interstellar bands (DIBs) observed by the astronomers in the visible and ultraviolet region of the electromagnetic spectrum [1, 2] remains a challenging task for molecular spectroscopists to date. The proposed carriers of these DIBs are dust grains [3] and carbon containing molecules [4, 5]. The later proposition emerged from studying various carbon chain molecules as well as polycyclic aromatic hydrocarbon (PAH) cations [4, 5]. The assignment of observations from radioastronomy so far relied mostly on the spectroscopic measurements in the laboratory in a rare gas matrix environment [6, 7]. However, the developments in the recent past have made it possible to compare the data obtained from gas phase laboratory measurements under the exotic condition of interstellar medium (ISM) [7].

Gas phase measurements of carbon chain molecules (Ref. [5] and references therein) and PAHs [8, 9] have been carried out. The coincidence of three DIBs reported at ∼670.70, 648.89 and 612.52 nm with an electronic transition in naphthalene radical cation and one broad DIB at ∼708.8 nm with an electronic transition in anthracene radical cation have been reported [8, 10] and this is also studied by us and discussed in Chapter 6 of this thesis. The coincidence of a DIB at 5069 Å with an electronic transition in diacetylene radical cation has also been reported [11]. All these experimental results understandably require support from complimentary theoretical calculations for an unambiguous assignment. The problem in theoretical calculations often emerges from the importance of many nuclear degrees of freedom and participation of many energetically close-lying electronic states in the dynamics of these large-sized molecules. In the recent past, we examined the electronic transitions in the naphthalene and anthracene radical cations by theoretical methods based on a full quantum mechanical representation and

[1] The subject of this Chapter is published in: S. N. Reddy & S. Mahapatra, Chem. Phys. **403**, 1 (2012).

reported close correspondence of the calculated spectra with those obtained from gas phase measurements as well as the observed DIBs [12–15].

The propadienylidene molecule is an important prototype of cumulene carbenes, $H_2C(=C:)_n$. Apparently, several members of this family have been detected in the dark molecular clouds by radioastronomy [16]. The linear isomer of propadienylidene (Y-shaped), hereafter designated as l-C_3H_2 was reported to absorb in the region of the DIBs observed at 5450 Å and 4881 Å [7]. The electronic absorption of l-C_3H_2 was first recorded in an Ar matrix environment [17,18]. In order to correlate the spectrum better with that expected in the gas phase measurements, it was recorded in the Ne matrix environment [6] as Ne seems to be more inert and is expected to impart less perturbation to the guest molecule. The recorded spectrum revealed an intense band structure in the 4000-6000 Å region followed by a very weak tail at further higher wavelengths. At the lower (∼2000-3000 Å) wavelength region another intense band was observed [6]. The intense absorption in the 4000-6000 Å region was assigned to the optically allowed $\widetilde{B}^1B_1 \leftarrow \widetilde{X}^1A_1$ transition whereas, the very weak structure at further higher wavelengths is assigned to the dipole forbidden $\widetilde{A}^1A_2 \leftarrow \widetilde{X}^1A_1$ transition [6]. The weak structure has been shown to result from intensity borrowing via $\widetilde{A}^1A_2$-$\widetilde{B}^1B_1$ vibronic coupling. The intense band between ∼200-300 Å region is attributed to the optically allowed $\widetilde{C}^1A_1 \leftarrow \widetilde{X}^1A_1$ transition in l-C_3H_2 [6].

The gas phase measurement of the electronic absorption spectrum of l-C_3H_2 was also attempted by CRD spectroscopy [19]. This experiment was unsuccessful and a life-time of less than a picosecond of the $\widetilde{B}$ state was envisaged for this failure. Furthermore, three rotationally resolved peaks attributed to a transition to the $\widetilde{A}$ state were predicted from this experiment. Very recently, a successful CRD spectroscopy measurement of l-C_3H_2 is reported [7]. Two very intense peaks obtained in this measurement are shown to correlate well with those obtained in the Ne matrix environment. The origin 0_0^0 peak of the $\widetilde{B}^1B_1 \leftarrow \widetilde{X}^1A_1$ transition is found to be buried in the continuum of levels of the $\widetilde{A}$ state. The two intense peaks assigned are due to the fundamental and the first overtone of a symmetric C=C stretching mode of l-C_3H_2 . The first intense peak placed at 5450 Å is due the fundamental of this mode recorded in the gas phase spectrum [7]. This is found to correlate with the 5445/5417 Å peak observed in Ne matrix environment [7]. With respect to the location of this fundamental peak, the location of its first overtone (the second intense peak) is estimated at ∼4887 (3) Å [7]. The energetic locations of these peaks correlate well with the location of the two DIBs [20]. It is intriguing to note that the observed peaks in the gas phase spectrum reveal a highly asymmetric structure and splitting [7]. These are quite important observations which will be discussed in relation to the theoretical model developed here.

The equilibrium geometry of the l-C_3H_2 molecule belongs to the C_{2v} symmetry point group in its electronic ground state ($\widetilde{X}^1A_1$). The nine vibrational modes of this molecule decompose into, $4a_1 \oplus 3b_2 \oplus 2b_1$ irreducible representations (IREPs) of the C_{2v} symme-

try point group. The first three excited electronic states of l-C_3H_2 belong to the $\widetilde{A}^1A_2$, $\widetilde{B}^1B_1$ and $\widetilde{C}^1A_1$ species of this equilibrium symmetry representation. The electronic and vibrational symmetries are designated by the upper-and lower-case symbols, respectively, throughout this chapter. In the following, we attempt to develop a theoretical model in order to look into specific details of the experimental observations mentioned above. It is evident from the experimental [6, 7] and also reduced dimensional theoretical studies [6] that nonadiabatic coupling of electronic states is a crucial factor governing the shape and energetic location of the vibronic peaks observed for this molecule. Very recently improved *ab initio* calculations of the potential energy surfaces (PESs) and the $\widetilde{B}$ state spectrum of l-C_3H_2 have been reported considering all relevant vibrational degrees of freedom [21]. These theoretical results are compared with the experimental Ne-matrix results [21]. Despite improvement in the electronic structure calculations reported in this work, the vertical energy gap of the $\widetilde{A}$ and $\widetilde{B}$ electronic states and the strength of the $\widetilde{A}$-$\widetilde{B}$ coupling appear to remain uncertain.

The theoretical model developed here relies on a diabatic representation of the electronic states in order to treat the nonadiabatic coupling terms as smooth potential coupling rather than diverging kinetic coupling in the complementary adiabatic electronic representation [22]. Elementary symmetry rules [23] are applied to construct a parameterized Hamiltonian in terms of the dimensionless normal coordinates of the vibrational modes and the parameters introduced therein are estimated by fitting adiabatic electronic energies calculated by various state-of-the-art *ab initio* methods over a large grid in the nuclear coordinate space. The theoretical findings of this chapter are compared with the most recent experimental and theoretical results and also discussed in relation to the astrophysical observations [6, 7, 21, 24].

3.2 Theory

3.2.1 The Hamiltonian

Following Ref. [22], the Hamiltonian for the coupled manifold of $\widetilde{A}$-$\widetilde{B}$-$\widetilde{C}$ singlet electronic states of l-C_3H_2 is constructed in terms of the dimensionless normal displacement coordinate ($\mathbf{Q}$) of its nine non-degenerate vibrational modes in a diabatic electronic basis as

$$\mathcal{H} = (\mathcal{T}_N + \mathcal{V}_0)\mathbf{1_3} + \begin{pmatrix} W_{\widetilde{A}} & W_{\widetilde{A}-\widetilde{B}} & 0 \\ & W_{\widetilde{B}} & W_{\widetilde{B}-\widetilde{C}} \\ h.c. & & W_{\widetilde{C}} \end{pmatrix}, \tag{3.1}$$

where $\mathbf{1_3}$ is a 3×3 unit matrix and $(\mathcal{T}_N + \mathcal{V}_0)$ is the Hamiltonian for the unperturbed electronic ground state of l-C_3H_2. This reference state is vertically well separated in energy from the excited states and is treated as harmonic. Accordingly, $\mathcal{T}_N$ and $\mathcal{V}_0$ are

given by

$$\mathcal{T}_N = -\frac{1}{2}\sum_{i=1}^{9}\omega_i\frac{\partial^2}{\partial Q_i^2}, \tag{3.2}$$

$$\mathcal{V}_0 = \frac{1}{2}\sum_{i=1}^{9}\omega_i Q_i^2. \tag{3.3}$$

The matrix Hamiltonian (with elements W) in Eq. 3.1 represents the diabatic energies of the given electronic states and their coupling energies. The elements of this Hamiltonian are expanded in a Taylor series around the equilibrium geometry of the reference state at ($\mathbf{Q}$=0) as [22]

$$\begin{aligned} W_j &= E_0^{(j)} + \sum_{i=1}^{4}\kappa_i^{(j)}Q_i + \frac{1}{2}\sum_{i=1}^{9}\gamma_i^{(j)}Q_i^2 + \frac{1}{2}\sum_{i=1}^{3}\sum_{l>i}^{3}\gamma_{il}^{(j)}Q_iQ_l \quad ; \\ j &\in \widetilde{A},\widetilde{B},\widetilde{C} \end{aligned} \tag{3.4}$$

$$W_{j-k} = \sum_i \lambda_i^{(j-k)}Q_i, \tag{3.5}$$

where $j-k \in \widetilde{A}$-$\widetilde{B}$, $\widetilde{B}$-$\widetilde{C}$ with $i \in b_2, b_1$ in that order. In the above equations the quantity $E_0^{(j)}$ represents the vertical excitation energy of the j^{th} electronic state. $\kappa_i^{(j)}$ and $\gamma_i^{(j)}$ are the linear and second-order coupling parameters of the i^{th} vibrational mode in the j^{th} electronic state. $\gamma_{il}^{(j)}$ is the intrastate inter-mode bilinear coupling parameter along i and l modes in the j^{th} electronic state. The quantity $\lambda_i^{(j-k)}$ describes the first-order coupling parameter between the j and k electronic states through the vibrational mode i. A linear interstate coupling is considered throughout this study.

3.3 Results and Discussion

3.3.1 Electronic ground and excited states of l-C_3H_2

In order to examine the electronic absorption spectrum, the reference electronic ground state of the l-C_3H_2 molecule is optimized at various levels of theory. The equilibrium geometry of the reference electronic ground state of l-C_3H_2 is optimized at the Møller-Plesset perturbation level of theory employing second order (MP2) and fourth order (MP4) corrections and also by the B3LYP [32] method using the aug-cc-pVTZ basis set of Dunning [33]. The optimized equilibrium geometry parameters are given in Table 3.1 along with the available literature data [19, 34, 35]. It can be seen from the table that the geometry parameters agree well with the literature data. The harmonic frequency

Table 3.1: Optimized parameters of the equilibrium minimum configuration (C_{2v}) of l-C_3H_2 in its electronic ground state ($\widetilde{X}^1A_1$) obtained using aug-cc-pVTZ basis set. The equilibrium geometry parameters available from the literature are given for comparison.

Bond length/	MP2	MP4	B3LYP	UMP2	RSPT3	Expt [19]
Bond angle	aug-cc-pVTZ			6-31G** [34]	CAS10 [35]	
C_1-C_2/Å	1.332	1.337	1.320	1.333	1.330	1.324
C_2-C_3/Å	1.285	1.295	1.280	1.292	1.290	1.291
C_1-H/Å	1.085	1.087	1.086	1.084	1.085	1.098
$\angle HCH$/deg.	117.3	117.2	116.5	116.6	-	-
$\angle HCC$/deg.	121.3	121.4	121.7	-	121.3	118.8

Table 3.2: Symmetry, designation and harmonic frequency (cm^{-1}) of nine vibrational modes of l-C_3H_2 in its $\widetilde{X}^1A_1$ electronic state calculated with the aug-cc-pVTZ basis set. The numbers in the parentheses in the sixth column represent the fundamental frequencies given in Ref. [34].

Symmetry	Mode	MP2	MP4	B3LYP	MP2	CCSD(T)	CAS(10) [35]
		aug-cc-pVTZ			6-31G** [34]	cc-pVTZ [17]	-
a_1	ν_1	3142	3107	3094	3206 [3050]	3146	3010
	ν_2	2034	1994	2039	2075 [1952]	2019	2066
	ν_3	1495	1486	1492	1542 [1447]	1503	1501
	ν_4	1126	1100	1148	1152	1125	1154
b_2	ν_5	3233	3195	3168	3304	3210	3085
	ν_6	1053	1047	1056	1080 [1025]	1057	1072
	ν_7	253	252	295	262	276	236
b_1	ν_8	1046	1022	1053	1051 [1000]	1049	975
	ν_9	211	218	238	225	240	254

(ω) of nine vibrational modes and their dimensionless normal displacement coordinates ($\mathbf{Q}$) are calculated at the MP2 level of theory using the same basis set and following the standard procedure [22]. All calculations are performed using the G03 [36] suite of program. The symmetry, harmonic frequency and designation according to Herzberg [37] nomenclature of nine vibrational modes of the l-C_3H_2 molecule are given in Table 3.2.

The vertical excitation energies (VEEs) of l-C_3H_2 along each of its nine vibrational modes are then calculated for various nuclear geometries, Q_i (i = 1-9) = -4.0 (0.25) 4.0, by the equation-of-motion coupled-cluster singles and doubles (EOM-CCSD) [38–40] and complete active space self consistent field-multi reference configuration interaction (CASSCF-MRCI) [41–43] method. The calculations are carried out employing the aug-cc-pVTZ basis set using the MOLPRO 2010.1 suite of programs [44]. The VEEs obtained at the reference equilibrium geometry are presented in Table 3.3. It can be seen that the calculated VEEs are in good accord with their values reported in the literature [18, 45].

Table 3.3: Vertical excitation energies (in eV) of the first three excited electronic states of l-C_3H_2 calculated at the equilibrium geometry of its electronic ground state. The oscillator strengths are given in the parentheses. The data available in the literature are also given in the Table.

State	EOM-CCSD	CASSCF(10,10)-MRCI	CASSCF(14,12)-MRCI	EOMEE-CCSD/ cc-pVQZ [18]	DFT(B3P86) [45]
$E^0_{A_2}$	1.930 (0.0000)	1.823	1.814	1.853	1.850 (0.0000)
$E^0_{B_1}$	2.764 (0.0086)	2.438	2.345	2.520	2.510 (0.008)
$E^0_{A_1}$	5.528 (0.1624)	5.510	5.544	5.350	5.460 (0.112)

The present CASSCF(14,12)-MRCI VEEs seem to be more accurate as compared to those reported in the literature and derived from high level *ab initio* calculations [21]. These VEEs plus the harmonic potentials of the electronic ground state of l-C_3H_2 define the adiabatic potential energies (V) of the excited electronic state of l-C_3H_2 along a given vibrational mode. The assumption that CASSCF(14,12)-MRCI VEEs are more accurate is expected to yield more accurate PESs of this seemingly simple system. This assumption is more rigorously tested and validated in the later part of the this chapter. We also calculated the adiabatic potential energies of the reference state along each vibrational mode. The resulting energies along a vibrational mode fit to a parabola quite well, justifying the harmonic approximation used for the reference state.

The calculated adiabatic potential energies (VEEs + harmonic potentials of the reference state along a given vibrational coordinate) of the first three excited electronic states of l-C_3H_2 are then used to estimate the parameters [cf., Eqs. [3.4-3.5] introduced in the electronic Hamiltonian, $(\mathcal{H} - \mathcal{T}_N \mathbf{1_3})$, given in Eq. 3.1. A non-linear least squares fit of the adiabatic electronic potential energies is carried out to the adiabatic functional form of, $(\mathcal{H} - \mathcal{T}_N \mathbf{1_3})$, to estimate the parameters. In Tables 3.4 and 3.5 the Hamiltonian parameter values derived from the EOM-CCSD energy data are given. From the data given in Table 3.4 it can be immediately seen that the Huang-Rhys factor ($\kappa^2/2\omega^2$) of all symmetric vibrational modes are generally small (except ν_4) in the $\widetilde{A}^1A_2$ state of l-C_3H_2. The mode ν_4 is however, expected to be only mildly excited. The coupling strength of ν_2 in the $\widetilde{B}^1B_1$ state and ν_4 in the $\widetilde{C}^1A_1$ state is much stronger and the coupling strength of the remaining symmetric vibrational modes is weak in all the three electronic states. The vibrational mode ν_4 is predominantly of C=C stretching type whereas the mode ν_2 represents a hybrid C=C stretching plus H_2C scissoring vibration. The $\widetilde{A}$ and $\widetilde{B}$ electronic states are vertically $<\sim$0.8 eV (the energy gap varies with the method of calculation, cf., Table 3.3) apart at the reference equilibrium geometry. Very strong $\widetilde{A}$-$\widetilde{B}$ interstate coupling along the ν_7 vibrational mode of b_2 symmetry is obtained from the electronic energy data. This mode describes C=C=C in-plane bending motion. The $\widetilde{B}$ and $\widetilde{C}$ states are vertically well separated (on an average by $\sim$3.0 eV) and also coupling between these states along ν_8 mode (C-H out-of-plane bending) of b_1 symmetry is not very significant. The data discussed above therefore reveal that the $\widetilde{A}$-$\widetilde{B}$ coupling

Table 3.4: The linear intrastate (κ) and interstate (λ) coupling parameters of the Hamiltonian [Eqs. 3.4 and 3.5] of l-C_3H_2 derived from the EOM-CCSD electronic structure data. The parameter values are given in eV. The numbers in the parentheses represent the quantity obtained by a finite-difference method.

mode	$\kappa^{(A)}$	$\kappa^{(B)}$	$\kappa^{(C)}$	λ^{A-B}	λ^{B-C}
	$\widetilde{A}^1A_2$	$\widetilde{B}^1B_1$	$\widetilde{C}^1A_1$	$\widetilde{A}^1A_2$-$\widetilde{B}^1B_1$	$\widetilde{B}^1B_1$-$\widetilde{C}^1A_1$
ν_1	0.0073	0.0450	-0.0201	-	-
ν_2	0.0445	-0.3571	0.0263	-	-
ν_3	-0.0481	0.0042	-0.0424	-	-
ν_4	0.1001	-0.0386	0.2345	-	-
ν_5	-	-	-	[0.024]	-
ν_6	-	-	-	0.065 [0.106]	-
ν_7	-	-	-	0.172 [0.179]	-
ν_8	-	-	-	-	0.154 [0.165]
ν_9	-	-	-	-	-

Table 3.5: Same as in Table 3.4 for the second order and bilinear coupling parameters.

Mode	$\gamma^{(A)}$	$\gamma^{(B)}$	$\gamma^{(C)}$
	$\widetilde{A}^1A_2$	$\widetilde{B}^1B_1$	$\widetilde{C}^1A_1$
ν_1	-0.0022	0.0001	-0.0084
ν_2	-0.0299	-0.0543	-0.0381
ν_3	-0.0192	-0.0030	-0.0045
ν_4	0.002	0.0025	0.0124
ν_5	-0.0034	-0.0006	-0.0118
ν_6	-0.0448	0.0091	-0.0052
ν_7	-0.0434	0.0946	-0.0905
ν_8	-0.0712	-0.0623	-0.0145
ν_9	0.0141	0.1318	-0.0587
$\nu_2\nu_3$	-0.0056	0.0065	-0.0075
$\nu_2\nu_4$	0.0099	-0.0053	-0.0008
$\nu_3\nu_4$	-0.0043	0.0006	-0.0013

along ν_7 is crucially important, for the vibronic structure of the $\widetilde{B}$ band of l-C_3H_2 and the symmetric vibrational mode ν_2 is expected to form the dominant progression in this band. The importance of these two modes in the vibronic dynamics of $\widetilde{A}$-$\widetilde{B}$ coupled electronic states of l-C_3H_2 has also been established in previous theoretical studies [6,21].

From Table 3.5 it can be seen that the bilinear coupling parameters between the symmetric vibrational modes are small (of the order of 10^{-3} eV or less). We also found that they do not have any noticeable impact on the vibronic structure of the concerned electronic states. The second order coupling constant along ν_2 in the $\widetilde{B}$ state is quite

large (cf., Table 3.5). Considering the harmonic frequency of this mode in the reference state (cf., Table 3.2) and the experimental results [6, 7, 24] (discussed later in the text) we expected a smaller value of this quantity. An experimental value of the frequency (fundamental) of this mode of ∼1952 cm^{-1} in the $\widetilde{B}$ state was reported by Maier and coworkers [34]. A second issue that surprised us is the large value of λ along ν_7 for the $\widetilde{A}$-$\widetilde{B}$ coupling obtained from the EOM-CCSD electronic structure data (cf., Table 3.4). This was treated as an adjustable parameter in previous theoretical studies [6] and a value of ∼-0.158 eV (-1278 cm^{-1}) has been recently reported for this quantity [21].

In order to arrive at the best estimates of the Hamiltonian parameters we explored alternative state-of-the-art quantum chemistry methods to calculate them. In this effort, we calculated the energies of the $\widetilde{A}$ and $\widetilde{B}$ electronic states by the CASSCF-MRCI method employing different active spaces. This is in anticipation that a multi-reference CI method would provide the best estimates of electronic energies in the vicinity of conical intersections. In this case, only the $\widetilde{A}$ and $\widetilde{B}$ states of l-C_3H_2 are considered as revealed by the foregoing discussion that the $\widetilde{B}$ state is mainly perturbed by the $\widetilde{A}$ state and its coupling to further higher energy states is negligible. We performed several trial calculations and among them the results obtained with CAS(10,10) and CAS(14,12) are collected in Tables 3.6-3.7 and 3.8-3.9, respectively. In comparison with the parameters given in Tables 3.4 and 3.5, it can be seen that different sets of data are quite similar. While the CASSCF(10,10)-MRCI data give a similar value of γ for the ν_2 vibrational mode in the $\widetilde{B}$ state as obtained from the EOM-CCSD data, magnitude of this quantity is almost 50% lowered in the CASSCF(14,12)-MRCI result. A large value of this quantity similar to our EOM-CCSD result is also reported in Ref. [21]. The $\widetilde{A}$-$\widetilde{B}$ coupling strength along ν_7 on the other hand, is significantly lowered in the CASSCF-MRCI data when compared to the same obtained from the EOM-CCSD data (cf., Table 3.4). Both finite-difference and least squares fit methods are used to calculate λ from the calculated *ab initio* electronic energies. It can be seen from Table 3.4 that fairly consistent results are obtained by both the methods. The finite-difference results are given in the parentheses. The results given in Tables 3.6 and 3.8 on the other hand, reveal a lower value λ obtained from the fit and a larger value of similar magnitude as in Table 3.4 obtained by using the finite-difference method. Considering all the values of λ presented in Tables 3.4, 3.6 and 3.8 it appears that this quantity may vary between ∼0.095 eV - ∼0.18 eV. The finite-difference method always overestimates its value. It is important to make some comments at this point. The energy difference of the $\widetilde{A}$ and $\widetilde{B}$ states decreases with improved *ab initio* method (shown later in the text) and these states are found to be closest in the CASSCF(14,12)-MRCI results. Considering this into account the coupling strength, $\lambda/\Delta E$ (ΔE is the difference in adiabatic energy of the two states), does not drop as much as λ itself (in the adiabatic picture) calculated with different electronic structure methods. A difference of the finite-difference results with those from the fit mainly arises from the neglect of the second-order (γ) term in the finite-difference method.

Table 3.6: Same as in Table 3.4, derived from the CASSCF(10,10)-MRCI electronic energy data.

mode	$\kappa^{(A)}$ $\widetilde{A}^1A_2$	$\kappa^{(B)}$ $\widetilde{B}^1B_1$	λ^{A-B} $\widetilde{A}^1A_2$-$\widetilde{B}^1B_1$
ν_1	0.0152	0.0529	-
ν_2	0.0288	-0.4141	-
ν_3	-0.0540	0.0031	-
ν_4	0.1101	-0.0086	-
ν_5	-	-	0.022
ν_6	-	-	[0.101]
ν_7	-	-	0.103 [0.152]
ν_8	-	-	-
ν_9	-	-	-

Table 3.7: Same as in Table 3.5 derived from the CASSCF(10,10)-MRCI electronic energy data.

Mode	$\gamma^{(A)}$ $\widetilde{A}^1A_2$	$\gamma^{(B)}$ $\widetilde{B}^1B_1$
ν_1	-0.0009	0.0020
ν_2	-0.0283	-0.0408
ν_3	-0.0179	-0.0020
ν_4	0.0028	0.0035
ν_5	-0.0062	-0.0025
ν_6	-0.0396	-
ν_7	-0.0421	0.0952
ν_8	-0.0859	-0.0817
ν_9	0.0201	0.1356

It is intriguing to note that in all cases the calculated electronic energies fit very well to the potential functions derived from the Hamiltonian of Eq. 3.1. The potential energy functions of the first three excited electronic states of l-C_3H_2 fit to the EOM-CCSD data are plotted along the normal coordinates of the four symmetric vibrational modes in Figs. 3.1(a-d). These represent one dimensional view of the complex multi-dimensional potential energy hypersurface along the representative vibrational mode keeping others at their equilibrium value at ($\mathbf{Q}$=0). Despite their limited significance, these plots are extremely important to assess various curve crossings among electronic states which happen to play key mechanistic role in the observed spectral feature and time-dependent dynamics of a given electronic state. The curves (solid, dashed and dotted) in Figs. 3.1 (a-d) represent the potential energy functions obtained from the theoretical model of Sec. 3.2 using the parameters of Tables 3.4 and 3.5 and the points superimposed on them are the calculated EOM-CCSD electronic energies. It can be seen that the model

Table 3.8: Same as in Table 3.4 derived from the CASSCF(14,12)-MRCI electronic energy data.

mode	$\kappa^{(A)}$ $\widetilde{A}^1A_2$	$\kappa^{(B)}$ $\widetilde{B}^1B_1$	λ^{A-B} $\widetilde{A}^1A_2$-$\widetilde{B}^1B_1$
ν_1	0.0161	0.0520	-
ν_2	0.0220	-0.4167	-
ν_3	-0.0542	0.0043	-
ν_4	0.1119	-0.0083	-
ν_5	-	-	-
ν_6	-	-	0.092 [0.097]
ν_7	-	-	0.095 [0.161]
ν_8	-	-	-
ν_9	-	-	-

Table 3.9: Same as Table 3.5 derived from the CASSCF(14,12)-MRCI electronic energy data.

Mode	$\gamma^{(A)}$ $\widetilde{A}^1A_2$	$\gamma^{(B)}$ $\widetilde{B}^1B_1$
ν_1	-0.0012	-0.0002
ν_2	-0.0161	-0.0233
ν_3	-0.0166	-0.0024
ν_4	0.0034	0.0040
ν_5	-	-
ν_6	-0.0438	0.0108
ν_7	-0.0698	0.0744
ν_8	-0.0802	-0.0828
ν_9	0.0256	0.1434

reproduces the calculated energy data extremely well. The low-energy crossing of $\widetilde{A}$ and $\widetilde{B}$ electronic states is immediately seen from panel b of Fig. 3.1. This crossing of the $\widetilde{A}$ and $\widetilde{B}$ states evolves into conical intersections in multi-dimensions [46]. It is already attested by the large coupling strength of the ν_7 vibrational mode that the $\widetilde{A}$-$\widetilde{B}$ coupling is expected to have much effect on the observed broadening and asymmetry of the peaks underlying the $\widetilde{B}$ band. It therefore emerges that the $\widetilde{A}$-$\widetilde{B}$ coupling (mainly along ν_7) is crucial to the understanding of the detailed structure of the $\widetilde{B}$ band of l-C_3H_2.

The potential energy functions of the $\widetilde{A}$ and $\widetilde{B}$ states calculated using the parameters of Tables 3.6-3.9 are also examined in detail and plotted in Fig. 3.2 and 3.3. Except some energy lowering, the potential energy curves along ν_1, ν_3 and ν_4 are by and large similar to the ones shown in Fig. 3.1. The curve crossing between the $\widetilde{A}$ and $\widetilde{B}$ states is clearly visible along ν_2 in Fig. 3.1(b). This crossing comes down in energy in the

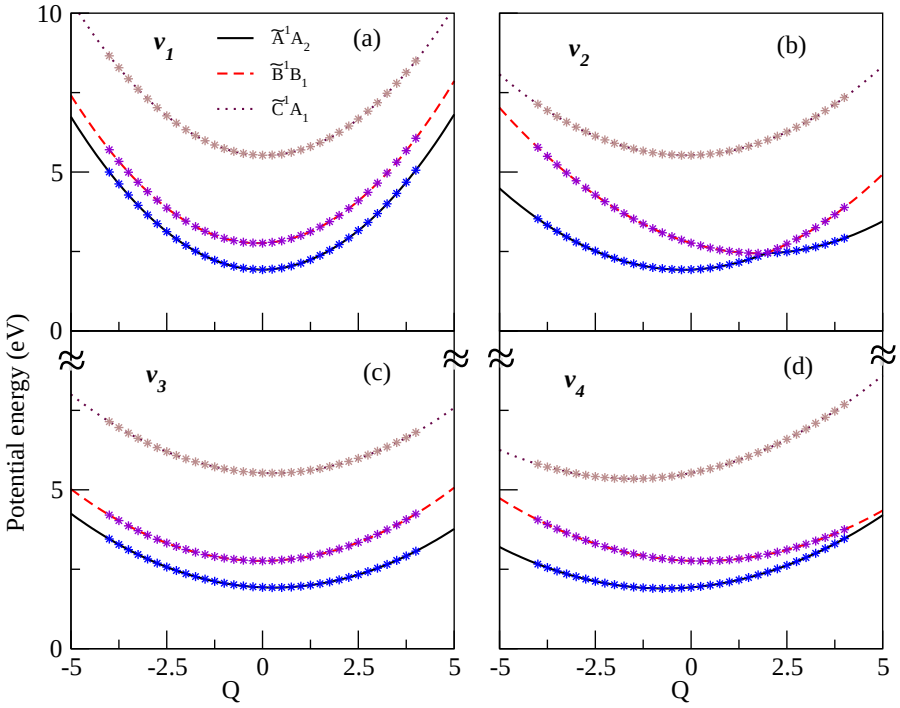

Figure 3.1: Adiabatic potential energy of first three excited electronic states of l-C_3H_2 along the normal displacement coordinates of the totally symmetric vibrational modes. The points in the figure represent calculated EOM-CCSD energies and the lines connecting them are the adiabatic potential energy functions derived from the diabatic electronic Hamiltonian.

CASSCF-MRCI electronic energy data obtained with the CASSCF(10,10)-MRCI and CASSCF(14,12)-MRCI (cf., panel b of Fig. 3.2 and 3.3), respectively. As in Fig. 3.1, the curves in Figs. 3.2 and 3.3 drawn by the solid and dashed lines represent the potential energy functions of the $\widetilde{A}$ and $\widetilde{B}$ electronic states, respectively, obtained from the present theoretical model of Sec. 3.2 and the points superimposed on them represent the electronic energies calculated by the CASSCF-MRCI method. The curve crossings along ν_2 occur at a shorter distance compared to the EOM-CCSD results of Fig. 3.1(b).

A perspective plot (schematic) of the $\widetilde{A}$ and $\widetilde{B}$ electronic states of l-C_3H_2 is presented in Fig. 3.4 along the coordinates of the most important ν_2 and ν_7 vibrational modes. The CASSCF(14,12)-MRCI results are used in this plot. It is shown below that these energy data provide the best agreement with the experimental results. The conical intersections of the $\widetilde{A}$ and $\widetilde{B}$ states are immediately visible from this figure. The degeneracy of the two electronic states along the symmetric vibrational mode ν_2 and avoided crossings along the nondegenerate vibrational mode ν_7 is obvious from the plot. The locus of the degeneracy in the subspace of symmetric vibrational modes defines the seam of conical intersections. The energetic minimum on this seam relative to the equilibrium minimum of a state plays the key mechanistic role in the nuclear dynamics on these electronic

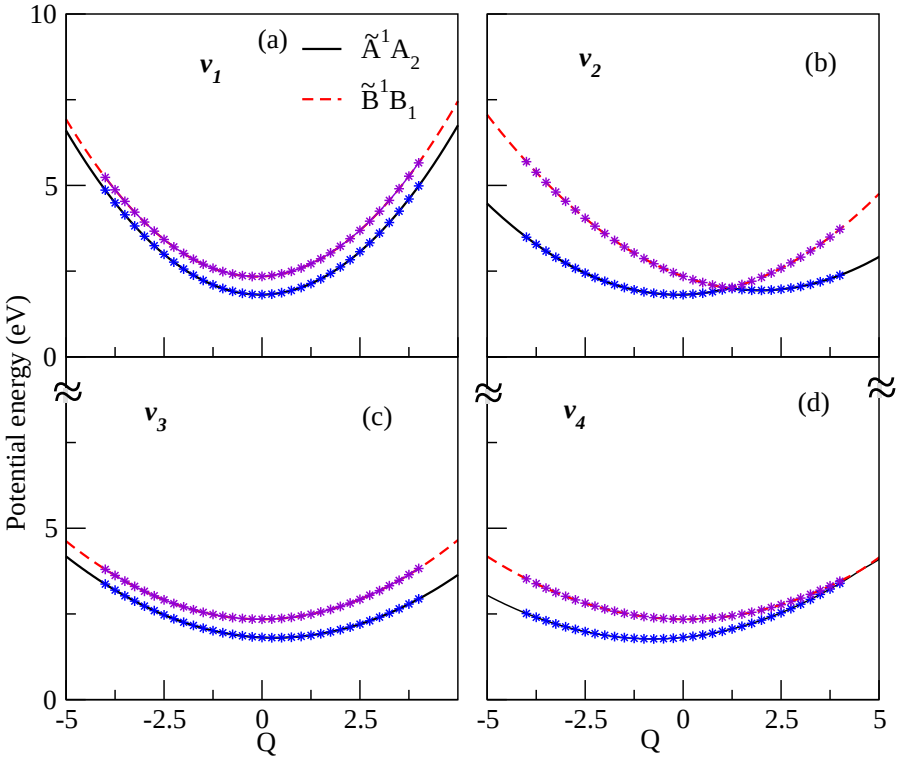

Figure 3.2: Same as in Fig. 3.1 for the $\widetilde{A}$ and $\widetilde{B}$ electronic states of l-C_3H_2. The superimposed points represent the potential energies calculated by the CASSCF(10,10)-MRCI method.

states.

To this end, we note that we have estimated the energetic minimum of $\widetilde{A}$-$\widetilde{B}$ conical intersections using the three sets of electronic structure data presented above. Using the EOM-CCSD [cf., Tables 3.4 and 3.5] data we find that the minimum of the seam of $\widetilde{A}$-$\widetilde{B}$ intersections occurs at ∼2.34 eV and is only ∼0.03 eV above the minimum of the $\widetilde{B}$ state. This seam minimum occurs at ∼2.03 eV (∼0.1 eV above the $\widetilde{B}$ state minimum) and ∼2.0 eV (∼0.08 eV above the $\widetilde{B}$ state minimum) using the CASSCF(10,10)-MRCI [cf., Tables 3.6 and 3.7] and CASSCF(14,12)-MRCI [cf., Tables 3.8 and 3.9] data, respectively. It is therefore clear that this seam minimum is within ∼0.1 eV above the minimum of the $\widetilde{B}$ state.

The lowering of this seam minimum in the CASSCF-MRCI data is also obvious from the potential energy plots given in Fig. (b) of 3.1, 3.2 and 3.3. It is noted before that the $\widetilde{C}$ state is energetically well separated and the minimum of the seam of $\widetilde{A}$-$\widetilde{C}$ intersections occurs at a very high energy (beyond 20 eV) and is not relevant for the present study. The minimum of the $\widetilde{B}$-$\widetilde{C}$ intersections however occurs ∼2.22 eV above the minimum of the $\widetilde{C}$ state estimated from the EOM-CCSD data. This seam minimum lies ∼5.0 eV

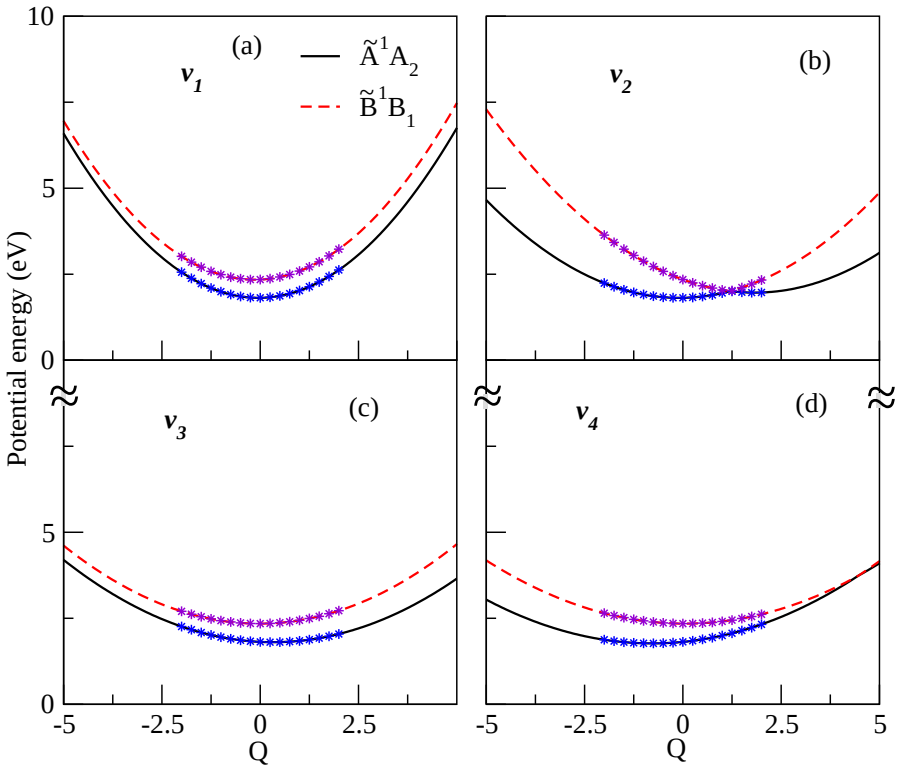

Figure 3.3: Same as in Fig. 3.1 for the $\widetilde{A}$ and $\widetilde{B}$ electronic states of l-C_3H_2. The superimposed points represent the potential energies calculated by the CASSCF(14,12)-MRCI method.

above the minimum of the $\widetilde{B}$ state. Therefore, the $\widetilde{B}$-$\widetilde{C}$ intersections may have some impact on the dynamics of the $\widetilde{C}$ state. However, they are expected to be unimportant for the dynamics of $\widetilde{A}$ and $\widetilde{B}$ electronic states. The impact of these energetic minima on the nuclear dynamics of all three excited electronic states is examined and discussed in the following section.

A careful examination of the coupling parameters of the Hamiltonian given in Tables 3.4-3.9 reveals the importance of 3 a_1 (ν_2-ν_4), 2 b_2 (ν_6, ν_7) and b_1 (ν_8) vibrational modes altogether in the nuclear dynamics of the $\widetilde{A}$-$\widetilde{B}$-$\widetilde{C}$ electronic states. We in the following, consider all these six vibrational modes and systematically examine the vibronic band structure of these electronic states of l-C_3H_2. We note that seven vibrational modes, excluding the high frequency a_1 and b_2 modes were included in the dynamical treatment in Ref. [21]. We however found one of the vibrational mode ν_9 (b_1) does not make any noticeable contribution to the energy spectrum discussed below.

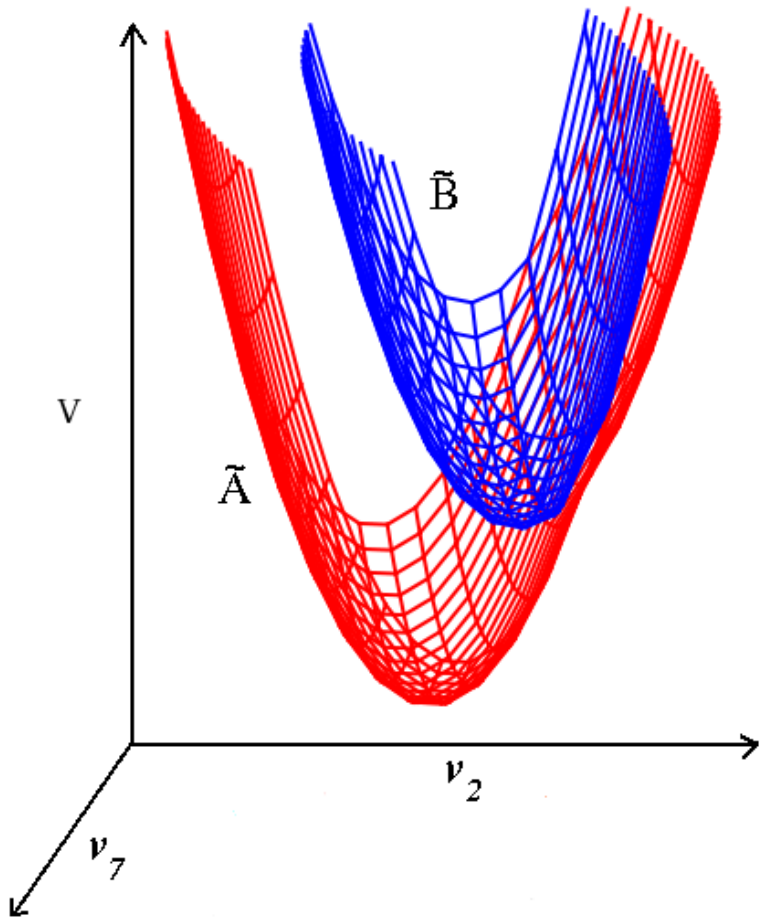

Figure 3.4: Perspective plot showing the $\widetilde{A}$-$\widetilde{B}$ conical intersections in l-C_3H_2.

3.3.2 Electronic Absorption bands of l-C_3H_2

The absorption bands of the $\widetilde{A}$, $\widetilde{B}$ and $\widetilde{C}$ electronic states of l-C_3H_2 are calculated with the aid of the diabatic vibronic Hamiltonian constructed in Sec. 3.2.1 The theoretical results are compared with the available data recorded in matrix environments [6, 7] and in the gas phase [7] and also with the available theoretical results [21]. It is stated in the introduction that the $\widetilde{A}$ state is optically dark. A transition to this state from the reference state is dipole forbidden. The oscillator strength has a value zero for this transition (cf., Table 3.3) in the adiabatic limit. Owing to a strong coupling of this state with the optically bright $\widetilde{B}$ state particularly along the $\sim$252 cm^{-1} (C=C=C in-plane bending) ν_7 vibrational mode of b_2 symmetry [cf., Table 3.4], one expects a significant intensity borrowing effects that would make this state visible in the absorption experiment. This is indeed true and a weak and structured tail is observed at the long wavelength region of the $\widetilde{B}$ band [6, 7]. Furthermore, we mention that the $\widetilde{A}$ state is also probed via pho-

todetachment of l-C_3H_2 anion [47].

To proceed further, we first concentrate on the specific details of the astrophysically relevant spectral features of the most important $\widetilde{B}^1B_1 \leftarrow \widetilde{X}^1A_1$ transition in l-C_3H_2. Two broad DIBs at 4887(3) and 5450 Å assigned recently by Maier and coworkers through absorption measurements in Ne matrix as well as in the gas phase by the CRD spectroscopy have been shown to closely match the profiles observed towards the star HD183143 and HD206267 by the astronomers [7, 20]. These are related to the aforesaid electronic transition in l-C_3H_2 based on the estimate of large column density of this hydrocarbon towards these stars. In a more recent work [24] it was found that the strength ratio of these DIBs is strongly variable. Also a third band apparently expected for l-C_3H_2 in the 5165-5185 Å region based on the results of Maier and coworkers [7] is missing in the new measurements [24]. These observations raised some doubts on the assignment proposed by Maier and coworkers [7]. Very recently it is discussed that there is insufficient evidence available at present to conclude that l-C_3H_2 is a DIB carrier [48]. These developments in the experimental research certainly require a rigorous theoretical study to build a synergy with the observed data. A theoretical work of this kind may also aid in a breakthrough assignment of molecular carrier of DIBs which is quite an obscure problem till date!

The set of *ab initio* electronic structure data presented in the previous section are utilized to examine the nuclear dynamics in the $\widetilde{A}$-$\widetilde{B}$-$\widetilde{C}$ electronic states of l-C_3H_2. The detailed structure of the electronic bands are calculated by a matrix diagonalization approach using the Lanczos recursion [26] as discussed in Sec. 2. The results presented below are converged with respect to the size of the vibrational basis and Lanczos iterations. The time-dependent dynamics of the $\widetilde{B}$ state is investigated by propagating WPs using the MCTDH suite of programs developed at Heidelberg [28].

The vibrational structure of the $\widetilde{B}$ state without including its coupling with the neighboring electronic states is examined first. The uncoupled $\widetilde{B}$ band obtained using the EOM-CCSD electronic structure data of Tables 3.4 and 3.5 is shown in Fig. 3.5(a). The vibrational stick spectrum calculated by the matrix diagonalization method is convoluted with a 15 meV full-width at the half maximum (FWHM) Lorentzian function to calculate the band envelope. The same Lorentzian function is used in the convolution of all spectra presented in this chapter. When compared with the experimental results of Maier *et al.* 2011 and Hodges *et al.* 2000, it can be seen that the intensity of the origin 0_0^0 peak is much too large in the theoretical results. Furthermore, the peaks observed in the experimental band structure are much broader. The intense peaks in the spectrum are ∼1802 cm^{-1} spaced corresponding to the frequency of the ν_2 vibrational mode in the $\widetilde{B}$ state. Much weaker excitation of the ν_4 and ν_3 vibrational modes is also found from the stick energy data. Line spacings of ∼1135 and ∼1509 cm^{-1} corresponding to the fundamentals of these two modes, respectively, are found. A short comment is in order at this point. The intensity distribution of the peaks in Fig. 3.5(a) apparently deviates significantly from that expected from the Huang-Rhys factor of ∼1.0 of the strong

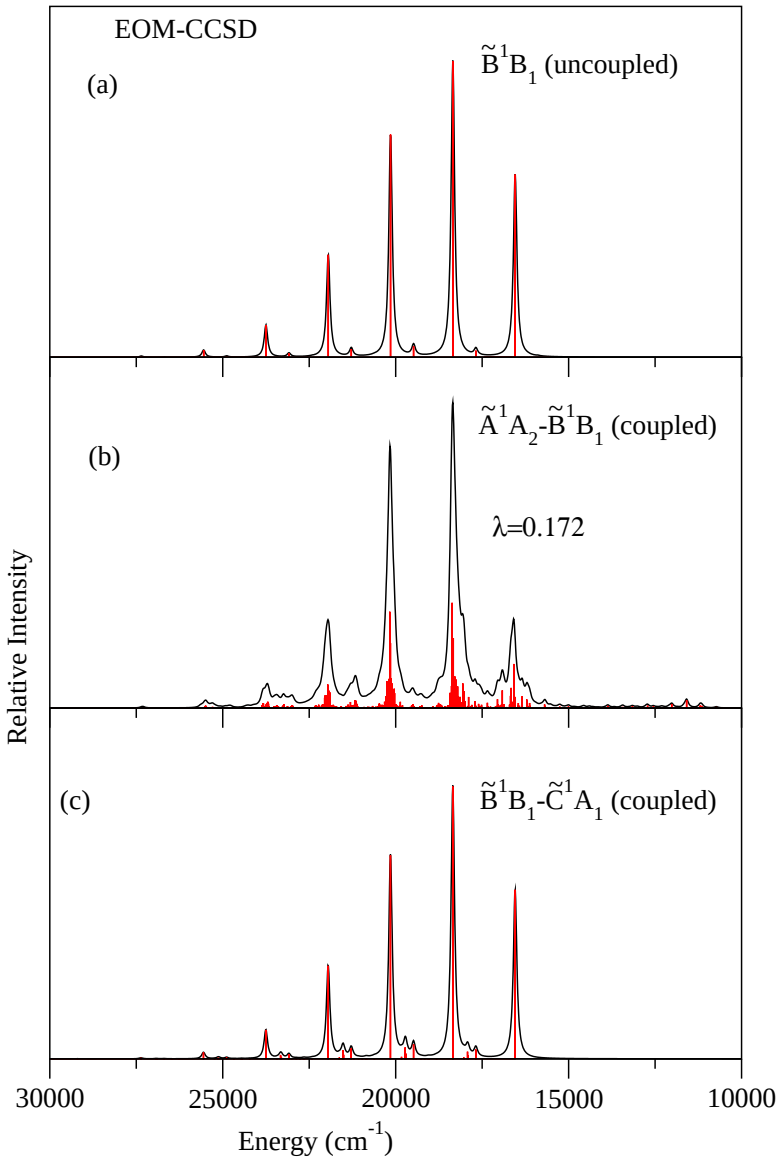

Figure 3.5: $\widetilde{B}^1B_1 \leftarrow \widetilde{X}^1A_1$ electronic absorption band of l-C_3H_2 calculated for the uncoupled $\widetilde{B}$ state (panel a), by including its coupling with the $\widetilde{A}$ state (panel b) and by including coupling with the $\widetilde{C}$ state (panel c). Relative intensity in arbitrary units is plotted as a function of the energy of the final vibronic levels. The EOM-CCSD electronic structure results of Tables 3.4 and 3.5 are used in the calculations.

condon active ν_2 vibrational mode within a linear vibronic coupling scheme [22]. This apparent discrepancy is presumably arising from the contribution of the large second-order coupling parameter (cf., Table 3.5) along ν_2.

A strong coupling of the $\widetilde{B}$ state with the neighboring $\widetilde{A}$ state along ν_7 vibrational

mode is evident from the electronic structure results of Table 3.4. These states are also coupled by the vibrational mode ν_6. However, the coupling is very weak in this case. To assess the effect of these couplings on the structure of the $\widetilde{B}$ band we show this band in Fig. 3.5(b) including its coupling with the $\widetilde{A}$ state. It can be seen in comparison with the spectrum of panel a that the $\widetilde{A}$-$\widetilde{B}$ coupling has much stronger impact on the vibronic structure of the $\widetilde{B}$ state. A huge increase of vibronic line density underneath each peak arising from the associated nonadiabatic coupling can be immediately seen from the spectrum of panel b. Each peak turns broad and diffuse and is in close accord with the experimental findings [6,7]. The cluster of lines are $\sim$2000 cm^{-1} spaced in the spectrum of panel b. Very weak structure of the $\widetilde{A}$ state is also visible in the low-energy side of the $\widetilde{B}$ band in panel b. The coupling of the $\widetilde{B}$ state with the $\widetilde{C}$ state is much weaker and these states are energetically far apart (cf., Table 3.3). The vibronic structure of the $\widetilde{B}$ band obtained in the $\widetilde{B}$-$\widetilde{C}$ coupled states situation is presented in panel c of Fig. 3.5. As expected, no significant impact of this coupling can be seen on the $\widetilde{B}$ band when compared with the same presented in panel b.

It is clear from the above discussion that the $\widetilde{A}$-$\widetilde{B}$ interstate coupling plays very important role in the detailed structure of the $\widetilde{B}$ band of l-C_3H_2. In Fig. 3.6, we present the structure of the $\widetilde{B}$ band calculated in the $\widetilde{A}$-$\widetilde{B}$ coupled states situation and using the parameters of Tables 3.4-3.9. The relative intensity in arbitrary units is plotted as a function of wave length. The available experimental and theoretical results are also presented in the figure. The results obtained with the EOM-CCSD parameters of Tables 3.4 and 3.5 are again included in panel a of Fig. 3.6 for a clearer comparison. The results obtained with CASSCF(10,10)-MRCI parameters [cf., Tables 3.6 and 3.7] are given in panel b. In this case the band is relatively less structured and the peaks are relatively sharp. The band presented in panel c is obtained by using the CASSCF(14,12)-MRCI parameter values [cf., Tables 3.8 and 3.9]. Now a comparison of different spectra and also with the available experimental and theoretical results reveals the following. The spectra presented in panel a are more structured. The weak peak in between two intense peaks is masked by the strong nonadiabatic coupling. This peak is however, visible in the results with a lower value of λ (cf., panel c). This is also visible in the uncoupled state spectrum presented in Fig. 3.5(a). This weak excitation is caused by the ν_4 vibrational mode in combination with ν_2 mode. The splitting of the peaks observed in the gas phase CRD spectroscopic results of Maier and coworkers [7] (cf., panel d of Fig. 3.6) is clearly obtained in the theoretical results. This structure undoubtedly arises from the strong coupling strength of the ν_7 vibrational mode, because this splitting is weak in the results with the lower value of λ and becomes strong with increasing value of λ. In the inset of Figs. 3.6(a-c) the corresponding band structure obtained with higher values of λ (the finite difference values given in Tables 3.4-3.9) is presented. It can be seen that a larger value of λ causes more splitting of the band structure. The estimated spacing of $\sim$2000 cm^{-1} of the main lines is in good agreement with the reported experimental value [7]. We mention that the experimental band structure presented in panel d of Fig. 3.6 corresponds well with the theoretically estimated energetic location of the peaks and also with the shape of the peaks. We note that a somewhat larger spacing of the two

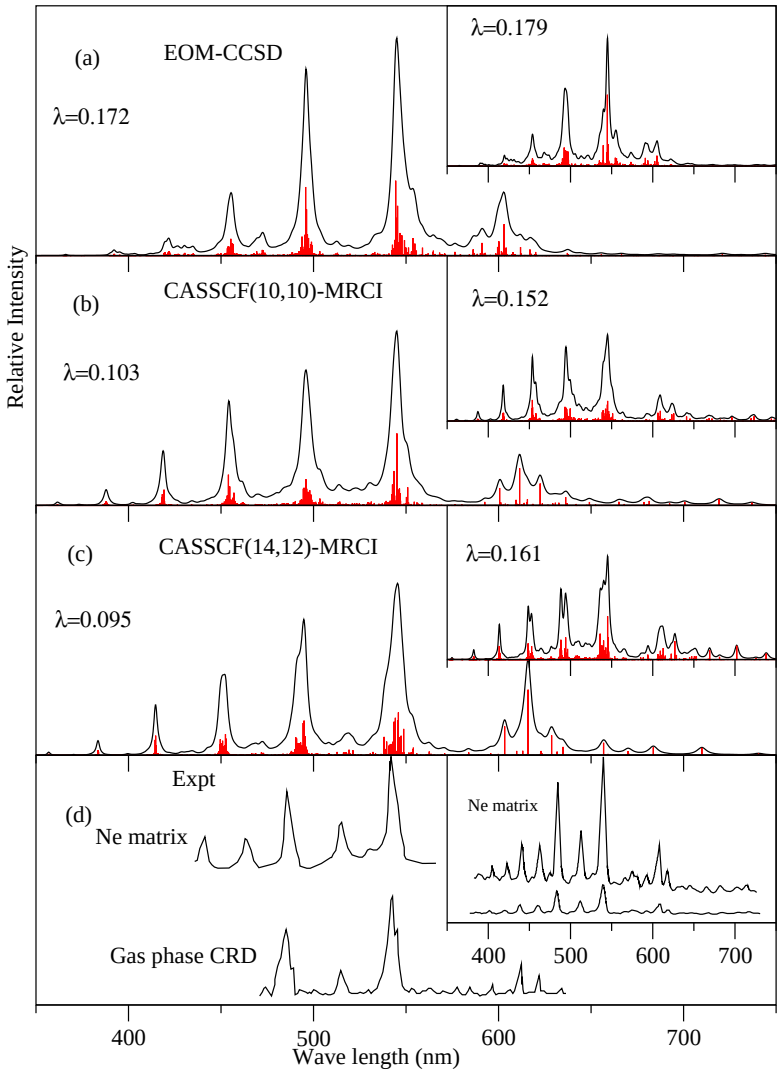

Figure 3.6: The $\widetilde{B}^1B_1 \leftarrow \widetilde{X}^1A_1$ absorption spectrum of l-C_3H_2 calculated with the EOM-CCSD (panel a), CASSCF(10,10)-MRCI (panel b) and CASSCF(14,12)-MRCI (panel c) electronic structure results (see text for details). The experimental results of Maier *et al.* [7] and presented in panel d. The experimental results of Hodges *et al.* [6] given in the inset of panel d.

main lines, than expected from the coupling parameter values of the ν_2 mode in the $\widetilde{B}$ state, is caused by the asymmetric nature of the peaks. The band structure obtained by Hodges *et al.* [6], is given in the inset of panel d for comparison.

Upon scaling the observed intense peak (first one after the origin 0_0^0 peak) with the 5450 Å DIB, the second one is observed at 4929 Å. This is very close to the value observed by the astronomers [7, 24]. Likewise, the third and fourth intense peaks appear at 4518 Å and 4134 Å respectively. In the Ne matrix spectrum recorded by Hodges *et al.* (cf., Table 1 of Ref. [6]) the first intense peak is reported at ∼5390 Å and the

second one at ∼4840 Å. The major progression was reported to be caused by a HCH bending type of mode with an average spacing between peaks of ∼2085 cm^{-1}. The weak intensity of the $\widetilde{A}$ band above 6000 Å reveals peaks at ∼6046 Å, ∼6160 Å and ∼6274 Å in the theoretical results of Fig. 3.6(c). These are vibronic peaks of the $\widetilde{A}$ state. Peaks at similar locations observed in the CRD experiment are however attributed to the rotationally resolved peaks of the $\widetilde{B}$ band [7]. We note that the theoretical results are sensitive to the vertical energy gap of the two states and the latter varies depending on the accuracy limit of the chosen electronic structure method. This is clearly obvious from the various sets of results presented in Fig. 3.6. The CASSCF(14,12)-MRCI results presented above offers the best estimate of this quantity available to date. We mention that the theoretical results presented in Ref. [21] are quite similar to ours presented above. An *ab initio* value of the vertical energy gap of ∼5817 cm^{-1} has been reported in this work. The vibronic band calculated by this author without adjustment of any parameters appears to be somewhat more structured than ours. The band structure calculated with an adjusted vertical energy gap of 4800 cm^{-1} [21] closely resemble to our CASSCF(14,12)-MRCI results of Fig. 3.6(c) although the combination peak in between the two main peaks is weaker in our results.

Finally, the vibronic structure of the $\widetilde{C}$ state considering its coupling with the $\widetilde{B}$ state presented in Fig. 3.7(a). The EOM-CCSD parameter values of Tables 3.4 and 3.5 are used in this case. The results obtained in the Ne matrix environment by Hodges *et al.* [6] are given in the panel b of Fig. 3.7. Although the matrix results cannot be directly compared with ours, the overall band shape is expected to be similar in both cases. This can be seen to be true from Fig. 3.7. The vibrational modes ν_4, ν_3 form major progression in the $\widetilde{C}$ band. Peak spacings of 1174, 1477 cm^{-1}, respectively, corresponding to the frequency of these modes in the $\widetilde{C}$ state can be estimated from the theoretical results. We note that we did not investigate any coupling of the $\widetilde{C}$ state with further higher excited electronic states of l-C_3H_2 because this chapter primarily focuses on the structure and dynamics of the $\widetilde{B}$ state.

3.4 Time-dependent dynamics of the $\widetilde{B}$ state

It appears from the foregoing discussions that the vibronic band structure of the $\widetilde{B}$ state of l-C_3H_2 obtained with the CASSCF(14,12)-MRCI electronic structure data, with λ=0.092 eV exhibits the best match with the gas phase experimental spectrum. We realized that the asymmetry and diffuseness caused by the nonadiabatic coupling are the crucial factors governing the overall structure of the peaks underlying the vibronic band. In order to check for consistency, we used various state-of-the-art electronic structure methods to derive the parameters of the given Hamiltonian (cf., Tables 3.4 - 3.9) in Sec. 3.2 we also checked the basis-set dependencies of the results and found that the chosen one is accurate enough considering the affordable computational cost. To examine the time-dependent dynamics of the $\widetilde{B}$ state we carried out WP propagation in the coupled manifold of $\widetilde{A}$-$\widetilde{B}$ electronic states by initially populating the $\widetilde{B}$ state. The WP propa-

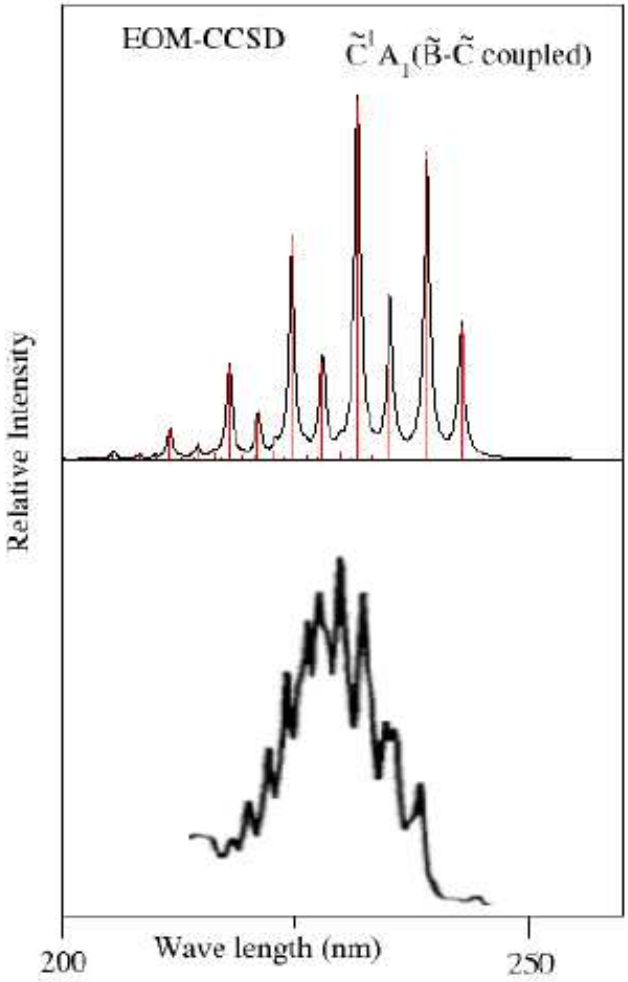

Figure 3.7: $\widetilde{C}^1A_1 \leftarrow \widetilde{X}^1A_1$ absorption spectrum of l-C_3H_2. Panel a: theoretical results using the EOM-CCSD electronic structure data; panel b: the Ne matrix results reproduced from Hodges *et al.*. [6]

gation is carried out using the MCTDH suite of program developed by the Heidelberg group [28] and the CASSCF(14,12)-MRCI Hamiltonian parameters given in Tables 3.8 & 3.9. The technical details of the calculations are given in Table 3.10. Time-dependence of adiabatic (solid curves) and diabatic (dashed curves) electronic populations are shown in Fig. 3.8.

In Fig. 3.9 time-dependence of the adiabatic (top panel) and diabatic (bottom panel) electronic populations of the $\widetilde{B}$ state are shown. The time-dependence of the population of the $\widetilde{A}$ state is discussed below however, the curves are not shown in Fig. 3.9 for brevity. All three sets of Hamiltonian parameters (cf., Tables 3.4 & 3.5, 3.6 & 3.7 and 3.8 & 3.9) are used to calculate the population curves of Fig. 3.9. The population curves obtained with three different sets of parameter values are shown by the solid (EOM-CCSD),

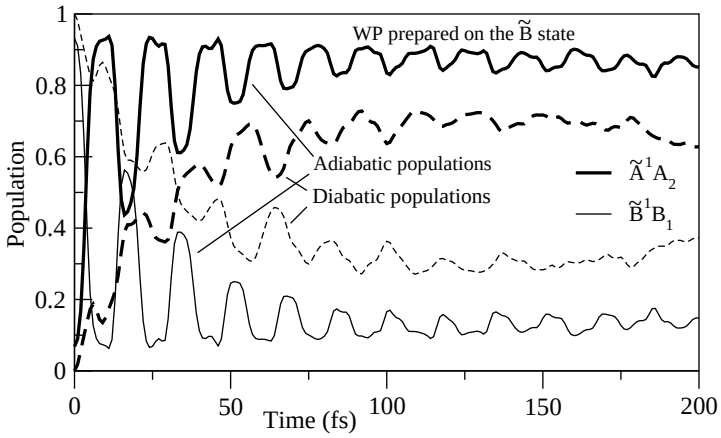

Figure 3.8: Time-dependence of electronic adiabatic (thick curves) and diabatic(dashed curves) populations of the $\widetilde{A}$ and $\widetilde{B}$ electronic states of l-C_3H_2 for an initial transition of the WP to the $\widetilde{B}$ state in the coupled $\widetilde{A}$-$\widetilde{B}$ states of l-C_3H_2 obtained by using the CASSCF(14,12)-MRCI Hamiltonian parameters of Tables 3.8 and 3.9).

dashed (CASSCF(10,10)-MRCI) and dotted (CASSCF(14,12)-MRCI) lines. Since the WP is initially prepared on the diabatic $\widetilde{B}$ state, its population is 1.0 at t=0 (cf., bottom panel of Fig. 3.9). This population decreases in time and flows to the diabatic $\widetilde{A}$ state.

The population of the latter state grows in time starting from a value of 0.0 at t=0 (cf., Fig. 3.8). Since a diabatic electronic state is an admixture of the adiabatic electronic states, the population of the adiabatic $\widetilde{B}$ state is $\sim$0.93 and that of the adiabatic $\widetilde{A}$ state is $\sim$0.07 at t=0 obtained with the CASSCF(14,12)-MRCI parameter values. Similar values (as obvious from the curves in Fig. 3.9) are also obtained with the other two parameter sets. Both the adiabatic and diabatic populations of the $\widetilde{B}$ state decrease monotonically in time and exhibit quasiperiodic recurrences. These recurrences are damped at longer times. The period of dominant recurrences is $\sim$17 fs (1962 cm^{-1}) which relates to the frequency of ν_2 vibrational mode. Furthermore, the adiabatic population decays faster than the diabatic population. The initial fast decay of populations of the $\widetilde{B}$ state relates to a nonradiative internal conversion rate of $\sim$28 fs ($\sim$98 fs), $\sim$28 fs ($\sim$84 fs) and $\sim$25 fs ($\sim$90 fs) in the adiabatic (diabatic) picture employing EOM-CCSD, CASSCF(10,10)-MRCI and CASSCF(14,12)-MRCI parameter sets, respectively. We note that these time scales represent the decay rate of the electronic states and can not be related to the width of the individual vibronic peaks seen in the spectra presented in Figs. 3.6. It is discussed in Sec. 3.3.2 that the observed band structure of $\widetilde{B}$ state exhibits best match with the theoretically calculated one employing the CASSCF(14,12)-MRCI parameter set. We reiterate that the electronic structure results obtained with the latter method seem to offer the best estimate of λ along ν_7 and the vertical energy gap of the $\widetilde{A}$ and $\widetilde{B}$ states of l-C_3H_2. The EOM-CCSD data clearly overestimate these parameters and as a result substantial fraction of the WP moves back and forth between

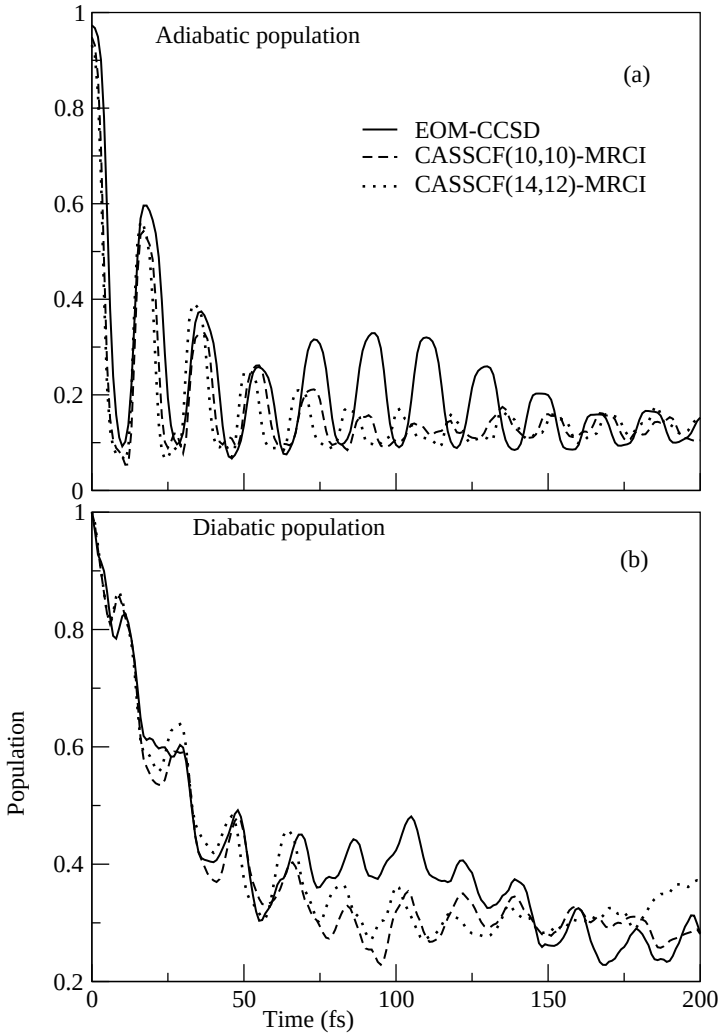

Figure 3.9: Non radiative decay of the adiabatic (panel a) and diabatic (panel b) $\widetilde{B}$ state of l-C_3H_2 calculated from the three sets of *ab initio* electronic structure data.

the two states and gives rise to large amplitude of oscillations in the adiabatic and diabatic population curves (solid lines) in Fig. 3.9.

3.5 Summarizing remarks

Electronic absorption spectroscopy of l-C_3H_2 molecule is theoretically studied in this chapter. This molecule is believed to be a potential carrier of two broad DIBs observed at ∼5450 and ∼4881 Å. This initiated intense experimental investigation of its electronic absorption spectroscopy in laboratory. While the earlier measurements relied on the molecule isolated in rare gas matrix environments, very recently successful measurements were carried out in the gas phase with a CRD set-up. A close correspondence of data recorded in laboratory and in radioastronomy has been reported. Further high

Table 3.10: Normal mode combinations and sizes of the primitive [52] and single-particle basis functions used in the converged MCTDH calculations for the coupled $\widetilde{A}$-$\widetilde{B}$ electronic states of l-C_3H_2.

Normal modes[a]	Primitive basis[b]	SPF basis[c] $[\widetilde{A},\ \widetilde{B}]$
(ν_3,ν_7)	(10,24)	[17,20]
(ν_4,ν_6)	(13,15)	[17,12]
(ν_8,ν_2)	(3,20)	[14,15]

[a] Vibrational mode bracketed together were treated as a single particle, e.g., particle 1 is 2-dimensional particle including modes ν_3 and ν_7. [b] The primitive basis is the number of harmonic oscillator DVR functions, in the dimensionless coordinate system required to represent the system dynamics along the relevant mode. The primitive basis for each particle is the product of the one-dimensional bases. The full primitive basis consists of a total of 28.05×10^5 functions. [c] The SPF basis is the number of single-particle functions used.

resolution measurements, in recent years, also raised some doubts on this correspondence and assignments. Theoretical studies were also reported and correspondence of the results with those observed in the matrix environment was established.

It is a fairly simple system by today's standard, however, it is clear from the results and discussion presented above that its electronic structure is notoriously difficult and represent a problem of outstanding complexity. Therefore, in the present contribution we carried out a thorough theoretical study from first principles in order to understand the observed experimental data. Our theoretical model relies on the *ab initio* electronic structure calculations at various sophisticated levels of theory. It is found that the $\widetilde{A}$ and $\widetilde{B}$ electronic states of this molecule are strongly coupled along the C=C=C in plane bending vibrational mode ν_7. The $\widetilde{B}^1B_1 \leftarrow \widetilde{X}^1A_1$ absorption occurs in the same wavelength region of the observed DIBs. This transition is optically allowed, and a vibronic coupling with the dipole forbidden $\widetilde{A}^1A_2$ state plays very crucial role in the detailed vibronic structure of the $\widetilde{B}$ band of l-C_3H_2 . The calculated structure of this band with different sets of electronic structure data is quite similar as regard to the two main intense peaks are concerned. Individual shape of these peaks however, strongly vary with the strength of the $\widetilde{A}$-$\widetilde{B}$ coupling. This coupling seems to vary significantly with the choice of electronic structure method and the method used to calculate it. It was treated as an adjustable parameter in a previous theoretical study [6] and a fairly large value of this parameter reported in a recent study [21]. We have estimated this coupling by a numerical finite difference scheme as well as by fitting the calculated *ab initio* electronic energies calculated over a large grid in the coordinate space. It is found that the finite difference results are always grater than the fit results. We believe that the latter are more accurate and trustworthy as the contribution of the second-order coupling term is ignored in the finite-difference calculations. The calculated parameters presented in Tables 3.4-3.9 are used without any adjustment in the calculation of various spectra presented in this chapter. It is generally found that the individual peaks underlying the $\widetilde{B}$ band are more sharp, structureless and less asymmetric in the limit of a lower value of the coupling. They tend to become structured diffuse and highly asymmetric in the limit of a higher value of this coupling. Examination of results from

all possible comparison calculations reveal that the Hamiltonian parameters estimated from the CASSCF(14,12)-MRCI electronic structure data [cf., Tables 3.8 and 3.9] offer the best match with the experimental findings. These set of parameters appears to be more accurate than those available in the literature. We however mention that the theoretical results obtained with three sets of parameter values are very close to each other. They reveal dominant progression of the ν_2 vibrational mode and a very weak progression of ν_4 in combination with ν_2 in the $\widetilde{B}$ band of l-C_3H_2.

As a result of strong vibronic coupling (vide supra) the location of the origin 0_0^0 peak of the $\widetilde{B}$ state turns out to be highly uncertain. It is essentially buried within the continuum of energy levels of the $\widetilde{A}$ state. On scaling the first fundamental 2_0^1 (2 refers to the ν_2 mode) peak at the location of the DIB at 5450 Å, the second 2_0^2 and third 2_0^3 peaks are located at ∼4929 and ∼4518 Å, respectively. These data compare well with the Ne matrix results at ∼5445/5417, 4856 and 4412 Å and CRD spectroscopy results at ∼5450, 4887(3) and 4425-4445 Å [7] and the Ne matrix results at ∼5390, 4840 and 4400 Å [6], in that order. Two broad DIBs located at 5450 and 4881 Å by radioastronomy correlate well with the findings given above. It is also found that the additional peak located in the 5165-5185 Å region of CRD spectroscopy results is extremely weak. It appears in between the 2_0^1 and 2_0^2 peaks and is a combination peak with the weakly active vibrational mode ν_4. The intensity of this peak is strongly affected by the vibronic coupling and is not visible in the strong coupling limit. Apparently this peak has not been observed in the recent high resolution measurements of Krełowski *et al.* [24]. Given a very low intensity of this peak and its mentioned sensitivity to the vibronic coupling strength, it is quite likely to be masked by numerous vibronic lines in that region. This remark follows the various theoretical analysis presented in this chapter. This weak peak is located at ∼5176 Å in the present theoretical results [cf., Fig. 3.6(c)] and compare very well with the CRD spectroscopy result [cf., Fig. 3.6(d)].

Based on the extensive analysis discussed above, it follows that the highly asymmetric nature of the peaks underlying the $\widetilde{B}$ band governs the spacing among them. Within the error limit of the available electronic structure methods these spacings are quite well reproduced. Considering the close agreement of the present theoretical data with the observed ones (both from radioastronomy and laboratory) strongly suggests that l-C_3H_2 is a very likely candidate to absorb in the region of the recorded DIBs. Furthermore, as found in this chapter that the decay rate of the $\widetilde{B}$ state is extremely fast, which strongly supports the observed diffuse vibronic band structure of this state. Therefore, keeping all possible ambiguities in mind, the thorough investigation carried out in this chapter reveals a strong synergy with the observed results. Therefore, despite the suggestions that l-C_3H_2 is too small to survive in the environment with strong UV radiation [49–51], the theoretical results of this chapter in conjunction with the recorded data suggest that l-C_3H_2 is a "likely candidate" of molecular carrier of 5450 and 4881 Å DIBs.

References

[1] L. M. Hobbs, D. G. York, T. P. Snow, T. Oka, J. A. Thorburn, M. Bishof, S. D. Friedman, B. J. McCall, B. Rachford, P. Sonnentrucker, D. E. Welty, Astrophys. J. **680**, 1256 (2008).

[2] L. M. Hobbs, D. G. York, J. A. Thorburn, T. P. Snow, M. Bishof, S. D. Friedman, B. J. McCall, T. Oka, B. Rachford, P. Sonnentrucker, D. E. Welty, Astrophys. J. **705**, 32 (2009).

[3] P. W. Merrill, R. F. Sanford, O. C. Wilson, G. C. Burwell, Astrophys. J. **86**, 274 (1937).

[4] G. H. Herbig, Astrophys. J. **542**, 334 (2000).

[5] J. P. Maier, G. A. H. Walker, D. A. Bohlender, Astrophys. J. **602**, 286 (2004).

[6] J. A. Hodges, R. J. McMahon, K. W. Sattelmeyer, J. F. Stanton, Astrophys. J. **544**, 838 (2000).

[7] J. P. Maier, G. A. H. Walker, D. A. Bohlender, F. J. Mazzotti, R. Raghunandan, J. Fulara, I. Garkusha, A. Nagy, Astrophys. J. **726**, 41 (2011).

[8] L. Biennier, F. Salama, L. J. Allamandola, J. J. Scherer, J. Chem. Phys. **118**, 7863 (2003).

[9] O. Sukhorukov, A. Staicu, E. Diegel, G. Rouillé, Th. Henning, F. Huisken, Chem. Phys. Lett. **386**, 259 (2004).

[10] S. Iglesias-Groth, A. Manchado, D. A. GarcÌa-Hernàndez, J. I. Gonzàlez Hernàndez, D. L. Lambert, Astrophys. J. **685**, L55 (2008).

[11] J. Krełowski, Y. Beletsky, G. A. Galazutdinov, R. Kołos, M. Gronowski, G. LoCurto, Astrophys. J. **714**, L64 (2010).

[12] V. S. Reddy, S. Mahapatra, J. Chem. Phys. **128**, 091104 (2008).

[13] V. S. Reddy, S. Ghanta, S. Mahapatra, Phys. Rev. Lett. **104**, 111102 (2010).

[14] S. Ghanta, V. S. Reddy, S. Mahapatra, Phys. Chem. Chem. Phys. **13**, 14523 (2011).

[15] S. Ghanta, V. S. Reddy, S. Mahapatra, Phys. Chem. Chem. Phys. **13**, 14531 (2011).

[16] P. Thaddeus, M. C. McCarthy, M. J. Travers, C. A. Gottlieb, W. Chen, Faraday Discuss. **109**, 121 (1998).

[17] R. A. Seburg, E. V. Patterson, J. F. Stanton, R. J. McMahon, J. Am. Chem. Soc. **119**, 5847 (1997).

[18] J. F. Stanton, J. T. DePinto, R. A. Seburg, J. A. Hodges, R. J. McMahon, J. Am. Chem. Soc. **119**, 429 (1997).

[19] E. Achkasova, M. Araki, A. Denisov, J. P. Maier, J. Mol. Spectrosc. **237**, 70 (2006).

[20] H. Linnartz, N. Wehres, H. VanWinckel, G. A. H. Walker, D. A. Bohlender, A. G. G. M. Tielens, T. Motylewski, J. P. Maier, Astron. Astrophys. **511**, L3 (2010).

[21] J. F. Stanton, Faraday Discuss. **150**, 331 (2011).

[22] H. Köppel, W. Domcke, L. S. Cederbaum, Adv. Chem. Phys. **57**, 59 (1984).

[23] E. B. Wilson Jr., J. C. Decius, P. C. Cross, Molecular vibrations (McGraw-Hill, New York, 1955).

[24] J. Krełowski, G. A. Galazutdinov, R. Kołos, Astrophys. J. **735**, 124 (2011).

[25] T. S. Venkatesan, S. Mahapatra, H. -D. Meyer, H. Köppel, L. S. Cederbaum, J. Phys. Chem. A **111**, 1746 (2007).

[26] J. Cullum, R. Willoughby, Lanczos Algorithms for Large Symmetric Eigenvalue Problems (Birkhäuser, Boston, 1985, Vols. I and II).

[27] H. Köppel, W. Domcke, in Encyclopedia of Computational Chemistry edited by P. V. R. Schleyer, (Wiley, New York, 1998), P. 3166.

[28] G. A. Worth, M. H. Beck, A. Jäckle, and H. -D. Meyer, The MCTDH Package, Version 8.2, (2000), University of Heidelberg, Heidelberg, Germany. H.-D. Meyer, Version 8.3 (2002), Version 8.4 (2007). See http://mctdh.uni-hd.de.

[29] H. -D. Meyer, U. Manthe, L. S. Cederbaum, Chem. Phys. Lett. **165**, 73 (1990).

[30] U. Manthe, H. -D. Meyer, L. S. Cederbaum, J. Chem. Phys. **97**, 3199 (1992).

[31] M. H. Beck, A. Jäckle, G. A. Worth, H. -D. Meyer, Phys. Rep. **324**, 1 (2000).

[32] A. D. Becke, J. Chem. Phys. **98**, 5648 (1993).

[33] R. A. Kendall, T. H. Dunning Jr., and R. J. Harrison, J. Chem. Phys. **96**, 6796 (1992).

[34] G. Maier, H. P. Reisenauer, W. Schwab, P. *Čár*sky, B. A. Hess Jr, L. J. Schaad, J. Am. Chem. Soc. **109**, 5183 (1987).

[35] P. Birza, A. Chirokolava, M. Araki, P. Kolek, J. P. Maier, J. Mol. Spectrosc. **229**, 276 (2005).

[36] M. J. Frisch *et al.*, Gaussian 03, Revision B. 05, Gaussian, Inc., Pittsburgh, (2003) PA.

[37] G. Herzberg, 1991, Molecular spectra & molecular structure II. Infrared and raman spectra of polyatomic molecules.

[38] H. Sekino, and R. J. Bartlett, Int. J. Quantum Chem., Quantum Chem. Symp. **18**, 255 (1984).

[39] J. Geertsen, M. Rittby, and R. J. Bartlett, Chem. Phys. Lett. **164**, 57 (1989).

[40] J. F. Stanton, R. J. Bartlett, J. Chem. Phys. **98**, 7029 (1993).

[41] H. -J. Werner, P. J. Knowles, J. Chem. Phys. **89**, 5803 (1988).

[42] P. J. Knowles, H. -J. Werner, Chem. Phys. Lett. **145**, 514 (1988).

[43] P. J. Knowles, H. -J. Werner, Theor. Chim. Acta. **84**, 95 (1992).

[44] MOLPRO, version 2010.1, a package of ab initio programs, H. -J. Werner, P. J. Knowles, G. Knizia, F. R. Manby, M. Schütz, and others, see http://www.molpro.net.

[45] B. Noller, M. Margraf, C. Schröter, T. Schultz, I. Fischer, Phys. Chem. Chem. Phys. **11**, 5353 (2009).

[46] Conical Intersections: Electronic Structure, Dynamics and Spectroscopy, edited by W. Domcke, D. R. Yarkony, H. Köppel (World Scientific, Singapore, 2004).

[47] M. S. Robinson, M. L. Polak, V. M. Bierbaum, C. H. DePuy, W. C. Lineberger, J. Am. Chem. Soc. **117**, 6766 (1995).

[48] T. Oka, and B. J. McCall, Science. **331**, 293 (2011).

[49] P. Hall, D. A. Williams, Astrophys. Space Sci. **229**, 49 (1995).

[50] R. P. A. Bettens, E. Herbst, Astrophys. J. **468**, 686 (1996).

[51] S. D. Taylor, W. W. Duley, MNRAS. **286**, 344 (1997).

[52] T. S. Venkatesan, S. Mahapatra, H. Köppel, L. S. Cederbaum, J. Mol. Struct. **838**, 100 (2007).

4 Theoretical Study on Molecules of Interstellar Interest.I. Radical Cation of Noncompact Polycyclic Aromatic Hydrocarbons[1]

4.1 Introduction

In continuation to our work on radical cation of naphthalene (Np^+) and anthracene (An^+) [1–4], we in this chapter set out to study the structure and dynamics of their higher homologs in the catacondensed series, viz., radical cation of tetracene (Tn^+), pentacene (Pn^+) and hexacene (Hn^+). The motivation behind this work primarily stems from the vast amount of data available from the experimental measurements on these systems by various groups (see Ref [5–13]) and also the data recorded by stellar spectroscopists [5, 14, 15]. In addition to this primary interest, it appears logical to understand how the electronic structure and dynamical properties of these molecules change with their growing size and whether they follow a certain trend. Electron-nuclear coupling (vibronic coupling) is an important mechanism that decides the fate of their electronic excited states [16,17]. It is therefore worthwhile to know how the energy of the electronic states and their coupling mechanism modifies with an increase in the number of fused benzene rings. This issue is discussed at length in the text.

Experimental photoelectron (PE) spectra from benzene to pentacene were measured by Michael *et al.* [7]. The measured line positions were compared with theoretical green's function calculations using an algebraic-diagrammatic construction scheme. Coropceanu *et al.* [18] also recorded the gas phase UV PE spectra (An to Pn) and discussed the importance of hole and electron-vibrational interactions in these oligoacene molecules. Experimental PE spectrum of Hn molecule was measured by Clar *et al.* [19] and Boschi *et al.* [13] and compared with theoretically calculated vertical ionization energies (VIEs). Eugene *et al.* [10] carried out electronic structure calculations (Np to Hn) and reported structural parameters and ionization energy values using a density functional method. Very recently ZEKE, resonance enhanced multiphoton ionization spectra of Tn [20] and Pn [21] molecules were recorded and the importance of vibronic coupling in the spectral progression was discussed in relation with the literature data [22, 23]. Spectra of

[1]The subject of this Chapter is published in: S. N. Reddy & S. Mahapatra, J. Phys. Chem. A, **117**, 8737 (2013).

Tn^+ and Pn^+ were also measured in rare gas matrix environments and the results were compared with DIB locations recorded by the stellar spectroscopists [5, 14, 24, 25].

We reiterate that detailed theoretical studies to understand the vast amount of experimental data discussed above are missing in the literature. In the present study we therefore attempt to investigate the quantum chemistry and dynamics of the four energetically low-lying electronic states of Tn^+, Pn^+ and Hn^+. We developed suitable vibronic coupling models for these cations with the aid of *ab initio* quantum chemistry calculations. First principles nuclear dynamics study is carried out thereafter to understand the structure of their photo-ionization bands and the time-dependent dynamics of electronic excited states. The theoretical results are compared with the experimental PE spectra, and discussed in relation to our earlier findings on Np^+ and An^+. In addition with photoelectron spectral studies, we set out to investigate the detailed examination of the band structures of Tn^+ and Pn^+ at higher energy resolution and their symbiosis with the experimental ZEKE spectroscopy results as well as the data available in the literature on stellar spectroscopy measurements. The excitations of vibrational modes, electronic nonadiabatic coupling effects, comparisons with the matrix isolation spectral studies and the relation with the DIBs are examined and discussed in relation with the experimental observations mentioned above.

4.2 Theoretical and computational details

4.2.1 The Hamiltonian

Oligoacene molecules, $C_{4n+2}\ H_{2n+4}$, considered in this work are Tn^+; n=4, Pn^+; n=5 and Hn^+; n=6. These radical cations in their neutral form contain linearly arranged fused benzene rings and are found (within the employed level of electronic structure theory) to possess a planar equilibrium configuration of D_{2h} point group symmetry. In the following, nuclear dynamics in the electronic ground ($\widetilde{X}$) and first three excited ($\widetilde{A}$, $\widetilde{B}$ and $\widetilde{C}$) states of these radical cations is examined quantum mechanically. Analogous to our previous work on Np^+ and An^+ [1–4], we construct suitable vibronic model Hamiltonians in terms of the dimensionless normal coordinates of the vibrational modes (Q) in accordance with the symmetry selection rules. The vibronic Hamiltonian for the four lowest (vide supra) electronic states of these three radical cations in a diabatic electronic basis [26] can be symbolically represented as

$$\mathcal{H} \;=\; (\mathcal{T}_N + \mathcal{V}_0)\mathbf{1_4} + \begin{pmatrix} W_{\widetilde{X}} & W_{\widetilde{X}-\widetilde{A}} & W_{\widetilde{X}-\widetilde{B}} & W_{\widetilde{X}-\widetilde{C}} \\ & W_{\widetilde{A}} & W_{\widetilde{A}-\widetilde{B}} & W_{\widetilde{A}-\widetilde{C}} \\ & & W_{\widetilde{B}} & W_{\widetilde{B}-\widetilde{C}} \\ h.c. & & & W_{\widetilde{C}} \end{pmatrix}, \tag{4.1}$$

where $\mathbf{1_4}$ is a 4×4 unit matrix and $(\mathcal{T}_N + \mathcal{V}_0)$ is the Hamiltonian for the unperturbed

electronic ground state of the neutral molecules. The nuclear motion in this reference state is treated as harmonic. Accordingly, $\mathcal{T}_N$ and $\mathcal{V}_0$ are given by

$$\mathcal{T}_N = -\frac{1}{2}\sum_{i=1}^{n}\omega_i\frac{\partial^2}{\partial Q_i^2}, \tag{4.2}$$

$$\mathcal{V}_0 = \frac{1}{2}\sum_{i=1}^{n}\omega_i Q_i^2. \tag{4.3}$$

The matrix Hamiltonian (with elements W) in Eq. 4.1 represents the diabatic energies of the given electronic states of the radical cation (diagonal elements) and their coupling energies (off-diagonal elements). Using the standard vibronic coupling theory [26] the elements of this Hamiltonian are expanded in a Taylor series around the equilibrium geometry of the reference state at ($\mathbf{Q}$=0)

$$W_j \;=\; E_0^{(j)} + \sum_{i\in a_g}\kappa_i^{(j)}Q_i + \frac{1}{2}\sum_{i\in all}\gamma_i^{(j)}Q_i^2 \;\;;\;\; j \;\in\; \widetilde{X}, \widetilde{A}, \widetilde{B} \textit{ and } \widetilde{C} \tag{4.4}$$

$$W_{j-k} \;=\; \sum_i \lambda_i^{(j-k)}Q_i, \tag{4.5}$$

with $j-k \in \widetilde{X}$-$\widetilde{A}$, $\widetilde{X}$-$\widetilde{B}$,$\widetilde{X}$-$\widetilde{C}$, $\widetilde{A}$-$\widetilde{B}$, $\widetilde{A}$-$\widetilde{C}$, $\widetilde{B}$-$\widetilde{C}$. In the above equations the quantity $E_0^{(j)}$ represents the vertical ionization energy of the j^{th} electronic state. $\kappa_i^{(j)}$ and $\gamma_i^{(j)}$ are the linear and second-order coupling parameters of the i^{th} vibrational mode in the j^{th} electronic state. The quantity $\lambda_i^{(j-k)}$ describes the first-order coupling parameter between the j and k electronic states through the coupling vibrational mode i of appropriate symmetry. The parameters introduced in the above Hamiltonian are calculated by performing extensive *ab initio* electronic structure calculations as described below.

4.2.2 Electronic structure calculations

Calculations of optimized equilibrium geometry, harmonic vibrational frequencies (ω_i) and dimensionless normal displacement coordinates ($\mathbf{Q}$) of the electronic ground state of neutral Tn, Pn and Hn molecules are carried out at the second-order Møller-Plesset perturbation (MP2) level of theory employing the correlation-consistent polarized valence double-ζ (cc-pVDZ) basis set of Dunning [27]. The Gaussian-03 suite of programs [28] is used for these calculations. The equilibrium configuration of the electronic ground state of all three molecules converged to the D_{2h} symmetry point group. It is noteworthy that energy of the equilibrium minimum of these linear chain of oligoacene molecules decreases linearly with increasing number of fused benzene ring. Starting from benzene the energies of the equilibrium minimum of the electronic ground state is calculated upto decacene. The results are shown in Fig. 4.1. The calculated *ab initio* energies

and a linear fit to these energies are shown by points and solid line in the figure, respectively. The root mean square deviation of the predicted (by the linear fit equation) and calculated energies is typically ∼0.0029 E_H. The normal vibrational modes of these molecules transform according to the following irreducible representation of the D_{2h} symmetry point group.

$$\text{Tn} : \Gamma_{vib} = 15a_g + 7a_u + 6b_{1g} + 14b_{1u} + 7b_{2g} + 14b_{2u} + 14b_{3g} + 7b_{3u}, \quad (4.6)$$

$$\text{Pn} : \Gamma_{vib} = 18a_g + 8a_u + 7b_{1g} + 17b_{1u} + 9b_{2g} + 17b_{2u} + 17b_{3g} + 9b_{3u}, \quad (4.7)$$

$$\text{Hn} : \Gamma_{vib} = 21a_g + 10a_u + 9b_{1g} + 20b_{1u} + 10b_{2g} + 20b_{2u} + 20b_{3g} + 10b_{3u}, \quad (4.8)$$

It can be seen from the above equations that fusion of an extra benzene ring to the linear chain includes 18 additional vibrational degrees of freedom. Therefore, it is clear that a full quantum mechanical treatment of these systems becomes extremely tedious (often impossible) with growing size of the molecules in terms of the electronic and vibrational degrees of freedom. In this work we attempt to examine the electronic energies along all vibrational modes of the mentioned systems and a meticulous selection of relevant electronic states and vibrational modes is carried out to investigate the quantum dynamics subsequently.

It is obvious from the Taylor expansion given in Eqs. 4.4-4.5 that the coupling parameters of the Hamiltonian matrix represent the derivatives (of appropriate order) of the adiabatic potential energy function of the radical cation with respect to the dimensionless normal displacement coordinates Q_i of the vibrational mode ν_i evaluated at the equilibrium geometry of the reference neutral system at $\mathbf{Q}$=0. The linear and second-order coupling parameters appearing in the Hamiltonian of Eq. 4.1 are defined elsewhere [1–4, 26, 29, 30].

The VIEs of the three molecules are calculated using OVGF method [31] employing the cc-pVDZ basis set. These VIEs are equated with the adiabatic energies of the electronic states. The VIEs are calculated along each vibrational mode as a function of its dimensionless normal coordinate in the range -5.0 $\leq Q_i \leq$ +5.0, using the Gaussian-03 program module [28]. These energies are then fit (using a least squares algorithm) to the adiabatic functional form of the diabatic electronic Hamiltonian of Eq. 4.1

$$\mathbf{S}^{\dagger}(\mathcal{H} - T_N 1)\mathbf{S} = V. \quad (4.9)$$

The parameters of the Hamiltonian estimated in that way are given in a, b and c of Tables 4.1, 4.2 and 4.3.

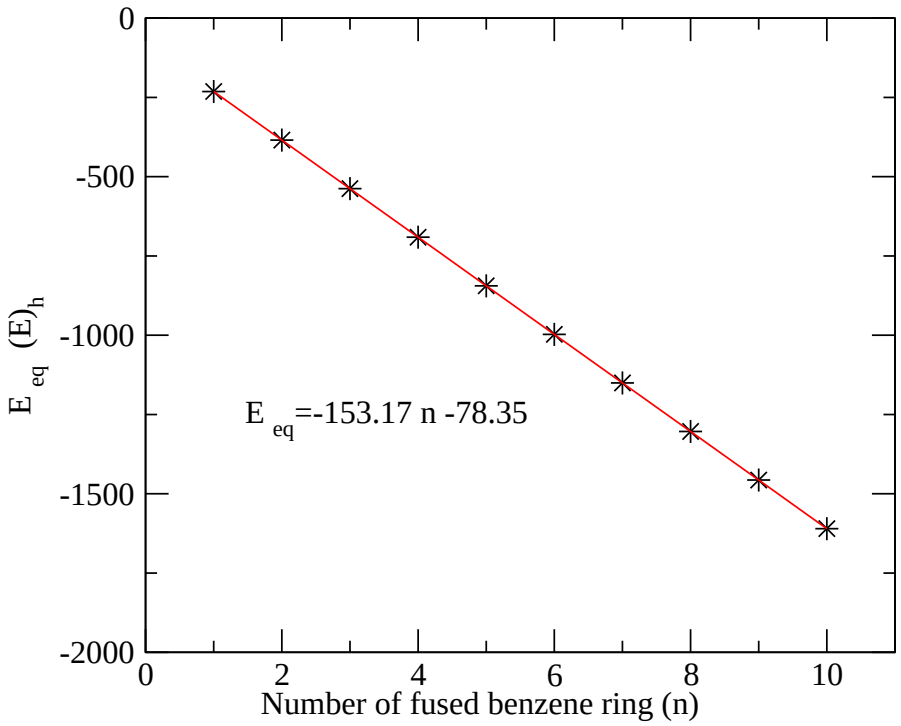

Figure 4.1: Dependence of the energy (E_{eq}) of the equilibrium minimum geometry optimized at the MP2 level of theory employing cc-pVDZ basis set as a function of the number of fused benzene ring (n) in the polycyclic aromatic hydrocarbon. The calculated *ab initio* energies are shown by the asterisks and a linear fit to these energies is shown by the straight line.

Table 4.1(a): Linear intrastate coupling parameters (κ_i) of the Hamiltonian of the $\widetilde{X}$, $\widetilde{A}$, $\widetilde{B}$ and $\widetilde{C}$ electronic states of Tn^+ along the totally symmetric modes. The dimensionless coupling strengths ($\kappa_i^2/2\omega^2$), are given in the parentheses. The vertical ionization energies of the ground and excited electronic states of this radical cation are also given. All quantities are given in eV.

mode	$\widetilde{X}^2A_u$	$\widetilde{A}^2B_{3u}$	$\widetilde{B}^2B_{2g}$	$\widetilde{C}^2A_u$
a_g ν_1	-0.0103 (0.0003)	-0.0150 (0.0007)	-0.0117 (0.0004)	-0.0149 (0.0006)
ν_2	0.0044 (0.0001)	0.0115 (0.0004)	0.0028 (0.0001)	0.0037 (0.0001)
ν_3	0.0055 (0.0001)	0.0159 (0.0008)	0.0065 (0.0001)	0.0072 (0.0001)
ν_4	-0.0864 (0.0966)	0.0723 (0.0676)	-0.1284 (0.2135)	-0.0994 (0.1279)
ν_5	0.0951 (0.1205)	-0.0302 (0.0121)	-0.0356 (0.0169)	0.0410 (0.0224)
ν_6	-0.0189 (0.0051)	-0.0140 (0.0029)	-0.0829 (0.1019)	0.0573 (0.0487)
ν_7	-0.0914 (0.1253)	-0.0353 (0.0187)	0.0072 (0.0008)	-0.0394 (0.0233)
ν_8	-0.0542 (0.0462)	-0.0123 (0.0024)	-0.0403 (0.0256)	0.0128 (0.0026)
ν_9	0.0492 (0.0523)	0.0053 (0.0006)	0.0005 (0.0001)	-0.0396 (0.0339)

Continued on next page

Table 4.1(a) – *Continued from previous page*

mode	$\widetilde{X}^2A_u$	$\widetilde{A}^2B_{3u}$	$\widetilde{B}^2B_{2g}$	$\widetilde{C}^2A_u$
ν_{10}	-0.0317 (0.0238)	0.0266 (0.0168)	-0.0272 (0.0175)	-0.0335 (0.0266)
ν_{11}	0.0139 (0.0058)	-0.0324 (0.0319)	0.0004 (0.0001)	-0.0062 (0.0012)
ν_{12}	-0.0081 (0.0028)	0.0107 (0.0050)	-0.0067 (0.0019)	0.0384 (0.0639)
ν_{13}	0.0002 (0.0001)	-0.0732 (0.300)	-0.0059 (0.0019)	-0.0087 (0.0042)
ν_{14}	-0.0004 (0.0001)	-0.0203 (0.0350)	0.0146 (0.0181)	0.0373 (0.1182)
ν_{15}	-0.0062 (0.0120)	-0.0233 (0.1766)	0.0154 (0.0772)	0.0309 (0.3107)
VIE	6.461	8.050	8.099	9.387

Table 4.1(b): Quadratic coupling parameters (γ_i) of the Hamiltonian of the $\widetilde{X}$, $\widetilde{A}$, $\widetilde{B}$ and $\widetilde{C}$ electronic states of Tn^+. All quantities are given in eV.

mode (ffrequency)	$\widetilde{X}^2A_u$	$\widetilde{A}^2B_{3u}$	$\widetilde{B}^2B_{2g}$	$\widetilde{C}^2A_u$
a_g ν_1(0.4014)	0.0024	0.0025	0.0022	0.0022
ν_2(0.3976)	0.0027	0.0027	0.0028	0.0027
ν_3(0.3958)	0.0029	0.0023	0.0018	0.0016
ν_4(0.1965)	0.0007	0.0020	0.0017	0.0022
ν_5(0.1937)	0.0015	-0.0019	0.0015	0.0086
ν_6(0.1836)	-0.0035	0.0038	0.0006	0.0085
ν_7(0.1826)	0.0035	0.0180	0.0008	0.0053
ν_8(0.1782)	-0.0013	0.0103	0.0045	0.0036
ν_9(0.1521)	0.0017	0.0045	0.0002	0.0049
ν_{10}(0.1452)	0.0041	0.0050	0.0038	0.0044
ν_{11}(0.1282)	0.0004	0.0019	-0.0004	-0.0001
ν_{12}(0.1074)	-0.0006	0.0001	-0.0011	0.0008
ν_{13}(0.0945)	-0.0013	-0.0019	-0.0011	-0.0011
ν_{14}(0.0767)	-0.0022	-0.0002	-0.0050	-0.0025
ν_{15}(0.0392)	-0.0006	-0.0006	-0.0002	0.0003
a_u ν_{16}(0.1160)	0.0076	0.0037	0.0014	-0.0056
ν_{17}(0.1031)	0.0114	0.0036	0.0063	-0.0074
ν_{18}(0.1009)	0.0047	0.0034	0.0017	-0.0067
ν_{19}(0.0642)	0.0010	-0.0122	-0.0046	-0.0085
ν_{20}(0.0528)	0.0036	-0.0046	-0.0001	-0.0092
ν_{21}(0.0370)	0.0056	-0.0156	-0.0052	-0.0046
ν_{22}(0.0108)	0.0055	-0.0130	0.0007	0.0004
b_{1g} ν_{23}(0.1151)	0.0079	0.0066	0.0047	0.0008
ν_{24}(0.0999)	0.0127	0.0064	0.0017	0.0020
ν_{25}(0.0905)	0.0093	0.0036	0.0037	-0.0011
ν_{26}(0.0549)	-0.0009	0.0004	-0.0107	-0.0102

Continued on next page

Table 4.1(b) – *Continued from previous page*

mode (frequency)		$\widetilde{X}^2A_u$	$\widetilde{A}^2B_{3u}$	$\widetilde{B}^2B_{2g}$	$\widetilde{C}^2A_u$
	$\nu_{27}(0.0439)$	-0.0002	-0.0086	-0.0096	-0.0114
	$\nu_{28}(0.0178)$	-0.0036	0.0006	-0.0099	-0.0061
b_{1u}	$\nu_{29}(0.3998)$	0.0032	0.0031	0.0030	0.0032
	$\nu_{30}(0.3971)$	0.0031	0.0032	0.0031	0.0031
	$\nu_{31}(0.3956)$	0.0030	0.0024	0.0019	0.0016
	$\nu_{32}(0.2086)$	-0.0067	-0.1010	0.0933	-0.0051
	$\nu_{33}(0.1975)$	0.0002	-0.0099	-0.0018	-0.0766
	$\nu_{34}(0.1747)$	0.0010	-0.0021	0.0018	-0.0101
	$\nu_{35}(0.1614)$	0.0001	-0.0192	0.0176	-0.0252
	$\nu_{36}(0.1585)$	0.0027	-0.0029	0.0067	-0.0014
	$\nu_{37}(0.1512)$	0.0013	-0.0031	0.0037	0.0030
	$\nu_{38}(0.1416)$	0.0019	-0.0034	0.0053	-0.0052
	$\nu_{39}(0.1148)$	-0.0007	-0.0006	-0.0011	-0.0036
	$\nu_{40}(0.0759)$	0.0004	-0.0239	0.0203	-0.0112
	$\nu_{41}(0.0536)$	-0.0024	-0.0017	0.0012	-0.0016
	$\nu_{42}(0.0200)$	0.0001	-0.0012	-0.0005	-0.0032
b_{2g}	$\nu_{43}(0.1161)$	0.0076	0.0038	0.0015	-0.0057
	$\nu_{44}(0.1035)$	0.0120	0.0043	0.0050	-0.0090
	$\nu_{45}(0.1022)$	0.0086	0.0041	-0.0033	0.0013
	$\nu_{46}(0.0674)$	0.0020	-0.0007	-0.0021	-0.0089
	$\nu_{47}(0.0589)$	-0.0040	-0.0117	-0.0041	-0.0044
	$\nu_{48}(0.0377)$	0.0035	-0.0004	0.0008	-0.0071
	$\nu_{49}(0.0230)$	0.0031	-0.0114	0.0020	-0.0073
b_{2u}	$\nu_{50}(0.4014)$	0.0025	0.0026	0.0023	0.0022
	$\nu_{51}(0.3976)$	0.0027	0.0028	0.0029	0.0027
	$\nu_{52}(0.3955)$	0.0034	0.0026	0.0021	0.0021
	$\nu_{53}(0.1994)$	0.0091	0.0040	0.0177	0.0124
	$\nu_{54}(0.1946)$	0.0176	0.0246	0.0056	-0.0045
	$\nu_{55}(0.1869)$	-0.0035	-0.0037	0.0032	0.0045
	$\nu_{56}(0.1801)$	-0.0100	0.0109	0.0086	0.0062
	$\nu_{57}(0.1644)$	-0.0021	0.0025	-0.0022	0.0085
	$\nu_{58}(0.1476)$	0.0040	0.0063	0.0050	0.0035
	$\nu_{59}(0.1450)$	0.0044	0.0061	0.0041	0.0047
	$\nu_{60}(0.1283)$	0.0004	0.0008	-0.0003	0.0001
	$\nu_{61}(0.0951)$	-0.0006	-0.0008	-0.0011	-0.0013
	$\nu_{62}(0.0774)$	-0.0036	-0.0010	-0.0044	-0.0017
	$\nu_{63}(0.0689)$	-0.0013	-0.0007	-0.0030	-0.0110
b_{3g}	$\nu_{64}(0.3998)$	0.0032	0.0030	0.0032	0.0031
	$\nu_{65}(0.3971)$	0.0031	0.0033	0.0031	0.0031
	$\nu_{66}(0.3953)$	0.0033	0.0026	0.0020	0.0020

Continued on next page

Table 4.1(b) – *Continued from previous page*

mode (frequency)		$\widetilde{X}^2A_u$	$\widetilde{A}^2B_{3u}$	$\widetilde{B}^2B_{2g}$	$\widetilde{C}^2A_u$
	$\nu_{67}(0.2077)$	-0.0292	0.0262	-0.0030	-0.0046
	$\nu_{68}(0.2048)$	-0.0035	-0.0131	-0.0127	0.0140
	$\nu_{69}(0.1833)$	-0.0006	-0.0016	-0.0028	-0.0058
	$\nu_{70}(0.1665)$	0.0010	-0.0008	0.0013	0.0006
	$\nu_{71}(0.1579)$	0.0019	0.0001	0.0017	0.0051
	$\nu_{72}(0.1476)$	-0.0007	0.0052	0.0028	0.0030
	$\nu_{73}(0.1412)$	0.0012	0.0024	-	-0.0015
	$\nu_{74}(0.1106)$	-0.0006	-0.0007	-0.0012	-0.0011
	$\nu_{75}(0.0964)$	0.0001	-0.0031	-0.0003	0.0018
	$\nu_{76}(0.0610)$	-0.0025	0.0004	-0.0010	-0.0004
	$\nu_{77}(0.0368)$	-0.0006	0.0008	-0.0028	-0.0016
b_{3u}	$\nu_{78}(0.1152)$	0.0079	0.0066	0.0048	0.0005
	$\nu_{79}(0.1047)$	0.0124	0.0062	0.0041	0.0008
	$\nu_{80}(0.0920)$	0.0057	0.0041	0.0030	-0.0010
	$\nu_{81}(0.0557)$	-0.0030	0.0018	-0.0068	-0.0136
	$\nu_{82}(0.0540)$	-0.0082	-0.0004	-0.0045	-0.0101
	$\nu_{83}(0.0321)$	-0.0088	-0.0015	-0.0071	-0.0088
	$\nu_{84}(0.0066)$	-0.0024	0.0029	-0.0068	-0.0118

Table 4.1(c): *Ab initio* calculated interstate coupling parameters of the Hamiltonian of Tn^+ along the coupling vibrational modes. The dimensionless coupling strengths ($\lambda_i^2/2\omega^2$), are given in the parentheses. All quantities are given in eV.

mode	λ^{j-k}	mode	λ^{j-k}	λ^{j-k}	mode	λ^{j-k}	λ^{j-k}
b_{1u}	$j-k \in \vec{A}$-$\vec{B}$	b_{2u}	$j-k \in \vec{X}$-$\vec{B}$	$j-k \in \vec{B}$-$\vec{C}$	b_{3g}	$j-k \in \vec{X}$-$\vec{A}$	$j-k \in \vec{A}$-$\vec{C}$
ν_{29}	-	ν_{50}	-	-	ν_{64}	-	0.0081 (0.0002)
ν_{30}	-	ν_{51}	0.0133 (0.0005)	-	ν_{65}	0.0114 (0.0004)	-
ν_{31}	-	ν_{52}	-	-	ν_{66}	-	-
ν_{32}	0.0734 (0.0619)	ν_{53}	0.0593 (0.0442)	-	ν_{67}	0.1493 (0.2583)	-
ν_{33}	0.0104 (0.0014)	ν_{54}	-	-	ν_{68}	-	0.0957 (0.1092)
ν_{34}	0.0071 (0.0008)	ν_{55}	0.0534 (0.0408)	0.0213 (0.0065)	ν_{69}	-	-
ν_{35}	0.0235 (0.0105)	ν_{56}	0.0883 (0.1202)	-	ν_{70}	-	0.0227 (0.0092)
ν_{36}	0.0114 (0.0026)	ν_{57}	-	0.0592 (0.0648)	ν_{71}	-	0.0416 (0.0347)
ν_{37}	0.0095 (0.0020)	ν_{58}	0.0218 (0.0109)	-	ν_{72}	0.0496 (0.0565)	-
ν_{38}	0.0107 (0.0028)	ν_{59}	-	0.0116 (0.0032)	ν_{73}	0.0221 (0.0122)	-
ν_{39}	-	ν_{60}	-	0.0099 (0.0030)	ν_{74}	-	-
ν_{40}	0.0261 (0.0591)	ν_{61}	-	-	ν_{75}	-	0.0414 (0.0922)
ν_{41}	0.0062 (0.0067)	ν_{62}	-	0.0302 (0.0761)	ν_{76}	0.0347 (0.1618)	-
ν_{42}	0.0033 (0.0136)	ν_{63}	-	-	ν_{77}	0.0242 (0.2162)	-

Table 4.2(a): Same as in Table 4.1(a) for Pn^+.

mode	$\widetilde{X}^2B_{2g}$	$\widetilde{A}^2A_u$	$\widetilde{B}^2B_{1g}$	$\widetilde{C}^2B_{2g}$
a_g ν_1	0.0090 (0.0002)	0.0087 (0.0002)	0.0111 (0.0004)	0.0123 (0.0005)

Continued on next page

Table 4.2(a) – *Continued from previous page*

mode	$\widetilde{X}^2B_{2g}$	$\widetilde{A}^2A_u$	$\widetilde{B}^2B_{1g}$	$\widetilde{C}^2B_{2g}$
ν_2	-0.0044 (0.0001)	-0.0023 (0.0001)	-0.0093 (0.0002)	-0.0030 (0.0001)
ν_3	0.0054 (0.0001)	0.0068 (0.0001)	0.0154 (0.0007)	0.0080 (0.0002)
ν_4	-0.0006 (0.0001)	-0.0006 (0.0001)	-0.0003 (0.0001)	0.0017 (0.0001)
ν_5	-0.011 (0.0016)	-0.0914 (0.1079)	0.0330 (0.0141)	-0.0747 (0.0721)
ν_6	-0.1090 (0.1596)	-0.0318 (0.0136)	0.0522 (0.0366)	-0.0624 (0.0523)
ν_7	0.0029 (0.0001)	0.0620 (0.0557)	0.0078 (0.0009)	-0.0293(0.0124)
ν_8	0.0738(0.0814)	-0.0232 (0.0080)	0.0269 (0.0108)	-0.0059 (0.0005)
ν_9	-0.0748 (0.0868)	-0.0563 (0.0492)	-0.0197 (0.0006)	-0.0484 (0.0363)
ν_{10}	-0.0186 (0.0063)	-0.0393 (0.0280)	-0.0030 (0.0002)	0.0631 (0.0722)
ν_{11}	0.0488 (0.0535)	0.0076 (0.0013)	0.0039 (0.0003)	-0.0022 (0.0001)
ν_{12}	-0.0318 (0.0241)	-0.0255 (0.0155)	0.0216 (0.0111)	-0.0269 (0.0172)
ν_{13}	-0.0145 (0.0064)	-0.0068 (0.0014)	0.0256 (0.0200)	0.0041 (0.0005)
ν_{14}	0.0088 (0.0039)	0.0074 (0.0028)	-0.0208 (0.0220)	-0.0055 (0.0015)
ν_{15}	-0.0030 (0.0005)	-0.0050 (0.0014)	-0.0674 (0.2543)	-0.0064 (0.0023)
ν_{16}	0.0001 (0.0001)	-0.0044 (0.0016)	-0.0014 (0.0002)	0.0242 (0.0485)
ν_{17}	0.0018 (0.0003)	-0.0048 (0.0020)	0.0184 (0.0302)	-0.0215 (0.0412)
ν_{18}	0.0086 (0.0350)	-0.0076 (0.0273)	0.0183 (0.1585)	-0.0187 (0.1655)
VIE	6.066	7.514	7.779	8.772

Table 4.2(b): Same as in Table 4.1(b) for Pn^+.

mode (frequency)	$\widetilde{X}^2B_{2g}$	$\widetilde{A}^2A_u$	$\widetilde{B}^2B_{1g}$	$\widetilde{C}^2B_{2g}$
a_g ν_1(0.4014)	0.0021	0.0019	0.0020	0.0019
ν_2(0.3976)	0.0022	0.0024	0.0022	0.0025
ν_3(0.3958)	0.0024	0.0016	0.0015	0.0014
ν_4(0.3954)	0.0031	0.0018	0.0020	0.0020
ν_5(0.1967)	-0.0037	0.0056	0.0032	0.0045
ν_6(0.1929)	0.0065	0.0029	0.0050	0.0035
ν_7(0.1858)	-0.0019	0.0003	-0.0015	0.0031
ν_8(0.1829)	0.0038	0.0078	0.0172	-0.0089
ν_9(0.1795)	-0.0057	0.0015	0.0095	0.0075
ν_{10}(0.1660)	-0.0007	-0.0017	0.0017	0.0023
ν_{11}(0.1492)	0.0022	0.0023	0.0043	0.0023
ν_{12}(0.1449)	0.0037	0.0037	0.0045	0.0034
ν_{13}(0.1281)	0.0005	-0.0002	0.0014	-0.0003
ν_{14}(0.0992)	-0.0002	-0.0007	-0.0001	-0.0014
ν_{15}(0.0945)	-0.0010	-0.0008	0.0057	-0.0009
ν_{16}(0.0777)	-0.0030	-0.0024	-0.0013	-0.0032
ν_{17}(0.0749)	-0.0012	-0.0026	-0.0003	-0.0057
ν_{18}(0.0325)	-0.0004	-0.0002	-0.0005	-0.0001

Continued on next page

Table 4.2(b) – *Continued from previous page*

mode	(frequency)	$\widetilde{X}^2B_{2g}$	$\widetilde{A}^2A_u$	$\widetilde{B}^2B_{1g}$	$\widetilde{C}^2B_{2g}$
a_u	$\nu_{19}(0.1160)$	0.0071	0.0037	0.0037	-0.0020
	$\nu_{20}(0.1031)$	0.0095	0.0080	0.0035	0.0005
	$\nu_{21}(0.1013)$	0.0067	-0.0008	0.0032	0.0021
	$\nu_{22}(0.0671)$	0.0017	0.0003	-0.0009	-0.0047
	$\nu_{23}(0.0594)$	-0.0035	-0.0030	-0.0093	-0.0040
	$\nu_{24}(0.0439)$	0.0051	0.0026	-0.0022	-0.0023
	$\nu_{25}(0.0285)$	0.0025	0.0011	-0.0107	-0.0040
	$\nu_{26}(0.0085)$	0.0049	0.0011	-0.0126	0.0008
b_{1g}	$\nu_{27}(0.1151)$	0.0069	0.0055	0.0059	0.0022
	$\nu_{28}(0.1018)$	0.0110	0.0052	0.0053	0.0018
	$\nu_{29}(0.0913)$	0.0059	0.0043	0.0033	0.0013
	$\nu_{30}(0.0551)$	-0.0016	-0.0047	0.0014	-0.0085
	$\nu_{31}(0.0532)$	-0.0030	-0.0054	0.0004	-0.0064
	$\nu_{32}(0.0346)$	-0.0064	-0.0055	-0.0020	-0.0066
	$\nu_{33}(0.0121)$	-0.0015	-0.0044	0.0011	-0.0078
b_{1u}	$\nu_{34}(0.3998)$	0.0027	0.0027	0.0024	0.0029
	$\nu_{35}(0.3971)$	0.0026	0.0026	0.0026	0.0027
	$\nu_{36}(0.3955)$	0.0025	0.0018	0.0017	0.0016
	$\nu_{37}(0.3951)$	0.0029	0.0017	0.0020	0.0019
	$\nu_{38}(0.2083)$	-0.0063	-0.0855	0.0739	-0.0056
	$\nu_{39}(0.2025)$	-0.0016	-0.0084	-0.0047	-0.0441
	$\nu_{40}(0.1829)$	-0.0005	-0.0015	-0.0017	-0.0069
	$\nu_{41}(0.1686)$	0.0008	0.0002	-0.0003	0.0007
	$\nu_{42}(0.1616)$	0.0004	-0.0141	0.0134	-0.0122
	$\nu_{43}(0.1580)$	0.0022	-0.0009	0.0032	-
	$\nu_{44}(0.1487)$	0.0014	-0.0025	0.0051	0.0021
	$\nu_{45}(0.1408)$	0.0014	-0.0008	0.0027	-0.0025
	$\nu_{46}(0.1121)$	-0.0004	-0.0007	-0.0016	-0.0013
	$\nu_{47}(0.1018)$	0.0001	-0.0013	-	-0.0014
	$\nu_{48}(0.0713)$	0.0001	-0.0140	0.0111	-0.0057
	$\nu_{49}(0.0436)$	-0.0001	-0.0039	0.0020	-0.0012
	$\nu_{50}(0.0147)$	0.0001	-0.0018	0.0005	-0.0016
b_{2g}	$\nu_{51}(0.1160)$	0.0071	0.0037	0.0037	-0.0020
	$\nu_{52}(0.1032)$	0.0101	0.0076	0.0036	-
	$\nu_{53}(0.1019)$	0.0096	-0.0006	0.0035	-0.0025
	$\nu_{54}(0.0998)$	0.0059	0.0024	0.0028	-0.0061
	$\nu_{55}(0.0643)$	0.0024	-0.0011	-0.0067	-0.0058
	$\nu_{56}(0.0555)$	0.0021	-0.0015	-0.0066	-0.0027
	$\nu_{57}(0.0396)$	0.0065	-0.0043	-0.0159	-0.0033
	$\nu_{58}(0.0300)$	0.0042	0.0040	-0.0036	-0.0072

Continued on next page

Table 4.2(b) – *Continued from previous page*

mode	(frequency)	$\widetilde{X}^2B_{2g}$	$\widetilde{A}^2A_u$	$\widetilde{B}^2B_{1g}$	$\widetilde{C}^2B_{2g}$
	ν_{59}(0.0179)	0.0025	0.0018	-0.0099	-0.0009
b_{2u}	ν_{60}(0.4014)	0.0022	0.0021	0.0021	0.0020
	ν_{61}(0.3976)	0.0023	0.0024	0.0022	0.0025
	ν_{62}(0.3956)	0.0027	0.0021	0.0019	0.0014
	ν_{63}(0.2055)	0.0342	0.0211	0.0292	0.0213
	ν_{64}(0.1960)	-0.0027	-0.0041	-0.0009	0.0038
	ν_{65}(0.1915)	-0.0045	0.0022	-0.0008	0.0066
	ν_{66}(0.1834)	-0.0031	-0.0089	0.0029	0.0083
	ν_{67}(0.1804)	-0.0025	0.0044	0.0121	-0.0020
	ν_{68}(0.1777)	-0.0039	0.0040	0.0077	0.0060
	ν_{69}(0.1556)	-0.0002	0.0015	0.0030	-0.0023
	ν_{70}(0.1478)	0.0038	0.0043	0.0057	0.0040
	ν_{71}(0.1450)	0.0033	0.0039	0.0047	0.0030
	ν_{72}(0.1280)	0.0004	-0.0001	0.0005	-0.0003
	ν_{73}(0.1098)	-0.0005	-0.0003	0.0003	-0.0015
	ν_{74}(0.0937)	-0.0006	-0.0010	-0.0022	-0.0008
	ν_{75}(0.0772)	-0.0018	-0.0040	-0.0005	-0.0041
	ν_{76}(0.0603)	-0.0009	-0.0016	-0.0008	-0.0019
b_{3g}	ν_{77}(0.3998)	0.0027	0.0027	0.0025	0.0028
	ν_{78}(0.3971)	0.0026	0.0027	0.0026	0.0027
	ν_{79}(0.3953)	0.0026	0.0021	0.0019	0.0014
	ν_{80}(0.2069)	-0.0030	-0.0144	-0.0156	0.0161
	ν_{81}(0.2055)	-0.0269	-0.0009	0.0161	-0.0021
	ν_{82}(0.1952)	0.0005	-0.0028	-0.0064	-0.0064
	ν_{83}(0.1749)	0.0008	0.0007	-0.0016	0.0001
	ν_{84}(0.1597)	0.0013	0.0011	-0.0003	0.0040
	ν_{85}(0.1583)	0.0017	0.0012	-0.0018	0.0046
	ν_{86}(0.1545)	0.0011	0.0001	-0.0015	0.0004
	ν_{87}(0.1471)	-0.0012	0.0025	0.0043	0.0022
	ν_{88}(0.1419)	0.0015	0.0007	0.0016	0.0001
	ν_{89}(0.1135)	-0.0003	-0.0010	-0.0003	-0.0010
	ν_{90}(0.0888)	0.0001	0.0001	-0.0051	0.0037
	ν_{91}(0.0615)	-0.0021	-0.0009	0.0002	-0.0006
	ν_{92}(0.0544)	-0.0022	-0.0008	0.0002	-0.0007
	ν_{93}(0.0289)	-0.0001	-0.0009	0.0002	-0.0024
b_{3u}	ν_{94}(0.1151)	0.0069	0.0055	0.0059	0.0023
	ν_{95}(0.1048)	0.0115	0.0050	0.0051	0.0025
	ν_{96}(0.0970)	0.0130	0.0028	0.0055	0.0014
	ν_{97}(0.0905)	0.0084	0.0049	0.0032	0.0015
	ν_{98}(0.0549)	0.0004	-0.0070	0.0005	-0.0082
	ν_{99}(0.0530)	-0.0063	-0.0032	-0.0010	-0.0083

Continued on next page

Table 4.2(b) – *Continued from previous page*

mode (frequency)	$\widetilde{X}^2B_{2g}$	$\widetilde{A}^2A_u$	$\widetilde{B}^2B_{1g}$	$\widetilde{C}^2B_{2g}$
ν_{100}(0.0432)	0.0016	-0.0068	-0.0079	-0.0089
ν_{101}(0.0228)	-0.0025	-0.0073	-0.0006	-0.0055
ν_{102}(0.0044)	-0.0008	-0.0040	0.0026	-0.0068

Table 4.2(c): Same as in Table 4.1(c) for Pn^+.

mode	λ^{j-k}	mode	λ^{j-k}	λ^{j-k}	mode	λ^{j-k}	λ^{j-k}
b_{1u}	$j-k \in \widetilde{A}$-$\widetilde{B}$	b_{2u}	$j-k \in \widetilde{X}$-$\widetilde{A}$	$j-k \in \widetilde{A}$-$\widetilde{C}$	b_{3g}	$j-k \in \widetilde{X}$-$\widetilde{B}$	$j-k \in \widetilde{B}$-$\widetilde{C}$
ν_{34}	-	ν_{60}	-	-	ν_{77}	-	0.0112 (0.0004)
ν_{35}	-	ν_{61}	0.0122 (0.0004)	0.0073 (0.0002)	ν_{78}	0.0020 (0.0001)	0.0086 (0.0002)
ν_{36}	-	ν_{62}	-	-	ν_{79}	-	-
ν_{37}	0.0033 (0.0001)	ν_{63}	-	0.0124 (0.0018)	ν_{80}	-	0.0899 (0.0944)
ν_{38}	0.1041 (0.1249)	ν_{64}	-	0.0504 (0.0331)	ν_{81}	0.1369 (0.2219)	-
ν_{39}	0.0152 (0.0028)	ν_{65}	0.0504 (0.0346)	0.0380 (0.0197)	ν_{82}	-	0.0056 (0.0004)
ν_{40}	-	ν_{66}	-	0.0740 (0.0814)	ν_{83}	-	0.0212 (0.0073)
ν_{41}	-	ν_{67}	0.0506 (0.0393)	-	ν_{84}	-	0.0329 (0.0212)
ν_{42}	0.0437 (0.0366)	ν_{68}	0.0538 (0.0458)	0.0252 (0.0100)	ν_{85}	-	0.0407 (0.0330)
ν_{43}	0.0158 (0.0050)	ν_{69}	0.0274 (0.0155)	-	ν_{86}	-	0.0222 (0.0103)
ν_{44}	0.0223 (0.0112)	ν_{70}	0.0156 (0.0056)	-	ν_{87}	0.0489 (0.0552)	-
ν_{45}	0.0147 (0.0054)	ν_{71}	0.0163 (0.0063)	-	ν_{88}	0.0057 (0.0008)	-
ν_{46}	-	ν_{72}	-	-	ν_{89}	0.0098 (0.0037)	-
ν_{47}	0.0098 (0.0046)	ν_{73}	0.0105 (0.0046)	-	ν_{90}	-	0.0475 (0.1431)
ν_{48}	0.0415 (0.1693)	ν_{74}	-	0.0116 (0.0077)	ν_{91}	0.0315 (0.1312)	-
ν_{49}	0.0199 (0.1042)	ν_{75}	-	-	ν_{92}	0.0338 (0.1930)	-
ν_{50}	0.0122 (0.3443)	ν_{76}	-	-	ν_{93}	0.0093 (0.0518)	-

Table 4.3(a): Same as in Table 4.1(a) for Hn^+.

mode	$\widetilde{X}^2A_u$	$\widetilde{A}^2B_{2g}$	$\widetilde{B}^2B_{3u}$	$\widetilde{C}^2A_u$
a_g ν_1	0.0081 (0.0002)	0.0069 (0.0001)	0.0101 (0.0003)	0.0097 (0.0003)
ν_2	0.0043 (0.0001)	0.0021 (0.0001)	0.0082 (0.0002)	0.0024 (0.0001)
ν_3	0.0053 (0.0001)	0.0064 (0.0001)	0.0159 (0.0008)	0.0081 (0.0002)
ν_4	0.0007 (0.0001)	-0.0005 (0.0001)	-0.0006 (0.0001)	-0.0006 (0.0001)
ν_5	0.0063 (0.0005)	-0.0685 (0.055)	0.0430 (0.0238)	-0.0685 (0.0605)
ν_6	0.0947 (0.1223)	0.0277 (0.0105)	-0.0571 (0.0444)	0.0657 (0.0588)
ν_7	-0.0019 (0.0001)	-0.0650 (0.0584)	0.0080 (0.0009)	0.0559 (0.0432)
ν_8	-0.0596 (0.0526)	0.0302 (0.0135)	-0.0211 (0.0065)	0.0215 (0.0068)
ν_9	0.0209 (0.0065)	0.0130 (0.0025)	0.0108 (0.0017)	0.0728 (0.0789)
ν_{10}	-0.0549 (0.0468)	-0.0416 (0.0269)	-0.0118 (0.0022)	0.0042 (0.0003)
ν_{11}	-0.0561 (0.05)	-0.0502 (0.0401)	-0.0097 (0.0015)	-0.0273 (0.0118)
ν_{12}	-0.0116 (0.0027)	-0.0343 (0.0234)	-0.0027 (0.0001)	0.0084 (0.0014)
ν_{13}	0.0462 (0.0488)	0.0080 (0.0015)	0.0031 (0.0002)	0.0040 (0.0004)
ν_{14}	-0.0340 (0.0276)	-0.0260 (0.0161)	0.0181 (0.0078)	-0.0231 (0.0127)
ν_{15}	-0.0139 (0.0005)	-0.0092 (0.0026)	0.0204 (0.0127)	-0.0012 (0.0001)
ν_{16}	0.0036 (0.0005)	0.0033 (0.0004)	-0.0032 (0.0004)	0.0074 (0.0022)
ν_{17}	0.0028 (0.0004)	0.0027 (0.0004)	-0.0660 (0.2403)	-0.0034 (0.0006)
ν_{18}	-0.0080 (0.0036)	-0.0072 (0.0029)	-0.0610 (0.2110)	-0.0044 (0.0011)

Continued on next page

Table 4.3(a) – *Continued from previous page*

mode	$\widetilde{X}^2A_u$	$\widetilde{A}^2B_{2g}$	$\widetilde{B}^2B_{3u}$	$\widetilde{C}^2A_u$
ν_{19}	0.0001 (0.0001)	0.0014 (0.0001)	0.0076 (0.0048)	-0.0121 (0.0122)
ν_{20}	0.0034 (0.0011)	-0.0004 (0.0001)	0.0144 (0.0207)	-0.0083 (0.0069)
ν_{21}	0.0096 (0.0600)	-0.0031 (0.0063)	0.0161 (0.1689)	-0.0119 (0.0923)
VIE	5.769	7.051	7.688	8.241

Table 4.3(b): Same as in Table 4.1(b) for Hn^+.

mode (frequency)	$\widetilde{X}^2A_u$	$\widetilde{A}^2B_{3u}$	$\widetilde{B}^2B_{2g}$	$\widetilde{C}^2A_u$
a_g ν_1(0.4014)	0.0018	0.0017	0.0018	0.0018
ν_2(0.3976)	0.0019	0.0020	0.0020	0.0022
ν_3(0.3957)	0.0020	0.0014	0.0014	0.0013
ν_4(0.3954)	0.0025	0.0018	0.0017	0.0015
ν_5(0.1969)	-0.0029	0.0012	-0.0014	0.0039
ν_6(0.1915)	0.0074	0.0030	0.0103	0.0042
ν_7(0.1901)	-0.0007	-0.0034	0.0001	0.0032
ν_8(0.1837)	0.0031	0.0056	0.0149	0.0013
ν_9(0.1832)	-0.0007	-0.0059	0.0041	0.0007
ν_{10}(0.1794)	0.0003	0.0037	0.0102	-0.0005
ν_{11}(0.1773)	-0.0017	0.0023	0.0072	0.0049
ν_{12}(0.1584)	0.0005	-0.0003	0.0021	-0.0001
ν_{13}(0.1479)	0.0025	0.0026	0.0040	0.0032
ν_{14}(0.1448)	0.0034	0.0037	0.0045	0.0032
ν_{15}(0.1280)	0.0005	0.0001	0.0013	-0.0003
ν_{16}(0.1109)	-0.0003	-0.0001	0.0006	-0.0004
ν_{17}(0.0952)	0.0001	-0.0007	0.0010	-0.0008
ν_{18}(0.0939)	-0.0009	-0.0004	0.0007	-0.0008
ν_{19}(0.0775)	-0.0017	-0.0030	-0.0006	-0.0027
ν_{20}(0.0707)	-0.0010	-0.0013	-0.0005	-0.0023
ν_{21}(0.0277)	-0.0003	-0.0002	-0.0004	-0.0001
a_u ν_{22}(0.1160)	0.0064	0.0046	0.0037	0.0007
ν_{23}(0.1031)	0.0080	0.0080	0.0033	0.0040
ν_{24}(0.1015)	0.0069	0.0015	0.0029	-0.0018
ν_{25}(0.0990)	0.0062	0.0026	0.0024	-0.0028
ν_{26}(0.0647)	0.0029	0.0006	-0.0035	-0.0028
ν_{27}(0.0570)	0.0006	-0.0020	-0.0065	-0.0019
ν_{28}(0.0412)	0.0073	-0.00029	-0.0146	-0.0028
ν_{29}(0.0367)	0.0054	0.0025	-0.0031	0.0008
ν_{30}(0.0231)	0.0020	0.0002	-0.0086	0.0010
ν_{31}(0.0071)	0.0041	0.0012	-0.0122	0.0010

Continued on next page

Table 4.3(b) – *Continued from previous page*

mode (frequency)		$\widetilde{X}^2A_u$	$\widetilde{A}^2B_{3u}$	$\widetilde{B}^2B_{2g}$	$\widetilde{C}^2A_u$
b_{1g}	$\nu_{32}(0.1151)$	0.0060	0.0055	0.0054	0.0034
	$\nu_{33}(0.1028)$	0.0096	0.0063	0.0047	0.0028
	$\nu_{34}(0.0949)$	0.0129	0.0035	0.0050	0.0031
	$\nu_{35}(0.0906)$	0.0077	0.0054	0.0031	0.0028
	$\nu_{36}(0.0549)$	0.0011	-0.0042	0.0008	-0.0065
	$\nu_{37}(0.0526)$	-0.0013	-0.0057	-0.0003	-0.0024
	$\nu_{38}(0.0428)$	0.0026	-0.0047	-0.0071	-0.0069
	$\nu_{39}(0.0264)$	-0.0016	-0.0059	-0.0011	-0.0041
	$\nu_{40}(0.0087)$	-0.0004	-0.0027	0.0014	-0.0040
b_{1u}	$\nu_{41}(0.3998)$	0.0024	0.0024	0.0022	0.0025
	$\nu_{42}(0.3971)$	0.0022	0.0023	0.0023	0.0024
	$\nu_{43}(0.3955)$	0.0021	0.0016	0.0015	0.0014
	$\nu_{44}(0.3952)$	0.0024	0.0018	0.0017	0.0015
	$\nu_{45}(0.2076)$	-0.0053	-0.0381	0.0317	-0.0089
	$\nu_{46}(0.2048)$	-0.0030	-0.0107	-0.0046	-0.0224
	$\nu_{47}(0.1932)$	0.0005	-0.0016	-0.0052	-0.0054
	$\nu_{48}(0.1755)$	0.0005	0.0005	-0.0016	0.0001
	$\nu_{49}(0.1626)$	-	-0.0047	0.0039	-0.0057
	$\nu_{50}(0.1601)$	0.0016	-0.0011	0.0027	-0.0003
	$\nu_{51}(0.1581)$	0.0014	0.0004	-0.0006	0.0007
	$\nu_{52}(0.1570)$	0.0014	0.0010	-0.0006	0.0003
	$\nu_{53}(0.1478)$	0.0011	-0.0008	0.0037	0.0024
	$\nu_{54}(0.1414)$	0.0013	0.0006	0.0017	-0.0008
	$\nu_{55}(0.1127)$	-0.0002	-0.0008	-0.0004	-0.0009
	$\nu_{56}(0.0979)$	0.0001	-0.0004	-0.0021	-0.0006
	$\nu_{57}(0.0692)$	-0.0004	-0.0049	0.0029	-0.0030
	$\nu_{58}(0.0571)$	-0.0017	-0.0011	0.0009	-0.0012
	$\nu_{59}(0.0358)$	0.0001	-0.0010	0.0007	-0.0022
	$\nu_{60}(0.0114)$	0.0001	-0.0009	-0.0001	-0.0010
b_{2g}	$\nu_{61}(0.1160)$	0.0064	0.0046	0.0037	0.0007
	$\nu_{62}(0.1032)$	0.0081	0.0080	0.0033	0.0039
	$\nu_{63}(0.1017)$	0.0088	0.0017	0.0033	-0.0023
	$\nu_{64}(0.1002)$	0.0078	0.0003	0.0031	0.0021
	$\nu_{65}(0.0667)$	0.0015	0.0006	-0.0007	-0.0022
	$\nu_{66}(0.0599)$	-0.0032	-0.0022	-0.0071	-0.0032
	$\nu_{67}(0.0486)$	0.0042	0.0019	-0.0019	-0.0001
	$\nu_{68}(0.0324)$	0.0029	0.0008	-0.0102	-0.0034
	$\nu_{69}(0.0249)$	0.0048	0.0037	-0.0039	-0.0012
	$\nu_{70}(0.0147)$	0.0019	0.0020	-0.0089	-0.0007
b_{2u}	$\nu_{71}(0.4014)$	0.0019	0.0018	0.0019	0.0018

Continued on next page

Table 4.3(b) – *Continued from previous page*

mode (frequency)		$\widetilde{X}^2A_u$	$\widetilde{A}^2B_{3u}$	$\widetilde{B}^2B_{2g}$	$\widetilde{C}^2A_u$
	$\nu_{72}(0.3976)$	0.0019	0.0021	0.0020	0.0022
	$\nu_{73}(0.3956)$	0.0022	0.0019	0.0016	0.0014
	$\nu_{74}(0.3952)$	0.0028	0.0017	0.0018	0.0018
	$\nu_{75}(0.2156)$	0.0377	0.0229	0.0337	0.0217
	$\nu_{76}(0.1962)$	-0.0024	-0.0110	-0.0058	0.0054
	$\nu_{77}(0.1925)$	-0.0060	0.0110	-0.0031	0.0019
	$\nu_{78}(0.1852)$	-0.0016	-0.0059	-0.0010	0.0065
	$\nu_{79}(0.1809)$	-0.0009	0.0051	0.0121	-0.0027
	$\nu_{80}(0.1789)$	-0.0098	0.0031	0.0071	0.0037
	$\nu_{81}(0.1669)$	-0.0004	-0.0023	0.0012	-0.0050
	$\nu_{82}(0.1518)$	0.0001	0.0036	0.0032	0.0002
	$\nu_{83}(0.1481)$	0.0033	0.0036	0.0050	0.0037
	$\nu_{84}(0.1450)$	0.0025	0.0035	0.0038	0.0029
	$\nu_{85}(0.1280)$	0.0005	0.0001	0.0004	-0.0003
	$\nu_{86}(0.1033)$	-0.0002	-0.0005	-0.0002	-0.0009
	$\nu_{87}(0.0938)$	-0.0006	-0.0010	-0.0036	-0.0007
	$\nu_{88}(0.0778)$	-0.0024	-0.0017	-0.0011	-0.0031
	$\nu_{89}(0.0764)$	-0.0010	-0.0026	-0.0004	-0.0046
	$\nu_{90}(0.0527)$	-0.0006	-0.0010	-0.0006	-0.0011
b_{3g}	$\nu_{91}(0.3998)$	0.0024	0.0024	0.0022	0.0025
	$\nu_{92}(0.3970)$	0.0022	0.0023	0.0023	0.0024
	$\nu_{93}(0.3953)$	0.0021	0.0019	0.0019	0.0014
	$\nu_{94}(0.3950)$	0.0027	0.0016	0.0017	0.0017
	$\nu_{95}(0.2074)$	-0.0021	-0.0120	-0.0321	0.0293
	$\nu_{96}(0.2034)$	-0.0270	-0.0027	0.0155	-0.0063
	$\nu_{97}(0.2005)$	-0.0009	-0.0024	-0.0084	-0.0052
	$\nu_{98}(0.1826)$	-0.0003	-0.0011	-0.0016	-0.0024
	$\nu_{99}(0.1696)$	0.0009	0.0006	-0.0007	0.0010
	$\nu_{100}(0.1594)$	0.0006	0.0003	-0.0050	0.0062
	$\nu_{101}(0.1581)$	0.0021	0.0016	-0.0009	0.0034
	$\nu_{102}(0.1501)$	0.0013	0.0004	0.0002	0.0002
	$\nu_{103}(0.1468)$	-0.0018	0.0021	0.0040	0.0014
	$\nu_{104}(0.1413)$	0.0014	0.0008	0.0003	0.0010
	$\nu_{105}(0.1132)$	-0.0003	-0.0006	-0.0008	-0.0007
	$\nu_{106}(0.1026)$	0.0003	-0.0006	-	-0.0008
	$\nu_{107}(0.0824)$	-0.0001	0.0001	-0.0069	0.0054
	$\nu_{108}(0.0596)$	-0.0020	-0.0007	-0.0003	-0.0003
	$\nu_{109}(0.0470)$	-0.0002	-0.0018	-	-0.0004
	$\nu_{110}(0.0232)$	0.0002	-0.0006	-0.0001	-0.0007
b_{3u}	$\nu_{111}(0.1151)$	0.0060	0.0055	0.0054	0.0034
	$\nu_{112}(0.1047)$	0.0106	0.0054	0.0045	0.0032
	$\nu_{113}(0.0991)$	0.0113	0.0054	0.0050	0.0015

Continued on next page

Table 4.3(b) – *Continued from previous page*

mode (frequency)	$\widetilde{X}^2A_u$	$\widetilde{A}^2B_{3u}$	$\widetilde{B}^2B_{2g}$	$\widetilde{C}^2A_u$
$\nu_{114}(0.0911)$	0.0056	0.0048	0.0030	0.0025
$\nu_{115}(0.0550)$	-	-0.0037	0.0010	-0.0061
$\nu_{116}(0.0531)$	-0.0047	-0.0045	0.0002	-0.0041
$\nu_{117}(0.0519)$	-0.0039	-0.0005	0.0003	-0.0095
$\nu_{118}(0.0364)$	-0.0047	-0.0042	-0.0022	-0.0055
$\nu_{119}(0.0167)$	-0.0011	-0.0029	0.0002	-0.0064
$\nu_{120}(0.0032)$	0.0001	-0.0024	0.0025	-0.0046

Table 4.3(c): Same as in Table 4.1(c) for Hn^+.

mode	λ^{j-k}	mode	λ^{j-k}	λ^{j-k}	mode	λ^{j-k}	λ^{j-k}
b_{1u}	$j-k \in \widetilde{A}$-$\widetilde{B}$	b_{2u}	$j-k \in \widetilde{X}$-$\widetilde{A}$	$j-k \in \widetilde{A}$-$\widetilde{C}$	b_{3g}	$j-k \in \widetilde{X}$-$\widetilde{B}$	$j-k \in \widetilde{B}$-$\widetilde{C}$
ν_{41}	-	ν_{71}	-	-	ν_{91}	-	0.0078 (0.0002)
ν_{42}	-	ν_{72}	-	0.0101 (0.0003)	ν_{92}	-	0.0063 (0.0001)
ν_{43}	-	ν_{73}	-	-	ν_{93}	-	-
ν_{44}	-	ν_{74}	-	0.0063 (0.0001)	ν_{94}	-	-
ν_{45}	0.1063 (0.1311)	ν_{75}	-	-	ν_{95}	-	0.0950 (0.1049)
ν_{46}	0.0312 (0.0116)	ν_{76}	-	0.0709 (0.0653)	ν_{96}	0.1441 (0.2509)	-
ν_{47}	-	ν_{77}	0.0737 (0.0733)	-	ν_{97}	-	0.0224 (0.0062)
ν_{48}	-	ν_{78}	-	0.0616 (0.0553)	ν_{98}	-	-
ν_{49}	0.0363 (0.0249)	ν_{79}	0.0428 (0.0279)	-	ν_{99}	-	0.0170 (0.0050)
ν_{50}	0.0248 (0.0120)	ν_{80}	0.0640 (0.0640)	0.0157 (0.0038)	ν_{100}	-	0.0403 (0.0319)
ν_{51}	-	ν_{81}	-	-	ν_{101}	-	0.0252 (0.0127)
ν_{52}	-	ν_{82}	0.0343 (0.0255)	-	ν_{102}	-	0.0061 (0.0008)
ν_{53}	0.0252 (0.0145)	ν_{83}	-	0.0062 (0.0009)	ν_{103}	0.0527 (0.0644)	-
ν_{54}	0.0112 (0.0031)	ν_{84}	0.0191 (0.0087)	-	ν_{104}	-	0.0111 (0.0030)
ν_{55}	-	ν_{85}	-	-	ν_{105}	-	0.0053 (0.0011)
ν_{56}	-	ν_{86}	-	-	ν_{106}	-	-
ν_{57}	0.0352 (0.1293)	ν_{87}	-	0.0112 (0.0071)	ν_{107}	-	0.0418 (0.1287)
ν_{58}	0.0179 (0.0491)	ν_{88}	0.0146 (0.0176)	-	ν_{108}	0.0286 (0.1151)	-
ν_{59}	0.0168 (0.1101)	ν_{89}	-	-	ν_{109}	0.0068 (0.0105)	-
ν_{60}	0.0114 (0.5000)	ν_{90}	-	-	ν_{110}	-	-

4.3 Results and discussion

4.3.1 Potential energy surface of electronic ground and excited states

The topography of the electronic states of Tn^+, Pn^+ and Hn^+ is examined in this section in order to understand the nuclear dynamics results presented and discussed subsequently. The adiabatic PESs of the $\widetilde{X}^2A_u$, $\widetilde{A}^2B_{3u}$, $\widetilde{B}^2B_{2g}$ and $\widetilde{C}^2A_u$ electronic states of Tn^+, $\widetilde{X}^2B_{2g}$, $\widetilde{A}^2A_u$, $\widetilde{B}^2B_{1g}$ and $\widetilde{C}^2B_{2g}$ electronic states of Pn^+ and $\widetilde{X}^2A_u$, $\widetilde{A}^2B_{2g}$, $\widetilde{B}^2B_{3u}$ and $\widetilde{C}^2A_u$ electronic states of Hn^+ are obtained by diagonalizing the diabatic electronic Hamiltonian of Eq. 4.1 and the parameters of Tables a, b, c of 4.1, 4.2 and 4.3. Examination of one dimensional cuts of the multidimensional PESs along the relevant vibrational modes of all three radical cations reveals that the C=C stretching vibration leads to low-energy crossings of the electronic states. This is analogous to the situation in Np^+ and An^+ studied by us in the recent past [1–4]. In case of Tn^+, the

inter-ring C=C stretching vibration ν_4 ($\sim$1585 cm^{-1}) leads to the low energy crossing between its $\widetilde{A}$ and $\widetilde{B}$ electronic states. In addition the 762 cm^{-1} ring breathing vibration ν_{13} also causes a crossing of these two states in Tn^+. In Pn^+ two vibrational modes ν_5 (outer-ring C=C stretch $\sim$1587 cm^{-1}) and ν_6 (inter-ring C=C stretch $\sim$1556 cm^{-1}) are quasi-degenerate and both of them are important for this curve crossing. Apart from these two the 762 cm^{-1} ring breathing vibration (ν_{15}) also leads to low-energy curve crossings between the $\widetilde{A}$ and $\widetilde{B}$ electronic states of Pn^+. Like Pn^+, the situation is analogous in Hn^+, and in this case the quasi-degenerate C=C stretching vibrations are ν_5 ($\sim$1588 cm^{-1}) and ν_6 ($\sim$1545 cm^{-1}). These crossings develop into conical intersections of electronic PESs in multi-dimensions. The ring breathing mode ν_{18} (758 cm^{-1}) apparently does not lead to a crossing of these electronic states in Hn^+.

One dimensional cuts of adiabatic potential energy surface of $\widetilde{X}$, $\widetilde{A}$, $\widetilde{B}$ and $\widetilde{C}$ electronic states along these vibrations (keeping others at their equilibrium position) are shown in Fig. 4.2 for Tn^+ (panel a and b), Pn^+ (panel c, d and e) and Hn^+ (panel f and g). In each panel the potential energy values obtained from the present vibronic model (developed in Sec. 4.2.1) and *ab initio* electronic structure calculations are shown by the solid lines and points, respectively. It can be seen from Fig. 4.2 that the computed *ab initio* energies are in excellent agreement with those obtained from the constructed vibronic model. We note that the $\widetilde{X}$ state is energetically well seperated (vertically) from the rest of the states for all the radical cations presented in Fig. 4.2. This is in contrast to our findings for Np^+ and An^+ (shown in Fig.1 of Ref [3]). In the latter case, the $\widetilde{X}$ state forms accessible intersections with the $\widetilde{A}$ state.

The energetic minimum of multidimensional seam of conical intersections is calculated for all three radical cations in order to assess their accessibility during the nuclear motion on a given electronic state of these radical cations. The energetic minimum of the $\widetilde{X}$-$\widetilde{A}$, $\widetilde{A}$-$\widetilde{B}$ and $\widetilde{X}$-$\widetilde{B}$ conical intersections is plotted as a function of the number of fused benzene rings in the noncompact PAH radical cations in Figs. 4.3 (a-c), respectively. These intersection seams primarily play decisive role as regard to the laboratory and interstellar observations discussed above. It can be seen from panel a that the energetic minimum of the $\widetilde{X}$-$\widetilde{A}$ conical intersections increases with increasing number of fused benzene rings. The energy is lowest in case of Np^+. On the other hand, the minimum energy of the $\widetilde{A}$-$\widetilde{B}$ conical intersections (panel b) decreases with increasing number of fused benzene rings. This energy is highest in case of Np^+ and lowest for Pn^+ and Hn^+. The energy of the $\widetilde{X}$-$\widetilde{B}$ conical intersections (panel c) is generally higher and does not follow a trend. This energy is highest ($\sim$15.44 eV) in An^+ and lowest ($\sim$11.53 eV) in Pn^+. It therefore emerges from the above results that, while nonradiative internal conversion to the $\widetilde{X}$ state upon photo-excitation to the $\widetilde{B}$ state is feasible due to relatively low-energy $\widetilde{X}$-$\widetilde{A}$ conical intersections in case of Np^+ and An^+, the same appears to be prohibitively difficult for Tn^+, Pn^+ and Hn^+. A cursory remark is in order here. While Np^+ and An^+ can decay to their electronic ground $\widetilde{X}$ state nonradiatively, the probability of such transition appears to be negligibly small in case of Tn^+, Pn^+ and

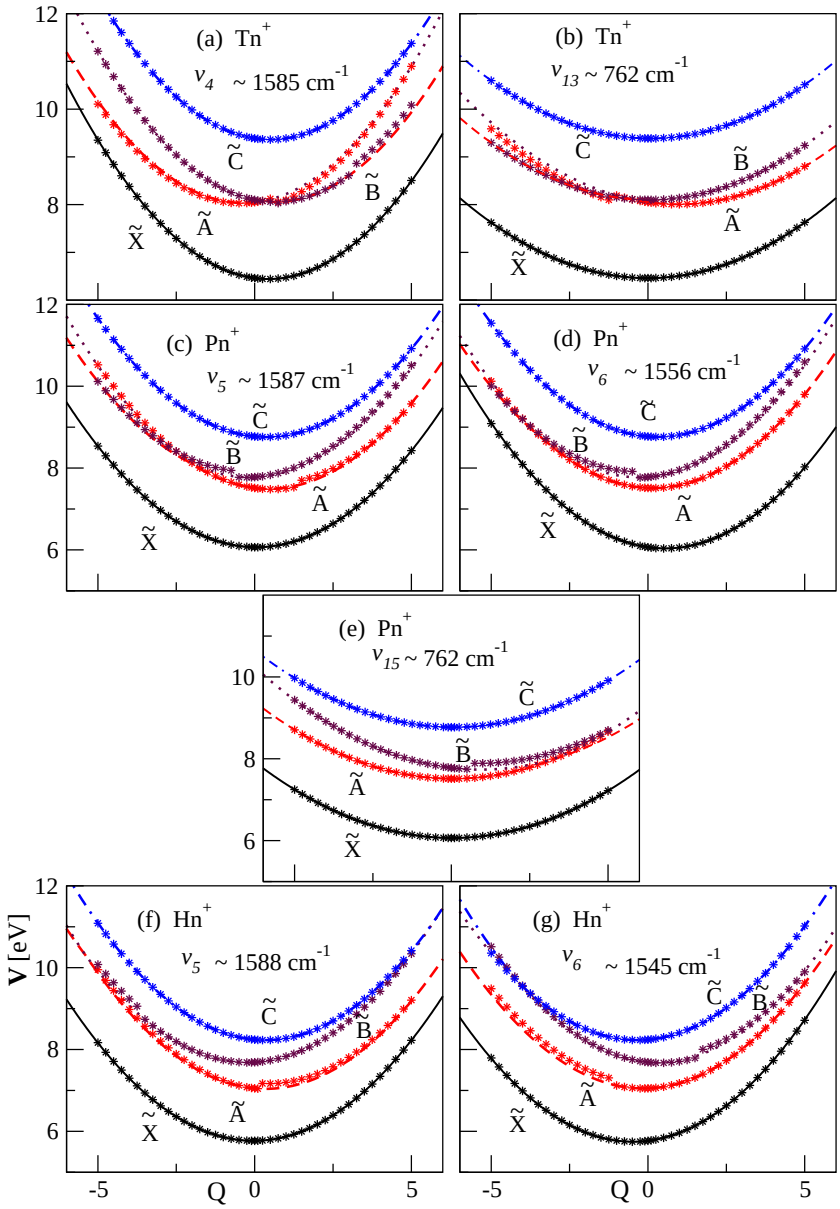

Figure 4.2: Adiabatic energies of the $\widetilde{X}$, $\widetilde{A}$, $\widetilde{B}$ and $\widetilde{C}$ electronic states of Tn^+ (panel a and b), Pn^+ (panel c, d and e) and Hn^+ (panel f and g) plotted along the dimensionless normal displacement coordinate of the vibrational mode indicated in the legend (see text for details). The electronic energies obtained from the present vibronic model and quantum chemistry calculations are shown by lines and points, respectively. For ready reference, the mode number and its harmonic frequency of the reference state is included in each panel.

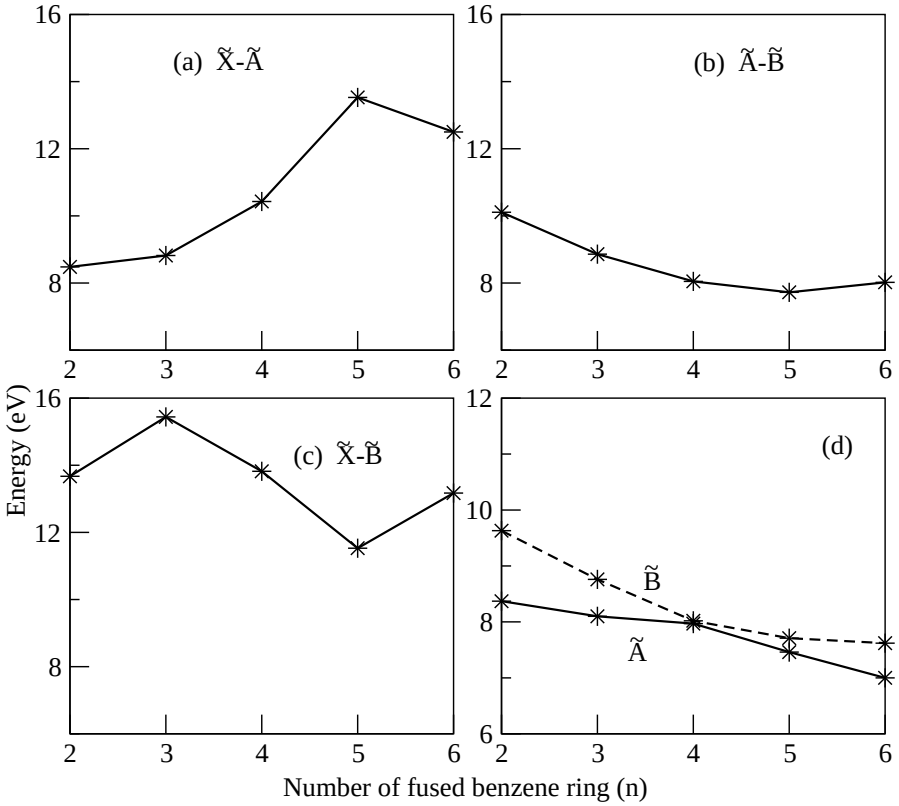

Figure 4.3: Energetic minimum of the seam of $\widetilde{X}$-$\widetilde{A}$(panel a), $\widetilde{A}$-$\widetilde{B}$(panel b) and $\widetilde{X}$-$\widetilde{B}$(panel c) conical intersections as a function of number of fused benzene rings in the noncompact polycyclic aromatic hydrocarbon radical cations (n=2; Np^+ to n=6; Hn^+). The energetic minimum of the $\widetilde{A}$ and $\widetilde{B}$ electronic states are shown in panel d.

Hn^+. Therefore it suffices to say that radiative transition to the electronic ground state is more likely in case of electronically excited Tn^+, Pn^+ and Hn^+.

The spectroscopy of the $\widetilde{B}$ state of these molecules is of interest to both stellar as well as laboratory spectroscopists attempting to assign molecular carrier of diffuse interstellar bands. In our previous study we found that the equilibrium minimum of the $\widetilde{B}$ state comes down in energy and becomes closer to the energy of the $\widetilde{A}$-$\widetilde{B}$ intersection minimum in An^+ when compared to the same for Np^+ (also see Fig. 4.3). As a result we obtained broad and diffuse band structure of the $\widetilde{B}$ state of An^+ in contrast to that of Np^+ [2]. These results were in good accord with those obtained from stellar and laboratory measurements [32–34]. The energetic minimum of the $\widetilde{A}$ and $\widetilde{B}$ states is plotted in panel d of Fig. 4.3 for n=2-6 and shown by points connected by solid and dashed lines, respectively. It can be seen from Fig. 4.3 (d) that the minimum of the $\widetilde{A}$ and $\widetilde{B}$ states almost coincides in case of Tn^+ and also for Pn^+. This is also obvious from the potential

energy curves plotted in Fig. 4.2. It should be noted that, in the latter plots curves are shown along the given vibrational mode keeping others at their equilibrium location at **Q**=0. In contrast, the energetic minima shown in Figs. 4.3 (a-d) are calculated taking all relevant vibrational modes into account and therefore includes the multimode effect. In other words, coupling due to relevant vibrational modes of the intersection space is included in calculating these energy points. In summary, the energy points plotted in Figs. 4.3 (a-d) reveal that the minimum of the $\widetilde{A}$ state moves away from the $\widetilde{X}$-$\widetilde{A}$ intersection minimum and the minimum of the $\widetilde{B}$ state becomes closer to the $\widetilde{A}$-$\widetilde{B}$ intersection minimum with increasing number of fused benzene ring in the these PAH radical cations.

The $\widetilde{C}$ state occurs vertically ∼2.93, ∼1.34 and ∼1.29 eV; ∼2.71, ∼1.26 and ∼1.0 eV; ∼2.47, ∼1.19 and ∼0.55 eV above the $\widetilde{X}$, $\widetilde{A}$ and $\widetilde{B}$ states (in that order) in Tn^+, Pn^+ and Hn^+, respectively. The energetic minimum of $\widetilde{X}$-$\widetilde{C}$, $\widetilde{A}$-$\widetilde{C}$ and $\widetilde{B}$-$\widetilde{C}$ conical intersections is located at ∼27.66, ∼10.68 and ∼12.56 eV, respectively, in Tn^+. These minimum energy points are located at ∼28.36, ∼13.78 and ∼9.73 eV in Pn^+ and at ∼25.87, ∼12.67 and ∼8.44 eV in Hn^+ in that order, respectively. The minimum of the $\widetilde{C}$ state occurs at ∼9.31, ∼8.71 and ∼8.18 eV in Tn^+, Pn^+ and Hn^+, respectively.

4.3.2 Vibronic structure of the electronic ground and excited states vs. photoelectron spectroscopy measurements

In this section we present and discuss the broad band vibronic structure of the $\widetilde{X}$, $\widetilde{A}$, $\widetilde{B}$ and $\widetilde{C}$ electronic states of all three viz., Tn^+, Pn^+ and Hn^+ radical cations calculated with the aid of the vibronic coupling model developed in Sec. 4.2. The resulting electronic band structures are compared with the available literature results from photoelectron spectroscopy measurements under low-resolution. Highly resolved vibronic structure of some of these electronic bands are examined, presented and discussed later in the text.

The relevant vibrational modes and their linear and quadratic coupling parameters required to describe the nuclear dynamics in the coupled $\widetilde{X}$-$\widetilde{A}$-$\widetilde{B}$-$\widetilde{C}$ electronic states of Tn^+, Pn^+ and Hn^+ are given in Tables a, b, c of 4.1, 4.2 and 4.3. The data listed in these tables reveal the importance of 18, 20 and 23 vibrational modes in the coupled states dynamics of Tn^+, Pn^+ and Hn^+, respectively. Prior to the simulation of the coupled states nuclear dynamics, we examined various uncoupled state spectra of these radical cations. This exercise helped us to follow the spectral progressions and relative contributions of various vibrational modes in the broad band structure measured in the photoelectron spectroscopy experiments.

The uncoupled state spectra are calculated by diagonalizing the corresponding Hamiltonian for all three radical cations in a harmonic oscillator basis of the vibrational modes of the reference state, shown in panel a, b and c of Fig. 4.4 for Tn^+, Pn^+ and Hn^+ respectively, in that order. It can be confirmed that the C=C stretching vibrations primarily

form dominant progressions in the uncoupled state spectrum of Tn^+, Pn^+ and Hn^+. In Tn^+, peak spacings of ∼0.184, ∼0.194 and ∼0.197 eV corresponding to symmetric vibrational modes ν_7, ν_5 and ν_4, respectively, are found in the $\widetilde{X}$ state. Peak spacings of ∼0.039, ∼0.094 and ∼0.200 eV corresponding to ν_{15}, ν_{13} and ν_4 vibrational modes, respectively, are found in the $\widetilde{A}$ state. The vibrational modes ν_{15}, ν_6 and ν_4 form dominant progressions in the $\widetilde{B}$ state and the peaks are ∼0.039, ∼0.184 and ∼0.197 eV spaced, respectively. In the $\widetilde{C}$ state ν_{15}, ν_{14}, ν_{12} and ν_4 vibrational modes form progressions with peak spacing of ∼0.039, ∼0.075, ∼0.108 and ∼0.198 eV, respectively. In case of Pn^+, peak spacings of ∼0.150, ∼0.177, ∼0.185 and ∼0.196 eV found in the $\widetilde{X}$ band are assigned to the excitation of vibrational modes ν_{11}, ν_9, ν_8 and ν_6, respectively. The vibrational modes ν_9 and ν_5 are strongly excited in the $\widetilde{A}$ state and the corresponding peak spacings of ∼0.180 and ∼0.199 eV, respectively, are found in this case. Dominant progression of ν_{18}, ν_{15} and ν_6 vibrational modes is found in the $\widetilde{B}$ state with corresponding peak spacings of ∼0.032, ∼0.097 and ∼0.195 eV, respectively. Peak spacings of ∼0.032, ∼0.167 and ∼0.199 eV are found in the $\widetilde{C}$ state and are assigned to the fundamentals of the ν_{18}, ν_{10} and ν_5 vibrational modes, respectively. In Hn^+, the dominant peaks are ∼0.027 and ∼0.195 eV spaced in the $\widetilde{X}$ state and are due to vibrational modes ν_{21} and ν_6, respectively. In the $\widetilde{A}$ state the vibrational modes ν_{11}, ν_7 and ν_5 form progressions and the peaks are ∼0.178, ∼0.188 and ∼0.197 eV spaced, respectively. Dominant progressions of ν_{21}, ν_{18} and ν_{17} vibrations are found in the $\widetilde{B}$ state. The peaks are ∼0.027, ∼0.094 and ∼0.096 eV spaced, respectively. In the $\widetilde{C}$ state peak spacings of ∼0.028, ∼0.184, ∼0.194 and ∼0.199 eV are found and assigned to the excitation of ν_{21}, ν_9, ν_6 and ν_5 vibrational modes, respectively. We note that the frequencies extracted above from the peak spacings correspond to their value given in Tables (b of 4.1, 4.2 and 4.3) modified by the second-order coupling constant of a given vibration in the given electronic state of the radical cation.

In the subsequent analysis we included the coupling among the $\widetilde{X}$-$\widetilde{A}$-$\widetilde{B}$-$\widetilde{C}$ electronic states to calculate the broad band vibronic spectra by propagating wave packets and employing the MCTDH method. The Heidelberg MCTDH suite of programs [35] is used for this purpose. It is well realized from the past studies on several vibronic coupling problems that the matrix diagonalization approach which requires extremely large computer hardware becomes tedious with systems of growing size in terms of increasing number of electronic and vibrational degrees of freedom. The diagonalization approach fails in the present case when all four coupled electronic states are considered along with the relevant vibrational modes (mentioned above) for all three radical cations. It can be seen from Table c of 4.1, 4.2 and 4.3 that except $\widetilde{X}$-$\widetilde{C}$, all other states are coupled in first-order for all three radical cations. The impact of these couplings on the vibronic structure of a given state depends on its energetic location relative to the energetic minimum of the relevant intersection seam [cf. Figs. 4.3 (a-d), and discussion in Sec. 4.3.1]. We will return to this point later in the text.

The WP is initially prepared in each of the mentioned electronic state of the radical

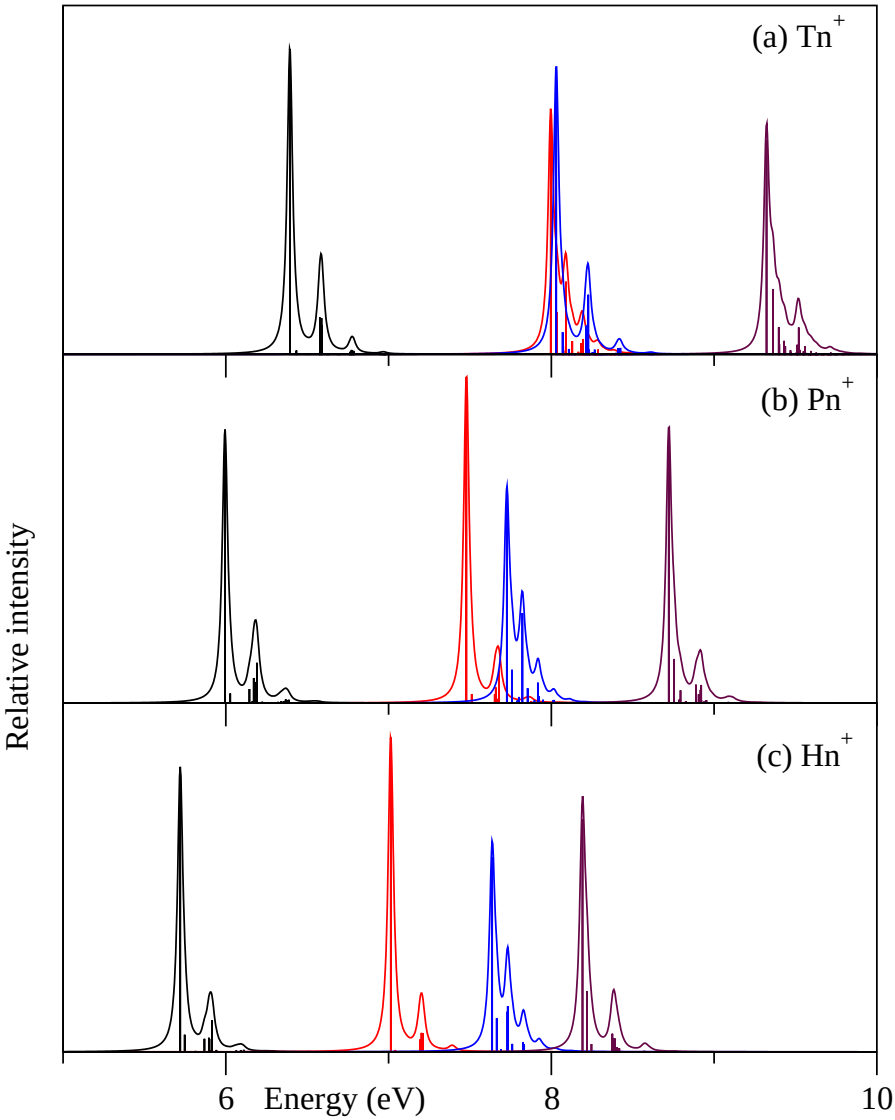

Figure 4.4: The quadratic uncoupled $\widetilde{X}$, $\widetilde{A}$, $\widetilde{B}$ and $\widetilde{C}$ vibronic bands of Tn^+(panel a), Pn^+(panel b) and Hn^+(panel c).

cation and then propagated for 200 fs in the coupled manifold of electronic states using the MCTDH algorithm. The technical details of the calculations viz., normal mode combination scheme, the sizes of primitive and single particle basis are given in Table 4.4 for Tn^+, Pn^+ and Hn^+, respectively. The convergence of the results is confirmed with respect to these technical parameters. At each time step (Δt=1.0 fs) the autocorrelation function of the WP, C(t), is recorded. The resulting autocorrelation function from four separate calculations are then combined, damped with an exponential function e^{-t/τ_r} (with τ_r=33 fs) and finally Fourier transformed to generate composite vibronic spectrum of each radical cation.

The vibronic band structure of the coupled $\widetilde{X}(1)$-$\widetilde{A}(2)$-$\widetilde{B}(3)$-$\widetilde{C}(4)$ electronic states of Tn^+ calculated by the theoretical approach mentioned above is shown in panel a of Fig. 4.5. For comparison, the experimental results are reproduced from Ref [18] and shown in panel b of Fig. 4.5. It can be seen that the present broad band theoretical results are in excellent agreement with the experiment. Now let us examine the detailed structure of each band presented in this figure. The structure of band (1) for the $\widetilde{X}$ state of Tn^+ does not reveal any noticeable difference when compared to the same obtained in the uncoupled state situation. The vibrational modes ν_4, ν_5 and ν_7 contribute most to the overall shape of this band. The former two modes are quasi-degenerate [cf., Table 4.1 b]. The contribution to the spectral intensity is nearly same for the modes ν_5 and ν_7 however, the mode ν_4 has $\sim$16 % less contribution compared to the other two. This can be understood from the coupling parameters given in Table 4.1(a). It can be seen from the latter the coupling parameter of the mode ν_4 is $\sim$10 % less than the other two. Very minor (hardly detectable) contributions to this band are also made by the $\widetilde{A}$ and $\widetilde{B}$ states through the vibrational modes ν_{67}, ν_{76} and ν_{77} of b_{3g} and ν_{56} of b_{2u} symmetry.

The second band in Fig. 4.5 represents a composite structure of the $\widetilde{A}(2)$ and $\widetilde{B}(3)$ electronic states of Tn^+. It can be seen from Fig. 4.5 that vibronic structure of these two states are highly overlapping. They differ significantly from their individual structures obtained in the uncoupled state situation. From the potential energy cuts given in Fig. 4.2 and also the related discussion presented in Sec. 4.3.1, it is clear that the energetic minimum of these two states and that of their intersection seam are quasi-degenerate [cf. Figs. 4.3 (b) and 4.3 (d)]. Because of this energetic proximity and moderate coupling via ν_{32} and ν_{40} vibrational modes of b_{1u} symmetry [cf. Table 4.1(c)] huge electronic nonadiabatic effects show up in their composite band structure (2,3). We will get back to this point again when we discuss on the electron population dynamics later in the text. Like the $\widetilde{X}$ state the structure of the $\widetilde{C}$ state (4) of Tn^+ also remains similar to that obtained in the uncoupled state situation. Weak perturbation in the coupled states vibronic structure [cf. Fig. (4.5)] arises due to coupling with the $\widetilde{A}$ and $\widetilde{B}$ states through vibrational modes of b_{3g} and b_{2u} symmetry [cf. Table 4.1(c)].

The vibronic band structure of the coupled $\widetilde{X}(1)$-$\widetilde{A}(2)$-$\widetilde{B}(3)$-$\widetilde{C}(4)$ electronic states of Pn^+ is shown in Fig. 4.6. The present theoretical results are shown in panel a and the experimental results reproduced from Ref [9] are shown in panel b. In this case also the theoretical band structures are in very good accord with the experiment. The band structure of Pn^+ in Fig. 4.6 is analogous to that of Tn^+ shown in Fig. 4.5. In this case also the structure of the $\widetilde{X}$ and $\widetilde{C}$ states remains similar to their uncoupled state results. However, the structure of the $\widetilde{A}(2)$-$\widetilde{B}(3)$ states is strongly perturbed by the vibronic coupling due to the vibrational modes of b_{1u} symmetry. It can be seen from Table 4.2(c) that coupling strengths of the b_{1u} modes are stronger between the $\widetilde{A}$ and $\widetilde{B}$ states of Pn^+ when compared to the same of Tn^+. Also the coupling is significant along four b_{1u} modes in Pn^+ instead of two in Tn^+. Furthermore, the energy gap between the

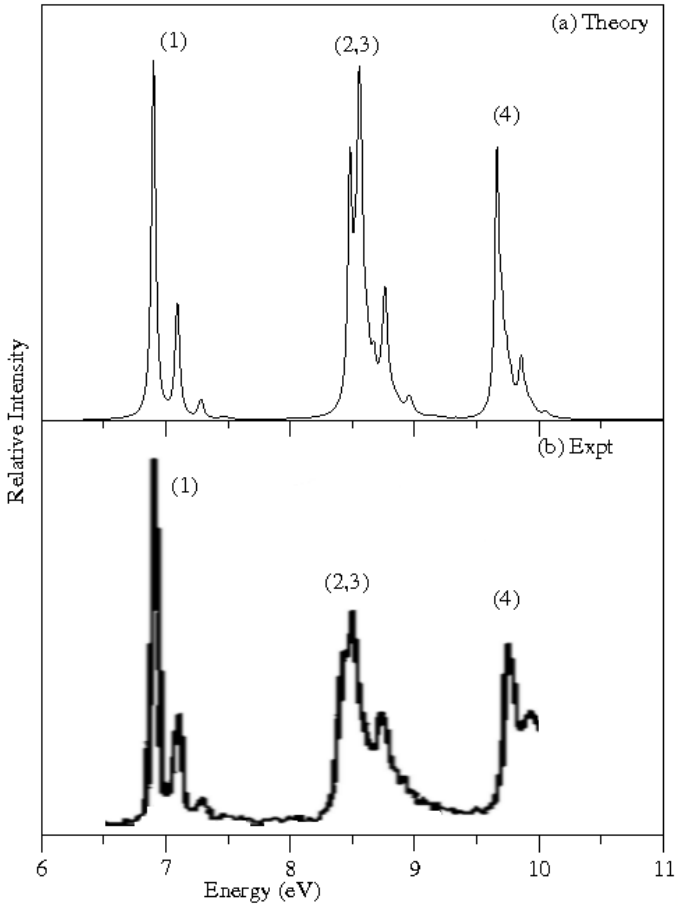

Figure 4.5: Broad band vibronic structure of the $\widetilde{X}(1)$-$\widetilde{A}(2)$-$\widetilde{B}(3)$-$\widetilde{C}(4)$ electronic states of Tn^+. Relative intensity (in arbitrary units) is plotted as a function of the energy of the vibronic states of Tn^+. The zero of the energy scale corresponds to the equilibrium minimum of the electronic ground state of the neutral reference. The present theoretical results are shown in panel a and the experimental photoelectron spectroscopy results (reproduced from Ref [18]) are shown in panel b for comparison.

minimum of $\widetilde{A}$-$\widetilde{B}$ crossing seam and the equilibrium minimum of the $\widetilde{A}$ and $\widetilde{B}$ states are of comparable magnitude in both the cations. The minimum of the $\widetilde{A}$ state occurs $\sim$0.264 eV ($\sim$0.083 eV in Tn^+) below the minimum of $\widetilde{A}$-$\widetilde{B}$ intersection and $\sim$0.016 eV ($\sim$0.027 eV in Tn^+) above the $\widetilde{B}$ state minimum (cf. Fig. 4.3). However, owing to much stronger coupling due to b_{1u} vibrational modes overall nonadiabatic effect is somewhat greater in Pn^+.

Theoretically calculated vibronic band structure of the coupled $\widetilde{X}(1)$-$\widetilde{A}(2)$-$\widetilde{B}(3)$-$\widetilde{C}(4)$ electronic states of Hn^+ is shown in panel a of Fig. 4.7. The experimental results

Table 4.4: Normal mode combinations and sizes of the primitive and single-particle basis functions used in the converged MCTDH calculations for the coupled $\widetilde{X}$-$\widetilde{A}$-$\widetilde{B}$-$\widetilde{C}$ electronic states of Tn^+, Pn^+, and Hn^+.

Normal modes	Primitive basis	SPF basis
	Tn^+	
$(\nu_{12},\nu_5,\nu_{62},\nu_{75})$	(6,8,6,8)	[8,10,6,8]
$(\nu_{77},\nu_4,\nu_{15},\nu_{32})$	(8,8,10,6)	[8,8,10,6]
$(\nu_{14},\nu_{56},\nu_7,\nu_{40},\nu_{67})$	(8,8,8,6,8)	[8,8,10,8]
$(\nu_{76},\nu_{57},\nu_6,\nu_{13},\nu_{68})$	(8,6,8,12,8)	[8,8,8,10]
	Pn^+	
$(\nu_{15},\nu_{38},\nu_{90},\nu_{10})$	(12,8,8,6)	[10,8,8,6]
$(\nu_{68},\nu_{11},\nu_{80},\nu_8)$	(4,5,8,8)	[6,8,8,10]
$(\nu_{50},\nu_6,\nu_{66},\nu_{17})$	(10,10,6,4)	[8,10,6,6]
$(\nu_9,\nu_{81},\nu_5,\nu_{48})$	(8,8,10,10)	[8,8,10,8]
$(\nu_{92},\nu_{91},\nu_{49},\nu_{18})$	(8,8,8,10)	[8,8,6,10]
	Hn^+	
$(\nu_{17},\nu_{57},\nu_{76},\nu_{95},\nu_{11})$	(12,8,6,8,6)	[10,8,6,8]
$(\nu_{45},\nu_{13},\nu_{107},\nu_{59},\nu_9)$	(6,6,8,8,6)	[6,6,8,8]
$(\nu_5,\nu_7,\nu_{80},\nu_{18},\nu_{103})$	(8,4,6,10,5)	[8,6,8,10]
$(\nu_{10},\nu_{108},\nu_{96},\nu_6)$	(6,8,10,8)	[6,8,10,10]
$(\nu_{78},\nu_{77},\nu_{60},\nu_{21})$	(4,6,8,8)	[6,6,8,10]

reproduced from Ref [19] are plotted in panel b of Fig. 4.7 for comparison. It can be seen that the theoretical results are in good agreement with the experimental ones. Four discrete bands for the four electronic states are obtained in this case. Analogous to Tn^+ and Pn^+ vibronic coupling effects on the $\widetilde{X}(1)$ and $\widetilde{C}(4)$ bands of Hn^+ are also insignificant. In contrast to Tn^+ and Pn^+, the coupling between the $\widetilde{A}(2)$ and $\widetilde{B}(3)$ states through the vibrational modes of b_{1u} symmetry is stronger [cf., Table 4.3(c)]. However, in Hn^+ these two states are energetically far apart ($\sim$0.64 eV) in contrast to those in Tn^+ and Pn^+ at the vertical configuration [cf., Table 4.1(a) and 4.2(a)]. Also the minimum of the $\widetilde{A}$-$\widetilde{B}$ intersection is located $\sim$1.02 and $\sim$0.40 eV above the minimum of the $\widetilde{A}$ and $\widetilde{B}$ state, respectively (cf. Fig. 4.3). As a result the net coupling effect is relatively minor on the vibronic structure of the $\widetilde{A}(2)$ and $\widetilde{B}(3)$ bands of Hn^+ and they are as non overlapping as can be seen from Fig. 4.7.

4.3.3 Time-dependent dynamics

Time-dependence of diabatic electronic populations in the coupled $\widetilde{X}$-$\widetilde{A}$-$\widetilde{B}$-$\widetilde{C}$ states dynamics of the above three molecules is examined and presented in Figs. 4.8, 4.9 and 4.10. It is observed that very minor population flows to all three excited electronic states when the WP is initially prepared on the $\widetilde{X}$ state of these radical cations. As

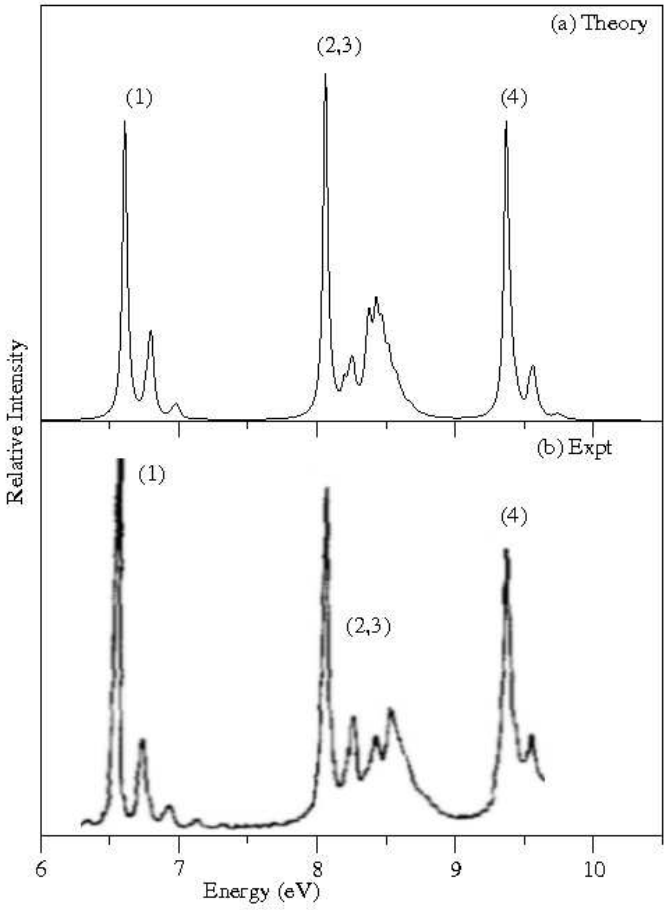

Figure 4.6: Same as in Fig. 4.5 for the $\widetilde{X}(1)$-$\widetilde{A}(2)$-$\widetilde{B}(3)$-$\widetilde{C}(4)$ coupled electronic states of Pn^+. The experimental results shown in panel b are reproduced from Ref [9].

discussed in Sec. 4.3.1 that the CIs of the $\widetilde{X}$ state with all other states (of all three radical cations) are located at higher energies. Therefore, these CIs are not accessible to the WP during its evolution on the $\widetilde{X}$ state. As a result sharp vibrational levels of the $\widetilde{X}$ state emerged in the photoionization band of all three molecules. The $\widetilde{C}$ state is coupled with further higher excited states and a detail examination of these couplings is beyond the scope of the present investigation. We therefore do not discuss on the diabatic electronic population of the $\widetilde{C}$ state here. The time dependence of the population of the $\widetilde{A}$ and $\widetilde{B}$ electronic states of these radical cations is interesting and important from the view point of their astrophysical relevance. For these two electronic states we investigated the population dynamics in the adiabatic representation as well. This is to provide a more realistic estimate of their decay rate that can be directly compared with experimental data.

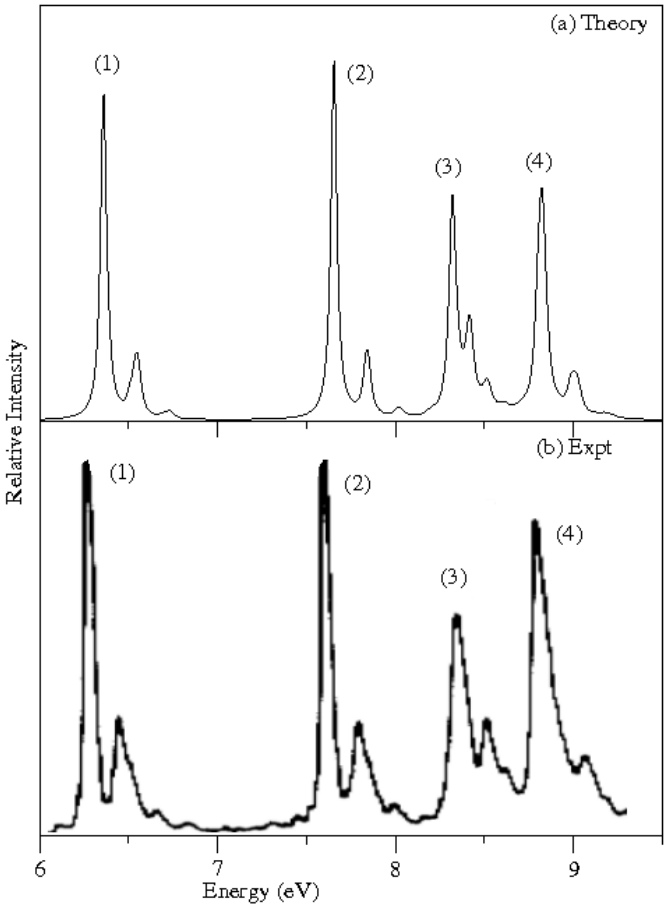

Figure 4.7: Same as in Fig. 4.5 for the $\widetilde{X}(1)$-$\widetilde{A}(2)$-$\widetilde{B}(3)$-$\widetilde{C}(4)$ coupled electronic states of Hn^+. The experimental results shown in panel b are reproduced from Ref [19].

In these plots the time dependence of electronic populations for an initial transition of the neutral molecule to the $\widetilde{A}$ and $\widetilde{B}$ ionic states are shown, respectively, in panels: b and c of Fig. 4.8, 4.9 and 4.10 for Tn^+, Pn^+ and Hn^+. These represents fractional populations and are obtained by propagating the WP in the coupled manifold of $\widetilde{X}$-$\widetilde{A}$-$\widetilde{B}$-$\widetilde{C}$ ionic states in each case. It can be immediately seen from these plots that the nuclear dynamics in the four coupled ionic states is solely governed by the $\widetilde{A}$-$\widetilde{B}$ vibronic coupling. The electronic population flows to these two electronic states only. Population flow to the rest of the electronic states is negligibly small. Apart from these general observations a closer look at the population curves reveals the following. First we note that (also indicated in the figure) the population of the $\widetilde{X}$, $\widetilde{A}$, $\widetilde{B}$ and $\widetilde{C}$ state is shown by the dotted, solid, dashed and dash with dotted lines, respectively. The population flow to the $\widetilde{B}$ state is quite small in case of Pn^+ and Hn^+ (panel b of Fig. 4.9, 4.10) when $\widetilde{A}$ state is initially populated. In contrast $\sim$10% of electron population moves to

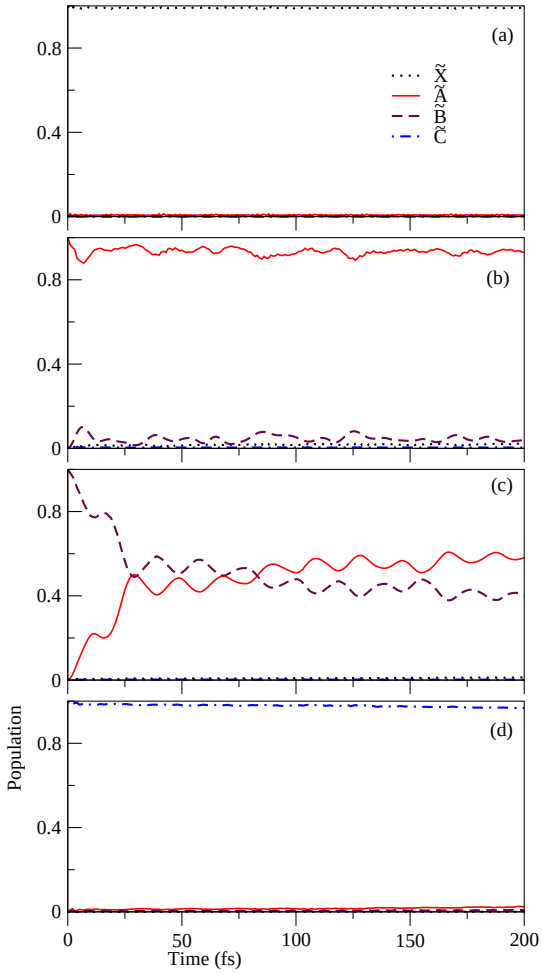

Figure 4.8: Time dependence of diabatic populations of the $\widetilde{X}$ (dotted lines), $\widetilde{A}$ (solid lines), $\widetilde{B}$ (dashed lines) and $\widetilde{C}$ (dashed and dotted lines) states for an initial transition of the WP to the $\widetilde{X}$ (panel a), $\widetilde{A}$ (panel b), $\widetilde{B}$ (panel c), $\widetilde{C}$ (panel d) in the coupled $\widetilde{X}$-$\widetilde{A}$-$\widetilde{B}$-$\widetilde{C}$ state dynamics of Tn^+.

the $\widetilde{B}$ state in case of Tn^+ (panel b of Fig. 4.8) in such situation. As can be seen from Figs. 4.3 (b and d), relative to the minimum of the $\widetilde{A}$ state the energetic minimum of the $\widetilde{A}$-$\widetilde{B}$ CIs progressively shifts to the higher energy from Tn^+ (∼0.08 eV) to Pn^+ (∼0.26 eV) to Hn^+ (∼1.02 eV). Because of this energetic proximity relatively large population flows to the $\widetilde{B}$ state of Tn^+ despite very weak coupling strength of the two b_{1u} vibrational modes [cf. Table 4.1(c)]. In contrast, coupling strength of b_{1u} vibrational modes is relatively stronger in Pn^+ and Hn^+ [cf. Table 4.2(c) and 4.3(c)] however, because of increasing energy gap between the $\widetilde{A}$-$\widetilde{B}$ intersection minimum and the minimum of the $\widetilde{A}$ state this coupling effect is quenched and very little population flows to the $\widetilde{B}$ state of Pn^+ and Hn^+.

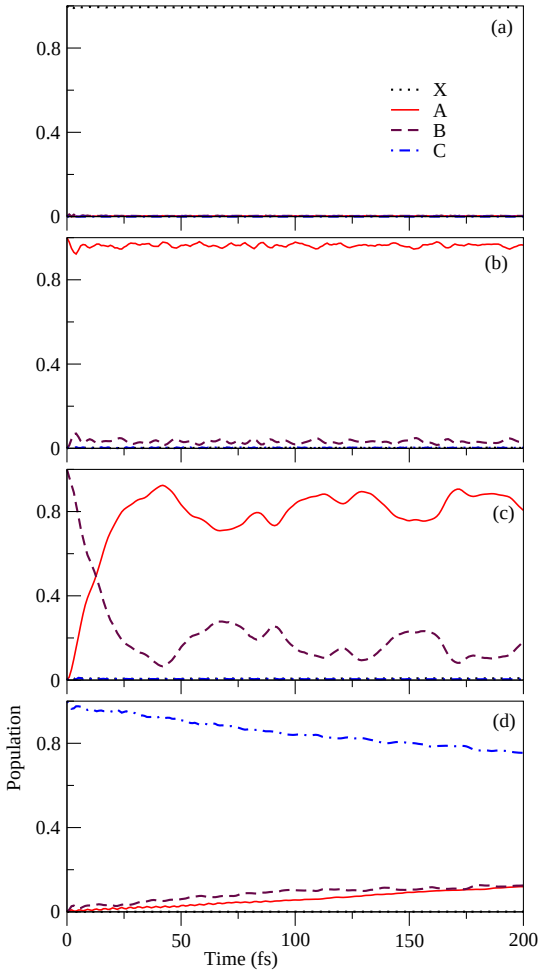

Figure 4.9: Same as in Fig. 4.8 shown for the diabatic populations of Pn^+.

The electron population dynamics appears to be more interesting and involved when the $\widetilde{B}$ state is initially populated. The time dependence of populations is shown in panel c of Fig. 4.8, 4.9 and 4.10 for Tn^+, Pn^+ and Hn^+, respectively, in this case. It can be seen from these figures that large population flows to the $\widetilde{A}$ state of all three radical cations in this situation. The $\widetilde{B}$ state population decreases monotonically in each case. The initial monotonic decrease of population relates to a decay rate of ∼91 fs, ∼21 fs and ∼93 fs of the $\widetilde{B}$ state of Tn^+, Pn^+ and Hn^+, respectively. The minimum of the $\widetilde{B}$ state is energetically quasi-degenerate with minimum of $\widetilde{A}$-$\widetilde{B}$ intersection in Tn^+ and Pn^+, whereas the latter occurs ∼0.4 eV above the $\widetilde{B}$ state minimum in Hn^+. The weak coupling of b_{1u} vibrational modes in Tn^+ causes a slower decay of its $\widetilde{B}$ state as compared to Pn^+ in which coupling effect is relatively stronger [cf. Table 4.2(c)]. Stronger coupling but larger energy separation in Hn^+ causes slower decay of its $\widetilde{B}$ state.

The adiabatic electronic populations of the $\widetilde{A}$ and $\widetilde{B}$ electronic states is calculated

next. From the discussions in the preceding paragraphs it is clear that only coupling between the $\widetilde{A}$ and $\widetilde{B}$ states plays the important role in the coupled states dynamics of all three radical cations. We therefore considered the coupling between the $\widetilde{A}$ and $\widetilde{B}$ states and performed calculations using a 2×2 coupled states Hamiltonian. In contrast to the diabatic electronic population, calculation of the adiabatic electronic population is more involved and a good convergence of the results (presented below) is achieved by such a reduction of the electronic and nuclear degrees of freedom. The time dependence of adiabatic population of the $\widetilde{A}$ and $\widetilde{B}$ electronic states are plotted in Fig. 4.11 for all three radical cations. for an initial ionization to the diabatic $\widetilde{A}$ state is very similar to that obtained in the diabatic electronic picture shown above for all three radical cations (panel a, c and e of Fig. 4.11). The population dynamics is however interesting when the cations are prepared initially in their diabatic $\widetilde{B}$ state. These population diagrams are shown in Fig. 4.11 for Tn^+ (panel b), Pn^+ (panel d) and Hn^+ (panel f). As before, the populations of the $\widetilde{A}$ and $\widetilde{B}$ states are shown by the solid and dashed lines, respectively. Since an adiabatic electronic state is an admixture of the diabatic component states, the initial adiabatic population differs from 1 or 0 as obtained in case of diabatic electronic populations. It can be seen from Fig. 4.11 that the initial adiabatic $\widetilde{A}$-$\widetilde{B}$ populations 0.323-0.677, 0.062-0.938 and 0.014-0.986 in case of Tn^+ (panel b), Pn^+ (panel d) and Hn^+ (panel f), respectively. In case of Tn^+, the population of the $\widetilde{B}$ state decreases in time starting from the value 0.677 to nearly zero at ∼11 fs. On the other hand, the population of the $\widetilde{A}$ state grows in time starting from a value 0.323 to nearly 1.0 at ∼11 fs. Thereafter, the population curves of both the states exhibit recurrences which is periodically damped at longer times. The time scale of ∼21 fs of these quasiperiodic recurrences relates to a vibrational frequency of ∼1588 cm^{-1}. This can be attributed to the condon active inter-ring C=C stretching mode of Tn^+. Notice that the beat structure due to this vibrational mode also appears in the diabatic $\widetilde{B}$ state population of Tn^+ in Fig. 4.8 (c). The initial sharp decay of adiabatic $\widetilde{B}$ state population relates to a decay rate of ∼22 fs in Tn^+.

The dynamical features portrayed above are quite different in case of Pn^+ (panel d) and Hn^+(panel f). In contrast to Tn^+, the quasiperiodic recurrences are highly overlapping and strongly damped in Pn^+ and Hn^+. The damping of the recurrences caused by the stronger anharmonicity of the lower adiabatic sheet which exhibits a "cusp" at the conical intersections. Furthermore, 9 a_{1g} + 4 b_{1u} and 10 a_{1g} + 4 b_{1u} vibrational modes were necessary in case of Pn^+ and Hn^+, respectively, in contrast to 8 a_{1g} + 2 b_{1u} modes in case of Tn^+ in the dynamics calculations. Increased multimode effect causes an overlap of the recurrences in Pn^+ and Hn^+ as compared to Tn^+. Furthermore as discussed in Sec. 4.3.1 two condon active C=C stretching modes are quasi degenerate in Pn^+ and Hn^+. In addition, condon activity of ∼762 cm^{-1} (ν_{15}) symmetric vibrational mode in Pn^+ and ∼768 cm^{-1} (ν_{17}) and ∼758 cm^{-1} (ν_{18}) vibrational modes in Hn^+ are also equally important. This contributes to the strongly overlapping recurrence pattern in Figs. 4.11 (d and f). The initial fast decay of the adiabatic population of the $\widetilde{B}$ state relates to a decay rate of ∼14 and ∼77 fs in case of Pn^+ and Hn^+, respectively.

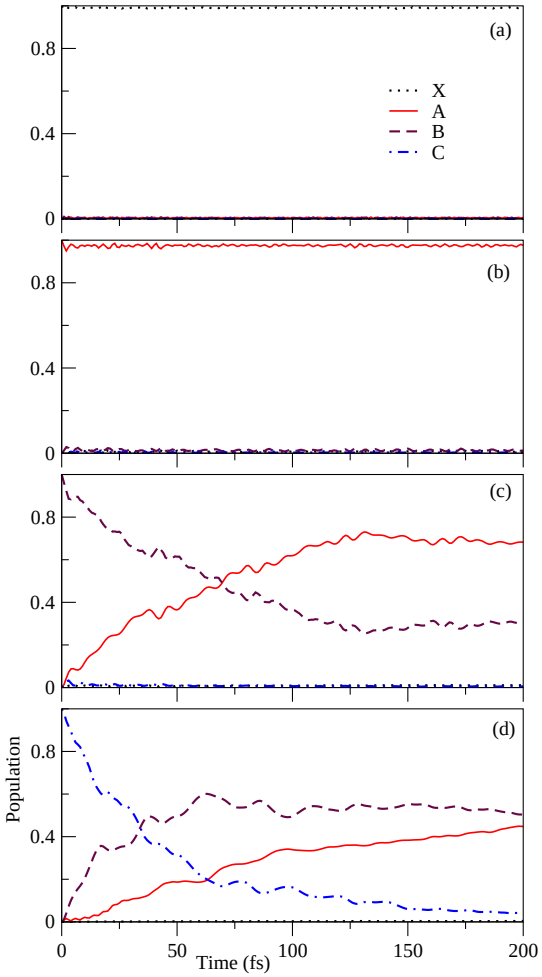

Figure 4.10: Same as in Fig. 4.8 shown for the diabatic populations of Hn^+.

To this end we compare the time dependence of adiabatic $\widetilde{B}$ state populations discussed above to our earlier findings on the same in case of Np^+ and An^+. Decay rates of ∼240 fs and ∼63 fs were estimated [2] from the initial decay of adiabatic $\widetilde{B}$ state population of Np^+ and An^+, respectively. The energetic minimum of $\widetilde{A}$-$\widetilde{B}$ conical intersections occurs at ∼0.48, ∼0.10, ∼0.027, ∼0.016 and ∼0.6 eV above the minimum of the $\widetilde{B}$ state of Np^+, An^+, Tn^+, Pn^+ and Hn^+, respectively. The decrease of the decay rate from Np^+ to Pn^+ can be partly related to the decrease of this energy gap. Like in Np^+, there are only two active coupling b_{1u} modes in Tn^+ and their coupling strength is weaker. Therefore, the decrease of decay rate is primarily due the decrease in the mentioned energy gap in Tn^+. In Pn^+ in addition to the energy decrease there are four relatively stronger active coupling b_{1u} modes. This explains the decrease of decay rate in this case. In Hn^+ there are four relatively stronger coupling b_{1u} modes. Their effect is somewhat quenched by the relatively large energy gap as noted above. Therefore its

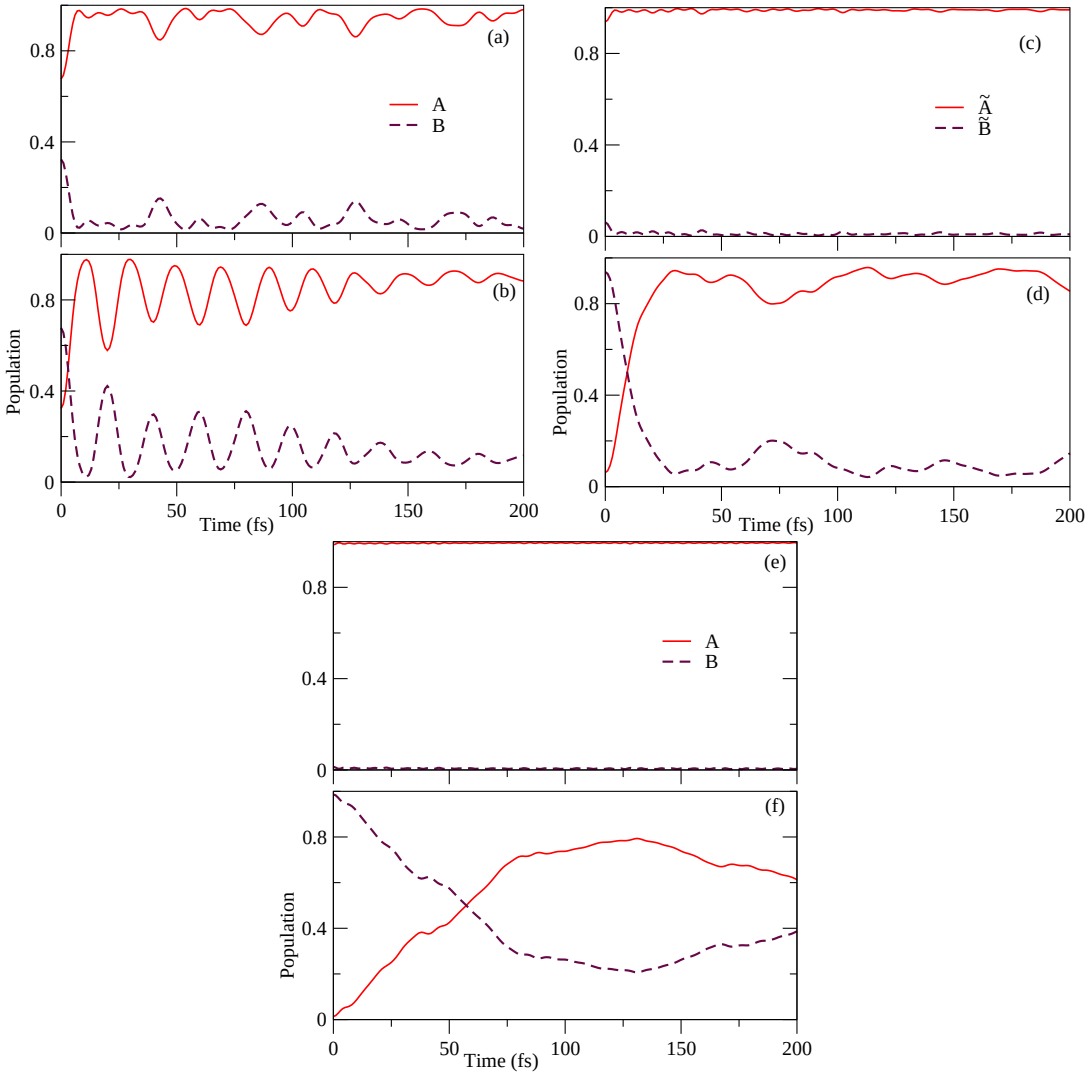

Figure 4.11: Time dependence of adiabatic populations of the $\widetilde{A}$ (solid lines) and $\widetilde{B}$ (dashed lines) electronic states for an initial transition of the WP to the diabatic $\widetilde{A}$ and $\widetilde{B}$ state of Tn^+ (panel a and b), Pn^+ (panel c and d) and Hn^+ (panel e and f) in the coupled $\widetilde{A}$-$\widetilde{B}$ states dynamics.

decay rate is somewhat slower but faster than in Np^+. In contrast to Tn^+, Pn^+ and Hn^+, in Np^+ and An^+ the $\widetilde{A}$ state forms energetically low-lying CIs with their $\widetilde{X}$ state. Therefore, electronically excited $\widetilde{B}$ state can decay nonradiatively to the $\widetilde{X}$ state via $\widetilde{A}$-$\widetilde{B}$ and $\widetilde{X}$-$\widetilde{A}$ CIs in Np^+ and An^+. Propensity of such a mechanism is negligible in Tn^+, Pn^+ and Hn^+. Therefore, the latter molecules are expected to have large quantum yield of fluorescence.

Table 4.5: Tn ZEKE spectral comparison.

mode	ZEKE (calc)	Theory
15^{+}	310 (304)	314
22^{+} 15^{+}	476 (474)	475 (XA coupled B_{3g} 76^{+})
15^{+2}	620 (608)	627
14^{+}	- (634)	610
13^{+}	777 (758)	757
22^{+2} 15^{+2}	786 (778)	766 (XA coupled B_{3g} 76^{+} 77^{+})
15^{+3}	924 (912)	941
14^{+} 15^{+}	951 (938)	923
13^{+} 15^{+}	1091 (1068)	1071
14^{+} 15^{+2}	1264 (1242)	1237

4.3.4 ZEKE spectral progression comparison in Tn^{+} and Pn^{+}

Here, we compare the theoretical vibrational energy levels of the $\widetilde{X}$ state of Tn^{+} with the reported experimental ZEKE spectroscopy findings within 0-1242 cm^{-1} spectral range [20, 22, 23]. The uncoupled $\widetilde{X}$ state spectrum is simulated within the matrix diagonalization scheme using only totally-symmetric vibrational modes (see Table 4.5). The obtained stick data with peak spacings at ∼314, ∼610 and ∼757 cm^{-1} are assigned to ν_{15}, ν_{14} and ν_{13} vibrational modes, respectively. The ZEKE findings at 310 and 777 cm^{-1} can be unambiguously assigned to ν_{15} and ν_{13} modes. The first and second overtones of ν_{15} vibrational mode are identified with the peak spacing of ∼627 and ∼941 cm^{-1}, and are fully consistent with the experimental values of 634 and 922 cm^{-1}. Peaks corresponding to ν_{14}+ν_{15}, ν_{13}+ν_{15}, ν_{14}+2ν_{15} are also identified at ∼923 ∼1071 and ∼1237 cm^{-1}, respectively. These combinations were also seen at 951, 1091 and 1267 cm^{-1} in the experiment.

Excitation of the non-totally symmetric vibrational modes in the $\widetilde{X}$ state spectrum is attributed to $\widetilde{X}$-$\widetilde{A}$ vibronic coupling mechanism. Peak spacing at ∼291 cm^{-1} corresponding to the excitation of ν_{77} (b_{3g}) is identified in the $\widetilde{X}$-$\widetilde{A}$ coupled state calculations along with its first overtone at ∼582 cm^{-1}. Similarly, peaks at ∼475 and ∼951 cm^{-1} are attributed to the fundamental and first overtone of the ν_{76} mode. The peak spacing at ∼767 cm^{-1} is the combination band of ν_{77}, and ν_{76} modes. From the literature the peaks at ∼475 (476) [474] cm^{-1}, ∼766 (786) [778] cm^{-1} are contrast to Zhang *et al.* [20], reported a_u (84 cm^{-1}) mode is responsible for these lines. Our assignments are in accordance with Amirav *et al.* [22, 23], findings of excitation of b_{3g} mode with the frequency of ∼494 cm^{-1}, however, contradict with the Zhang *et al.* [20] findings where excitation of a_u mode with frequency 84 cm^{-1} was reported. Additional peaks with very weak intensity, mostly the combinations associated with excitation a_g and b_{3g} modes, were also found in the $\widetilde{X}$-$\widetilde{A}$ coupled state calculation, however, an unambiguous assignment is very difficult.

Table 4.6: Pn ZEKE spectral comparison.

mode	ZEKE (calc)	Theory
33^{+2}	198 (198)	-
101^{+} 102^{+}	221 (225)	-
33^{+4}	396 (396)	-
18^{+2}	520 (522)	521
18^{+4}	1047 (1044)	1042

Assignment of the vibrational progression in the experimental ZEKE spectrum of the $\widetilde{X}$ state of Pn^+ is also carried out based on the uncoupled and couple state calculations (c.f Table 4.6). The fundamental, first, second and third overtones of ν_{18} of corresponding to the peak spacings at ∼261, ∼521, ∼782 and ∼1042 cm^{-1} are identified in the uncoupled $\widetilde{X}$ state spectrum. The appearance of the b_{2u} vibrational modes in the ZEKE spectrum due to $\widetilde{X}$-$\widetilde{A}$ vibronic coupling mechanism, in principle, can be seen. However, due to lack of low frequency b_{2u} modes, their excitation is not seen in the lower energy part of the experimental spectrum. The $\widetilde{X}$-$\widetilde{B}$ coupled state calculations revealed the excitation of ν_{93} mode of b_{3g} symmetry with the fundamental and first overtone peaks at ∼232 and ∼465 cm^{-1}, respectively. The ZEKE spectral progression of 221 cm^{-1} can be attributed to ν_{93} mode. The peak spacings of ∼424 and 483 cm^{-1} in the $\widetilde{X}$-$\widetilde{B}$ coupled state progression are identified as the fundamental excitation of ν_{92} and ν_{91} vibrational modes. In addition, the combination band of ν_{18} and ν_{93} vibrational modes is also observed with peak spacing of ∼493 cm^{-1}.

4.3.5 DIBs related to $D_0 \rightarrow D_2$ of Tn^+ and $D_0 \rightarrow D_1$ of Pn^+

In Fig. 4.12, we show the experimental and theoretical findings corresponding to the $D_0 \rightarrow D_2$ electronic transition in Tn^+. The theoretical uncoupled spectrum of $\widetilde{B}$ (panel a) is calculated using the totally symmetric modes only and the coupled state spectrum (panel b) is calculated by introducing the b_{1u} symmetry modes responsible for $\widetilde{A}$-$\widetilde{B}$ vibronic coupling mechanism. The abscissa in the theoretical spectra is taken as energy relative to the $\widetilde{X}$ state of Tn^+ and an appropriate energy shift is applied along the abscissa to reproduce the experiment. The vibrational progression is examined by assuming the origin peak (0_0^0) at ∼865.0 nm in the uncoupled $\widetilde{B}$ state spectrum. The observed second strongest absorption peak at ∼760.3 nm, (cf., panel a) is attributed to the excitation of ν_4 vibrational mode of frequency 1585 cm^{-1}. This mode is of predominantly C=C symmetric stretching type. The assignments are fully consistent with the photoelectron (∼865 and ∼750 nm) [24] and matrix isolated absorption (∼868 and ∼745 nm) measurements. The observed additional peak at 832 nm in the coupled state spectrum (panel b) is attributed to the excitation of b_{1u} symmetry mode owing to the $\widetilde{A}$-$\widetilde{B}$ vibronic coupling.

Similarly, the theoretical vibrational energy level structure of the $\widetilde{A}$ state Pn^+ and

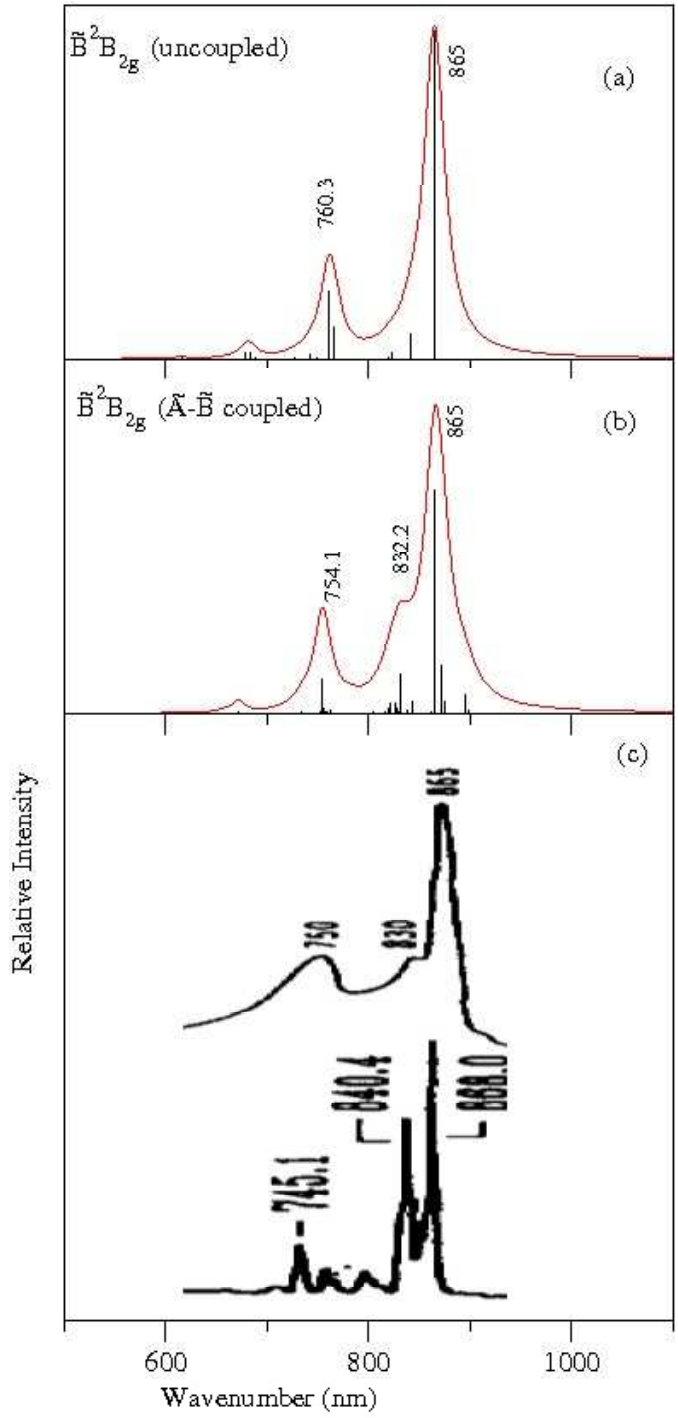

Figure 4.12: The $D_0 \rightarrow D_2$ photoelectron band of Tn. Panel a: uncoupled $D_0 \rightarrow D_2$ band; panel b: calculated by including $\widetilde{A}$-$\widetilde{B}$ vibronic coupling; Panel c: Experimental absorption spectrum of Tn cation Reproduced from Ref [24].

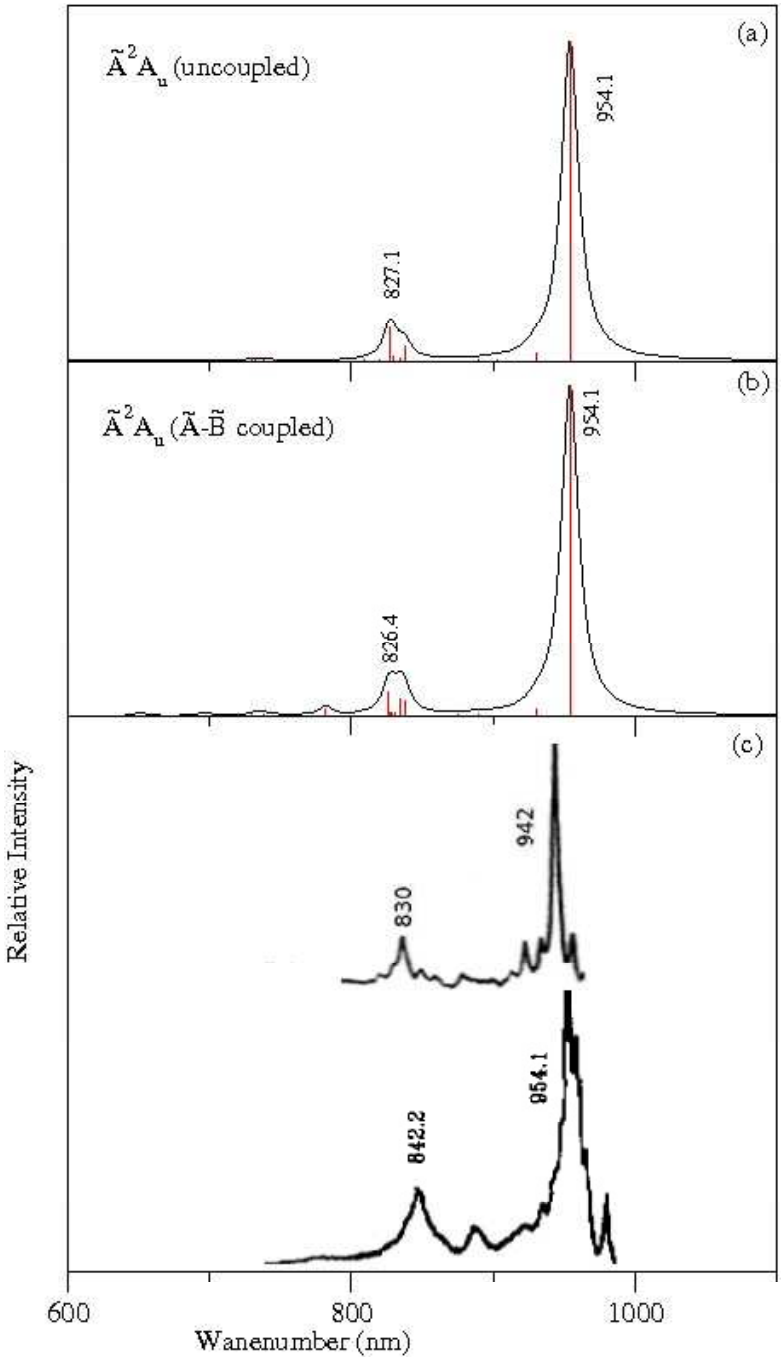

Figure 4.13: The $D_0 \rightarrow D_1$ photoelectron band of Pn. Panel a: calculated uncoupled $D_0 \rightarrow D_1$ band; Panel b: calculated by including $\widetilde{A}$-$\widetilde{B}$ vibronic coupling; Panel c: (top) The experimental matrix (Ne) absorption spectrum of Pn^+ reproduced from [5]; Panel c (bottom): The experimental matrix(Ar) absorption spectrum of Pn^+ reproduced from [25].

the experimental $D_0 \rightarrow D_1$ spectral profile of Pn^+ are shown in Fig. 4.13. The intense peak (origin 0_0^0) at the ∼954.1 nm the other peak (from 0_0^0) observed at ∼827.1 nm in the theoretical spectrum (cf. panel a) are caused by the excitation of ν_5 vibrational mode (C=C symmetric stretch). The coupled state spectrum (panel b) also calculated by introducing the b_{1u} symmetry modes responsible for $\widetilde{A}$-$\widetilde{B}$ vibronic coupling mechanism. In both cases these peak spacings are in excellent agreement with the matrix absorption spectral findings of Salama *et al.* [5] (∼954.1 nm and ∼842.2 nm) and Szczepanski *et al.* [25] (∼942 nm and ∼830 nm).

Salama *et al.* [5, 14] proposed that the observed ∼864.9 and ∼862.1 nm DIBs may be associated with the laboratory experimental findings of strong absorption peak at ∼865 nm corresponding to the $D_0 \rightarrow D_2$ transition of Tn^+. The peaks at ∼842.2 and ∼830 nm [5, 24] corresponding to the second strong absorption of $D_0 \rightarrow D_1$ transition of Pn^+ may be a possible carrier of ∼828.325 nm DIB [14]. Based on the peak at ∼865 nm (origin 0_0^0 of Tn^+) and ∼827.1 nm (second strongest transition of Pn^+) seen in the theoretical spectrum of Tn^+ and Pn^+, respectively, can be attributed (with caution) to the astrophysical DIBs.

4.4 Summarizing remarks

In continuation to our earlier work on the PAH radical cations, Np^+ and An^+, (attempting to relate their spectral features to the observed diffuse interstellar bands), in this chapter we performed a detailed theoretical study on the structure and dynamics of their higher homologs, Tn^+, Pn^+ and Hn^+. *Ab initio* quantum chemistry calculations are carried out to establish the potential energy surfaces and the coupling surfaces of four energetically lowest $\widetilde{X}$, $\widetilde{A}$, $\widetilde{B}$ and $\widetilde{C}$ electronic states of these three cations. With the aid of these electronic structure data and standard vibronic coupling theory coupled states Hamiltonians are developed in a diabatic electronic basis. Employing these Hamiltonians first principles calculations are carried out to examine the spectroscopy and dynamics of these PAH radical cations in their mentioned electronic states.

It is found that the dynamics of $\widetilde{X}$ and $\widetilde{C}$ states of these cations remains essentially unperturbed by the neighboring $\widetilde{A}$ and $\widetilde{B}$ states. In contrast, the latter two states are coupled with each other and form low-energy CIs. The dynamics of these two states is therefore strongly influenced by the associated nonadiabatic coupling. These two states are very close to each other at the vertical configuration and the energetic minimum of the seam of CIs is very close to their equilibrium minimum both in case of Tn^+ and Pn^+. As a result highly overlapping band structures of these two states are obtained for Tn^+ and Pn^+. The situation is somewhat different in case of Hn^+. In this case the $\widetilde{A}$ and $\widetilde{B}$ states are energetically well separated and also the minimum of the seam of CIs is well separated from their equilibrium minimum. Therefore, despite having coupling vibrational modes of larger strength electronic nonadiabatic effect is not as prominent as in case of Tn^+ and Pn^+ in the band structures of $\widetilde{A}$ and $\widetilde{B}$ electronic states of Hn^+. The

theoretical band structures are found to be in very good accord with those measured in the photoelectron spectroscopy experiment. Only Tn^+ and Pn^+ exhibits highly overlapping $\widetilde{A}$-$\widetilde{B}$ band structure in this series of catacondensed PAH radical cations starting from Np^+.

The decay of the adiabatic $\widetilde{B}$ electronic state is another important aspect of this study. Mechanism of this decay dynamics is discussed at length for Tn^+, Pn^+ and Hn^+ and compared with our earlier findings on Np^+ and An^+. It is found that the decay rate of the adiabatic $\widetilde{B}$ state is fastest in case of Pn^+ (13 fs) and slowest in case of Np^+ (240 fs). The $\widetilde{B}$ state is optically bright in all these radical cations and transition to this state take place upon absorption of UV photon of appropriate frequency. While electronically excited (to the $\widetilde{B}$ state) Np^+ and An^+ can nonradiatively decay to their electronic ground $\widetilde{X}$ state through $\widetilde{A}$-$\widetilde{B}$ and $\widetilde{X}$-$\widetilde{A}$ conical intersections, the propensity of such transition is negligible in case of Tn^+, Pn^+ and Hn^+. In the latter cations the $\widetilde{X}$-$\widetilde{A}$ intersections occur at much higher energies. Therefore, it suffices to say here that the probability of internal conversion is much greater in case of Np^+ and An^+ compared to the higher homologs for which the quantum yield of fluorescence emission is expected to be higher.

The spectroscopy of the $\widetilde{A}$ and $\widetilde{B}$ states of these PAH radical cations is particularly important in relation to the stellar spectroscopy. In the recent past we discovered correlation of peak locations of the $\widetilde{B}$ band of both Np^+ and An^+ with those in the star Cernis 52 and HD281159 observed through space telescope [34,36]. A detailed time-independent quantum nuclear dynamics study has been performed to explore the precise location of vibrational energy levels of $D_0 \rightarrow D_2$ transition of Tn^+ and $D_0 \rightarrow D_1$ transition of Pn^+ in relation to the assignment of the astrophysical observation of $\sim$864.9, $\sim$862.1 and $\sim$828.3 nm DIBs. The theoretical findings are in excellent agreement with the laboratory high resolution electronic spectral data. Based on the critical vibrational progression findings, the electronic transitions in the Tn^+ and Pn^+ can be tentatively assigned to the observed DIBs and these molecular cations may play crucial role in the interstellar space.

References

[1] V. S. Reddy, S. Mahapatra, J. Chem. Phys. **128**, 091104 (2008).

[2] V. S. Reddy, S. Ghanta, S. Mahapatra, Phys. Rev. Lett. **104**, 111102 (2010).

[3] S. Ghanta, V. S. Reddy, S. Mahapatra, Phys. Chem. Chem. Phys. **13**, 14523 (2011).

[4] S. Ghanta, V. S. Reddy, S. Mahapatra, Phys. Chem. Chem. Phys. **13**, 14531 (2011).

[5] F. Salama, Origins of Life and Evolution of the Biosphere, **28**, 349 (1998).

[6] O. Parisel, G. Berthier, Y. Ellinger, Astron. Astrophys. **266**, L1 (1992).

[7] M. S. Deleuze, A. B. Trofimov, L. S. Cederbaum, J. Chem. Phys. **115**, 5859 (2001).

[8] M. S. Deleuze, J. Chem. Phys. **116**, 7012 (2002).

[9] W. Schmidt, J. Chem. Phys. **66**, 828 (1977).

[10] E. S. Kadantsev, M. J. Stott, A. Rubio, J. Chem. Phys. **124**, 134901 (2006).

[11] G. Malloci, G. Mulas, C. Joblin, Astron. Astrophys. **426**, 105 (2004).

[12] R. Mondal, C. Tönshoff, D. Khon, D. C. Neckers, H. F. Bettinger, J. Am. Chem. Soc. **131**, 14281 (2009).

[13] R. Boschi, E. Clar, W. Schmidt, J. Chem. Phys. **60**, 4406 (1974).

[14] F. Salama, G. A. Galazutdinov, J. Krełowski, L. J. Allamandola, F. A. Musaev, Astrophys. J. **526**, 265 (1999).

[15] F. Salama, C. Joblin, L. J. Allamandola, Planet. Space Sci. **43**, 1165 (1995).

[16] S. Mahapatra, Acc. Chem. Res. **42**, 1004 (2009).

[17] S. Mahapatra, Int. Rev. Phys. Chem. **23**, 483 (2004).

[18] V. Coropceanu, M. Malagolo, D. A. da Dilva Filho, N. E. Gruhn, T. G. Bill, J. L. Brédas, Phys. Rev. Lett. **89**, 275503 (2002).

[19] E. Clar, J. M. Robertson, R. Schlögl, W. Schmidt, J. Am. Chem. Soc. **103**, 1320 (1981).

[20] J. Zhang, L. Pei, W. Kong, J. Chem. Phys. **128**, 104301 (2008).

[21] J. Zhang, F. Han, L. Pei, W. Kong, A. Li, Astrophys. J. **715**, 485 (2010).

[22] A. Amirav, U. Even, J. Jortner, J. Chem. Phys. **71**, 2319 (1979).

[23] A. Amirav, U. Even, J. Jortner, J. Chem. Phys. **75**, 3770 (1981).

[24] J. Szczepanski, J. Drawdy, C. Wehlburg, M. Vala, Chem. Phys. Lett. **245**, 539 (1995).

[25] J. Szczepanski, C. Wehlburg, M. Vala, Chem. Phys. Lett. **232**, 221 (1995).

[26] H. Köppel, W. Domcke, L. S. Cederbaum, Adv. Chem. Phys. **57**, 59 (1984).

[27] T. H. Dunning, Jr., J. Chem. Phys. **90**, 1007 (1989).

[28] M. J. Frisch, G. W. Trucks, H. B. Schlegel, *et al.*, *Gaussian 03,* Revision B. 05, Gaussian, Inc., Pittsburgh PA, 2003.

[29] L. S. Cederbaum, W. Domcke, Adv. Chem. Phys. **36**, 205 (1977).

[30] S. N. Reddy, S. Mahapatra, Chem. Phys. **403**, 1 (2012).

[31] L. S. Cederbaum, J. Phys. B. **8**, 290 (1975).

[32] L. Biennier, F. Salama, L. J. Allamandola, J. J. Scherer, J. Chem. Phys. **118**, 7863 (2003).

[33] O. Sukhorukov, A. Staicu, E. Diegel, G. Rouillé, T. Henning, F. Huisken, Chem. Phys. Lett. **386**, 259 (2004).

[34] S. Iglesias-Groth, A. Manchado, D. A. GarcÌa-Hernàndez, J. I. Gonzàlez Hernàndez, D. L. Lambert, Astrophys. J. **685**, L55 (2008).

[35] a) G. A. Worth, M. H. Beck, A. Jäckle, H.-D. Meyer, *The MCTDH Package,* Version 8.2, (2000), University of Heidelberg, Heidelberg, Germany. H.-D. Meyer, Version 8.3 (2002), Version 8.4 (2007). ML-MCTDH implemented in forthcoming version 8.5 (2011), see http://mctdh.uni-hd.de/; b) H.-D. Meyer, U. Manthe, L.S. Cederbaum, Chem. Phys. Lett. **165**, 73 (1990); c) U. Manthe, H.-D. Meyer, L. S. Cederbaum, J. Chem. Phys. **97**, 3199 (1992); d) M. H. Beck, A. Jäckle, G. A. Worth, H.-D. Meyer, Phys. Rep. **324**, 1 (2000).

[36] G. Galazutdinov, B. -C. Lee, I. -O. Song, M. Kazmierczak, J. Krełowski, Mon. Not. R. Astron. Soc. **412**, 1259 (2011).

5 Theoretical Study on Molecules of Interstellar Interest.II. Radical Cation of Compact Polycyclic Aromatic Hydrocarbons

5.1 Introduction

This chapter deals with the study of structure and dynamics of some polycyclic aromatic hydrocarbons viz., radical cation of phenanthrene (Pnt^+), pyrene (Py^+) and acenaphthene (Acn^+). The aim is to understand and interpret the vast amount of experimental [1–14] and astrophysical Ultraviolet/visible spectroscopy data of these molecules [9]. In addition to this primary interest, it appears logical to understand how the electronic structure and dynamical properties of these molecules change from benzene molecule and whether they follow a certain trend. Electron-nuclear coupling (vibronic coupling) is an important mechanism that decides the fate of their electronic excited states. It is therefore worthwhile to know how the energy of the electronic states and their coupling mechanism modifies from linear to side chain structures. This issue is discussed at length in this chapter.

Several experimental groups have reported the photoelectron spectra of several PAHs, and the observed ionization potentials were compared with theoretically calculated molecular orbital energies [15–19], It is noted that high resolution gas phase spectral studies such as matrix isolation measurements on these systems and also the data recorded by stellar spectroscopists are the major sources to solve the problems in PAH-DIB hypothesis. From literature, these molecular cations are predicted to be the carrier of the DIBs. In case of Pnt^+ $D_0 \rightarrow D_2$ transition apparently results the 8572 Å DIB. Studies on Py^+ over past several decades reveal that $D_0 \rightarrow D_5$ transition may not be responsible for 4430 Å DIB on the other hand, the substituted Py^+ or Py^+-like species may be responsible for this DIB. In addition, $D_0 \rightarrow D_2$ band of Acn^+ is likely to be a carrier of the 6491.88 Å DIB. Very recently ZEKE, resonance enhanced multiphoton ionization spectra of Py [20] are recorded by Kong *et al.* and these authors discussed the importance of vibronic coupling in the spectral progressions. Except a few electronic structure calculations [21–28] a detailed theoretical study is not carried out on this molecules till date. The observations noted above will be discussed in relation to the theoretical model developed here.

A detailed investigation of the vibronic structure and dynamics of the ground and three low-lying excited electronic states of radical cation of Pnt^+, Py^+ and Acn^+ is carried out, and the theoretical findings are compared with the available laboratory experimental and astrophysical observations [1–14]. As stated above, the prime goal is to assign the following DIBs: 8572 Å of Pnt^+ $D_0 \rightarrow D_2$ and 6491.88 Å of Acn^+ $D_0 \rightarrow D_2$. In addition, the life times and nonradiative decay mechanisms of the excited electronic states are also studied to elucidate the high photostability of these species. Here, both time-independent and time-dependent approaches will be employed to explore the excited state dynamics of these radical cations.

5.2 Theoretical and computational details

5.2.1 The Hamiltonian

Pnt, Py and Acn possess planar equilibrium structure in the ground-electronic state and belong to C_{2v}, D_{2h} and C_{2v} point group symmetry, respectively. Removal of an electron from the four HOMOs of the respective neutral species results the ground ($\widetilde{X}$) and first three excited ($\widetilde{A}$, $\widetilde{B}$ and $\widetilde{C}$) states of their radical cations. Based on elementary symmetry selection rules and dimensionless normal coordinates of the vibrational modes (Q), the vibronic Hamiltonian for the four lowest (vide supra) electronic states in the diabatic electronic basis [29] can be written as

$$\mathcal{H} = (\mathcal{T}_N + \mathcal{V}_0)\mathbf{1_4} + \begin{pmatrix} W_{\widetilde{X}} & W_{\widetilde{X}-\widetilde{A}} & W_{\widetilde{X}-\widetilde{B}} & W_{\widetilde{X}-\widetilde{C}} \\ & W_{\widetilde{A}} & W_{\widetilde{A}-\widetilde{B}} & W_{\widetilde{A}-\widetilde{C}} \\ & & W_{\widetilde{B}} & W_{\widetilde{B}-\widetilde{C}} \\ h.c & & & W_{\widetilde{C}} \end{pmatrix}. \tag{5.1}$$

Here, $\mathbf{1_4}$ is a 4×4 unit matrix. $(\mathcal{T}_N + \mathcal{V}_0)$ is the Hamiltonian for the unperturbed electronic ground state of the neutral molecule. In the harmonic approximation, the kinetic energy ($\mathcal{T}_N$) and potential energy ($\mathcal{V}_0$) terms are expressed as are given by

$$\mathcal{T}_N = -\frac{1}{2}\sum_{i=1}^{n} \omega_i \frac{\partial^2}{\partial Q_i^2}, \tag{5.2}$$

$$\mathcal{V}_0 = \frac{1}{2}\sum_{i=1}^{n} \omega_i Q_i^2. \tag{5.3}$$

In Eq. 5.1; the diagonal elements of the Hamiltonian matrix represent the diabatic energies of the given electronic states, and their coupling energies are the off-diagonal elements. Employing the standard vibronic coupling theory [29], the elements of this

Hamiltonian are expanded in a Taylor series around the equilibrium geometry of the reference state at (**Q**=0)

$$W_j = E_0^{(j)} + \sum_{i \in a_g \ or \ a_1} \kappa_i^{(j)} Q_i + \frac{1}{2} \sum_{i \in all} \gamma_i^{(j)} Q_i^2 \ ; \ j \in \widetilde{X}, \widetilde{A}, \widetilde{B} \ and \ \widetilde{C} \quad (5.4)$$

$$W_{j-k} = \sum_i \lambda_i^{(j-k)} Q_i, \quad (5.5)$$

with $j-k \in \widetilde{X}$-$\widetilde{A}$, $\widetilde{X}$-$\widetilde{B}$,$\widetilde{X}$-$\widetilde{C}$, $\widetilde{A}$-$\widetilde{B}$, $\widetilde{A}$-$\widetilde{C}$, $\widetilde{B}$-$\widetilde{C}$. In the above equations the quantity $E_0^{(j)}$ denotes the vertical ionization energy of the j^{th} electronic state. The linear and quadratic coupling parameters of the i^{th} vibrational mode in the j^{th} electronic state are represented as $\kappa_i^{(j)}$ and $\gamma_i^{(j)}$, respectively. The quantity $\lambda_i^{(j-k)}$ describes the first-order coupling parameter between the j and k electronic states through the coupling vibrational mode i of appropriate symmetry. Evaluation of the coupling parameters of the above Hamiltonian employing extensive *ab initio* electronic structure calculations is described below.

5.2.2 Electronic structure and nuclear dynamics

optimized equilibrium geometry, harmonic vibrational frequencies (ω_i) and dimensionless normal displacement coordinates (**Q**) of the electronic ground state of neutral Pnt, Py and Acn molecules are carried out at the B3LYP level of theory employing the 6-311G* basis set. The Gaussian 03 suite of programs [30] is used for these calculations. The normal vibrational modes of these molecules transform according to the following irreducible representation of the their symmetry point group:

$$\mathrm{Pnt}(\mathrm{C_{2v}}) : \Gamma_{vib} = 23a_1 + 11a_2 + 10b_1 + 22b_2, \quad (5.6)$$

$$\mathrm{Py}(\mathrm{D_{2h}}) : \Gamma_{vib} = 13a_g + 5a_u + 4b_{1g} + 12b_{1u} + 7b_{2g} + 12b_{2u} + 12b_{3g} + 7b_{3u}, \quad (5.7)$$

$$\mathrm{Acn}(\mathrm{C_{2v}}) : \Gamma_{vib} = 20a_1 + 10a_2 + 11b_1 + 19b_2, \quad (5.8)$$

a full-dimensional quantum mechanical treatment of these systems becomes extremely tedious (often impossible) with growing size of the molecules in terms of the electronic and vibrational degrees of freedom. In the following the electronic energies along all vibrational modes of the mentioned systems are calculated, and then a meticulous selection of relevant electronic states and vibrational modes is carried out based on the Hamiltonian parameters extracted from them to investigate the subsequent nuclear quantum dynamics on the coupled manifold of electronic states.

The VIEs of the above molecules are calculated using outer-valence Green's function

(OVGF) method [31] employing the 6-311G* basis set at various nuclear displacement along the dimensionless normal coordinate in the range -4.0 $\leq Q_i \leq$ +4.0, using the Gaussian-03 program module [30]. As stated in Chapter 2, these energies plus harmonic potentials are equated to the adiabatic functional form of the diabatic electronic Hamiltonian of Eq. 5.1 using a least squares algorithm.

$$\mathbf{S}^{\dagger}(\mathcal{H} - T_N 1)\mathbf{S} \;=\; V. \tag{5.9}$$

The estimated coupling parameters of the Hamiltonian are provided in Tables 5.1, 5.2 and 5.3. Based on the excitation strength, only 20 modes out of the 66 vibrational modes of Pnt^+, 22 out of 72 of Py^+, and 24 out of 60 of $Acn^+$are found relevant for quantum dynamics study.

Table 5.1(a): Linear intrastate coupling parameters (κ_i) of the Hamiltonian of the $\widetilde{X}$, $\widetilde{A}$, $\widetilde{B}$ and $\widetilde{C}$ electronic states of Pnt^+ along the totally symmetric modes. The dimensionless coupling strength ($\kappa_i^2/2\omega^2$), are given in the parentheses. The vertical ionization energy of the ground and excited electronic states of this radical cation are also given. All quantities are given in eV.

mode	$\widetilde{X}^2B_1$	$\widetilde{A}^2A_2$	$\widetilde{B}^2A_2$	$\widetilde{C}^2B_1$
a_g ν_1	-0.0084 (0.0002)	-0.0142 (0.0006)	-0.0058 (0.0001)	-0.0080 (0.0002)
ν_2	-0.0148 (0.0007)	-0.0131 (0.0005)	-0.0138 (0.0006)	-0.0161 (0.0008)
ν_3	0.0078 (0.0002)	0.0095 (0.0003)	0.0054 (0.0001)	0.0054 (0.0001)
ν_4	0.0020 (0.0001)	-0.0026 (0.0001)	-0.0006 (0.0001)	-0.0016 (0.0001)
ν_5	0.0013 (0.0001)	0.0070 (0.0001)	0.0004 (0.0001)	0.0047 (0.0001)
ν_6	0.1523 (0.2722)	-0.1044 (0.1279)	0.0406 (0.0193)	0.0104 (0.0013)
ν_7	-0.0043 (0.0002)	0.0866 (0.0897)	-0.0818 (0.0800)	0.0857 (0.0878)
ν_8	-0.0268 (0.0094)	0.0066 (0.0006)	0.0480 (0.0304)	-0.0252 (0.0084)
ν_9	-0.0255 (0.0097)	-0.0535 (0.0427)	0.0078 (0.0009)	0.0462 (0.0318)
ν_{10}	-0.0591 (0.0536)	-0.0114 (0.0020)	0.0592 (0.0538)	0.0350 (0.0188)
ν_{11}	0.0949 (0.1545)	0.0868 (0.1293)	0.0094 (0.0015)	-0.0274 (0.0129)
ν_{12}	-0.0336 (0.0208)	0.0321 (0.0190)	0.0376 (0.0260)	-0.0692 (0.0882)
ν_{13}	0.0538 (0.0582)	-0.0227 (0.0103)	0.0717 (0.1033)	-0.0516 (0.0535)
ν_{14}	-0.0154 (0.0051)	-0.0273 (0.0161)	0.0012 (0.0001)	-0.0307 (0.0203)
ν_{15}	-0.0056 (0.0007)	0.0448 (0.0460)	-0.0170 (0.0066)	0.0112 (0.0029)
ν_{16}	0.0327 (0.0251)	-0.0177 (0.0073)	0.0021 (0.0001)	-0.0334 (0.0262)
ν_{17}	-0.0087 (0.0020)	0.0036 (0.0003)	-0.0067 (0.0012)	0.0041 (0.0004)
ν_{18}	0.0050 (0.0007)	0.0320 (0.0294)	0.0259 (0.0192)	0.0442 (0.0561)
ν_{19}	-0.0101 (0.0046)	0.0022 (0.0002)	-0.0524 (0.1252)	0.0329 (0.0494)
ν_{20}	0.0023 (0.0003)	0.0556 (0.1917)	0.0036 (0.0008)	0.0498 (0.1538)
ν_{21}	0.0482 (0.2426)	-0.0401 (0.1679)	-0.0126 (0.0166)	-0.0462 (0.2229)
ν_{22}	0.0253 (0.1225)	-0.0484 (0.4485)	0.0278 (0.1480)	0.0226 (0.0978)
ν_{23}	0.0199 (0.2074)	-0.0206 (0.222)	0.0072 (0.0271)	-0.0003 (0.0001)

Continued on next page

Table 5.1(a) – *Continued from previous page*

mode	$\widetilde{X}^2B_1$	$\widetilde{A}^2A_2$	$\widetilde{B}^2A_2$	$\widetilde{C}^2B_1$
VIE	7.607	7.873	8.914	9.598

Table 5.1(b): Quadratic coupling parameters (γ_i) of the Hamiltonian of the $\widetilde{X}$, $\widetilde{A}$, $\widetilde{B}$ and $\widetilde{C}$ electronic states of Pnt^+. All quantities are given in eV.

mode (frequency)	$\widetilde{X}^2B_1$	$\widetilde{A}^2A_2$	$\widetilde{B}^2A_2$	$\widetilde{C}^2B_1$
a_1 ν_1(0.3977)	0.0021	0.0024	0.0015	0.0014
ν_2(0.3951)	0.0028	0.0035	0.0024	0.0029
ν_3(0.3938)	0.0038	0.0025	0.0021	0.0022
ν_4(0.3930)	0.0043	0.0040	0.0036	0.0036
ν_5(0.3916)	0.0042	0.0044	0.0038	0.0038
ν_6(0.2064)	-0.0099	-0.0052	0.0073	-0.0029
ν_7(0.2045)	-0.0075	-0.0036	0.0069	0.0057
ν_8(0.1946)	-0.0034	-0.0075	0.0088	-0.0014
ν_9(0.1831)	0.0012	-0.0003	-0.0010	0.0037
ν_{10}(0.1805)	0.0052	0.0054	0.0117	0.0064
ν_{11}(0.1707)	0.0100	0.0122	0.0153	0.0107
ν_{12}(0.1647)	0.0044	0.0009	0.0061	0.0050
ν_{13}(0.1577)	0.0011	0.0039	0.0044	0.0012
ν_{14}(0.1522)	0.0067	0.0086	0.0123	0.0084
ν_{15}(0.1477)	0.0057	0.0044	0.0047	0.0035
ν_{16}(0.1460)	0.0106	0.0091	0.0104	0.0084
ν_{17}(0.1386)	0.0007	0.0021	-0.0008	-0.0005
ν_{18}(0.1320)	0.0016	0.0021	-0.0001	-0.0001
ν_{19}(0.1047)	-0.0008	-0.0023	-0.0001	-0.0001
ν_{20}(0.0898)	-0.0025	-0.0027	-0.0001	-0.0001
ν_{21}(0.0692)	-0.0021	-0.0013	-0.0007	0.0001
ν_{22}(0.0511)	0.0002	-0.0018	-0.0004	-0.0014
ν_{23}(0.0309)	-0.0010	-0.0020	-0.0027	-0.0022
a_2 ν_{24}(0.1210)	0.0095	0.0091	0.0086	0.0023
ν_{25}(0.1187)	0.0069	0.0073	0.0067	0.0060
ν_{26}(0.1149)	0.0096	0.0093	0.0057	0.0046
ν_{27}(0.1081)	0.0044	0.0039	0.0011	-0.0009
ν_{28}(0.0990)	-0.0040	0.0058	-0.0126	-0.0114
ν_{29}(0.0942)	0.0049	0.0008	0.0025	-0.0132
ν_{30}(0.0742)	-0.0114	-0.0140	-0.0148	-0.0154
ν_{31}(0.0671)	-0.0087	-0.0007	-0.0049	-0.0077
ν_{32}(0.0495)	-0.0101	-0.0027	-0.0161	-0.0132
ν_{33}(0.0301)	-0.0081	-0.0064	-0.0046	-0.0114

Continued on next page

Table 5.1(b) – *Continued from previous page*

	mode (frequency)	$\widetilde{X}^2B_1$	$\widetilde{A}^2A_2$	$\widetilde{B}^2A_2$	$\widetilde{C}^2B_1$
	$\nu_{34}(0.0117)$	-0.0048	-0.0094	0.0011	-0.0188
b_1	$\nu_{35}(0.1210)$	0.0088	0.0075	0.0051	0.0011
	$\nu_{36}(0.1169)$	0.0096	0.0089	0.0047	0.0022
	$\nu_{37}(0.1086)$	0.0077	0.0077	0.0016	0.0007
	$\nu_{38}(0.1017)$	0.0097	-0.0015	0.0033	-0.0031
	$\nu_{39}(0.0920)$	0.0025	0.0081	-0.0067	0.0014
	$\nu_{40}(0.0897)$	0.0042	-0.0074	-0.0157	-0.0214
	$\nu_{41}(0.0628)$	-0.0048	-0.0097	-0.0105	-0.0089
	$\nu_{42}(0.0541)$	-0.0048	-0.0100	-0.0117	-0.0130
	$\nu_{43}(0.0284)$	0.0021	-0.0052	-0.0103	-0.0048
	$\nu_{44}(0.0124)$	-0.0079	0.0020	-0.0148	-0.0009
b_2	$\nu_{45}(0.3960)$	0.0029	0.0028	0.0022	0.0016
	$\nu_{46}(0.3947)$	0.0029	0.0039	0.0027	0.0029
	$\nu_{47}(0.3928)$	0.0039	0.0039	0.0037	0.0033
	$\nu_{48}(0.3917)$	0.0041	0.0043	0.0037	0.0037
	$\nu_{49}(0.3911)$	0.0044	0.0040	0.0034	0.0034
	$\nu_{50}(0.2059)$	-0.0216	-0.0007	0.0148	0.0174
	$\nu_{51}(0.1999)$	-0.0379	0.0462	-0.0215	0.0262
	$\nu_{52}(0.1912)$	-0.0085	0.0024	-0.0089	0.0053
	$\nu_{53}(0.1857)$	-0.0051	0.0056	0.0021	-0.0039
	$\nu_{54}(0.1800)$	0.0014	0.0011	-0.0008	0.0028
	$\nu_{55}(0.1699)$	-0.0089	0.0392	0.0220	0.0243
	$\nu_{56}(0.1624)$	0.0015	0.0013	0.0023	0.0037
	$\nu_{57}(0.1545)$	-0.0047	0.0048	0.0021	0.0073
	$\nu_{58}(0.1480)$	-0.0070	0.0172	0.0044	0.0079
	$\nu_{59}(0.1449)$	-0.0001	0.0030	0.0026	0.0024
	$\nu_{60}(0.1319)$	0.0011	-0.0006	-0.0008	0.0003
	$\nu_{61}(0.1263)$	-0.0037	-0.0006	0.0004	0.0034
	$\nu_{62}(0.1103)$	-0.0072	0.0020	-0.0004	0.0010
	$\nu_{63}(0.0903)$	-0.0018	-0.0017	-0.0031	0.0003
	$\nu_{64}(0.0786)$	-0.0097	0.0037	-0.0070	0.0041
	$\nu_{65}(0.0628)$	-0.0061	0.0018	-0.0028	0.0041
	$\nu_{66}(0.0554)$	-0.0044	0.0011	-0.0012	0.0003

Table 5.1(c): *Ab initio* calculated Interstate coupling parameters of the Hamiltonian of Pnt^+ along the coupling vibrational modes. The dimensionless coupling strength ($\lambda_i^2/2\omega^2$), are given in the parentheses. All quantities are given in eV.

mode	λ^{j-k}	λ^{j-k}	λ^{j-k}	λ^{j-k}
b_2	$j-k \in \widetilde{X}$-$\widetilde{A}$	$j-k \in \widetilde{X}$-$\widetilde{B}$	$j-k \in \widetilde{A}$-$\widetilde{C}$	$j-k \in \widetilde{B}$-$\widetilde{C}$
ν_{45}	-	-	-	-
ν_{46}	0.0084 (0.0001)	-	-	0.0054 (0.0001)
ν_{47}	-	-	-	-
ν_{48}	0.0037 (0.0001)	-	-	-
ν_{49}	-	-	-	0.0011 (0.0001)
ν_{50}	0.0409 (0.0197)	0.1158 (0.1581)	0.0923 (0.1005)	0.0226 (0.0060)
ν_{51}	0.1044 (0.1364)	0.1054 (0.1390)	-	0.1009 (0.1274)
ν_{52}	0.0285 (0.0111)	-	0.0351 (0.0168)	0.0511 (0.0357)
ν_{53}	0.0284 (0.0117)	0.0503 (0.0367)	-	-
ν_{54}	-	-	0.0278 (0.0119)	0.0250 (0.0096)
ν_{55}	0.0660 (0.0754)	0.1010 (0.1767)	-	0.0189 (0.0062)
ν_{56}	-	0.0173 (0.0057)	0.0335 (0.0213)	0.0146 (0.0040)
ν_{57}	0.0266 (0.0148)	0.0482 (0.0487)	0.0305 (0.0195)	0.0301 (0.0190)
ν_{58}	0.0462 (0.0487)	0.0671 (0.1028)	-	0.0243 (0.0135)
ν_{59}	0.0145 (0.0050)	0.0301 (0.0216)	-	-
ν_{60}	-	-	0.0183 (0.0096)	0.0126 (0.0046)
ν_{61}	0.0147 (0.0068)	0.0376 (0.0443)	0.0417 (0.0545)	0.0225 (0.0159)
ν_{62}	0.0259 (0.0275)	0.0485 (0.0967)	-	0.0154 (0.0097)
ν_{63}	-	-	0.0298 (0.0544)	0.0240 (0.0353)
ν_{64}	0.0323 (0.0844)	0.0326 (0.0860)	-	0.0448 (0.1624)
ν_{65}	0.0242 (0.0742)	0.0343 (0.1491)	0.0304 (0.1172)	0.0349 (0.1544)
ν_{66}	0.0195 (0.0619)	0.0331 (0.1784)	-	0.0152 (0.0376)

Table 5.2(a): Same as in Table 5.1(a) for Py^+.

mode	$\widetilde{X}^2B_{1g}$	$\widetilde{A}^2B_{2g}$	$\widetilde{B}^2B_{3u}$	$\widetilde{C}^2A_u$
a_g ν_1	0.0175 (0.0010)	0.0187 (0.0011)	0.0139 (0.0006)	0.0170 (0.0009)
ν_2	-0.0068 (0.0001)	-0.0124 (0.0005)	-0.0060 (0.0001)	-0.0070 (0.0001)
ν_3	0.0007 (0.0001)	-0.0078 (0.0002)	-0.0022 (0.0001)	-0.0015 (0.0001)
ν_4	0.1509 (0.2642)	-0.1219 (0.1724)	0.1212 (0.1704)	0.0380 (0.0167)
ν_5	-0.0042 (0.0002)	0.0703 (0.0626)	0.0646 (0.0529)	-0.0937 (0.1113)
ν_6	-0.0670 (0.0715)	-0.0677 (0.0731)	0.0033 (0.0002)	0.0203 (0.0066)
ν_7	0.0117 (0.0024)	-0.0106 (0.0020)	-0.0970 (0.1667)	0.1019 (0.1839)
ν_8	0.1064 (0.2299)	0.0179 (0.0065)	-0.0250 (0.0127)	0.0287 (0.0167)
ν_9	-0.0230 (0.0125)	0.0327 (0.0252)	-0.0240 (0.0136)	-0.0171 (0.0069)
ν_{10}	-0.0123 (0.0041)	-0.0479 (0.0624)	0.0273 (0.0203)	-0.0121 (0.0040)

Continued on next page

Table 5.2(a) – *Continued from previous page*

mode	$\widetilde{X}^2B_{1g}$	$\widetilde{A}^2B_{2g}$	$\widetilde{B}^2B_{3u}$	$\widetilde{C}^2A_u$
ν_{11}	0.0160 (0.0125)	-0.0306 (0.0457)	-0.0508 (0.1260)	0.0456 (0.1015)
ν_{12}	0.0194 (0.0345)	-0.0509 (0.2378)	-0.0245 (0.0551)	-0.0402 (0.1483)
ν_{13}	-0.0216 (0.0893)	0.0639 (0.7818)	-0.0597 (0.6824)	-0.0276 (0.1459)
VIE	7.068	7.953	8.728	9.116

Table 5.2(b): Same as in Table 5.1(b) for Py^+.

mode (frequency)	$\widetilde{X}^2B_{1g}$	$\widetilde{A}^2B_{2g}$	$\widetilde{B}^2B_{3u}$	$\widetilde{C}^2A_u$
a_g ν_1(0.3949)	0.0025	0.0032	0.0023	0.0022
ν_2(0.3937)	0.0029	0.0026	0.0031	0.0021
ν_3(0.3916)	0.0044	0.0044	0.0038	0.0038
ν_4(0.2076)	0.0043	-0.0018	0.0022	0.0011
ν_5(0.1986)	-0.0005	-0.0027	0.0017	0.0030
ν_6(0.1771)	-0.0003	0.0023	0.0061	0.0010
ν_7(0.1680)	0.0010	0.0042	-0.0027	0.0026
ν_8(0.1569)	-0.0004	0.0068	0.0070	0.0048
ν_9(0.1455)	0.0041	0.0037	0.0008	0.0030
ν_{10}(0.1356)	0.0002	0.0021	0.0016	0.0001
ν_{11}(0.1012)	0.0001	-0.0019	-0.0015	-0.0008
ν_{12}(0.0738)	-0.0008	0.0009	-0.0010	0.0001
ν_{13}(0.0511)	0.0010	-0.0012	0.0001	-0.0006
a_u ν_{14}(0.1190)	0.0084	0.0087	-0.0024	0.0086
ν_{15}(0.1099)	0.0139	0.0065	0.0064	0.0038
ν_{16}(0.0850)	0.0007	0.0011	-0.0300	-0.0070
ν_{17}(0.0498)	-0.0064	-0.0042	-0.0103	-0.0157
ν_{18}(0.0189)	-0.0043	-0.0082	-0.0109	-0.0012
b_{1g} ν_{19}(0.1120)	0.0133	0.0070	0.0083	0.0048
ν_{20}(0.1000)	0.0095	0.0022	0.0067	0.0025
ν_{21}(0.0666)	0.0012	-0.0019	-0.0108	-0.0072
ν_{22}(0.0309)	0.0014	-0.0078	-0.0046	-0.0111
b_{1u} ν_{23}(0.3948)	0.0028	0.0035	0.0025	0.0024
ν_{24}(0.3917)	0.0041	0.0042	0.0037	0.0037
ν_{25}(0.3912)	0.0040	0.0039	0.0037	0.0034
ν_{26}(0.2033)	-0.0079	-0.0138	-0.0001	0.0161
ν_{27}(0.1845)	-0.0009	-0.0101	0.0112	-0.0066
ν_{28}(0.1816)	0.0017	-0.0075	0.0089	0.0027
ν_{29}(0.1578)	-0.0018	-0.0014	0.0050	0.0078

Continued on next page

Table 5.2(b) – *Continued from previous page*

mode	(frequency)	$\widetilde{X}^2B_{1g}$	$\widetilde{A}^2B_{2g}$	$\widetilde{B}^2B_{3u}$	$\widetilde{C}^2A_u$
	$\nu_{30}(0.1385)$	0.0013	-0.0010	0.0023	0.0012
	$\nu_{31}(0.1259)$	-0.0009	-0.0042	0.0029	0.0008
	$\nu_{32}(0.1037)$	-0.0043	-0.0030	-0.0020	0.0002
	$\nu_{33}(0.0874)$	-0.0010	-0.0050	0.0016	-0.0023
	$\nu_{34}(0.0630)$	-0.0010	-0.0023	-0.0006	-0.0004
b_{2g}	$\nu_{35}(0.1207)$	0.0102	0.0087	0.0105	0.0096
	$\nu_{36}(0.1183)$	0.0089	0.0079	0.0093	0.0082
	$\nu_{37}(0.1050)$	0.0015	-0.0019	-0.0051	-0.0026
	$\nu_{38}(0.0965)$	-0.0005	0.0088	0.0047	-0.0074
	$\nu_{39}(0.0725)$	-0.0068	-0.0178	-0.0053	-0.0155
	$\nu_{40}(0.0636)$	-0.0066	-0.0017	-0.0164	-0.0063
	$\nu_{41}(0.0325)$	-0.0060	-0.0050	-0.0080	-0.0039
b_{2u}	$\nu_{42}(0.3937)$	0.0030	0.0025	0.0029	0.0021
	$\nu_{43}(0.3926)$	0.0040	0.0034	0.0029	0.0031
	$\nu_{44}(0.2046)$	-0.0112	-0.0081	0.0019	0.0106
	$\nu_{45}(0.1884)$	-0.0136	0.0051	0.0195	0.0008
	$\nu_{46}(0.1814)$	-0.0040	0.0055	0.0065	0.0041
	$\nu_{47}(0.1668)$	0.0229	0.0210	0.0056	0.0239
	$\nu_{48}(0.1531)$	0.0045	0.0031	0.0005	0.0050
	$\nu_{49}(0.1501)$	0.0040	0.0018	0.0033	0.0089
	$\nu_{50}(0.1450)$	0.0116	0.0124	0.0054	0.0120
	$\nu_{51}(0.1217)$	0.0010	-0.0021	-0.0004	0.0037
	$\nu_{52}(0.0688)$	-0.0045	-0.0014	0.0034	-0.0007
	$\nu_{53}(0.0446)$	-0.0024	-0.0003	0.0001	-0.0020
b_{3g}	$\nu_{54}(0.3928)$	0.0039	0.0033	0.0027	0.0032
	$\nu_{55}(0.3913)$	0.0038	0.0037	0.0037	0.0033
	$\nu_{56}(0.2019)$	-0.0239	0.0338	-0.0328	0.0290
	$\nu_{57}(0.1911)$	-0.0031	-0.0003	-0.0048	-0.0142
	$\nu_{58}(0.1788)$	0.0029	0.0039	0.0019	0.0009
	$\nu_{59}(0.1738)$	-0.0019	0.0380	-0.0212	0.0374
	$\nu_{60}(0.1573)$	0.0007	0.0041	0.0020	0.0011
	$\nu_{61}(0.1491)$	0.0003	0.0064	0.0026	-0.0045
	$\nu_{62}(0.1400)$	-0.0008	0.0040	-0.0044	0.0025
	$\nu_{63}(0.0931)$	-0.0010	-0.0011	-0.0030	0.0002
	$\nu_{64}(0.0632)$	-0.0040	0.0029	-0.0063	0.0020
	$\nu_{65}(0.0574)$	-0.0022	0.0009	-0.0154	0.0131
b_{3u}	$\nu_{66}(0.1194)$	0.0102	0.0106	0.0086	0.0088
	$\nu_{67}(0.1060)$	0.0072	0.0048	0.0057	0.0026
	$\nu_{68}(0.0930)$	0.0068	0.0071	0.0065	-0.0027
	$\nu_{69}(0.0897)$	-0.0016	-0.0016	-0.0043	-0.0238

Continued on next page

Table 5.2(b) – *Continued from previous page*

mode (frequency)	$\widetilde{X}^2B_{1g}$	$\widetilde{A}^2B_{2g}$	$\widetilde{B}^2B_{3u}$	$\widetilde{C}^2A_u$
$\nu_{70}(0.0619)$	-0.0039	-0.0156	-0.0032	-0.0091
$\nu_{71}(0.0265)$	0.0009	-0.0018	0.0023	-0.0085
$\nu_{72}(0.0122)$	-0.0043	0.0004	-0.0001	-0.0124

Table 5.2(c): Same as in Table 5.1(c) for Py^+.

mode	λ^{j-k}	λ^{j-k}	mode	λ^{j-k}	λ^{j-k}	mode	λ^{j-k}	λ^{j-k}
b_{1u}	$j-k \in \widetilde{X}$-$\widetilde{C}$	$j-k \in \widetilde{A}$-$\widetilde{B}$	b_{2u}	$j-k \in \widetilde{X}$-$\widetilde{B}$	$j-k \in \widetilde{A}$-$\widetilde{C}$	b_{3g}	$j-k \in \widetilde{X}$-$\widetilde{A}$	$j-k \in \widetilde{B}$-$\widetilde{C}$
ν_{23}	-	-	ν_{42}	-	-	ν_{54}	-	0.0058 (0.0001)
ν_{24}	-	-	ν_{43}	-	-	ν_{55}	-	-
ν_{25}	-	-	ν_{44}	0.0749 (0.0670)	0.0760 (0.0690)	ν_{56}	0.1132 (0.1572)	0.0985 (0.1190)
ν_{26}	0.1131 (0.1547)	0.0532 (0.0342)	ν_{45}	0.1216 (0.2083)	-	ν_{57}	0.0249 (0.0085)	-
ν_{27}	-	0.0677 (0.0673)	ν_{46}	0.0678 (0.0698)	-	ν_{58}	0.0135 (0.0028)	-
ν_{28}	0.0228 (0.0079)	0.0589 (0.0526)	ν_{47}	-	0.0350 (0.0220)	ν_{59}	0.0842 (0.1173)	0.0857 (0.1216)
ν_{29}	0.0711 (0.1015)	0.0360 (0.0260)	ν_{48}	-	0.0232 (0.0115)	ν_{60}	0.0273 (0.0151)	-
ν_{30}	-	0.0260 (0.0176)	ν_{49}	-	0.0460 (0.0469)	ν_{61}	0.0371 (0.0309)	-
ν_{31}	0.0295 (0.0274)	0.0379 (0.0453)	ν_{50}	-	-	ν_{62}	0.0324 (0.0268)	0.0265 (0.0179)
ν_{32}	0.0488 (0.1107)	0.0152 (0.0107)	ν_{51}	-	0.0417 (0.0587)	ν_{63}	-	0.0179 (0.0184)
ν_{33}	-	0.0366 (0.0877)	ν_{52}	0.0579 (0.3541)	0.0146 (0.0225)	ν_{64}	0.0393 (0.1933)	0.0296 (0.1097)
ν_{34}	0.0160 (0.0322)	0.0186 (0.0436)	ν_{53}	0.0326 (0.2671)	-	ν_{65}	0.0262 (0.1042)	0.0592 (0.5318)

Table 5.3(a): Same as in Table 5.1(a) for Acn^+.

mode	$\widetilde{X}^2A_2$	$\widetilde{A}^2B_1$	$\widetilde{B}^2B_1$	$\widetilde{C}^2A_2$
a_g ν_1	0.0177 (0.0010)	0.0218 (0.0015)	0.0173 (0.0010)	0.0319 (0.0033)
ν_2	0.0053 (0.0001)	-0.0012 (0.0001)	0.0065 (0.0001)	0.0053 (0.0001)
ν_3	-0.0032 (0.0001)	-0.0072 (0.0002)	-0.0029 (0.0001)	-0.0055 (0.0001)
ν_4	0.0060 (0.0001)	-0.0115 (0.0004)	0.0070 (0.0002)	0.0234 (0.0019)
ν_5	0.0930 (0.1042)	-0.0437 (0.0230)	0.0666 (0.0534)	0.0112 (0.0015)
ν_6	-0.1012 (0.1238)	0.1029 (0.1280)	-0.1186 (0.1700)	-0.0243 (0.0071)
ν_7	-0.0393 (0.0220)	0.0061 (0.0005)	-0.0184 (0.0048)	-0.0643 (0.0589)
ν_8	0.0978 (0.1441)	0.0221 (0.0073)	-0.0507 (0.0387)	0.1139 (0.1954)
ν_9	0.0986 (0.1495)	-0.0191 (0.0056)	-0.0262 (0.0105)	0.0034 (0.0002)
ν_{10}	-0.0953 (0.1514)	-0.0270 (0.0121)	0.0224 (0.0084)	-0.0207 (0.0071)
ν_{11}	0.0005 (0.0001)	-0.0276 (0.0150)	-0.0012 (0.0001)	-0.0337 (0.0223)
ν_{12}	0.0406 (0.0341)	0.0336 (0.0234)	0.0345 (0.0246)	0.0493 (0.0503)
ν_{13}	0.0466 (0.0489)	-0.0607 (0.0830)	0.0217 (0.0106)	-0.0094 (0.0020)
ν_{14}	-0.0131 (0.0049)	0.0670 (0.1282)	-0.0086 (0.0021)	0.1157 (0.3824)
ν_{15}	0.0016 (0.0001)	0.0496 (0.0777)	0.0391 (0.0483)	0.0335 (0.0354)
ν_{16}	-0.0053 (0.0010)	-0.0180 (0.0117)	0.0051 (0.0009)	-0.0394 (0.0560)
ν_{17}	-0.0039 (0.0007)	-0.0289 (0.0407)	-0.0162 (0.0128)	-0.0216 (0.0227)
ν_{18}	0.0047 (0.0017)	-0.0376 (0.1107)	-0.0509 (0.2029)	-0.0326 (0.0832)
ν_{19}	-0.0150 (0.0239)	0.0595 (0.3761)	-0.0630 (0.4217)	0.0065 (0.0045)
ν_{20}	0.0121 (0.0265)	-0.0331 (0.1987)	0.0445 (0.3592)	-0.0041 (0.0030)

Continued on next page

Table 5.3(a) – *Continued from previous page*

mode	$\widetilde{X}^2A_2$	$\widetilde{A}^2B_1$	$\widetilde{B}^2B_1$	$\widetilde{C}^2A_2$
VIE	7.405	8.341	9.368	10.595

Table 5.3(b): Same as in Table 5.1(b) for Acn^+.

mode (frequency)	$\widetilde{X}^2A_2$	$\widetilde{A}^2B_1$	$\widetilde{B}^2B_1$	$\widetilde{C}^2A_2$
a_1 ν_1 (0.3944)	0.0033	0.0037	0.0026	0.0027
ν_2 (0.3926)	0.0043	0.0042	0.0035	0.0034
ν_3 (0.3912)	0.0052	0.0054	0.0045	0.0044
ν_4 (0.3778)	0.0008	0.0018	0.0001	-0.0052
ν_5 (0.2037)	-0.0029	-0.0124	0.0179	0.0114
ν_6 (0.2034)	-0.0001	0.0018	0.0129	0.0069
ν_7 (0.1873)	-0.0101	-0.0005	-0.0092	-0.0247
ν_8 (0.1822)	0.0036	0.0009	0.0113	0.0012
ν_9 (0.1803)	0.0025	0.0116	0.0063	0.0075
ν_{10} (0.1732)	0.0025	0.0080	0.0112	0.0047
ν_{11} (0.1594)	0.0007	0.0014	0.0014	0.0007
ν_{12} (0.1554)	-0.0014	0.0042	0.0012	-0.0035
ν_{13} (0.1490)	0.0036	0.0058	0.0049	0.0066
ν_{14} (0.1323)	-0.0004	0.0041	0.0005	0.0054
ν_{15} (0.1258)	-0.0027	0.0001	-0.0022	-0.0009
ν_{16} (0.1177)	-0.0010	0.0010	0.0017	-0.0027
ν_{17} (0.1013)	0.0014	-0.0086	0.0044	-0.0017
ν_{18} (0.0799)	-0.0016	-0.0004	-0.0002	-0.0013
ν_{19} (0.0686)	-0.0021	-0.0003	-0.0009	-0.0017
ν_{20} (0.0525)	-0.0037	0.0001	-0.0025	-0.0028
a_2 ν_{21} (0.3790)	0.0052	0.0044	0.0014	0.0012
ν_{22} (0.1556)	-0.0095	0.0021	0.0001	-0.0585
ν_{23} (0.1276)	-0.0087	0.0016	-0.0129	-0.0261
ν_{24} (0.1187)	0.0110	0.0085	0.0077	-0.0330
ν_{25} (0.1086)	0.0125	0.0035	0.0052	-0.0353
ν_{26} (0.0937)	0.0072	0.0041	-0.0029	-0.0028
ν_{27} (0.0781)	-0.0073	-0.0292	-0.0130	-0.0208
ν_{28} (0.0553)	-0.0061	-0.0098	-0.0130	-0.0148
ν_{29} (0.0292)	0.0041	-0.0128	-0.0094	-0.0124
ν_{30} (0.0105)	0.0095	0.0050	-0.0131	0.0003
b_1 ν_{31} (0.3816)	0.0029	0.0033	0.0014	-0.0027
ν_{32} (0.1469)	-0.0010	0.0047	-0.0101	-0.0184
ν_{33} (0.1199)	0.0111	0.0073	0.0038	-0.0405
ν_{34} (0.1116)	0.0126	0.0067	0.0065	-0.0422

Continued on next page

Table 5.3(b) – *Continued from previous page*

mode (frequency)	$\widetilde{X}^2A_2$	$\widetilde{A}^2B_1$	$\widetilde{B}^2B_1$	$\widetilde{C}^2A_2$
ν_{35} (0.1062)	0.0012	0.0001	-0.0044	-0.0219
ν_{36} (0.0987)	-0.0015	0.0068	-0.0033	-0.0174
ν_{37} (0.0952)	-0.0077	0.0007	-0.0318	-0.0193
ν_{38} (0.0700)	-0.0095	0.0005	-0.0174	-0.0092
ν_{39} (0.0588)	-0.0044	-0.0224	-0.0083	-0.0248
ν_{40} (0.0272)	0.0006	-0.0012	-0.0056	-0.0053
ν_{41} (0.0204)	-0.0149	0.0010	-0.0118	-0.0129
b_2 ν_{42} (0.3942)	0.0038	0.0039	0.0028	0.0030
ν_{43} (0.3924)	0.0046	0.0043	0.0038	0.0036
ν_{44} (0.3911)	0.0053	0.0054	0.0045	0.0045
ν_{45} (0.3764)	0.0030	0.0030	-0.0005	0.0012
ν_{46} (0.2061)	-0.0364	0.0480	0.0035	0.0038
ν_{47} (0.1907)	-0.0118	-0.0040	0.0106	0.0119
ν_{48} (0.1870)	-0.0035	0.0010	-0.0074	0.0125
ν_{49} (0.1839)	-0.0131	0.0001	-0.0104	-0.0122
ν_{50} (0.1725)	0.0139	0.0153	0.0151	0.0122
ν_{51} (0.1629)	0.0028	0.0097	0.0075	0.0034
ν_{52} (0.1552)	0.0067	0.0118	0.0136	0.0032
ν_{53} (0.1537)	0.0001	0.0014	-0.0007	0.0074
ν_{54} (0.1464)	0.0046	0.0183	0.0064	0.0153
ν_{55} (0.1375)	-0.0010	-0.0003	-0.0026	0.0016
ν_{56} (0.1289)	0.0015	0.0040	0.0008	0.0026
ν_{57} (0.1042)	-0.0028	0.0001	-0.0048	-0.0014
ν_{58} (0.0828)	-0.0035	0.0005	0.0008	-0.0003
ν_{59} (0.0634)	-0.0084	0.0064	-0.0015	-0.0001
ν_{60} (0.0561)	-0.0021	-0.0005	-0.0006	-0.0005

Table 5.3(c): Same as in Table 5.1(c) for Acn^+.

mode	λ^{j-k}	λ^{j-k}	λ^{j-k}	λ^{j-k}
b_2	$j-k \in \widetilde{X}$-$\widetilde{A}$	$j-k \in \widetilde{X}$-$\widetilde{B}$	$j-k \in \widetilde{A}$-$\widetilde{C}$	$j-k \in \widetilde{B}$-$\widetilde{C}$
ν_{42}	-	-	-	0.0093 (0.0003)
ν_{43}	-	-	-	-
ν_{44}	-	-	-	-
ν_{45}	-	-	-	0.0228 (0.0018)
ν_{46}	0.1522 (0.2727)	0.1527 (0.2745)	-	0.0095 (0.0011)
ν_{47}	0.0444 (0.0271)	0.1068 (0.1568)	0.0948 (0.1236)	0.0195 (0.0052)
ν_{48}	0.0328 (0.0154)	-	0.0824 (0.0971)	0.0809 (0.0936)
ν_{49}	0.0535 (0.0423)	0.0329 (0.0160)	-	-
ν_{50}	0.0186 (0.0058)	0.0261 (0.0114)	-	-

Continued on next page

Table 5.3(c) – *Continued from previous page*

mode	λ^{j-k}	λ^{j-k}	λ^{j-k}	λ^{j-k}
ν_{51}	0.0403 (0.0306)	0.0492 (0.0456)	-	-
ν_{52}	0.0345 (0.0247)	0.0568 (0.0670)	-	-
ν_{53}	0.0185 (0.0072)	-	0.0586 (0.0727)	0.0508 (0.0546)
ν_{54}	0.0581 (0.0787)	0.0294 (0.0202)	-	0.0530 (0.0655)
ν_{55}	0.0117 (0.0036)	-	0.0333 (0.0293)	0.0364 (0.0350)
ν_{56}	0.0247 (0.0183)	-	-	0.0247 (0.0183)
ν_{57}	0.0260 (0.0311)	-	-	0.0330 (0.0501)
ν_{58}	0.0308 (0.0692)	0.0453 (0.1496)	-	-
ν_{59}	0.0603 (0.4523)	0.0587 (0.4286)	-	0.0219 (0.0596)
ν_{60}	0.0193 (0.0592)	0.0252 (0.1009)	0.0038 (0.0023)	0.0077 (0.0094)

5.3 Results and discussion

5.3.1 Potential energy surface of electronic ground and excited states

In this section, the topography of the electronic states of Pnt^+, Py^+ and Acn^+ is investigated to evaluate the critical points such as energetic minimum of CIs and the equilibrium minimum of a state. These data facilitate to interpret the nuclear dynamics results presented and discussed in the next sections. The adiabatic PESs are obtained by diagonalization of the respective diabatic electronic Hamiltonian of Eq. 5.1. One dimensional cuts of adiabatic potential energies of $\widetilde{X}$, $\widetilde{A}$, $\widetilde{B}$ and $\widetilde{C}$ electronic states along one of the C=C stretching vibration are shown in Fig. 5.1 for Pnt^+ (panel a and b), Py^+ (panel c, d and e) and Acn^+ (panel f). In each panel the potential energy values obtained from the present vibronic model (developed in Sec. 5.2.1) and *ab initio* electronic structure calculations are shown by the solid lines and points, respectively. It can be seen from Fig. 5.1 that the computed *ab initio* energies are in excellent agreement with those obtained from the constructed vibronic model.

Examination of one dimensional cuts of the multidimensional PESs of radical cations reveals low-energy crossings of the electronic states. In case of Pnt^+, the quasi-degenerate inter-ring C=C stretching vibrations ν_6 and ν_7 ($\sim$1665 cm^{-1} and $\sim$1649 cm^{-1}, respectively) leads to the crossing between its $\widetilde{X}$ and $\widetilde{A}$ electronic states. In Py^+ three inter-ring C=C stretching vibrational modes ν_4, ν_5 and ν_7 ($\sim$1674, $\sim$1601 and $\sim$1355 cm^{-1}) are important for this curve crossings. This situation is analogous in Pnt^+, in this case the former two vibrations are quasi-degenerate. In case of Acn^+, only one C=C stretching vibrational mode ν_6 ($\sim$1640 cm^{-1}) causes curve crossings at larger displacements. These crossings develop into CIs of electronic PESs in multi-dimensions.

The energetic minimum of multidimensional seam of conical intersections is calculated for all three radical cations in order to assess their accessibility during the nuclear motion on a given electronic state of these radical cations. The vertical energy gap between $\widetilde{X}$-$\widetilde{A}$, $\widetilde{A}$-$\widetilde{B}$ and $\widetilde{B}$-$\widetilde{C}$ states occurs ∼0.26, ∼1.04 and ∼0.68 eV; ∼0.88, ∼0.77 and ∼0.39 eV; ∼0.94, ∼1.03 and ∼1.23 eV (in that order) in Pnt^+, Py^+ and Acn^+, respectively. The energetic minimum of the $\widetilde{A}$, $\widetilde{B}$ and $\widetilde{C}$ electronic states of Pnt^+, Py^+ and Acn^+ are 7.72, 8.83 and 9.49 eV; 7.81, 8.60 and 9.02 eV and 8.21, 9.23 and 10.46 eV, respectively. The energetic minimum of $\widetilde{X}$-$\widetilde{A}$, $\widetilde{X}$-$\widetilde{B}$, $\widetilde{X}$-$\widetilde{C}$, $\widetilde{A}$-$\widetilde{B}$, $\widetilde{A}$-$\widetilde{C}$ and $\widetilde{B}$-$\widetilde{C}$ conical intersections is located at ∼7.73, ∼10.74, ∼11.91, ∼9.33, ∼12.46 and ∼9.66 eV, respectively, in Pnt^+. These seam minimum energy points are located at ∼8.00, ∼11.71, ∼15.40, ∼8.71, ∼9.66 and ∼9.05 eV in Py^+ and at ∼8.44, ∼13.11, ∼23.53, ∼9.49, ∼18.59 and ∼11.40 eV in Acn^+ in that order, respectively. It should be noted that the energy gap between minimum of $\widetilde{A}$ and $\widetilde{X}$-$\widetilde{A}$ conical intersection of Pnt^+, Py^+ and Acn^+ are ∼0.01, ∼0.19 and ∼0.23 eV, respectively, and these energy separations are more likely to play a decisive role in the nonradiative internal conversion dynamics.

5.3.2 Vibronic structure of the electronic ground and excited states vs photoelectron spectroscopy measurements

In this section, a detailed study of the vibronic structures of the $\widetilde{X}$, $\widetilde{A}$, $\widetilde{B}$ and $\widetilde{C}$ electronic states of all three viz., Pnt^+, Py^+ and Acn^+ radical cations is presented, and the findings are compared with the experimental low-resolution photoelectron spectroscopy measurements. The relevant vibrational modes and corresponding linear and quadratic coupling parameters required to describe the nuclear dynamics in the coupled $\widetilde{X}$-$\widetilde{A}$-$\widetilde{B}$-$\widetilde{C}$ electronic states of Pnt^+, Py^+ and Acn^+ are given in Tables a, b, c of 5.1, 5.2 and 5.3. Based on coupling strength, only 20, 22 and 24 vibrational modes of Pnt^+, Py^+ and Acn^+, respectively, are selected for quantum nuclear dynamics study.

Prior to time-dependent dynamics, reduced-dimensional calculations within time-independent approach are also performed to explore the vibronic structures of radical cations. This exercise allowed to interpret the spectral progressions and relative contributions of various vibrational modes in the broad band structure measured in the photoelectron spectroscopy experiments. The uncoupled state spectra are calculated by diagonalizing the corresponding Hamiltonian for all three radical cations in a harmonic oscillator basis of the vibrational modes of the reference state, shown in panel a, b and c of Fig. 5.2 for Pnt^+, Py^+ and Acn^+, respectively, in that order. It is found that the C=C stretching vibrations primarily form dominant progressions in the uncoupled state spectrum of Pnt^+, Py^+ and Acn^+. In Pnt^+, peak spacings of ∼0.030, ∼0.051, ∼0.068, ∼0.176 and ∼0.201 eV corresponding to symmetric vibrational modes ν_{23}, ν_{22}, ν_{21}, ν_{11} and ν_6, respectively, are found in the $\widetilde{X}$ state. Peak spacings of ∼0.030, ∼0.050, ∼0.068, ∼0.088, ∼0.177, ∼0.203 and ∼0.204 eV corresponding to ν_{23}, ν_{22}, ν_{21}, ν_{20}, ν_{11}, ν_7 and ν_6 vibrational modes, respectively, are found in the $\widetilde{A}$ state. The vibrational modes ν_{22}, ν_{19}, ν_{13} and ν_7 form dominant progressions in the $\widetilde{B}$ state and the peaks

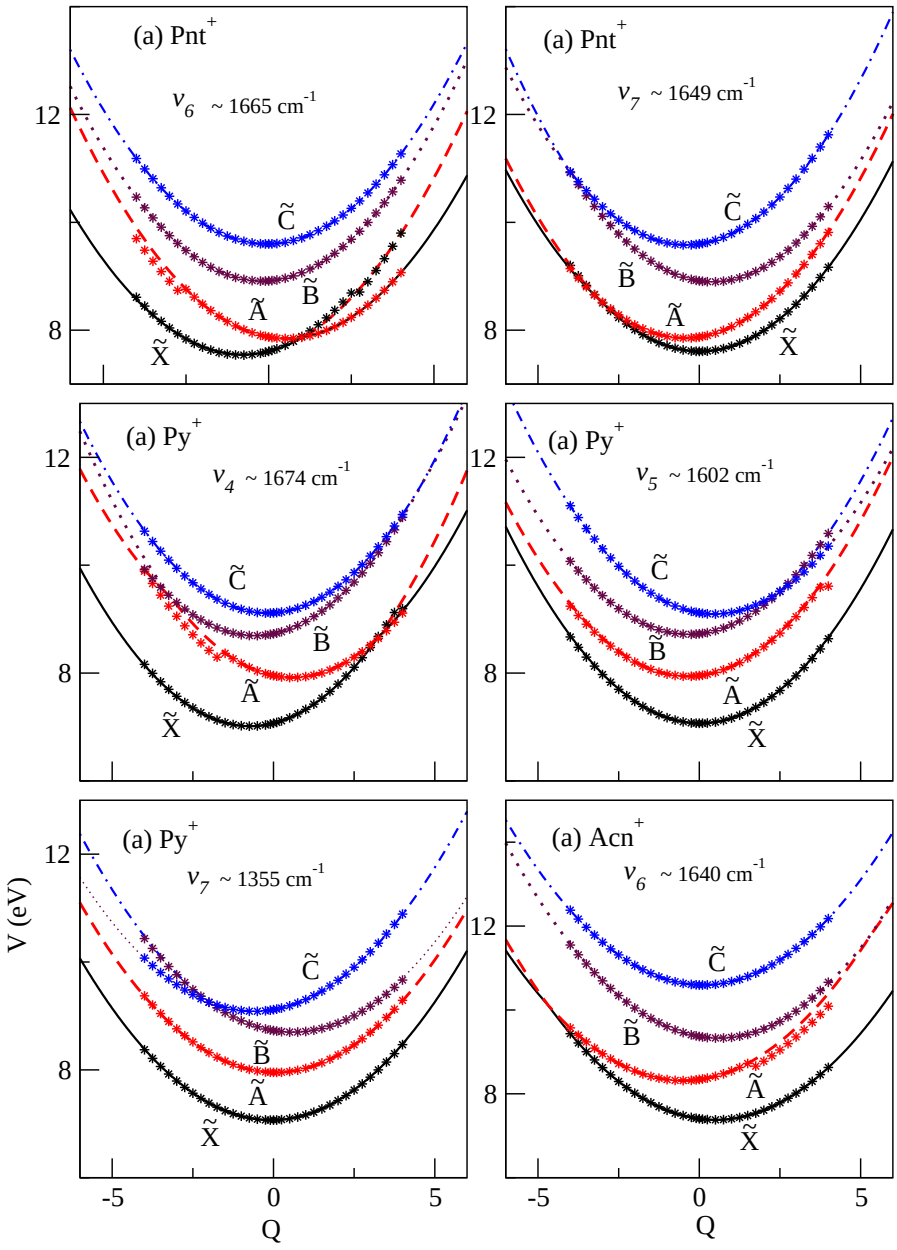

Figure 5.1: Adiabatic energies of the $\widetilde{X}$, $\widetilde{A}$, $\widetilde{B}$ and $\widetilde{C}$ electronic states of Pnt^+ (panel a and b), Py^+ (panel c, d and e) and Acn^+ (panel f) plotted along the dimensionless normal displacement coordinate. The electronic energies obtained from the present vibronic model and quantum chemistry calculations are shown by lines and points, respectively. For ready reference, the mode number and its harmonic frequency of the reference state is included in each panel.

are ∼0.051, ∼0.105, ∼0.160, and ∼0.208 eV spaced, respectively. In the $\widetilde{C}$ state ν_{22}, ν_{21}, ν_{20}, ν_{12} and ν_7 vibrational modes form progressions with peak spacing of ∼0.050, ∼0.069, ∼0.090, ∼0.167 and ∼0.207 eV, respectively.

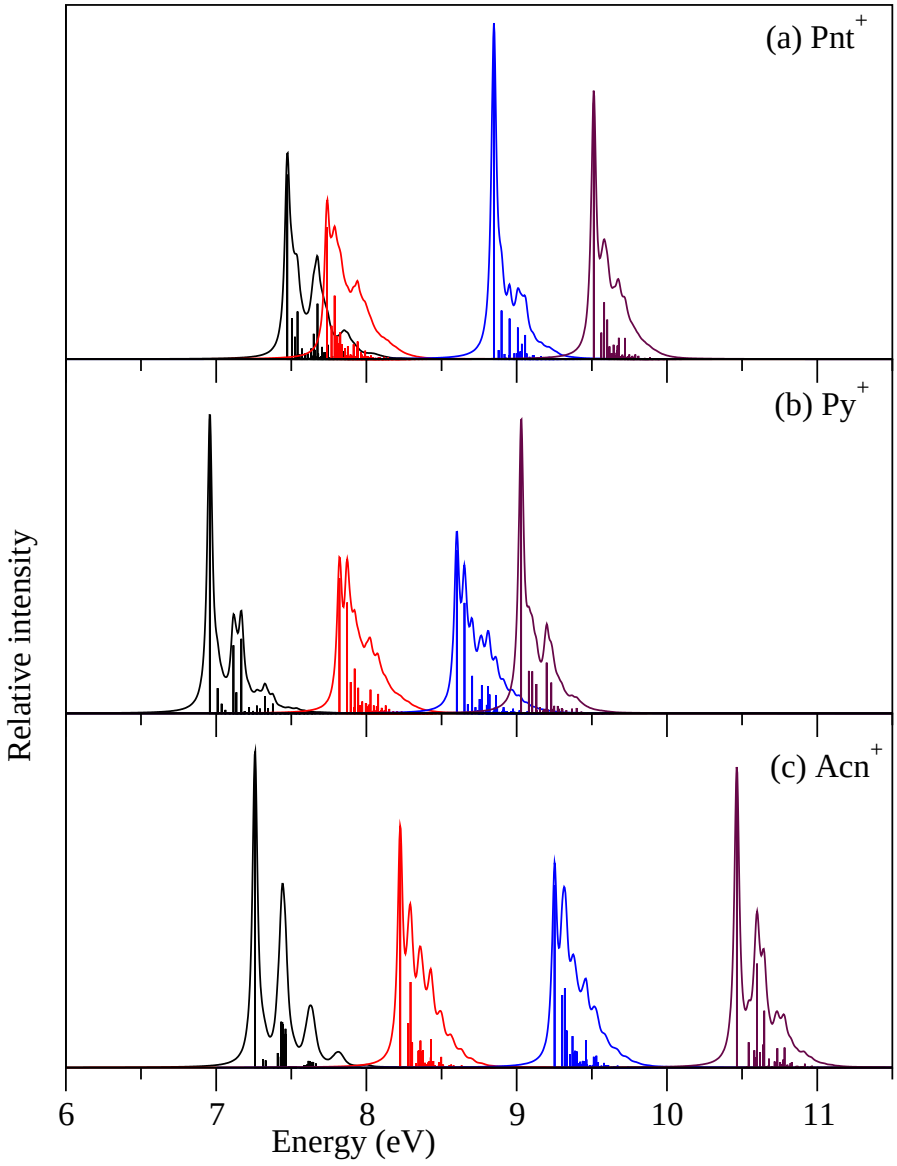

Figure 5.2: The quadratic uncoupled $\widetilde{X}$, $\widetilde{A}$, $\widetilde{B}$ and $\widetilde{C}$ vibronic bands of Pnt^+(panel a), Py^+(panel b) and Acn^+(panel c)

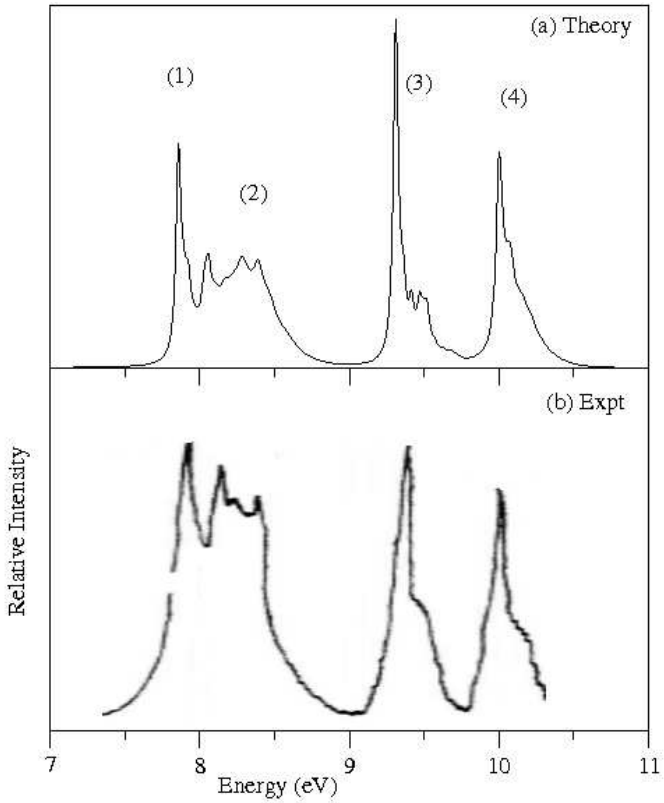

Figure 5.3: Broad band vibronic structure of the $\widetilde{X}(1)$-$\widetilde{A}(2)$-$\widetilde{B}(3)$-$\widetilde{C}(4)$ electronic states of Pnt^+. Relative intensity (in arbitrary units) is plotted as a function of the energy of the vibronic states of Pnt^+. The zero of the energy scale corresponds to the equilibrium minimum of the electronic ground state of the neutral reference. The present theoretical results are shown in panel a and the experimental photoelectron spectroscopy results (reproduced from Ref [17]) are shown in panel b for comparison.

In case of Py^+, peak spacings of ∼0.052, ∼0.157, ∼0.177 and ∼0.210 eV found in the $\widetilde{X}$ band are assigned to the excitation of vibrational modes ν_{13}, ν_8, ν_6 and ν_4, respectively. The vibrational modes ν_{13}, ν_{12} and ν_4 are strongly excited in the $\widetilde{A}$ state and the corresponding peak spacings of ∼0.050, ∼0.074 and ∼0.207 eV, respectively, are found in this case. Dominant progression of ν_{13}, ν_{11}, ν_7 and ν_4 vibrational modes are found in the $\widetilde{B}$ state with corresponding peak spacings of ∼0.051, ∼0.100, ∼0.167 and ∼0.209 eV, respectively. Peak spacings of ∼0.051, ∼0.074, ∼0.101, ∼0.169 and ∼0.200 eV are

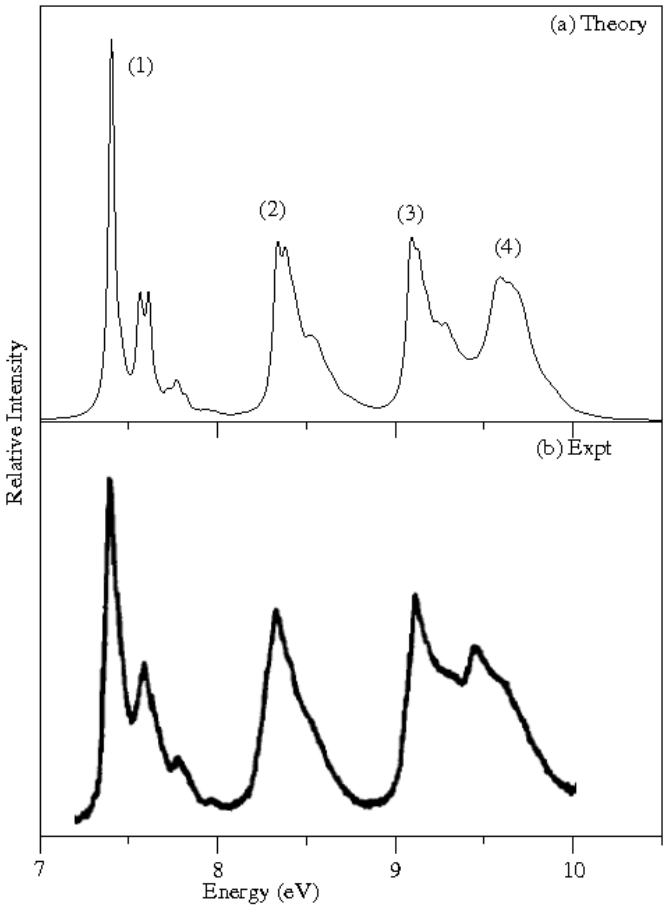

Figure 5.4: Same as in Fig. 5.3 for the $\widetilde{X}(1)$-$\widetilde{A}(2)$-$\widetilde{B}(3)$-$\widetilde{C}(4)$ coupled electronic states of Py^+. The experimental results shown in panel b are reproduced from Ref [15].

found in the $\widetilde{C}$ state and are assigned to the fundamentals of the ν_{13}, ν_{12}, ν_{11}, ν_7 and ν_5 vibrational modes, respectively.

In Acn^+, the dominant peaks are ∼0.174, ∼0.182, ∼0.184, ∼0.202 and ∼0.203 eV spaced in the $\widetilde{X}$ state and are due to the vibrational modes ν_{10}, ν_9, ν_8, ν_5 and ν_6, respectively. In the $\widetilde{A}$ state the vibrational modes ν_{20}, ν_{19}, ν_{18}, ν_{14} and ν_6 form progressions and the peaks are ∼0.053, ∼0.068, ∼0.080, ∼0.134 and ∼0.204 eV spaced, respectively. Dominant progressions of ν_{20}, ν_{19}, ν_{18} and ν_6 vibrations are found in the $\widetilde{B}$ state. The peaks are ∼0.051, ∼0.068, ∼0.080 and ∼0.210 eV spaced, respectively. In the $\widetilde{C}$ state

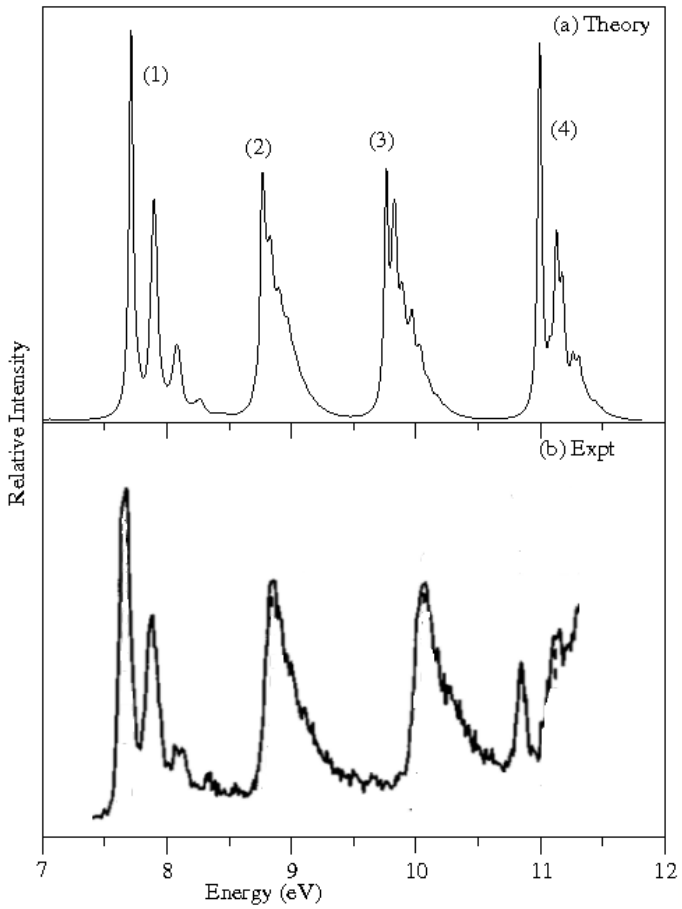

Figure 5.5: Same as in Fig. 5.3 for the $\widetilde{X}(1)$-$\widetilde{A}(2)$-$\widetilde{B}(3)$-$\widetilde{C}(4)$ coupled electronic states of Acn^+. The experimental results shown in panel b are reproduced from Ref [19].

peak spacings of ∼0.079, ∼0.135 and ∼0.183 eV are found and assigned to the excitation of ν_{18}, ν_{14} and ν_8 vibrational modes, respectively. It is to be noted that the frequencies extracted above from the peak spacings correspond to their value given in Tables (b of 5.1, 5.2 and 5.3) modified by the second-order coupling constant of a given vibration in the given electronic state of the radical cation.

In the subsequent analysis, the coupling among the $\widetilde{X}$-$\widetilde{A}$-$\widetilde{B}$-$\widetilde{C}$ electronic states is introduced to understand the broad band vibronic spectra. These calculations are performed by propagating wave packets within the MCTDH method [32]. The WP is initially pre-

pared in each of the mentioned electronic state of the radical cation and then propagated for 200 fs in the coupled manifold of electronic states. The technical details of the calculations viz., normal mode combination scheme, the size of primitive and single particle basis are given in Table 5.4 for Pnt^+, Py^+ and Acn^+, respectively. The convergence of the results is confirmed with respect to these technical parameters. At each time step (Δt=1.0 fs) the autocorrelation function of the WP, C(t), is recorded. The resulting autocorrelation function from four separate calculations are then combined, damped with an exponential function e^{-t/τ_r} (with τ_r=33 fs) and finally Fourier transformed to generate composite vibronic spectrum of each radical cation.

The vibronic band structure of the coupled $\widetilde{X}(1)$-$\widetilde{A}(2)$-$\widetilde{B}(3)$-$\widetilde{C}(4)$ electronic states of Pnt^+ calculated by the theoretical approach mentioned above is shown in panel a of Fig. 5.3. For comparison, the experimental results, reproduced from Ref [17], are also shown in panel b of Fig. 5.3. The theoretical findings are in excellent agreement with the experiment. Now let us examine the detailed structure of each band presented in this figure. The first band represents a composite structure of the $\widetilde{X}(1)$ and $\widetilde{A}(2)$ electronic states of Pnt^+. It can be seen from Fig. 5.3 that vibronic structure of these two states are highly overlapping. They differ significantly from their individual structures obtained in the uncoupled state situation. From the potential energy cuts given in Fig. 5.1 and also the related discussion presented in Sec. 5.3.1, it is clear that the energetic minimum of these two states and that of their intersection seam are very close in energy. Because of this energetic proximity and strong coupling via b_2 vibrational modes [cf. Table 5.1(c)] huge electronic nonadiabatic effects show up in their composite band structure (1,2). We will return to this point again when we discuss on the electron population dynamics later in the text. The structure of the $\widetilde{B}$ and $\widetilde{C}$ states (3 and 4) of Pnt^+ also remains similar to that obtained in the uncoupled state situation. Weak perturbation in the coupled states vibronic structure [cf. Fig. 5.3] arises due to coupling with the $\widetilde{X}$-$\widetilde{B}$, $\widetilde{A}$-$\widetilde{C}$ and $\widetilde{B}$-$\widetilde{C}$ states through vibrational modes of b_2 symmetry [cf. Table 5.1(c)].

The vibronic band structure of the coupled $\widetilde{X}(1)$-$\widetilde{A}(2)$-$\widetilde{B}(3)$-$\widetilde{C}(4)$ electronic states of Py^+ is shown in Fig. 5.4. The theoretical results (shown in panel a) are in good accord with the experiment of Ref [15] (panel b). It is interesting to note that the vibronic structure of the $\widetilde{X}$ state remains similar to their uncoupled state results. Structures of $\widetilde{A}$ state in the coupled state calculations partially differ from the uncoupled state results, where the weak perturbation in the coupled states situation [cf. Fig. 5.4] arises due to coupling with the $\widetilde{X}$-$\widetilde{A}$, $\widetilde{A}$-$\widetilde{B}$ and $\widetilde{A}$-$\widetilde{C}$ states through vibrational modes of b_{3g}, b_{1u} and b_{2u} symmetry. However, the structure of the $\widetilde{B}(2)$-$\widetilde{C}(3)$ states is strongly perturbed by the vibronic coupling due to the vibrational modes of b_{3g} symmetry [cf. Table 5.2(c)]. It can be seen from Table 5.2(c) that coupling strengths of the b_{3g} modes are stronger between the $\widetilde{B}$ and $\widetilde{C}$ states of Py^+. Furthermore, the energy gap between the minimum of $\widetilde{B}$-$\widetilde{C}$ crossing seam and the equilibrium minimum of the $\widetilde{B}$ and $\widetilde{C}$ states are very close in energy. The minimum of the $\widetilde{B}$ state occurs ~0.45 eV below the minimum of $\widetilde{B}$-$\widetilde{C}$ intersection and ~0.03 eV above the $\widetilde{C}$ state minimum (cf. Fig. 5.4). However,

Table 5.4: Normal mode combinations and size of the primitive and single-particle basis functions used in the converged MCTDH calculations for the coupled $\widetilde{X}$-$\widetilde{A}$-$\widetilde{B}$-$\widetilde{C}$ electronic states of Pnt^+, Py^+, and Acn^+.

Normal modes	Primitive basis	SPF basis
	Pnt^+	
(ν_{21},ν_{18},ν_{55},ν_{66})	(14,4,10,10)	[12,8,8,10]
(ν_{65},ν_{20},ν_{50},ν_{23})	(10,12,10,14)	[10,10,8,12]
(ν_{10},ν_{12},ν_{64},ν_{22})	(4,6,10,20)	[10,8,8,12]
(ν_{19},ν_{51},ν_{13},ν_{6})	(8,10,8,14)	[8,10,10,12]
(ν_{62},ν_{11},ν_{58},ν_{7})	(8,10,8,6)	[10,8,12,10]
	Py^+	
(ν_{11},ν_{26},ν_{65},ν_{8})	(8,8,35,15)	[14,8,12,10]
(ν_{33},ν_{10},ν_{52},ν_{64})	(6,4,16,12)	[8,14,10,12]
(ν_{5},ν_{32},ν_{12},ν_{59})	(8,6,12,6)	[12,12,14,10]
(ν_{7},ν_{53},ν_{44},ν_{29})	(10,15,4,6)	[14,8,12,10]
(ν_{4},ν_{27},ν_{13})	(14,4,30)	[8,14,10,12]
(ν_{6},ν_{45},ν_{56})	(6,12,8)	[12,14,10,8]
	Acn^+	
(ν_{18},ν_{7},ν_{57},ν_{47})	(14,4,4,10)	[10,8,12,8]
(ν_{5},ν_{16},ν_{53},ν_{46})	(8,4,4,14)	[12,10,8,10]
(ν_{9},ν_{12},ν_{60},ν_{19})	(10,4,6,20)	[10,12,8,10]
(ν_{6},ν_{54},ν_{48},ν_{14})	(10,4,6,18)	[8,12,10,10]
(ν_{59},ν_{10},ν_{20},ν_{8})	(18,10,18,10)	[10,8,10,12]
(ν_{58},ν_{15},ν_{52},ν_{13})	(10,6,4,6)	[10,12,10,8]

owing to much stronger coupling due to b_{3g} vibrational modes overall nonadiabatic effect is large in this case. A similar behavior is observed between $\widetilde{X}$ and $\widetilde{A}$ states of Pnt^+.

The final vibronic structure of the coupled $\widetilde{X}(1)$-$\widetilde{A}(2)$-$\widetilde{B}(3)$-$\widetilde{C}(4)$ electronic states of Acn^+ and the experimental spectrum reproduced from Ref [19] are plotted in panel a and b of Fig. 5.5, respectively. Four discrete vibronic bands correspond to four electronic states obtained from the coupled states calculation remain very similar to the uncoupled state results. This observation drive us to the conclusion that the vibronic coupling effects are insignificant in Acn^+ . Unlike the strong overlapping pattern of the vibronic bands of Pnt^+ and Py^+, all four bands display similar structures both in the uncoupled and coupled states situations. This is due to fact that the electronic states of Acn^+ are energetically well separated at the vertical configuration, thus the inter-state vibronic coupling effects are negligible on the vibronic structures of Acn^+.

5.3.3 Time-dependent dynamics

Time-dependence of diabatic electronic populations in the coupled $\widetilde{X}$-$\widetilde{A}$-$\widetilde{B}$-$\widetilde{C}$ states dynamics of the Pnt^+, Py^+ and Acn^+ is presented in Figs. 5.6, 5.7 and 5.8. It is observed that very minor population flows to higher excited electronic states when the WP is initially prepared on the $\widetilde{X}$ state of these radical cations (cf. panel a of Fig. 5.6, 5.7 and 5.8). As shown in Sec. 5.3.1, the CIs of the $\widetilde{X}$ state with all other states (of all three radical cations) are located at higher energies. Therefore, these CIs are not accessible to the WP during its evolution on the $\widetilde{X}$ state. The $\widetilde{C}$ state is coupled with further higher excited states and a detail examination of these couplings is beyond the scope of the present investigation. We therefore do not discuss on the diabatic electronic population of the $\widetilde{C}$ state here. The time dependence of the population of the $\widetilde{A}$ and $\widetilde{B}$ electronic states of these radical cations is interesting and important from the view point of their astrophysical relevance.

The time dependence of electronic populations for an initial transition of the neutral molecule to the $\widetilde{A}$ and $\widetilde{B}$ ionic states are shown, respectively, in panels: b and c of Fig. 5.6, 5.7 and 5.8 for Pnt^+, Py^+ and Acn^+. These represents fractional populations and are obtained by propagating the WP in the coupled manifold of $\widetilde{X}$-$\widetilde{A}$-$\widetilde{B}$-$\widetilde{C}$ ionic states in each case. It can be immediately seen from these plots that the nuclear dynamics in the four coupled ionic states is solely governed by the vibronic coupling. One of the important feature to be highlighted here is the population decay when the WP initially placed on $\widetilde{A}$ state. Apart from these general observations a closer look at the population curves reveals the following. We note that (also indicated in the figure) the population of the $\widetilde{X}$, $\widetilde{A}$, $\widetilde{B}$ and $\widetilde{C}$ state is shown by the dotted, solid, dashed and dashed with dotted lines, respectively. The population flow to the $\widetilde{X}$ state is quite large in case of all molecular cations (panel b of Fig. 5.6-5.8) when $\widetilde{A}$ state is initially populated. In case of Pnt^+ electron population rapidly moves to the $\widetilde{X}$ state ($\sim$90% within 25 fs) when compare to the same for Py^+ and Acn^+. As can be explained by the energy gap, relative to the minimum of the $\widetilde{A}$ state the energetic minimum of the $\widetilde{X}$-$\widetilde{A}$ CIs progressively shifts to the higher energy from Pnt^+ ($\sim$0.01 eV) to Py^+ ($\sim$0.19 eV) to Acn^+ ($\sim$0.23 eV). Because of this energetic proximity relatively large population flows to the $\widetilde{X}$ state of Pnt^+ despite moderate coupling strength of the b_2 vibrational modes [cf. Table 5.1(c)]. In contrast, coupling strength of b_{3g} vibrational modes is relatively stronger in case of Py^+ [cf. Table 5.2(c)] however, because of increasing energy gap between the $\widetilde{X}$-$\widetilde{A}$ intersection minimum and the minimum of the $\widetilde{A}$ state this coupling effect is quenched and moderate population flows to the $\widetilde{X}$ state of Py^+ and Acn^+.

It can be seen from Table c of 5.1-5.3 that except $\widetilde{X}$-$\widetilde{C}$ and $\widetilde{A}$-$\widetilde{B}$ in case of Pnt^+ and Acn^+, all other states are coupled in first-order for all three radical cations. When the WP is propagated on the $\widetilde{A}$ state no population flows to the $\widetilde{B}$ state (because no $\widetilde{A}$-$\widetilde{B}$ coupling in case of Pnt^+, Acn^+ and negligibly small coupling in case of Py^+). The impact of these couplings on the vibronic structure of a given state depends on its

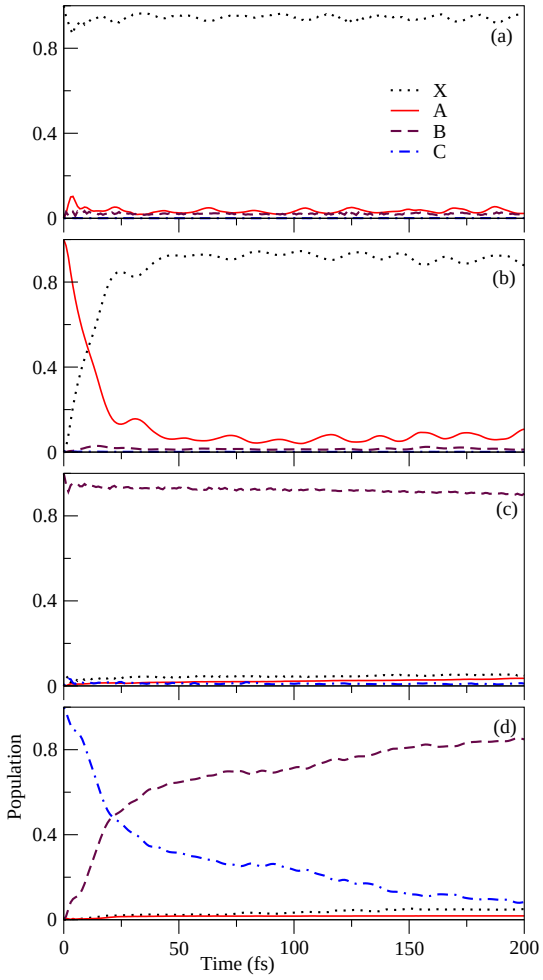

Figure 5.6: Time dependence of diabatic populations of the $\widetilde{X}$ (dotted lines), $\widetilde{A}$ (solid lines), $\widetilde{B}$ (dashed lines) and $\widetilde{C}$ (dashed and dotted lines) states for an initial transition of the WP to the $\widetilde{X}$ (panel a), $\widetilde{A}$ (panel b), $\widetilde{B}$ (panel c), $\widetilde{C}$ (panel d) in the coupled $\widetilde{X}$-$\widetilde{A}$-$\widetilde{B}$-$\widetilde{C}$ state dynamics of Pnt^+.

energetic location relative to the energetic minimum of the relevant intersection seam (discussion in Sec. 5.3.1]. The initial monotonic decrease of population relates to a decay rate of ∼20 fs, ∼42 fs and ∼52 fs of the $\widetilde{A}$ state of Pnt^+, Py^+ and Acn^+, respectively.

The electron population dynamics appears to be more interesting and involved when the $\widetilde{B}$ state is initially populated. The time dependence of populations is shown in panel c of Fig. 5.6, 5.7 and 5.8 for Pnt^+, Py^+ and Acn^+, respectively. As can be seen from the figures that large population flows to the $\widetilde{X}$ and $\widetilde{A}$ states of Py radical cations in

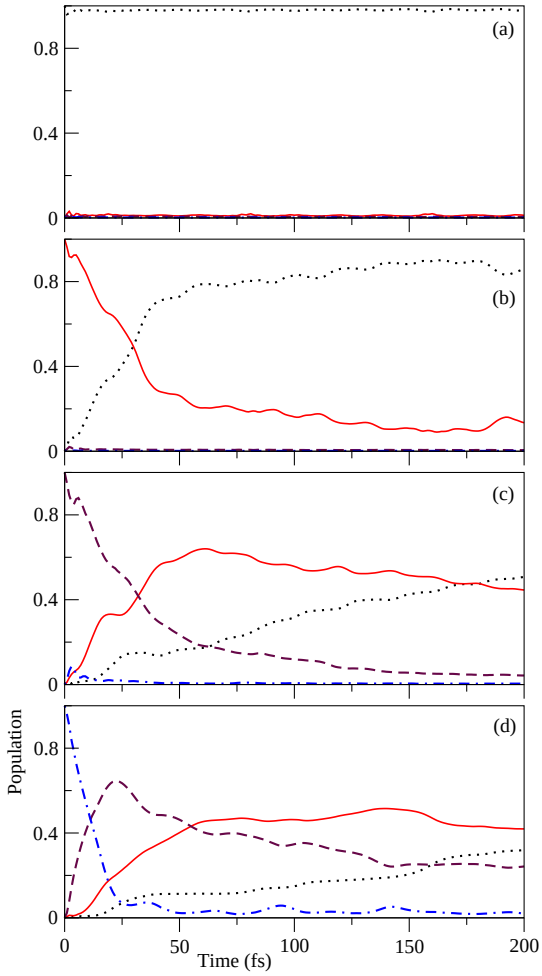

Figure 5.7: Same as in Fig. 5.6 shown for the diabatic populations of Py^+.

this situation (cf. panel c of Fig. 5.7). The initial monotonic decrease of population relates to a decay rate of ∼37 fs, of the $\widetilde{B}$ state of Py^+. As the $\widetilde{A}$-$\widetilde{B}$ coupling is absent in Pnt^+ and Acn^+, population transfer from $\widetilde{B}$ to the lower electronic states is not observed in the dynamics.

5.3.4 ZEKE spectral progression comparison in Py^+

Here we compare the theoretical vibrational energy levels of the $\widetilde{X}$ state of Py^+ with the reported experimental ZEKE spectroscopy findings within 0-1520 cm^{-1} spectral range [20]. The uncoupled $\widetilde{X}$ state spectrum is simulated within the matrix diagonalization scheme using only low-frequency totally-symmetric vibrational modes. The obtained stick data with peak spacings at ∼416 and ∼592 cm^{-1} are assigned to ν_{13} and

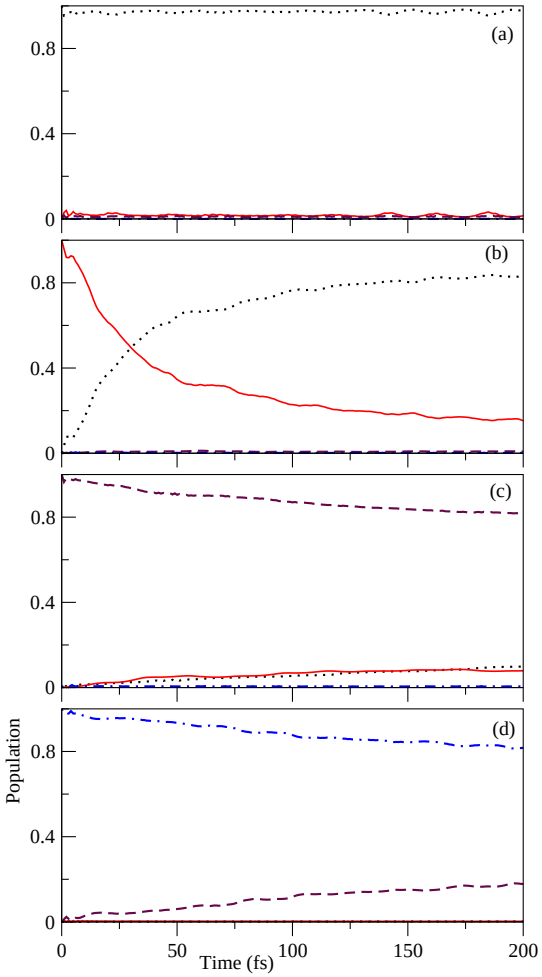

Figure 5.8: Same as in Fig. 5.6 shown for the diabatic populations of Acn^+.

ν_{12} vibrational modes, respectively. The ZEKE findings at 412 and 598 cm^{-1} can be unambiguously assigned to ν_{13} and ν_{12} modes. The first overtones of ν_{12} vibrational mode is identified with the peak spacing of ∼1184 cm^{-1}, and are fully consistent with the experimental value 1196 cm^{-1}. Peaks corresponding to $\nu_{13}+\nu_{12}$, $2\nu_{13}+\nu_{12}$ are also identified at ∼1008 and ∼1424 cm^{-1}, respectively. These combinations were also seen at 1010 and 1422 cm^{-1} in the experiment.

Excitation of the non-totally symmetric vibrational modes in the $\widetilde{X}$ state spectrum is attributed to vibronic coupling mechanism. From our theoretical model $\widetilde{X}$-$\widetilde{C}$ and $\widetilde{A}$-$\widetilde{B}$ electronic states are coupled through the b_{1u} vibrational modes, $\widetilde{X}$-$\widetilde{B}$ and $\widetilde{A}$-$\widetilde{C}$ electronic states are coupled through the b_{2u} vibrational modes and $\widetilde{X}$-$\widetilde{A}$ and $\widetilde{B}$-$\widetilde{C}$ electronic states are coupled through the b_{3g} vibrational modes. In coupled states calculations,

peak spacing at ∼445, ∼482 and ∼751 cm^{-1} corresponding to the excitation of ν_{65}, ν_{64} and ν_{63} of b_{3g} are identified in the coupled state calculations are in good agreement with experimental findings at ∼457, ∼499 and ∼738, cm^{-1}. In addition to the fundamental vibrations, combination of ν_{12}+ν_{65}, ν_{12}+ν_{64}, ν_{12}+ν_{63} and ν_{12}+ν_{13}+ν_{64} bands at ∼1037, ∼1074, ∼1343 and ∼1490 cm^{-1} are found and are fully consistent with their experimental locations at ∼1055, ∼1097, ∼1336 and ∼1509 cm^{-1}, respectively, in that order. Additional peaks, mostly the combinations associated with excitation of a_g, b_{1u}, b_{2u} and b_{3g} modes, were also found in the $\widetilde{X}$-$\widetilde{A}$-$\widetilde{B}$-$\widetilde{C}$ coupled state calculation, however, an unambiguous assignment of these corresponding peaks are very difficult.

5.3.5 DIBs related to $D_0 \rightarrow D_2$ of Pnt^+ and Acn^+

In Fig. 5.9, the experimental and theoretical findings corresponding to the $D_0 \rightarrow D_2$ transition in Pnt^+ are shown. The theoretical uncoupled state spectrum of the $\widetilde{B}$ state (panel a) is calculated by using only the totally symmetric modes and the coupled state spectrum (panel b) is calculated by introducing the b_2 symmetry modes responsible for $\widetilde{X}$-$\widetilde{A}$-$\widetilde{B}$-$\widetilde{C}$ vibronic coupling mechanism. The experimental results reproduced from Ref [4] are plotted in panel c of Fig. 5.9 for comparison. The abscissa in the theoretical spectrum is taken as energy from the $\widetilde{X}$ state of Pnt^+ and an appropriate energy shift is applied along the abscissa in order to reproduce the experimental adiabatic ionization position. Here, the vibrational progression is examined by locating the origin peak (0_0^0) at ∼891.9 nm. The observed second strongest absorption peak at ∼860.4 nm (cf., panel a) in the spectrum is attributed to the excitation of ν_{22} vibrational mode of frequency 412 cm^{-1}. These findings are in good agreement with experimental gas-phase (∼891.9 and ∼852.0 nm) and matrix isolation absorption (∼898.3 and ∼856.8 nm) studies [4, 7].

Likewise, the theoretical uncoupled and coupled vibrational energy level structures of the $\widetilde{B}$ state of Acn^+ and the experimental $D_0 \rightarrow D_2$ band of Acn^+ are shown in Fig. 5.10. To compare with the experiment, the most intense peak (origin 0_0^0) was placed at ∼646.3 nm. Although the theoretical vibrational level intensities (panel a and b) differ from the experimental spectrum, the energetic location of the peak positions is found to be in good accord with the experimental gas-phase (∼646.3 nm) and matrix isolation spectral studies (648.1 nm) [2, 12].

Salama *et al.* [11, 12] proposed that the observed ∼857.2 and ∼649.2 nm DIBs may be associated with the laboratory experimental absorption peak of ∼856.8 nm and ∼648.1 nm corresponding to the $D_0 \rightarrow D_2$ transition in Pnt^+ and $D_0 \rightarrow D_2$ transition in Acn^+, respectively. Based on the peak at ∼860.4 nm (second strongest transition of Pnt^+) and ∼646.3 nm (origin 0_0^0 of Acn^+) seen in the theoretical $D_0 \rightarrow D_2$ spectrum of Pnt^+ and Acn^+, respectively, "may be" attributed to the astrophysical DIBs. It can be seen that our theoretical spectra is in good agreement with the experimental results reproduced from Ref [3, 4, 12].

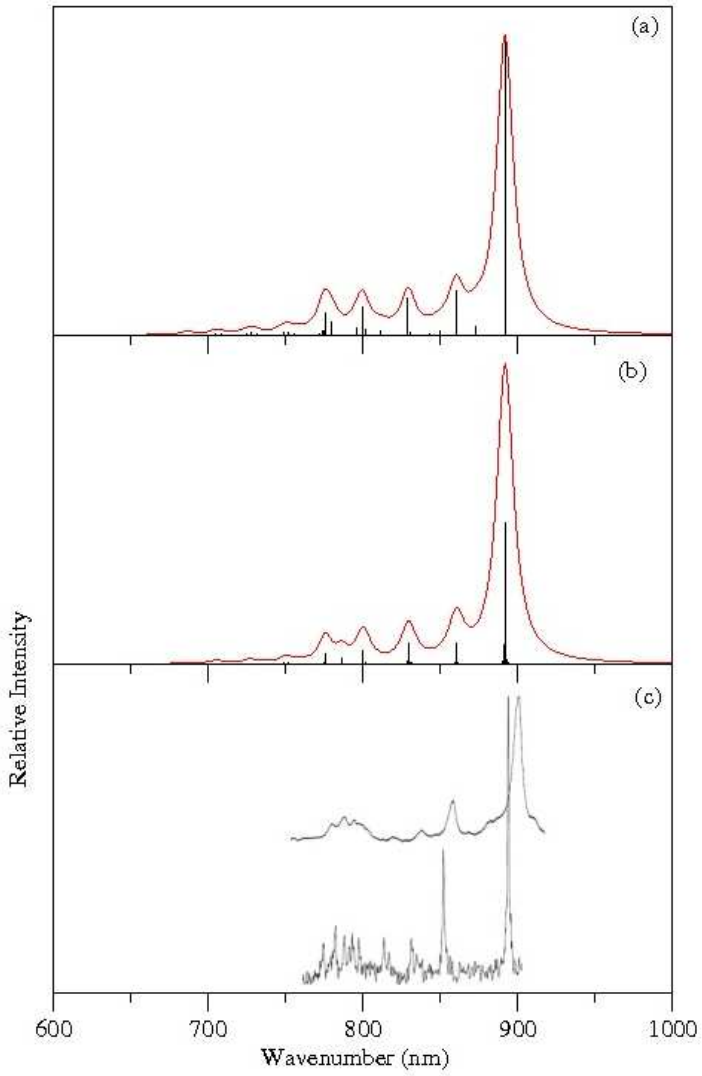

Figure 5.9: The $D_0 \rightarrow D_2$ photoelectron band of Pnt. Panel a: uncoupled $D_0 \rightarrow D_2$ band; Panel b: calculated by including $\widetilde{X}$-$\widetilde{A}$-$\widetilde{B}$-$\widetilde{C}$ coupling; Panel c: Experimental absorption spectrum of Pnt cation Reproduced from Ref [4], top: isolated in Ne matrix; bottom: gas-phase photo fragmentation spectrum.

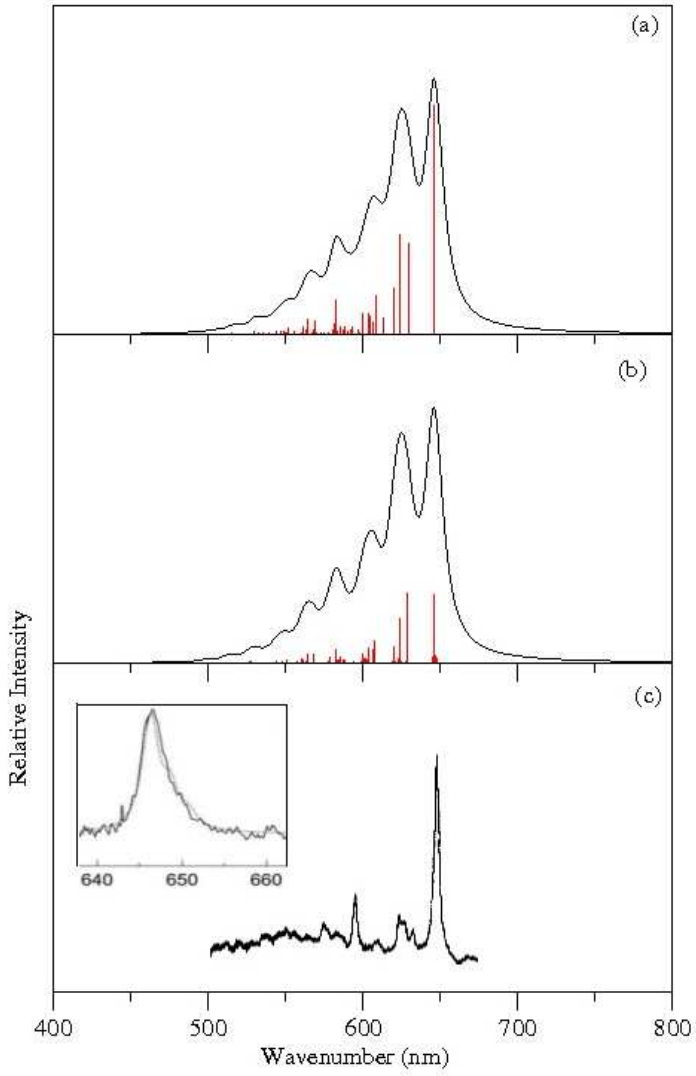

Figure 5.10: The $D_0 \rightarrow D_2$ photoelectron band of Acn. Panel a: calculated uncoupled $D_0 \rightarrow D_2$ band; Panel b: calculated with $\widetilde{X}$-$\widetilde{A}$-$\widetilde{B}$-$\widetilde{C}$ coupled vibronic band; Panel c: The experimental matrix(Ne) absorption spectrum of Acn^+ reproduced from Ref. [12]; In the inset the origin 0_0^0 peak of $D_0 \rightarrow D_2$ band, reproduced from Ref. [3].

5.4 Summarizing remarks

Detailed study regarding the structure and dynamics of side chain PAHs, Pnt^+, Py^+ and Acn^+ is presented in this Chapter. *Ab initio* quantum chemistry calculations are carried out to establish the potential energy surfaces and coupling surfaces of the $\widetilde{X}$, $\widetilde{A}$, $\widetilde{B}$ and $\widetilde{C}$ electronic states. With the aid of these electronic structure data and the standard diabatic vibronic coupling Hamiltonians, the spectroscopy and dynamics of these PAH radical cations are studied in detail to determine the energetic location and spectral profile of some of the DIBs.

It is found that the dynamics of $\widetilde{X}$ state of Pnt^+ cation strongly perturbed by the neighboring $\widetilde{A}$ state. These two states are very close to each other at the vertical configuration and the energetic minimum of the seam of CIs is very close to their equilibrium minimum. The similar behavior can be observed in the $\widetilde{B}$ and $\widetilde{C}$ states of Py^+. These perturbations are negligibly small remaining all electronic states, as a result non overlapping band structures of these states are obtained. In case of Acn^+ all electronic states are vertically well separated, as a result the overall vibronic coupling effect is quenched by the energy separation.

The decay of the $\widetilde{A}$ electronic state is another important aspect of this study. Mechanism of this decay dynamics is discussed at length for Pnt^+, Py^+ and Acn^+ and compared with our earlier findings on Np^+-Hn^+. It is found that the decay rate of the $\widetilde{A}$ state is fastest in case of Pnt^+ (20 fs). In all these radical cations and transition to this state take place upon absorption of UV photon of appropriate frequency. While electronically excited (to the higher electronic states) in all three radical cations (Pnt^+, Py^+ and Acn^+) can nonradiatively decay to their electronic ground $\widetilde{X}$ state through the conical intersections, the propensity of such transition is negligible in case of An^+, Tn^+, Pn^+ and Hn^+. In the latter cations the $\widetilde{X}$-$\widetilde{A}$ intersections occur at much higher energies. Therefore, it suffices to say here that the probability of internal conversion is much greater in case of Pnt^+, Np^+, Py^+ and Acn^+ compared to the higher homologs (An^+, Tn^+, Pn^+ and Hn^+) for which the quantum yield of fluorescence emission is expected to be higher.

The spectroscopy of the $\widetilde{A}$ and $\widetilde{B}$ states of these PAH radical cations is particularly important in relation to the stellar spectroscopy. In the recent past we discovered correlation of peak locations of the $\widetilde{B}$ band of Np^+, An^+ and Tn^+ and $\widetilde{A}$ band of Pn^+ with those in the matrix and stellar spectral results. A detailed time-independent quantum nuclear dynamics study has been performed to explore the precise location of vibrational energy levels of $D_0 \rightarrow D_2$ transition of Pnt^+ and Acn^+ in relation to the assignment of the astrophysical observation of $\sim$857.2 and $\sim$649.18 nm DIBs. The theoretical findings are in excellent agreement with the laboratory high resolution electronic spectral data. Based on the critical vibrational progression findings, the electronic transitions in the Pnt^+ and Acn^+ can be tentatively assigned to the observed DIBs and these molecular cations may play crucial role in the interstellar space.

References

[1] P. Bréchignac, T. Pino and N. Boudin, Spectrochimica Acta. A, 57, 745 (2001).

[2] L. Biennier, F. Salama, L. J. Allamandola and J. J. Scherer, J. Chem. Phys. **118**, 7863 (2003).

[3] L. Biennier, F. Salama, M. Gupta, A. O'Keefe, Chem. Phys. Lett. **387**, 287 (2004).

[4] P. Bréchignac and T. Pino, Astron. Astophys, **343**, L49 (1999).

[5] X. Tan and F. Salama, Chem. Phys. Lett. **422**, 518 (2006).

[6] F. Salama and L. J. Allamandola, Nature, **358**, 42 (1992).

[7] F. Salama, C. Joblin and L. J. Allamandola, J. Chem. Phys. **101**, 10252 (1994).

[8] F. Salama, C. Joblin, L. J. Allamandola, Planet. Space Sci. **43**, 1165 (1995).

[9] F. Salama, G. A. Galazutdinov, J. Krełowski, L. J. Allamandola, F. A. Musaev, Astrophys. J. **526**, 265 (1999).

[10] F. Salama and L. J. Allamandola, J. Chem. Soc., Faraday Trans. **89**, 2277 (1993).

[11] F. Salama, Origins of Life and Evolution of the Biosphere, **28**, 349 (1998).

[12] T. M. Halasinski, F. Salama and L. J. Allamandola, Astrophys. J. **628**, 555 (2005).

[13] F. Salama and L. J. Allamandola, Adv. Space Res. **15**, 3(413) (1995).

[14] M. K. Crawford, A. G. G. M. Tielens and L. J. Allamandola, Astrophys. J. **293**, L45 (1985).

[15] R. Boschi and W. Schmidt, Tetrahedron Letters. **25**, 2577 (1972).

[16] W. Schmidt, J. Chem. Phys. **66**, 828 (1977).

[17] R. Boschi, J. N. Murrell, W. Schmidt, Faraday Discuss. Chem. Soc, **54**, 116 (1972).

[18] N. S. Hush, A. S. Cheung and P. R. Hilton, Journal of Electron Spectroscopy and Related Phenomena, **7**, 385 (1975).

[19] T. Bally, C. Carra, M. P. Fülscher and Z. Zhu, J. Chem. Soc., Perkin Trans. *2*, 1759 (1998).

[20] J. Zhang, F. Han and W. Kong, J. Phys. Chem. A. **114**, 11117 (2010).

[21] F. Aiga, J. Phys. Chem. A, **116**, 663 (2012).

[22] C. Niederalt, S. Grimme and S. D. Peyerimhoff, Chem. Phys. Lett. **245**, 455 (1995).

[23] M. Vala and J. Szczepanski, J. Phys. Chem. **98**, 9187 (1994).

[24] M. S. Deleuze, J. Chem. Phys. **116**, 7012 (2002).

[25] R. González-Luque, L. Serrano-Andrés, M. Merchán and M. P. Fülsher Theor Chem Acc, **110**, 224 (2003).

[26] O. Parisel, G. Berthier, Y. Ellinger, Astron. Astrophys. **266**, L1 (1992).

[27] A. M. Tokmachev, M. Boggio-Pasqua, M. J. Bearpark and M. A. Robb, J. Phys. Chem. A, **112**, 10881 (2008).

[28] S. Hirata, T. J. Lee, M. Head-Gordon, J. Chem. Phys. **111**, 8904 (1999).

[29] H. Köppel, W. Domcke, L. S. Cederbaum, Adv. Chem. Phys. **57**, 59 (1984).

[30] M. J. Frisch, G. W. Trucks, H. B. Schlegel, *et al.*, *Gaussian 03,* Revision B. 05, Gaussian, Inc., Pittsburgh PA, 2003.

[31] L. S. Cederbaum, J. Phys. B. **8**, 290 (1975).

[32] a) G. A. Worth, M. H. Beck, A. Jäckle, H.-D. Meyer, *The MCTDH Package,* Version 8.2, (2000), University of Heidelberg, Heidelberg, Germany. H.-D. Meyer, Version 8.3 (2002), Version 8.4 (2007). ML-MCTDH implemented in forthcoming version 8.5 (2011), see http://mctdh.uni-hd.de/; b) H.-D. Meyer, U. Manthe, L. S. Cederbaum, Chem. Phys. Lett. **165**, 73 (1990); c) U. Manthe, H.-D. Meyer, L. S. Cederbaum, J. Chem. Phys. **97**, 3199 (1992); d) M. H. Beck, A. Jäckle, G. A. Worth, H.-D. Meyer, Phys. Rep. **324**, 1 (2000).

6 Spectroscopy and dynamics of electronically excited diacetylene radical cation vis-â-vis the observed diffuse interstellar bands

6.1 Introduction

Unsaturated hydrocarbons and their derivatives are important constituents in common reaction schemes [1]. Among these hydrocarbons, polyacetylenes are the most complex ones and appears to be identified in the atmospheres of planets, and in the chemistry of the interstellar medium [2, 3], due to their unstable and highly reactive nature. Reactions of metastable diacetylene may play a role in the formation of larger hydrocarbons in these atmospheres and it was also thought to be involved in the reactions responsible for soot formation in hydrocarbon flames [4]. These polyacetylenes also may serve as building blocks of PAHs in the interstellar medium [3, 5]. Very recent experiments on polyacetylenes, revealed many discrepancies on the assignment of the 5069 Å DIB [3] as a carrier of the diacetylene radical cation, $C_4H_2{}^+$. The origin 0_0^0 peak of the $\widetilde{X}^2\Pi_g \rightarrow \widetilde{A}^2\Pi_u$ transition was found to be the important as per the astronomical data.

Numerous studies have been devoted to understand the geometric structures and spectroscopy of diacetylene [3, 6–33]. Experimental photoelectron spectra of acetylene and diacetylene were measured by Baker *et al.* [7, 31]. Theoretical and experimental ionization energies were reported by Kaiser *et al.*, and implications of these energies to the redox chemistry involved in planets [9] have been predicted. Very recent studies of Gronowski *et al.* on structural isomers of neutral and radical cation of C_4H_2 reveal that the linear isomer (diacetylene) is the most stable structure [8]. In addition to matrix isolation spectral studies [10, 14, 15, 17, 23, 24], laboratory gas phase and astronomical spectral studies [3, 11, 12, 23] were also performed on $C_4H_2{}^+$. Motylewski *et al.* [11] reported gas-phase visible absorption spectra of $\widetilde{X}^2\Pi_g \rightarrow \widetilde{A}^2\Pi_u$ transition in $C_4H_2{}^+$ and observed the origin line at 5068.65 Å with the aid of cavity ring-down spectroscopy technique. Krełowski *et al.* [3] reported a new DIB centered at 5068.8 Å, which appears to match both the width and mean wavelength reported by Motylewski *et al.* [11]. Very recent studies [12] disagree the observation of $\widetilde{X}^2\Pi_g \rightarrow \widetilde{A}^2\Pi_u$ transition in $C_4H_2{}^+$ occurring at 5067.9 Å with the 5069 Å DIB.

The studies on spectroscopy of $\widetilde{X}$ and $\widetilde{A}$ states of $C_4H_2^+$ reveals the vibrational energy progressions of these bands. In the $\widetilde{X}$ state, excitation of C≡C symmetric stretch (ν_2) and asymmetric C-H stretch (ν_4) vibrational modes with an energy separation of ∼2121 and ∼2703 cm^{-1}, respectively was reported by Baker *et al.* [7]. In the $\widetilde{A}$ state progression of C≡C stretching mode (ν_3) is observed by the same group at ∼861 cm^{-1}. Callomen *et al.* [29] observed only four vibrational modes and their combination bands in the spectrum of the $\widetilde{A}$ band occurring at ∼861, ∼971 ∼2177 and ∼3137 cm^{-1} and assigned them to ν_3, $2\nu_7$, ν_2 and ν_1 vibrational modes, respectively, in that order. Bondybey *et al.* [17] observed the progressions in $\widetilde{X}$ state, at ∼3143, ∼2177 and ∼865 cm^{-1} and assigned to the fundamentals of ν_1, ν_2 and ν_3 vibrations, respectively. In addition, the progression ∼973 cm^{-1} was assigned to the second overtone of C-C bending (ν_7) vibration. The peaks corresponding to these progressions in the $\widetilde{A}$ state are identified at ∼2821, ∼2002, ∼807 and ∼864 cm^{-1}, respectively, in that order. In addition to the totally symmetric modes, excitation of RT active modes are also identified in the spectral progressions by various groups [11, 15, 23, 30, 31].

The equilibrium geometry of C_4H_2 molecule belongs to the $D_{\infty h}$ symmetry point group in its electronic ground state. The 13 vibrational modes of this molecule decompose into, $3\sigma_g \oplus 2\sigma_u \oplus 2\pi_g \oplus 2\pi_u$ irreducible representations (IREPs) of the $D_{\infty h}$ symmetry point group. The ground and first excited doublet degenerate electronic states of $C_4H_2^+$ belong to the $\widetilde{X}^2\Pi_g$ and $\widetilde{A}^2\Pi_u$ terms of this equilibrium symmetry representation. It is worthwhile to note that except a few computational studies on the electronic structure of the electronic ground and excited states [8, 13, 18, 19, 26] of this system, a detailed quantum dynamics study to elucidate the vibronic structure of the experimental observations noted above is missing in the literature. The present effort is aimed towards this endeavor.

The theoretical model developed here relies on a diabatic representation of the electronic states in order to treat the nonadiabatic coupling terms as smooth potential coupling rather than diverging kinetic coupling in the complementary adiabatic electronic representation [34]. Elementary symmetry rules [35] are applied to construct a parameterized Hamiltonian in terms of the dimensionless normal coordinates of the vibrational modes and the parameters introduced therein are estimated by fitting adiabatic electronic energies calculated by *ab initio* electronic structure calculations over a large grid in the nuclear coordinate space. The theoretical findings of this paper are compared with the most recent experimental and theoretical results and also discussed in relation to the astrophysical observations [3, 7, 11, 12, 15, 23, 30, 31].

6.2 Theoretical and computational details

6.2.1 The vibronic Hamiltonian

In this section a Hamiltonian describing the vibronic interaction of a Π_g and Π_u electronic states of $C_4H_2^+$ in terms of the dimensionless normal displacement coordinates of the reference electronic ground state, in accordance with the symmetry selection rules is constructed.

The first-order coupling within (intra) and between (inter) electronic states is governed by the selection rules; $(\Gamma_j)^2 \supset (\Gamma_{\sigma_g^+})$ and $\Gamma_j \otimes \Gamma_k \supset \Gamma_i$, respectively [34]. The symbol, Γ represents the IREP, j and k are the electronic state indices, σ_g^+ represents the totally symmetric vibrational mode and the symbol, i, represents the symmetry of the vibrational mode that transforms according to, $\Gamma_j \otimes \Gamma_i \otimes \Gamma_k \supset \Sigma_g^+$. Now for the degenerate, Π_g ($\widetilde{X}^2\Pi_g$) and Π_u ($\widetilde{A}^2\Pi_u$) electronic states the symmetrized direct product in the $D_{\infty h}$ symmetry point group transforms into,

$$\begin{aligned} \Pi_g \otimes \Pi_g &= \delta_g + \sigma_g^+ + \sigma_g^-, \\ \Pi_u \otimes \Pi_u &= \delta_g + \sigma_g^+ + \sigma_g^-. \end{aligned}$$

While the vibrational modes of σ_g^+ symmetry can not split the electronic degeneracy (are condon active), and the lack of vibrational modes of δ_g symmetry that can lift this electronic degeneracy makes first order RT term vanish. But the electronic degeneracy of Π_g and Π_u states is lifted by the π_g and π_u modes in second order. For the rest of the off-diagonal elements of the Hamiltonian written below the following symmetry rule apply. With the given symmetry representation of the electronic states and the vibrational modes [in Eq. 6.1] the following rules can be derived from the character table of the $D_{\infty h}$ symmetry point group.

$$\Pi_g \otimes \Pi_u = \delta_u + \sigma_u^+ + \sigma_u^-,$$

The relative sign of various elements of the Hamiltonian is determined by explicitly checking the invariance of the Hamiltonian with respect to the symmetry operations of the D_{6h} point group, following similar works on benzene and cyclopropane radical cation [37–39]. With these considerations the vibronic Hamiltonian can be written as

$$\mathcal{H} = (\mathcal{T}_N + \mathcal{V}_0)\mathbf{1_4} + \begin{pmatrix} W_{\widetilde{X}x} & W_{\widetilde{X}x-\widetilde{X}y} & W_{\widetilde{X}x-\widetilde{A}x} & 0 \\ & W_{\widetilde{X}y} & 0 & W_{\widetilde{X}y-\widetilde{A}y} \\ & & W_{\widetilde{A}x} & W_{\widetilde{A}x-\widetilde{A}y} \\ h.c & & & W_{\widetilde{A}y} \end{pmatrix}, \tag{6.1}$$

In the above, $\mathcal{H}_0 = \mathcal{T}_N + \mathcal{V}_0$, represents the Hamiltonian (assumed to be harmonic) of the reference electronic ground (S_0) state of C_4H_2 with

$$\mathcal{T}_N = -\frac{1}{2}\sum_{i\ \in\ \sigma_g^+,\ \sigma_u^+} \omega_i \frac{\partial^2}{\partial Q_i^2} - \frac{1}{2}\sum_{i\ \in\ \pi_g,\ \pi_u} \omega_i \left(\frac{\partial^2}{\partial Q_{ix}^2} + \frac{\partial^2}{\partial Q_{iy}^2}\right), \tag{6.2}$$

and

$$\mathcal{V}_0 = \frac{1}{2}\sum_{i\ \in\ \sigma_g^+,\ \sigma_u^+} \omega_i Q_i^2 + \frac{1}{2}\sum_{i\ \in\ \pi_g,\ \pi_u} \omega_i \left(Q_{ix}^2 + Q_{iy}^2\right). \tag{6.3}$$

The quantity $\mathbf{1_4}$ is a 4×4 diagonal unit matrix. The matrix Hamiltonian (with elements W) in Eq. 6.1 represents the adiabatic energies of the given electronic states of the radical cation (diagonal elements) and their coupling energies (off-diagonal elements). The elements of this matrix are expanded in a standard Taylor series around the reference equilibrium geometry at, $\mathbf{Q} = \mathbf{0}$, in the following way

$$\begin{aligned} W_{jx/jy} \;=\; & E_0^{(j)} + \sum_{i\ \in\ \sigma_g^+} \kappa_i^j Q_i + \frac{1}{2}\sum_{i\ \in\ \sigma_g^+,\ \sigma_u^+} \gamma_i^j Q_i^2 + \frac{1}{2}\sum_{i\ \in\ \pi_g,\ \pi_u} [\gamma_i^j (Q_{ix}^2 + Q_{iy}^2)] \\ & \pm\frac{1}{2}\sum_{i\ \in\ \pi_g,\ \pi_u} \eta_i^j (Q_{ix}^2 - Q_{iy}^2);\ j\ \in\ \widetilde{X}, \widetilde{A} \end{aligned} \tag{6.4}$$

$$W_{jx-jy} \;=\; -\sum_{i\ \in\ \pi_g,\ \pi_u} \eta_i^j (Q_{ix} Q_{iy})\ ;\ j\ \in\ \widetilde{X}, \widetilde{A} \tag{6.5}$$

$$W_{jx-kx/jy-ky} \;=\; \sum_{i\ \in\ \sigma_u^+} \lambda_i^{(j-k)} Q_i\ ;\ j\ \in\ \widetilde{X}\ and\ k\ \in\ \widetilde{A} \tag{6.6}$$

In the above equations the quantity E^j represents the VIE of the j^{th} electronic state. The two components of the degenerate states and modes are labeled with x/y throughout this study. The quantity κ_i^j and η_i^j represents the linear intrastate and quadratic RT coupling parameters [34] for the symmetric (σ_g^+) and degenerate (π_g, π_u) vibrational modes, respectively, for the j^{th} electronic state. The first-order PJT coupling parameter of the i^{th} vibrational mode between the electronic states j and k is given by λ_i^{j-k} and γ_i^j are the second-order parameters of the i^{th} vibrational mode for the j^{th} electronic state. The summations run over the normal modes of vibration of specified symmetry as noted in the index. The + and - sign applicable to the x and y components of the degenerate state, respectively. The calculated VIEs are fit to the adiabatic counterpart

Table 6.1: Symmetry and harmonic frequencies (in cm^{-1}) of vibrational modes of the ground electronic state of C_4H_2.

Symm.	Mode	MP2/aug-cc-pVTZ	(fc)CCSD(T)/cc-pVQZ [13]	Ref. [32]	Expt. [33]	Description
σ_g^+	ν_1	3475	3457	3489	3332	C-H symmetric stretch
	ν_2	2185	2235	2222	2189	C≡C symmetric stretch
	ν_3	897	892	885	872	C-C symmetric stretch
σ_u^+	ν_4	3475	3458	3490	3333	C-H asymmetric stretch
	ν_5	2001	2057	2050	2019	C≡C asymmetric stretch
π_g	ν_6	608	632	638	626	C-H bend
	ν_7	448	481	490	483	C-C bend
π_u	ν_8	619	634	641	628	C-H bend
	ν_9	219	220	223	220	C-C bend

Table 6.2: *Ab initio* calculated linear (κ_i / $\lambda_i^{X,A}$) and quadratic (γ_i / η_i) coupling constants for the $\widetilde{X}^2\Pi_g$ and $\widetilde{A}^2\Pi_u$ electronic states of $C_4H_2^+$. All quantities are given in the eV unit.

Mode (Freq)	κ_i or η_i	γ_i	κ_i or η_i	γ_i	$\lambda_i^{X,A}$
	$\widetilde{X}^2\Pi_g$		$\widetilde{A}^2\Pi_u$		
σ_g^+ ν_1 (0.4309)	-0.0135 (0.0005)	0.0022	-0.0203 (0.0011)	0.0013	-
ν_2 (0.2710)	-0.2393 (0.3900)	0.0103	-0.0645 (0.0283)	0.0098	-
ν_3 (0.1112)	0.0396 (0.0634)	-0.0029	-0.1372 (0.7611)	0.0090	-
σ_u^+ ν_4 (0.4309)	-	0.0011	-	0.0019	0.0234 (0.0014)
ν_5 (0.2481)	-	-0.0083	-	0.0352	0.1737 (0.2451)
π_g ν_6 (0.0754)	0.0086 (0.0065)	-0.0014	0.0057 (0.0028)	-0.0085	-
ν_7 (0.0556)	0.0093 (0.0140)	0.0052	-0.0068 (0.0075)	-0.0229	-
π_u ν_8 (0.0768)	0.0123 (0.0128)	0.0021	-0.0083 (0.0058)	-0.0082	-
ν_9 (0.0271)	0.0014 (0.0013)	-0.0375	0.0012 (0.0009)	-0.0356	-

of diabatic electronic Hamiltonian of Eq. 6.1 by a least squares procedure to estimate the parameters of the Hamiltonian defined above.

6.2.2 Electronic structure calculations

The equilibrium molecular structure of C_4H_2 in its electronic ground state is optimized within the MP2 level of theory employing Dunning's aug-cc-pVTZ basis set [40] using Gaussian 03 suite of programs [41]. Harmonic vibrational frequencies (ω_i) and mass-weighted normal displacement coordinates are calculated. The latter coordinates are multiplied by $\sqrt{\omega_i}$ (in atomic units) to transform them to their dimensionless form (Q_i) [42]. In this definition equilibrium geometry of C_4H_2 occurs at $\mathbf{Q}$=0. The calculated

harmonic frequencies of the 13 vibrational modes (including degeneracy) including their symmetry and description along with the available literature data are given in Table 6.1. The vertical ionization energies (VIEs) of C_4H_2 along each relevant vibrational mode for various nuclear geometries, $Q_i = \pm 0.10$ and $\pm$ 0.25 to $\pm$ 4.0 with a spacing of 0.25, are computed at the equation-of-motion coupled-cluster singles and doubles (EOMIP-CCSD) level of theory using aug-cc-pVTZ basis set. All the EOMIP-CCSD calculations are performed using CFOUR suite of programs [43]. These *ab initio* energies are fit to the adiabatic counterpart of the diabatic electronic Hamiltonian of Eq. 6.1 by a least squares procedure to estimate the parameters of the Hamiltonian defined in Sec. 6.2.1. The VIEs and the parameters of the Hamiltonian estimated in that way are given in Table 6.2. Full dimensional calculations are carried out including all 13 vibrational modes in the nuclear dynamics study presented later in the text.

6.3 Results and discussion

6.3.1 Adiabatic potential energy surfaces and conical intersections

In this section the topography of the adiabatic PESs of the degenerate ground and first excited doublet electronic states of $C_4H_2^+$ obtained by diagonalizing the diabatic electronic Hamiltonian are examined. According to the symmetry selection rules given in Sec. 6.2.1, the totally symmetric vibrational modes ν_1-ν_3 of C_4H_2 cannot split the degeneracy of the $\widetilde{X}^2\Pi_g$ and $\widetilde{A}^2\Pi_u$ electronic states. One dimensional cuts of the multidimensional PESs of $C_4H_2^+$ are viewed along the given totally symmetric (σ_g^+) vibrational mode, keeping others at their equilibrium values are shown in Fig. 6.1. The RT effect lifts the degeneracy of $\widetilde{X}$ and $\widetilde{A}$ electronic states when the molecule is distorted along π_g (ν_6-ν_7) and π_u (ν_8-ν_9) vibrational modes. To obtain the adiabatic PES of $C_4H_2^+$ along π_g mode, one needs to diagonalize the Hamiltonian of Eq. 6.1. Retaining only the x components of π_g mode these PESs are plotted in Fig. 6.2(a-b). In analytic form the PESs are given by

$$V_{\pm} = E + \frac{1}{2}(\omega + \gamma \pm \eta)(Q_x^2 + Q_y^2)$$

Similarly, one dimensional cuts of the adiabatic PESs of electronic states of $C_4H_2^+$ along π_u vibrational are calculated and plotted in Fig. 6.2(c-d). The calculated vertical ionization energies plus the ground-state potential energy of C_4H_2 along the given mode are shown by the points in the respective diagram. A least square fit of the adiabatic counterpart of the diabatic electronic Hamiltonian of Eq. 6.1 is shown by the solid lines superimposed on the points. It can be seen From Figs. 6.1 and 6.2 that the computed *ab initio* energies are very well fit to the present vibronic coupling model and also for fairly large internuclear displacements along all the symmetric vibrational modes.

The relevant stationary points of the PESs viz., the energetic minimum ($V_{min}^{(ci)}$) of the

seam of CIs and the energetic minimum (V_{min}) of the electronic states are calculated. The multi dimensional energetic minimum of $\widetilde{X}$ and $\widetilde{A}$ states occurs at $\sim$ 10.23 and $\sim$ 12.85 eV, and the $\widetilde{X}$-$\widetilde{A}$ seam minimum occurs at higher energies, $\sim$ 27.16 eV. It is therefore clear that this seam would not have much effect on the nuclear dynamics studies. This is discussed in relation to the electron population dynamics later in the text.

6.3.2 Vibronic structure of the electronic states

Uncoupled state spectrum

In order to demonstrate the effect of nonadiabatic coupling on the vibronic structure of the photoionization bands of C_4H_2, the vibrational energy level structure of the uncoupled $\widetilde{X}$ and $\widetilde{A}$ states of $C_4H_2{}^+$ are first examined. The coupling between the states is included subsequently and the final results are compared with the experiment and discussed. The uncoupled state spectra shown in Fig. 6.3 are calculated by the time-independent matrix diagonalization approach as discussed in Chapter 2. The theoretical stick line spectrum of each electronic state is calculated with the vibronic Hamiltonian of Eq. 6.1 and including all totally symmetric vibrational modes ν_1-ν_3. A Lorentzian line shape function of 20 meV full width at the half maximum (FWHM) is used to convolute the stick line spectrum in each case and to generate the respective spectral envelope.

In the uncoupled states situation and in absence of any intermode coupling terms, the Hamiltonian for $\widetilde{X}^2\Pi_g$ and $\widetilde{A}^2\Pi_u$ states are separable in terms of the σ_g^+, π_g and π_u modes. One can therefore calculate spectra separately for including totally symmetric modes and including with RT coupling modes in addition with totally symmetric modes. The spectra obtained by including only the σ_g^+ (ν_1-ν_3) modes are shown in Fig. 6.3(a). In the $\widetilde{X}$ state excitation of ν_1, ν_2 and ν_3 modes is weak, strong and moderate, respectively. The fundamentals due to ν_1, ν_2, and ν_3 vibrations are $\sim$0.432, $\sim$0.276 and $\sim$0.110 eV spaced, respectively, from the origin peak of the $\widetilde{X}$ band. Since the coupling strength of the ν_2 mode is particularly strong, this mode forms an extended progression in the $\widetilde{X}$ state spectrum, the same trend can be observed for the ν_3 mode in the $\widetilde{A}$ state. Peak spacing of $\sim$0.431, $\sim$0.276 and $\sim$0.116 eV due to the fundamentals of ν_1, ν_2 and ν_3 vibrational modes, respectively, is found from the $\widetilde{A}$ band. In this state the coupling strength of ν_1, ν_2 and ν_3 vibrational modes is weak, moderate and strong, respectively, in that order.

The spectra convoluted by including RT π_g and π_u modes (ν_6-ν_9) in addition to totally symmetric modes are shown in the bottom panel of the same Figure. The coupling strength of these RT coupling modes is weak in both $\widetilde{X}$ and $\widetilde{A}$ states, as a result, the coupling effect is small when these modes are included in the dynamics. The overall spectral envelop is very similar to the spectra obtained with totally symmetric modes, but the broadening of the peaks is clearly visible from the bottom panel, due to the RT coupling effect.

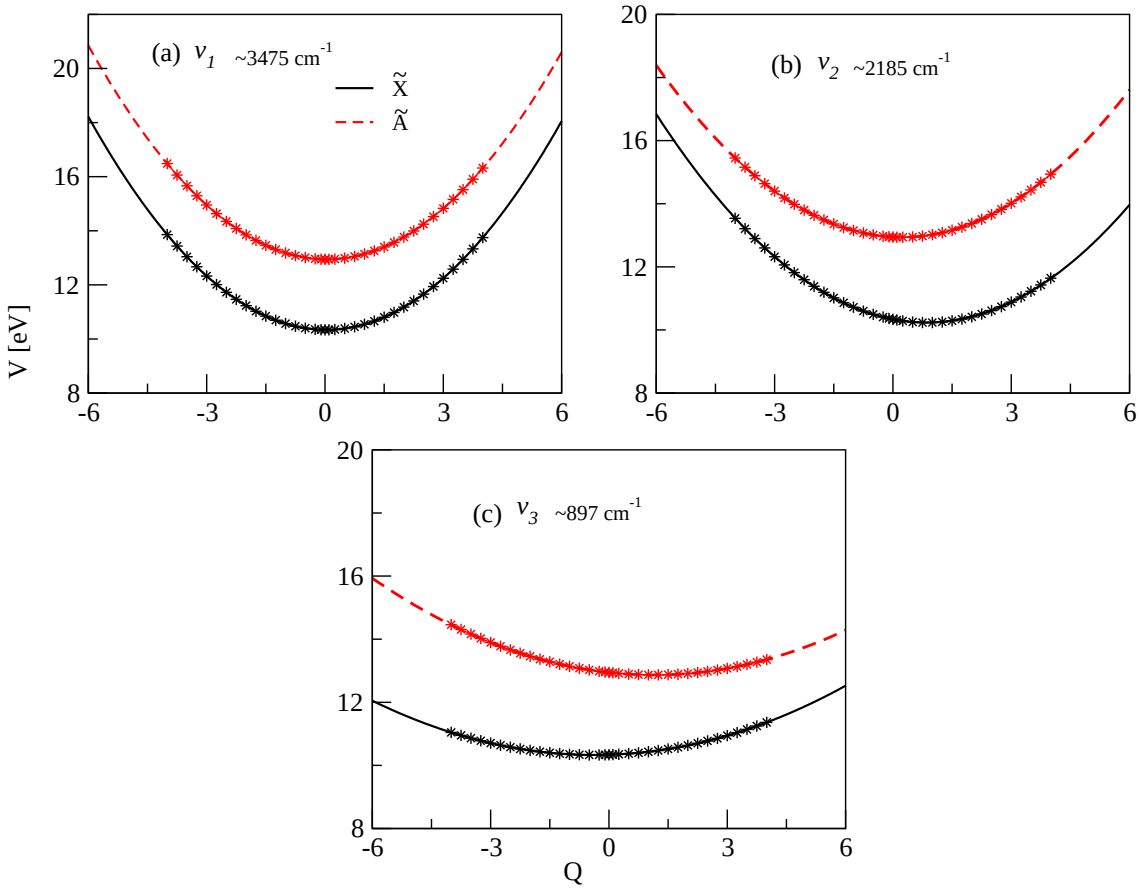

Figure 6.1: Adiabatic potential energy surfaces of the $\widetilde{X}$ and $\widetilde{A}$ electronic states of $C_4H_2^+$ along the totally symmetric vibrational modes (ν_1-ν_3). The energies obtained from the present vibronic model are shown by the solid lines and the computed *ab initio* energies are shown by the points.

To this end some of the spectral progressions reported in experiments are compared with our theoretical findings. Excitation of the ν_2 vibrational mode in the $\widetilde{X}$ band is reported by Baker *et al.* [7]. From Table 6.2, it can be seen that this mode has the strongest excitation strength compared to all other symmetric modes in the $\widetilde{X}$ state. Our theoretical analysis reveals that the fundamental of ν_2 appears at ~2227 cm^{-1} as compared to its value ~2121 cm^{-1} reported in the experiment of Baker *et al.* [7]. Bondybey *et al.* also identified the fundamental ν_1, ν_2, ν_3 modes and the overtone of ν_7 vibrational mode at ~3143, ~2177, ~865 and ~973 cm^{-1} respectively. These results are in good accord with our theoretical progressions of ~3484, ~2227, ~885 and ~1007 cm^{-1}, respectively, in that order. In the $\widetilde{A}$ state major progressions are formed by ν_1, ν_2, ν_3 and the overtone

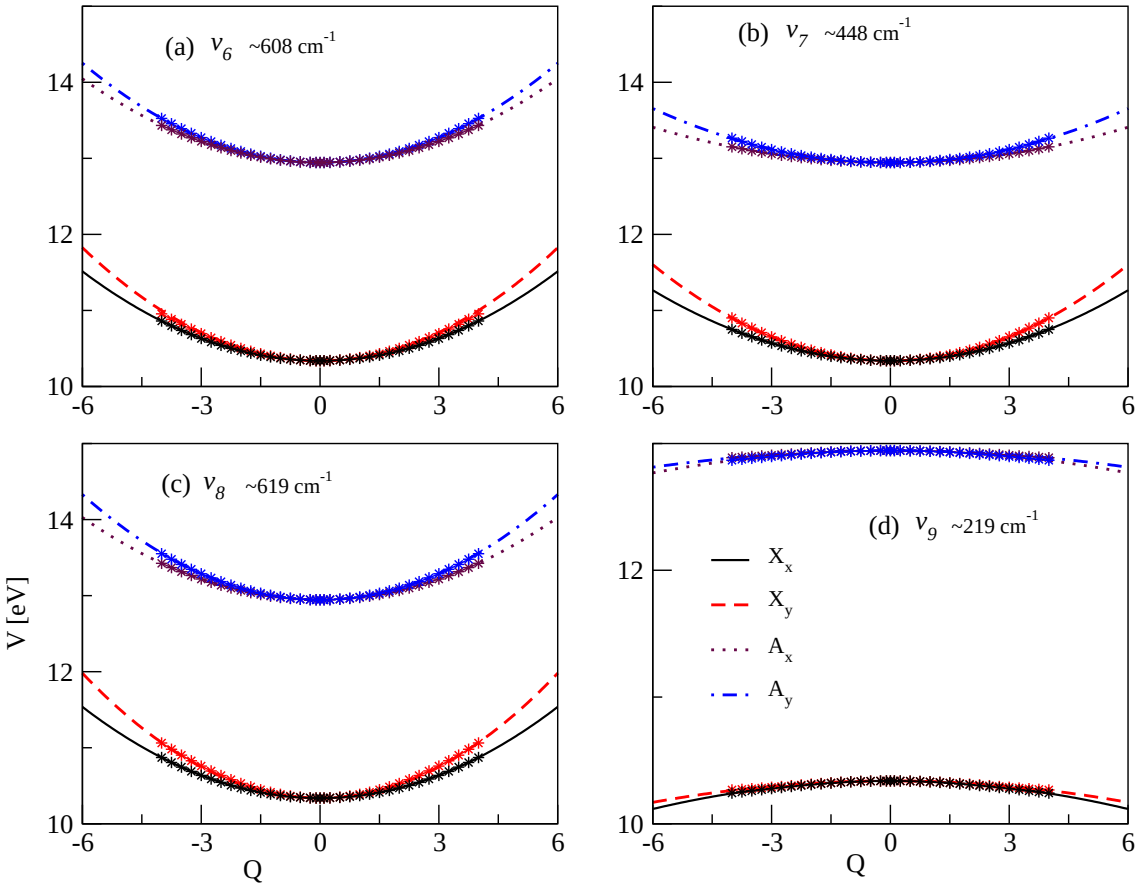

Figure 6.2: Same as in Fig. 6.1 for the degenerate π_g (ν_6-ν_7) and π_u (ν_8-ν_9).

Table 6.3: Vibrational energy progressions of $\widetilde{A}^2\Pi_u$ state and the comparison with experimental studies.

Mode	our theory	Ref. [29]	Ref. [30]	Ref [23]	Ref. [17]
ν_1	3481	3137	3158	-	2821
ν_2	2224	2177	2096	1961	2002
ν_3	932	861	987	806	807
$2\nu_7$	755	971	-	862	861

of ν_7 vibrational mode. Many groups identified the progressions in $\widetilde{A}$ state and assigned to the corresponding vibrational modes. A comparative account of the results is given in Table 6.3.

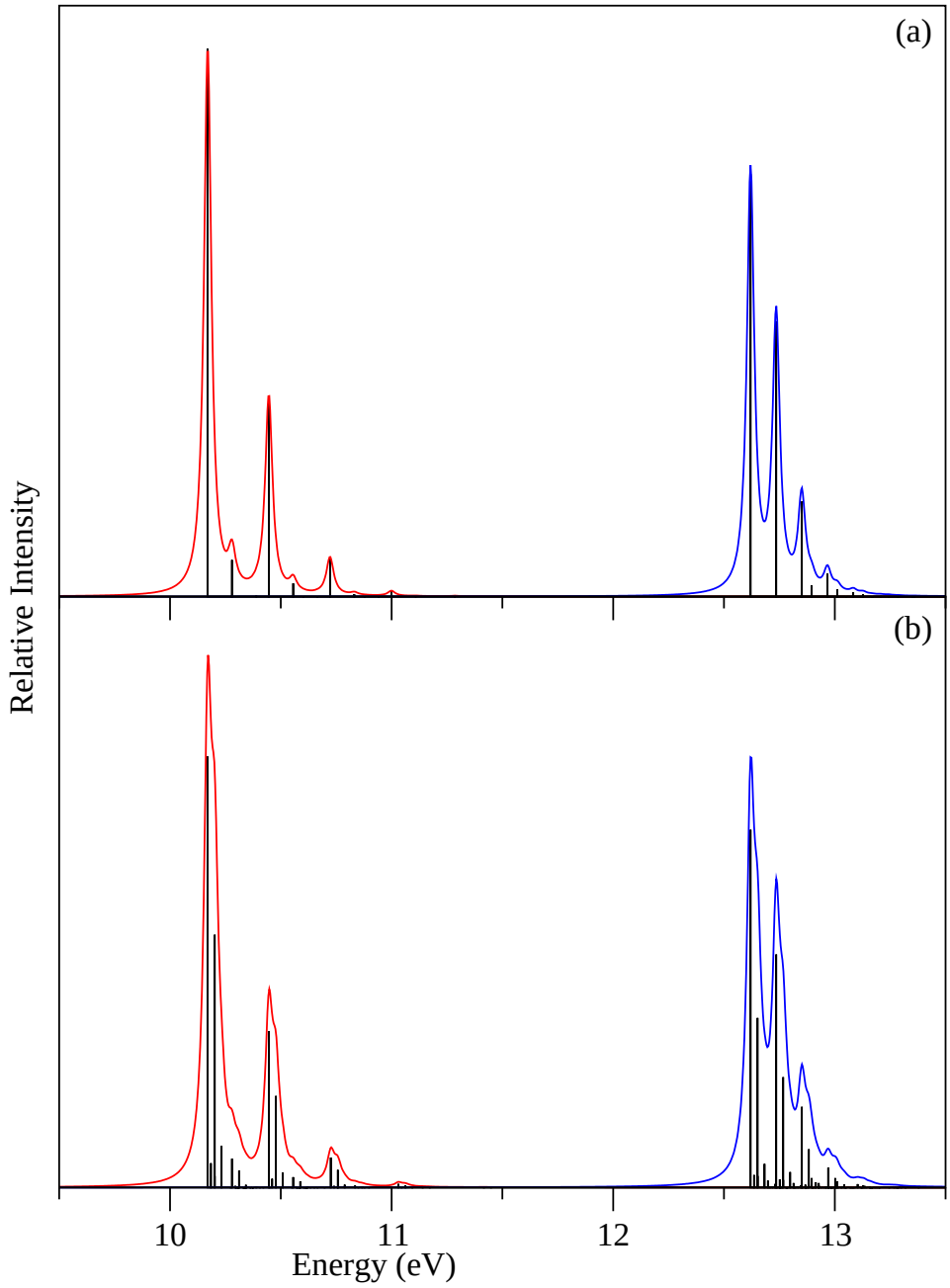

Figure 6.3: Vibrational energy level spectrum of the uncoupled $\widetilde{X}$ and $\widetilde{A}$ electronic states of $C_4H_2^+$ computed with (a) totally symmetric vibrational modes (σ_g), (b) including with RT coupling vibrational modes (π_g and π_u).

Table 6.4: Normal mode combinations and size of the primitive and single-particle basis functions used in the converged MCTDH calculations for the coupled $\widetilde{X}$-$\widetilde{A}$ electronic states of $C_4H_2^+$.

Normal modes	Primitive basis	SPF basis
(ν_1,ν_4,ν_{6y},ν_{8x},ν_{9y})	(4,4,6,6,6)	[10,12,8,12]
(ν_2,ν_5,ν_{7x},ν_{8y})	(8,8,6,6)	[12,10,8,10]
(ν_3,ν_{6x},ν_{7y},ν_{9x})	(10,6,6,6)	[8,12,10,10]

Coupled state spectrum

So far the PJT coupling between the $\widetilde{X}$ and $\widetilde{A}$ electronic states is not considered. On inclusion of this coupling, the separation of the Hamiltonian in terms of the symmetric and degenerate vibrational modes for the degenerate electronic states as explored above is no longer possible. It is therefore necessary to follow the nuclear dynamics simultaneously on four (two degenerate) coupled electronic states. Full dimensional calculations are therefore carried out including all 9 nondegenerate plus degenerate vibrational modes. The WP propagation approach within the MCTDH framework has been undertaken to accomplish this task. The MCTDH suite of program modules developed by the Heidelberg group [44] is utilized for this purpose. The initial WP pertinent to the vibronic ground state of neutral C_4H_2 is vertically launched on each of the mentioned electronic states of the radical cation separately and then propagated upto 200 fs in the coupled manifold of four electronic states. Four independent calculations are carried out and the autocorrelation function of the WP as well as the diabatic electronic population is recorded at an interval of 1.0 fs throughout the entire propagation duration. The numerical details of the mode combinations, sizes of the primitive and single particle basis used in the WP propagation are given in Table 6.4.

In order to generate the composite photoionization band, the autocorrelation function from four different calculations are combined with equal weightage, damped with an exponential function, $e^{(-t/\tau_r)}$ (with τ_r = 33 fs) and Fourier transformed to the energy domain. Damping of the time autocorrelation function with the given exponential function is equivalent to convolution of the energy spectrum with a Lorentzian function of 40 meV FWHM. The resulting theoretical band structure is plotted in panel a of Fig. 6.4 along with the experimental results (reproduced from Ref. [7]) in panel b. In Fig. 6.4 the relative intensity in arbitrary units is plotted as a function of the energy (in eV) of the final vibronic state. It can be seen from Fig. 6.4 that the present theoretical results nicely reproduce the observed complex and overlapping band structure of $C_4H_2^+$.

6.3.3 Time-dependent population dynamics

In this section, the time-dependence of the diabatic electronic populations in the coupled $\widetilde{X}$-$\widetilde{A}$ electronic states is presented and discussed. In order to calculate the latter

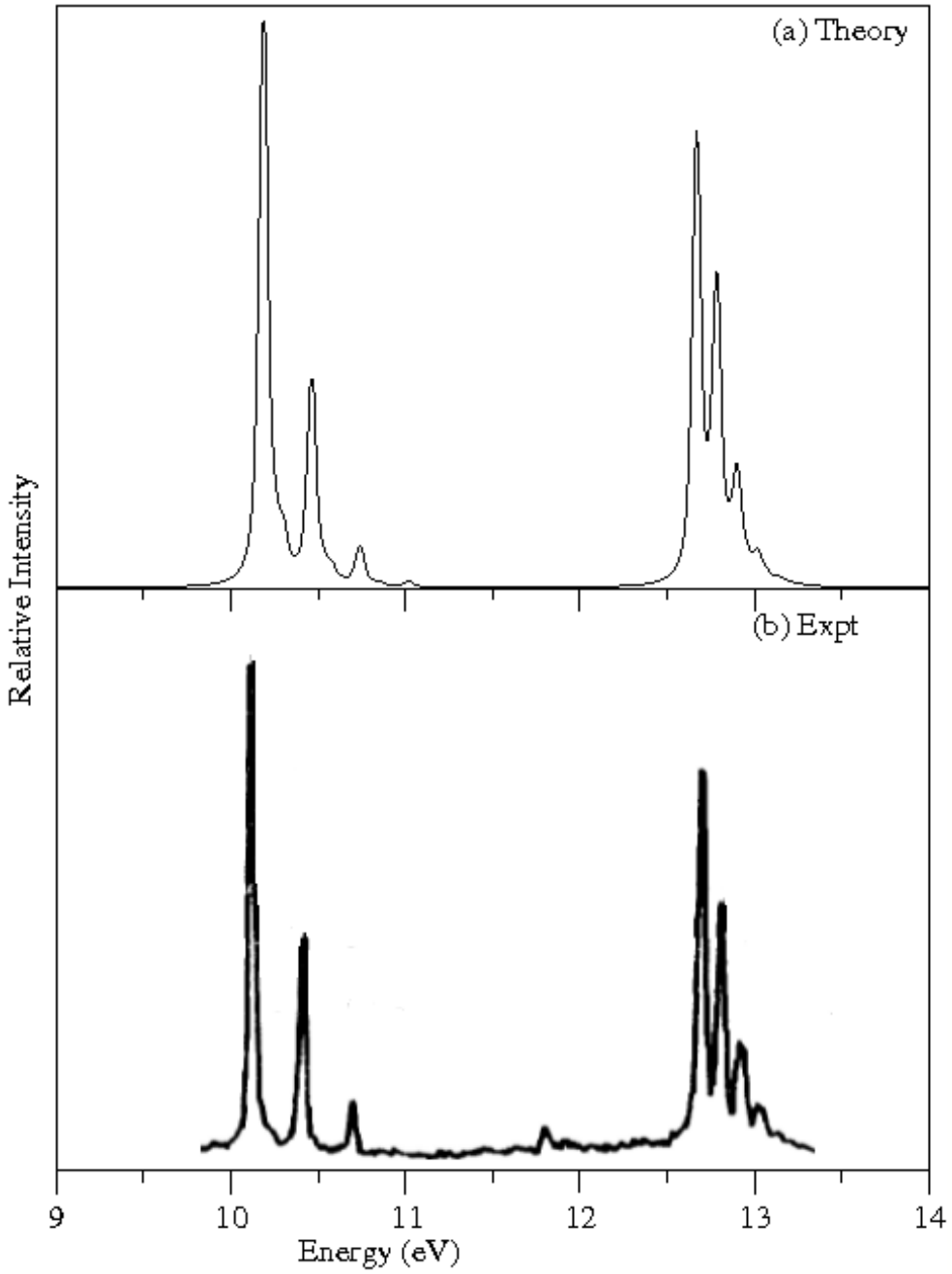

Figure 6.4: Broad band vibronic structure of the $\widetilde{X}$-$\widetilde{A}$ electronic states of $C_4H_2{}^+$. Relative intensity (in arbitrary units) is plotted as a function of the energy of the vibronic states of $C_4H_2{}^+$. The present theoretical results are shown in panel a and the experimental photoelectron spectroscopy results (reproduced from Ref [7].

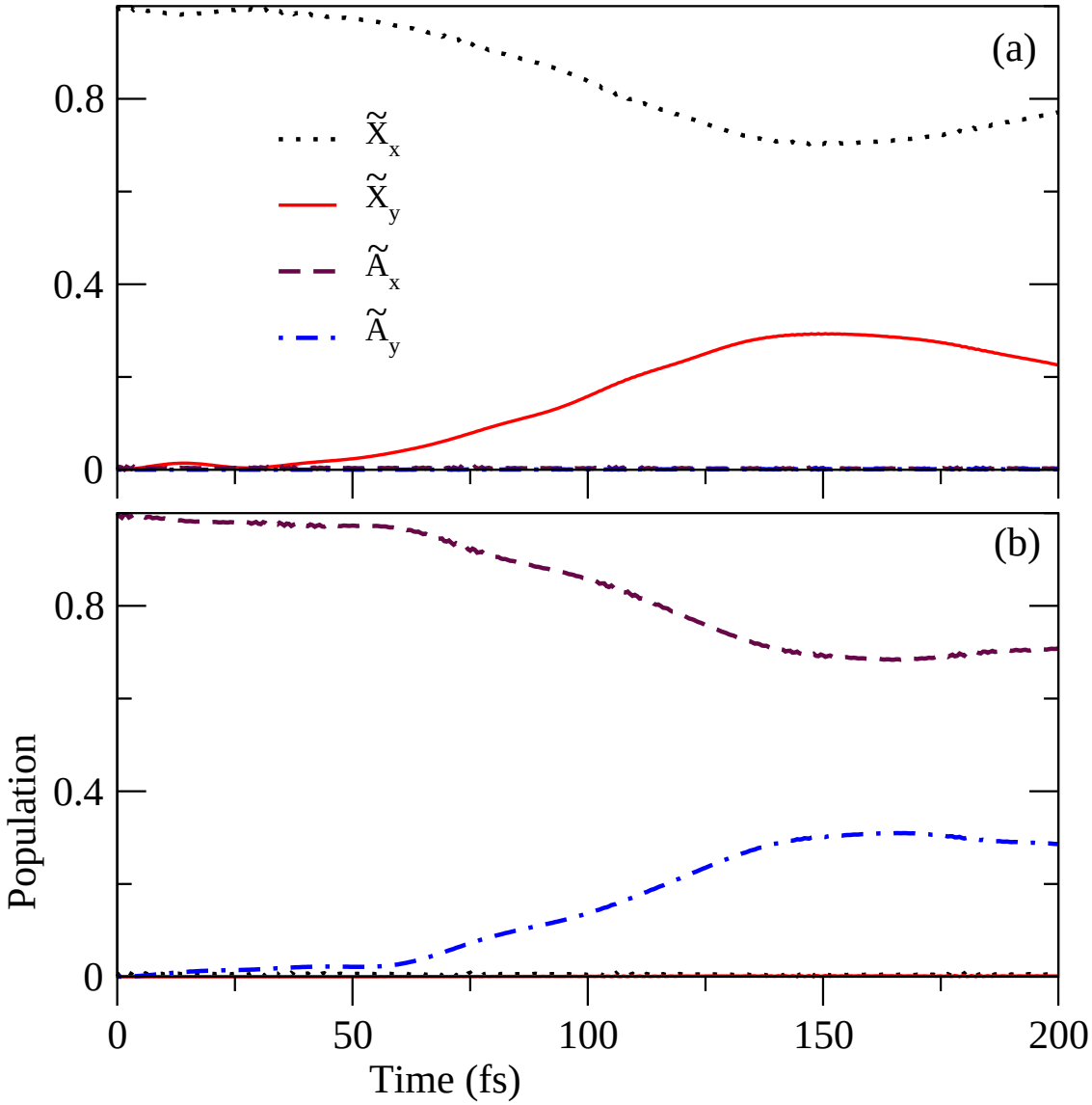

Figure 6.5: Time dependence of diabatic populations of the $\widetilde{X}$-$\widetilde{A}$ coupled states nuclear dynamics of $C_4H_2^+$. The results obtained by initially locating the WP on the $\widetilde{X}$ state in panel (a) and $\widetilde{A}$ state in panel (b).

the time-dependence of the diabatic electronic populations for an initial transition to each of the above electronic states separately recorded. The results are shown in Fig. 6.5(a-b). Interesting observations on the dynamical mechanism can be obtained from these population curves in conjunction with the coupling parameters given in Table 6.2 and the stationary points on the PESs detailed in Sec. 6.3.1.

In panel a and b of Fig. 6.5, the population dynamics is shown for an initial transition of the WP to one of the two RT split components of the $\widetilde{X}$ and $\widetilde{A}$ electronic states, respectively. Due to the RT effect where the decay and growth of the population of x and y components of the degenerate electronic state occur in both cases. The population transfer to the counter component is large in the both cases. The $\widetilde{X} \leftrightarrow \widetilde{A}$ population transfer is quite negligible, even though moderate PJT coupling of these states along ν_5 vibrational mode. These two electronic states are vertically well separated, as discussed in Sec. 6.3.1 that the CI of the $\widetilde{X}$ state with $\widetilde{A}$ state are located at higher energies. Therefore, these CI is not accessible to the WP during its evolution on both the electronic states. As a result, sharp vibrational levels of the $\widetilde{X}^2\Pi_g$ and $\widetilde{A}^2\Pi_u$ states emerged in the photoionization bands of C_4H_2.

6.3.4 DIBs related to $D_0 \rightarrow D_1$ of $C_4H_2^+$

Recent experimental spectral studies on $C_4H_2^+$ reveal that the strongest transition of $D_0 \rightarrow D_1$ occurring very close to the 5069 Å DIB. The 0_0^0 peak position of the $\widetilde{A}$ band was reported by Motolewski *et al.* [11] at 5068.65 Å and the same was observed at 5067.8 Å by Maier *et al.* [12]. This peak is very close to the 5069 Å DIB. Krełowski *et al.* proposed that the spectral profile of the 5069 Å DIB is in good agreement with $D_0 \rightarrow D_1$ transition of $C_4H_2^+$ and this molecular cation could be responsible for the 5069 Å DIB [3]. Very recent experimental studies confirmed that neither the $\widetilde{A}^2\Pi_u$ band shape nor the wavelength of the absorption maximum of $C_4H_2^+$ could be associated with the 5069 Å DIB [12]. However, the origin of the $D_0 \rightarrow D_1$ transition of $C_4H_2^+$ is vary close to the 5069 Å DIB and strongly supports the earlier claims.

6.4 Summarizing remarks

Multimode vibronic dynamics in the energetically lowest two important electronic states of $C_4H_2^+$ is investigated in this article. Detailed *ab initio* electronic structure calculations are carried out to construct the potential energy surfaces of these two electronic states and their coupling surfaces. A diabatic vibronic coupling model is thereby established and the nuclear dynamics is studied on the coupled manifold of five electronic states by time-independent and time-dependent quantum mechanical methods. The vibronic structure of each electronic state is carefully examined in both uncoupled and coupled states situations and the spectral progressions are assigned and compared with available experimental data. The final composite vibronic band structure is calculated by a wave packet propagation method and the theoretical results obtained are found to be in good accord with the experiment. The nonadiabatic coupling among the two electronic states is quenched by the large energy separation, which leads nearly discrete band structures of the two states.

Krełowski *et al.* proposed that the spectral profile of the 5069 Å DIB is in good agreement with $D_0 \rightarrow D_1$ transition of $C_4H_2^+$ and this molecular cation could be responsible for the 5069 Å DIB [3]. Very recent experimental studies confirmed that neither the $\widetilde{A}^2\Pi_u$ band shape nor the wavelength of the absorption maximum of $C_4H_2^+$ could be associated with the 5069 Å DIB [12]. However, the origin of the $D_0 \rightarrow D_1$ transition of $C_4H_2^+$ is vary close to the 5069 Å DIB and strongly supports the earlier claims.

References

[1] T. Henning, F. Salama, Science, **282**, 2204 (1998).

[2] R. I. Kaiser, A .M. Mebel, Chem. Rev. Soc. **41**, 5490 (2012).

[3] J. Krełowski, Y. Beletsky, G. A. Galazutdinov, R. Kołos, M. Gronowski and G. Locurto, Astrophys. J. **714**, L64 (2010).

[4] T. S. Zwier and M. Allen, Icarus, **123**, 578 (1996).

[5] J. R. Pardo, J. Cernicharo, Astrophys. J. **654**, 978 (2007).

[6] J. Fulara, D. Lessen, P. Freivogel and J. P. Maier, Nature, **366**, 439 (1993).

[7] C. Baker and D. W. Turner, Chemical Communications, 797 (1967).

[8] M. Gronowski, R. Kołos and J. Krełowski, Chem. Phys. Lett. **582**, 56 (2013).

[9] R. I. Kaiser, B. J. Sun, H. M. Lin, A. H. H. Chang, A. M. Mebel and O. Kostko, Astrophys. J. **719** 1884 (2010).

[10] J. Fulara, M. Grutter and J. P. Maier, J. Phys. Chem. A, **111**, 11831 (2007).

[11] T. Motylewski, H. Linnartz, O. Vaizert, J. P. Maier *et al.* Astrophys. J. **531**, 312 (2000).

[12] J. P. Maier, S. Chakrabarty, F. J. Mazzotti *et al.* Astrophys. J. **729**, L20 (2011).

[13] S. Thorwirth, M. E. Harding, D. Muders, J. Gauss, J. Mol. Spectrosc. **251**, 220 (2008).

[14] M. Allan, E. Kloster-Jensen & J. P. Maier, Chem. Phys. **7**, 11 (1976).

[15] T. Bally, W. Tang, & M. Jungen, Chem. Phys. Lett. **190**, 453 (1992).

[16] D. Zhao, K. D. Doney, H. Linnartz, J. Mol. Spectrosc. **296**, 1 (2014).

[17] V. L. Bondybey & J. H. English, J. Chem. Phys. **71**, 777 (1979).

[18] A. L. Sobolewski and L. Adamowicz, J. Chem. Phys. **102**, 394 (1995).

[19] J. Zhang, X. Guo, and Z. Cao, J. Chem. Phys. **131**, 144307 (2009).

[20] F. Vila, P. Borowski and K. D. Jordan, J. Phys. Chem. A, **104**, 9009 (2000).

[21] R. Raghunandan, F. J. Mazzotti, A. M. Esmail, and J. P. Maier, J. Phys. Chem. A, **115**, 9365 (2011).

[22] M. Schwell, *et al.* Mol. Phys. **110**, 2843 (2012).

[23] T. W. Schmidt, T. Pino, J. van Wijngaarden, K. Tikhomirow, F. Guthe, & J. P Maier, J. Mol. Spectrosc. **222**, 86 (2003).

[24] P. Freivogel *et al.* Chem. Phys. **189**, 335 (1994).

[25] C. Ramos, P. R. Winter, T. S. Zwier, S. T. Pratt, J. Chem. Phys. **116**, 4011 (2002).

[26] N. Kohima, P. Rosmus, J. P. Maier, Mol. Phys. **104**, 3281 (2006).

[27] L. Bizzocchi, F. Tamassia, C. D. Esposti, L. Fusina, E. Cane, L. Dore, Mol. Phys. **109**, 2181 (2011).

[28] J. Szczapanski *et al.* Phys. Chem. Chem. Phys. **7**, 738 (2005).

[29] J. H. Callomon, Can. J. Phys. **34**, 1046 (1956).

[30] W. L. Smith, Proc. R. Soc. A, **300**, 519 (1967).

[31] C. Baker and D. W. Turner, Proc. R. Soc. A, **308**, 19 (1968).

[32] G. A. Williams, J. N. Macdonald, J. Mol. Struct. **320**, 217 (1994).

[33] G. Guelachvili, A. M. Craig, D. A. Ramsay, J. Mol. Spectrosc. **105**, 156 (1984).

[34] H. Köppel, W. Domcke, L. S. Cederbaum, Adv. Chem. Phys. **57**, 59 (1984).

[35] E. B. Wilson Jr., J. C. Decius, P. C. Cross, Molecular vibrations (McGraw-Hill, New York, 1955).

[36] W. Lichten, Phys. Rev, **164**, 131 (1967). (b) F. T. Smith, Phys. Rev, **179**, 111 (1969). (c) T. F. O'Mal1ey, T. F. Adv. At. Mol. Phys. **7**, 223 (1971). (d) T. Pacher, L. S. Cederbaum and H. Köppel, Adv. Chem. Phys. **84**, 293 (1993).

[37] M. Döscher, H. Köppel, and P. Szalay, J. Chem. Phys. **117**, 2645, (2002).

[38] T. S. Venkatesan, H.-D. Meyer, H. Köppel, L. S. Cederbaum and S. Mahapatra, J. Phys. Chem. A, **111**, 1746 (2007).

[39] T. Mondal, S. R. Reddy and S. Mahapatra, J. Chem. Phys. **137**, 054311 (2012).

[40] Jr. T. H. Dunning, J. Chem. Phys. **90**, 1007 (1989).

[41] M. J. Frisch *et al.*, Gaussian 03, Revision B. 05, Gaussian, Inc., Pittsburgh PA, 2003.

[42] E. B. Wilson, J. C. Decius and P. C. Cross, Molecular vibrations; McGraw-Hill: New York, 1955.

[43] CFOUR, a quantum chemical program package written by J. F. Stanton, J. Gauss, M. E. Harding, P. G. Szalay with contributions from A. A. Auer, R. J. Bartlett, U. Benedikt, C. Berger, D. E. Bernholdt, Y. J. Bomble, L. Cheng, O. Christiansen, M. Heckert, O. Heun, C. Huber, T. -C. Jagau, D. Jonsson, J. Jusélius, K. Klein, W. J. Lauderdale, D. A. Matthews, T. Metzroth, L. A. Mück, D. P. O'Neill, D. R. Price, E. Prochnow, C. Puzzarini, K. Ruud, F. Schiffmann, W. Schwalbach, C. Simmons, S. Stopkowicz, A. Tajti, J. Vázquez, F. Wang, J. D. Watts and the integral packages MOLECULE (J. Almlöf, P. R. Taylor), PROPS (P. R. Taylor), ABACUS (T. Helgaker, H. J. Aa. Jensen, P. Jørgensen, J. Olsen), and ECP routines by A. V. Mitin, C. van Wüllen. For the current version, see http://www.cfour.de.

[44] a) G. A. Worth, M. H. Beck, A. Jäckle, H.-D. Meyer, *The MCTDH Package,* Version 8.2, (2000), University of Heidelberg, Heidelberg, Germany. H.-D. Meyer, Version 8.3 (2002), Version 8.4 (2007). ML-MCTDH implemented in forthcoming version 8.5 (2011), see http://mctdh.uni-hd.de/; b) H.-D. Meyer, U. Manthe, L. S. Cederbaum, Chem. Phys. Lett. **165**, 73 (1990); c) U. Manthe, H.-D. Meyer, L. S. Cederbaum, J. Chem. Phys. **97**, 3199 (1992); d) M. H. Beck, A. Jäckle, G. A. Worth, H.-D. Meyer, Phys. Rep. **324**, 1 (2000).

7 Conclusions and Future Directions

Motivated by the astrophysical observations and laboratory experimental spectroscopy measurements, a theoretical mechanistic description of vibronic dynamics of electronically excited propadienylidene, diacetylene radical cation ($C_4H_2^+$) and radical cations of non-compact (Tn^+, Pn^+ and Hn^+) and compact (Pnt^+, Py^+ and Acn^+) PAHs is presented in this thesis. This study involves construction of model molecular vibronic Hamiltonians, and estimation of the vibronic coupling parameters of the Hamiltonians with the aid of *ab initio* electronic structure calculations using Gaussian, Molpro and Cfour suite of programs. Subsequent quantum nuclear dynamics simulations both in time-independent and time-dependent approaches are performed to uncover the spectroscopy and dynamics of these molecules. The advantage of this approach is its conceptual and technical simplicity and the outcomes of outstanding quality. Our results revealed the importance of vibronic coupling effects in the spectroscopy. The results obtained by our theoretical model are in excellent agreement with the experimental photoelectron and absorption spectral studies. Some of these bands are in excellent agreement with the high resolution ZEKE and MIS studies.

Important findings of the present work are discussed below

Chapter 3. (a) The transition to the $\widetilde{A}$ state from the reference ground state is optically dark in propadienylidene cation. Owing to a strong coupling of the $\widetilde{A}$ state with the optically bright $\widetilde{B}$ state, particularly along the $\sim$252 cm^{-1} (C=C=C in-plane bending) ν_7 vibrational mode of b_2 symmetry, one expects a significant intensity borrowing effects that would make this state visible in the absorption experiment. This is indeed true and a weak and structured tail is observed at the long wavelength region of the $\widetilde{B}$ band.

(b) The intense peaks in the $\widetilde{B}$ state spectrum are $\sim$2000 cm^{-1} spaced corresponding to the frequency of the ν_2 vibrational mode, is in good agreement with experimental value. Much weaker excitation of the ν_4 and ν_3 vibrational modes is also found from the the theoretical vibrational progression.

(c) Vibronic coupling effects in the spectrum due to $\widetilde{B}$-$\widetilde{C}$ coupling are negligibly small compared to the $\widetilde{A}$-$\widetilde{B}$ coupling. In the $\widetilde{C}$ state the vibrational modes ν_4 and ν_3 form major progressions, peak spacings are 1174 and 1477 cm^{-1}, respectively, in that order.

(d) The initial fast decay of populations of the $\widetilde{B}$ state relates to a nonradiative internal conversion rate of $\sim$28 fs ($\sim$98 fs), $\sim$28 fs ($\sim$84 fs) and $\sim$25 fs ($\sim$90 fs) in the adiabatic

(diabatic) picture employing EOM-CCSD, CASSCF(10,10)-MRCI and CASSCF(14,12)-MRCI electronic structure derived Hamiltonian parameter sets, respectively.

(e) As a result of strong $\widetilde{A}$-$\widetilde{B}$ vibronic coupling (vide supra), the location of the origin 0_0^0 peak of the $\widetilde{B}$ state turns out to be highly uncertain. It is essentially buried within the continuum of energy levels of the $\widetilde{A}$ state.

(f) On scaling the first fundamental 2_0^1 (2 refers to the ν_2 mode) peak at the location of the DIB at 5450 Å, the second 2_0^2 and third 2_0^3 peaks are located at ∼4929 and ∼4518 Å, respectively. These data compare well with the Ne matrix results at ∼5445/5417, 4856 and 4412 Å and CRD spectroscopy results at ∼5450, 4887(3) and 4425-4445 Å and the Ne matrix results at ∼5390, 4840 and 4400 Å, in that order. Two broad DIBs located at 5450 and 4881 Å by radioastronomy correlate well with the findings given above.

Chapter 4. (a) It is noteworthy that energy of the equilibrium minimum of these linear chain of oligoacene molecules decreases linearly with increasing number of fused benzene ring. Starting from benzene the energies of the equilibrium minimum of the electronic ground state is calculated upto decacene. The root mean square deviation of the predicted (by the linear fit equation) and calculated energies is typically ∼0.0029 E_H.

(b) Examination of one dimensional cuts of the multidimensional PESs along the relevant vibrational modes of all three radical cations reveals that the C=C stretching vibration leads to low-energy crossings of the electronic states.

(c) In all three radical cations $\widetilde{X}$ state is energetically well separated (vertically) from the rest of the states. This is in contrast to our findings for Np^+ and An^+. In the latter case, the $\widetilde{X}$ state forms accessible intersections with the $\widetilde{A}$ state.

(d) The energetic minimum of the multi dimensional seam of CIs is calculated, $\widetilde{X}$-$\widetilde{A}$ CIs increases with increasing number of fused benzene rings. $\widetilde{A}$-$\widetilde{B}$ CIs decreases with increasing number of fused benzene rings and the energetic minimum of the $\widetilde{A}$ and $\widetilde{B}$ states decreases with increasing number of fused benzene rings.

(e) Unlike the nonradiative decay from $\widetilde{A}$ state to $\widetilde{X}$ state via $\widetilde{X}$-$\widetilde{A}$ CIs in Np^+ and An^+, the probability of such transition appears to be negligibly small in case of Tn^+, Pn^+ and Hn^+. Therefore it suffices to say that radiative transition to the electronic ground state is more likely in case of electronically excited Tn^+, Pn^+ and Hn^+.

(f) In case of Tn^+ and Pn^+, $\widetilde{A}$ and $\widetilde{B}$ states are highly overlapping and a strong deviation of vibronic structure in the uncopuled and coupled spectra is observed.

(g) Vertical energy gap between $\widetilde{A}$ and $\widetilde{B}$ electronic states increases from Tn^+ to Hn^+, as a result the $\widetilde{A}$-$\widetilde{B}$ vibronic coupling decreases from Tn^+ to Hn^+.

(h) The adiabatic population decay rate of $\widetilde{B}$ state of Np^+, An^+, Tn^+, Pn^+ and Hn^+ are 240, 63, 22, 14 and 77 fs, respectively.

(i) From the ZEKE spectral analysis of $\widetilde{X}$ state of Tn^+, the peaks at ∼475 (476) [474] cm^{-1}, ∼766 (786) [778] cm^{-1} are in contrast to Zhang *et al.*, who reported a_u (84 cm^{-1}) mode is responsible for these lines. Our assignments are in accordance with the findings of that assigned it to the excitation of the Amirav *et al.*, b_{3g} mode with frequency of ∼494 cm^{-1}.

(j) Salama *et al.* proposed that the observed ∼864.9 and ∼862.1 nm DIBs may associated with the laboratory experimental strong absorption peak of ∼865 nm corresponding to the $D_0 \rightarrow D_2$ transition of Tn^+. The peaks at ∼842.2 and ∼830 nm corresponding to the second strong absorption of $D_0 \rightarrow D_1$ transition of Pn^+ may be a possible carrier of ∼828.325 nm DIB. Based on the peak at ∼865 nm (origin 0_0^0 of Tn^+) and ∼827.1 nm (second strongest transition of Pn^+) seen in the theoretical spectrum of Tn^+ and Pn^+, respectively, can be cautiously attributed to the astrophysical DIBs.

Chapter 5. (a) Examination of one dimensional cuts of the multidimensional PESs along the relevant vibrational modes of all three radical cations reveals that the C=C stretching vibration leads to low-energy crossings of the electronic states. This is analogous to the situation in Np^+-Hn^+ studied by us in the recent past.

(b) A large population transfer from $\widetilde{A}$ state to $\widetilde{X}$ state is observed in the three cations, Pnt^+, Py^+ and Acn^+. For instance, ∼90% of population transfer with in 25 fs is seen in Pnt^+. The population transfer rate ($Pnt^+ > Py^+ > Acn^+$) can be attributed to the energy gap between the the minimum of the $\widetilde{A}$ state and energetic minimum of the $\widetilde{X}$-$\widetilde{A}$ CIs (Pnt^+ (∼0.01 eV) to Py^+ (∼0.19 eV) to Acn^+ (∼0.23 eV)).

(c) The impact of these couplings on the vibronic structure of a given state depends on its energetic location relative to the energetic minimum of the relevant intersection seam. The initial monotonic decrease of population relates to a decay rate of ∼20 fs, ∼42 fs and ∼52 fs of the $\widetilde{A}$ state of Pnt^+, Py^+ and Acn^+, respectively.

(d) Energetic and electronic population decay data revealed faster internal conversion rates for Pnt^+, Np^+, Py^+ and Acn^+ compared to the higher homologs (An^+, Tn^+, Pn^+ and Hn^+). Higher quantum yield of fluorescence emission is expected to the latter series of molecules.

(e) Calculated peaks at ∼860.4 nm (second strongest transition of Pnt^+) and ∼646.3 nm (origin 0_0^0 of Acn^+) are in good agreement with the astrophysical DIBs (∼857.2 and ∼649.2 nm) and laboratory experimental absorption peaks (∼856.8 nm and ∼648.1 nm).

Chapter 6. (a) The vibronic structure of each electronic state is carefully examined in both uncoupled and coupled states situations and the spectral progressions are assigned and compared with available experimental data.

(b) The nonadiabatic coupling among the two electronic states is quenched by the large energy separation, which leads to a sharp band structure of the two states.

(c) The $D_0 \rightarrow D_1$ transition in $C_4H_2{}^+$ occurs very close to the DIB position at 5069 Å. Therefore, the theoretical results of this paper in conjunction with the recorded data suggest that $C_4H_2{}^+$ is a "likely candidate" of a molecular carrier of the 5069 Å DIB.

In conclusion, present theoretical findings demonstrate the importance of electronic nonadiabatic interactions in the (broad) diffuse nature of the observed vibronic bands and ultrafast nonradiative decay of photoexcited molecular systems. The present work sheds new insights into the interpretation and understanding of the electronic transitions of molecules of astrophysical relevance.

It should be also noted that the present study only deals with the photophysics of the doublet low-lying excited electronic states of PAH^+. For a complete understanding, an extended study on higher doublet excited electronic states (> 20 eV) these cations and also singlet electronic states of their neutral counterparts is planned for future. From the experimental point of view, this study can be extended to the carbon chains including hydrogens, bare carbon clusters and acetylene series to search for new DIBs. There is a possibility of hetero atom substituted PAH molecules and acetylene substituted PAH molcules to be a likely carrier of DIBs. Finally, findings of the present work are expected to initiate study in the experimental, observational and theoretical fields of interstellar chemistry and physics of aromatic hydrocarbons.

Curriculam Vitae:

S. Nagaprasad Reddy
Prof. S. Mahapatra Lab,
School of Chemistry,
University of Hyderabad
Hyderabad, 500046,
India.
Email:snpreddy063@gmail.com

List of Publications

1. Samala Nagaprasad Reddy and S. Mahapatra, 'Theoretical Study of Electronic Absorption Spectroscopy of Propadienylidene Molecule *Vis-â-vis* the Observed Diffuse Interstellar Bands', *Chem. Phys.*, 403, 1, (2012).

2. Bharat Kumar Tripuramalli, Paulami Manna, Samala Nagaprasad Reddy and, Samar K. Das, 'Factors Effecting the Conformational Modulation of Flexible Ligands in the Self-Assembly Process of Coordination Polymers: Synthesis, Structural Characterization, Magnetic Properties and Theoretical Studies of $[Co(pda)(bix)]_n$, $[Ni(pda)(bix)(H_2O)]_n$, $[Cu(pda)(bix)_2(H_2O)_2]_n.8nH_2O$, $[Co_2(\mu\text{-}OH)(pda)(ptz)]_n.nH_2O$, $[Co(hfipbb)(bix)_{0.5}]_n$, and $[Co(2,6\text{-}pydc)(bix)_{1.5]n}.4nH_2O$', *Cryst. Growth. Des.*, 12, 777, (2012).

3. Samala Nagaprasad Reddy and S. Mahapatra, 'Theoretical Study on Molecules of Interstellar Interest.I. Radical Cation of Noncompact Polycyclic Aromatic Hydrocarbons', *J. Phys. Chem. A*, 117, 8737, (2013).

4. Ramababu Bolligarla, Samala Nagaprasad Reddy, Gummadi Durgaprasad, Vudagandla Sreenivasulu, and Samar K. Das, 'Influence of the Substituents on the Electronic and Electrochemical Properties of a New Square-Planar Nickel-Bis(quinoxaline-6,7-dithiolate) System: Synthesis, Spectroscopy, Electrochemistry, Crystallography, and Theoretical Investigation', *Inorg. Chem.*, 52, 66, (2013).

5. N. Krishna Reddy, H. Singh, Samala Nagaprasad Reddy, K. Arun Kumar and S. Mahapatra, 'Optimal Initiation of Electronic Excited State Mediated Intramolecular H-Transfer in Malonaldehyde by UV-Laser Pulses', *(Accepted in the European Physical Journal D).*

6. V. Sivaranjana Reddy, Samala Nagaprasad Reddy and S. Mahapatra, 'Strong Non-Adiabatic Effects in the Low-Lying Electronic States of Diborane Radical Cation', *(Manuscript submitted).*

7. A. Marciniak, T. Barillot, A. Rouzee, V. Despre, M. Galbraith, J. Klei, C-H. Yang, C. T. L. Smeenk, V. Loriot, Samala Nagaprasad Reddy, S. Mahapatra, M. J. J. Varakking and F. Lepine 'Multi-Electronic XUV Excitation Followed by Ultrafast Non-Adiabatic Relaxation in PAH Molecules: A Model for Laboratory Astro Chemistry', *(Manuscript Submitted).*

8. Samala Nagaprasad Reddy and S. Mahapatra, 'Theoretical Study on Molecules of Interstellar Interest.II. Radical Cation of Noncompact Polycyclic Aromatic Hydrocarbons', *(Manuscript Under Preperation).*

9. Samala Nagaprasad Reddy and S. Mahapatra, 'Theoretical Study on Molecules of Interstellar Interest.III. Radical Cation of Compact Polycyclic Aromatic Hydrocarbons', *(Manuscript Under Preperation).*

10. Samala Nagaprasad Reddy and S. Mahapatra, 'Spectroscopy and Dynamics of Electronically Excited Diacetylene Radical Cation *Vis-â-vis* the Observed Diffuse Interstellar Bands', *(Manuscript Under Preperation).*

11. Samala Nagaprasad Reddy and S. Mahapatra, 'Excited State Intramolecular Proton Transfer Process in 2'-Hydroxy Chalcones: A Theoretical Study', *(Manuscript Under Preperation).*

Presentations in Conferences and Symposiums

1. Samala Nagaprasad Reddy and S. Mahapatra, 'Theoretical Study on Spectroscopy and Photophysics of Pyracene and Acenaphthene', Presented Poster at '*Spectroscopy and Dynamics of Molecules and Clusters (SDMC-2011)*', February 18th-20th, 2011. Held at Corbett National Park, Uttarakhand, India.

2. Samala Nagaprasad Reddy and S. Mahapatra, 'Theoretical Study on Vibronic Interactions and Absorption Spectroscopy of Propadienylidene molecule', Presented Poster at '*Applied Theory on Molecular Systems (ATOMS-2011)*', November 2nd-5th, 2011. Held at Indian Institute of Chemical Technology, Hyderabad, India.

3. Samala Nagaprasad Reddy and S. Mahapatra, 'Theoretical Study on Molecules of Interstellar Interest.I. Radical Cation of Noncompact Polycyclic Aromatic Hydrocarbons', Presented Poster at '*Theoretical Chemistry Symposium 2012 (TCS-2012)*', December 19th-22nd, 2012. Held at IIT Guwahati, India.

4. Samala Nagaprasad Reddy and S. Mahapatra, 'Vibronic Interactions and Photo-Physics of Polycyclic Aromatic Hydrocarbons: A theoretical Study', Presented Poster at '*Current Trends in Theoretical Chemistry Symposium 2013 (CTTC-2013)*', September 26th-28th, 2013. Held at BARC, Mumbai, India.

5. Samala Nagaprasad Reddy and S. Mahapatra, Poster Presented at Annual In-House Symposium '*Chemfest-2011, Chemfest-2012 and Chemfest-2013*', February, Held at School of Chemistry, University of Hyderabad, India.

6. Samala Nagaprasad Reddy and S. Mahapatra, 'Polycyclic Aromatic Hydrocarbons-DIB Hypothesis: A theoretical Study' Delivered an Oral Presentation at Annual In-House Symposium '*Chemfest-2014*', February 21st and 22nd, Held at School of Chemistry, University of Hyderabad, India.

7. Samala Nagaprasad Reddy and S. Mahapatra, 'Theoretical Study on Vibronic Interactions and Photo-Physics of Low-Lying Excited Electronic States of Polycyclic Aromatic Hydrocarbons', Delivered an oral presentation at '*International Symposium on molecular spectroscopy 2014 (ISMS-2014)*', June 16th-20th, 2014. Held at University of Illinois, Champaign Urbana, Illinois, Chicago, USA.